

**TECHNICAL
TRANSACTIONS**

**ELECTRICAL
ENGINEERING**

**ISSUE
3-E (13)**

**YEAR
2016 (113)**

**CZASOPISMO
TECHNICZNE**

ELEKTROTECHNIKA

**ZESZYT
3-E (13)**

**ROK
2016 (113)**



**WYDAWNICTWO
POLITECHNIKI
KRAKOWSKIEJ**

TECHNICAL TRANSACTIONS

ELECTRICAL ENGINEERING

ISSUE 3-E (13)
YEAR 2016 (113)

CZASOPISMO TECHNICZNE

ELEKTROTECHNIKA

ZESZYT 3-E (13)
ROK 2016 (113)

Chairman of the Cracow
University of Technology Press
Editorial Board

Tadeusz Tatara

Przewodniczący Kolegium
Redakcyjnego Wydawnictwa
Politechniki Krakowskiej

Chairman of the Editorial Board

Józef Gawlik

Przewodniczący Kolegium
Redakcyjnego Wydawnictw
Naukowych

Scientific Council

Jan Błachut
Tadeusz Burczyński
Leszek Demkowicz
Joseph El Hayek
Zbigniew Florjańczyk
Józef Gawlik
Marian Giżejowski
Sławomir Gzell
Allan N. Hayhurst
Maria Kuśnierova
Krzysztof Magnucki
Herbert Mang
Arthur E. McGarity
Antonio Monestiroli
Günter Wozny
Roman Zarzycki

Rada Naukowa

Electrical Engineering Series Editor

Piotr Drozdowski

Redaktor Serii Elektrotechnika

Section Editor
Native Speaker
Typesetting
Cover Design

Dorota Sapek
Justin Nnorom
Anna Basista
Michał Graffstein

Sekretarz Sekcji
Weryfikacja językowa
Skład i łamanie
Projekt okładki

Basic version of each Technical Transactions magazine is its online version

Pierwotną wersją każdego zeszytu Czasopisma Technicznego jest jego wersja online

www.ejournals.eu/Czasopismo-Techniczne www.technicaltransactions.com www.czasopismotechniczne.pl

Series: Electrical Engineering

3-E/2016

Editor-in-chef:

Piotr DROZDOWSKI, Cracow University of Technology, Poland

Editorial Board:

Konrad DĄBAŁA, Electrotechnical Institute in Warsaw, Poland
Zygfryd GŁOWACZ, AGH University of Science and Technology, Poland
Zbigniew HANZELKA, AGH University of Science and Technology, Poland
Vasyl HUDYM, Cracow University of Technology, Poland
Mariusz JAGIEŁA, Opole University of Technology, Poland
Adam JAGIEŁŁO, Cracow University of Technology, Poland
Krzysztof KARWOWSKI, Gdańsk University of Technology, Poland
Krzysztof KLUSZCZYŃSKI, Silesian University of Technology, Poland
Czesław KOWALSKI, Wrocław University of Technology, Poland
Roman KROK, Silesian University of Technology, Poland
Stefan Tadeusz KULIG, Technische Universität Dortmund, Germany
Marian ŁUKANISZYN, Opole University of Technology, Poland
Witold MAZGAJ, Cracow University of Technology, Poland
Stefan PASZEK, Silesian University of Technology, Poland
Krzysztof PIENKOWSKI, Wrocław University of Technology, Poland
Andrzej POCHANKE, Warsaw University of Technology, Poland
Mihaela POPESCU, University of Craiova, Romania
Zbigniew PORADA, Cracow University of Technology, Poland
Jan PROKOP, Rzeszow University of Technology, Poland
Mieczysław RONKOWSKI, Gdańsk University of Technology, Poland
Volodymyr SAMOTYY, Cracow University of Technology, Poland
Maciej SIWCZYŃSKI, Cracow University of Technology, Poland
Bohumil SKALA, University of West Bohemia, Czech Republic
Grzegorz SKARPETOWSKI, Cracow University of Technology, Poland
Tadeusz SOBCZYK, Cracow University of Technology, Poland
Dariusz SPAŁEK, Silesian University of Technology, Poland
Adam SZELAĞ, Warsaw University of Technology, Poland
Adam WARZECHA, Cracow University of Technology, Poland
Tomasz WĘGIEL, Cracow University of Technology, Poland
Konrad WEINREB, Cracow University of Technology, Poland
Mieczysław ZAJĄC, Cracow University of Technology, Poland

Executive Editors:

Maciej SUŁOWICZ, Cracow University of Technology, Poland

WOJCIECH CZUCHRA*

THE INFLUENCE OF CONVERTER CABLES SCREENING ATTENUATION ON RADIATED ELECTROMAGNETIC DISTURBANCES FROM CONVERTER DRIVE

WPLYW TŁUMIENNOŚCI EKROWANIA KABLI PRZEKSZTAŁTNIKOWYCH NA EMISJĘ ZABURZEŃ ELEKTROMAGNETYCZNYCH PROMIENIOWANYCH NAPĘDU PRZEKSZTAŁTNIKOWEGO

Abstract

Screening attenuation as a parameter of screened cables used in converter systems is one of the indicators of screen efficiency. Catalogue data rarely considers that parameter, especially with the division on frequency bandwidths. Screening efficiency may be deduced by analysis of the cable's construction and type, but based on this, it may only be roughly estimated. The results of screening attenuation tests in a wide frequency bandwidth for chosen cable types are presented in the article. The methods of cable parameters testing based on standard PN-EN 50289-1-6:2009: Communication cables – Specifications for test methods. Part 1–6: Electrical test methods – Electromagnetic performance, were used. Afterwards, the emission of radiated electromagnetic disturbances of the converter drive was measured. The converter was using chosen cable types, for which screening attenuation was determined. Comparisons of the obtained results were presented and the influence of the screen type and cable parameters on the emission of radiated electromagnetic disturbances was analyzed. The obtained measurement results and presented analysis in the field of electromagnetic compatibility may be useful for designers of converter drive systems.

Keywords: cables attenuation, radiated electromagnetic disturbances, converter drive, electromagnetic compatibility

Streszczenie

Tłumienność ekranowania jako parametr kabli ekranowanych stosowanych w układach przekształtnikowych jest jednym z wyznaczników skuteczności działania ekranu. Dane katalogowe rzadko uwzględniają ten parametr kabli szczególnie z podziałem na pasma częstotliwości. O skuteczności ekranowania można wnioskować analizując budowę i rodzaj zastosowanego ekranu kabla lecz na tej podstawie można ją określić jedynie szacunkowo. W artykule przedstawiono wyniki badań tłumienności ekranowania w szerokim paśmie częstotliwości dla wybranych rodzajów kabli ekranowanych. Zastosowano metody badań parametrów kabli na podstawie normy PN-EN 50289-1-6:2009: Kable telekomunikacyjne – Metody badań – Część 1–6: Metody badań właściwości elektrycznych – Właściwości elektromagnetyczne. Następnie zmierzono emisję zaburzeń elektromagnetycznych promieniowanych falownikowego napędu przekształtnikowego wykorzystującego wybrane wcześniej rodzaje kabli dla których wyznaczone były tłumienności ekranowania. Zaprezentowano zestawione porównania uzyskanych wyników i przeanalizowano wpływ rodzaju ekranu i parametrów kabli na emisję zaburzeń elektromagnetycznych promieniowanych. Uzyskane wyniki pomiarów i przedstawione analizy z zakresu kompatybilności elektromagnetycznej mogą być przydatne dla projektantów przekształtnikowych układów napędowych.

Słowa kluczowe: tłumienność ekranowania kabli, zaburzenia elektromagnetyczne promieniowane, napęd przekształtnikowy, kompatybilność elektromagnetyczna

* Ph.D. Eng. Wojciech Czuchra, Department of Traction and Traffic Control, Faculty of Electrical and Computer Engineering, Cracow University of Technology.

1. Introduction

Electromagnetic compatibility of converter drive systems includes, among others, issues of radiated electromagnetic disturbance emission. Standard PN-EN 61800-3 defines the scope of standard measurements of that emission in the bandwidth from 30 MHz to 1 GHz [1]. A high operating frequency together with high signals' steepness at output of converters used in drive systems may be a reason of the increased levels of radiated electromagnetic disturbances generated by the system. The generated disturbances, which depend on system parameters and the control method, occur in a frequency bandwidth considered in standard [1] for typical power drive systems. In some systems, there are several converter drive systems differing in parameters and purpose. Electrical traction vehicles may be an example, where the considered systems operate as main drives or auxiliary drives. The emission of radiated disturbances for those systems is investigated in a much wider frequency bandwidth – from 9 kHz to 1 GHz [2, 3]. Application of screened cables with low attenuation properties may cause a necessity to reduce emission by additional filtering methods with application of individually designed RFI filters [4].

At the design and construction stage, there is a possibility for proper selection of converter cables with respect to their attenuation parameters. Screening attenuation parameter is usually provided by telecommunication cables manufacturers. In the case of cables used in converter drive systems, catalogue data rarely provides that parameter. Manufacturers of screened cables used for motor control in converter drives provide data about the screen efficiency in a very limited range. The only reference to the screen effectiveness evaluation is the type of screen and a description of its performance. By taking into consideration the way of screen production, its effectiveness may be only roughly determined. The need of conducting individual and comparative tests of various types of screened converter cables appears, which will allow to evaluate their electromagnetic attributes (screening).

The effectiveness of a cable screen can be determined by conducting suitable measurements. Screen effectiveness can be determined by measurements of transfer impedance or screening attenuation [5, 6]. Numerous publications mainly present the results of transfer impedance measurements of screened cables. Analyses of cables' screening efficiency are most often conducted based on standard methods, but alternative, simplified or modified methods are also proposed [7]. Primary tests regard electromagnetic attributes of screened cables or various cable connections [7]. Theoretical analysis and simulation methods in that scope are proposed as well [5, 6]. The standard PN-EN 50289-1-6: Communication cables – Specifications for test methods. Part 1–6: Electrical test methods – Electromagnetic performance [8] is the basic document, which describes the methods of cable testing. The article presents test results of converter cables' screening attenuation in a wide frequency range of 1 MHz to 1 GHz with the use of the triaxial method. A comparison of the obtained results was conducted for chosen screened cable types with division into frequency subscopes. The frequency range, for which screening attenuation measurements were performed, is a typical band for determining that value. The determination of the cables' screening properties for lower frequency ranges about several dozen kHz is an important issue, but it requires the use of measuring methods and determination of another parameter e.g. transfer impedance Z_T .

2. Tested system and research methodology

2.1. Determination of cables screening attenuation

In the triaxial method, a measuring set for screening attenuation consists of three coaxial elements [8]. The tested circuit consists of an outer and an inner circuit, where the inner circuit is the tested cable, while the outer one consists of a screen and coaxial pipe (Fig. 1).

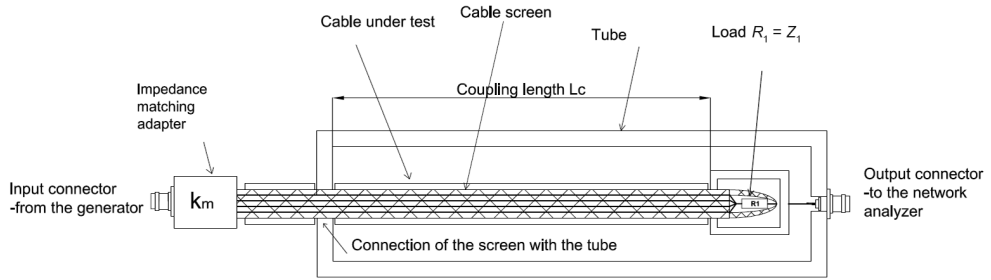


Fig. 1. The arrangement for determining the screening attenuation of screened cables

An aluminum pipe with an inner diameter of 50 mm and length of 2.2 m acts as the outer conductor of the outer circuit and it is connected to the screen at the side of the signal input. The inner diameter of the pipe in relation to cable screen's diameter is matched to ensure characteristic impedance of the outer circuit equal or higher than the receiver input resistance. The pipe must be long enough to wave overlapping in narrow frequency ranges. One end of the cable is loaded with well-screened resistor R_1 , of which value equals to the characteristic impedance of coaxial system Z_1 . The method of determining the unknown characteristic impedance Z_1 is precisely described in standard PN-EN 50289-1-6. There is a joint on the other end of the circuit, which enables connection with a generator.

Screening attenuation is a ratio of power inserted into a cable (P_{feed}) and the maximal peak radiated power ($P_{rad,max}$) [8]:

$$a_s = 10 \cdot \log_{10} \left| \frac{P_{feed}}{P_{rad,max}} \right| \quad (1)$$

Two types of screened cables were chosen for testing: LiYCY $4 \times 2.5 \text{ mm}^2$ (single screen) and 2YSLCY $4 \times 2.5 \text{ mm}^2$ (double screen), destined for converter systems. The first one contains a screen made of tinned copper strings with a coverage density of 80%, while the second one contains a screen made of aluminum foil and a screen made of tinned copper wire braiding with a coverage density of 80%. The tested screened cables are considered as a quasi-coaxial circuit and all conductors were connected together at both ends. Double

screens also are connected together on both ends along the whole circumference. The tested cable sample was connected to a generator, outer circuit (pipe) and spectrum analyzer. The measurement of the voltage ratio at the output of the outer circuit and at the input of the tested cable was conducted with automatic frequency tuning, in a whole measured range. Spectrum analyzer Rohde&Schwarz type FSL3 with an operating frequency range from 9 kHz to 3 GHz, equipped with a generator with a bandwidth of 1 MHz–1 GHz, was used for carrying out the measurements.

To determine the real value of screening attenuation, the losses introduced by conforming system and connection cords must be taken into account. Connection cord attenuation was included in the calibration process. Screening attenuation of the cable a_s in [dB] at standardized environment impedance was calculated from formula (2):

$$a_s = 20 \cdot \log_{10} \left| \frac{U_1}{U_2} \right|_{\min} + 10 \cdot \log_{10} \left(\frac{2 \cdot Z_s}{Z_1} \right) - a_z \quad (2)$$

where:

- a_z – conforming system attenuation in [dB],
- Z_1 – characteristic impedance of tested cable in [Ω],
- Z_s – standardized environment impedance in [Ω] (equals 150 Ω),
- U_1 – voltage at generator's output in [V],
- U_2 – voltage at receiver's input in [V].

The view of the measuring stand equipped with a system used for testing the screening attenuation of converter cables is shown in Fig. 2. The measuring stand was verified by measurements of coaxial cable with a known value of screening attenuation.



Fig. 2. The view of the measuring stand

2.2. Measurement of radiated electromagnetic disturbances emission

The conducted measurements of radiated electromagnetic disturbances emission had an engineering, comparative character. Measurements were conducted with equipment, which parameters meet standard requirements, for antenna as well as for spectrum analyzer.

During measurements the following measuring devices were used: spectrum analyzer Rohde&Schwarz type FSL3, TRILOG broadband antenna VULB 9168 with measured bandwidth from 30 MHz to 1 GHz. Measurement of the radiated emission carried out at 3 m from investigated converter drive and the measurement results were converted to a standard distance of 10 m by the subtraction of 10 dB. Two measurement rounds were carried out, with a single screened cable between converter and motor, and with a double screened one. The length of both cables was 4 m. The converter was operating with a carrier frequency of 3 kHz, an output frequency of 50 Hz and a phase supply current of 4 A. Despite the fact that the measurement ground did not fulfil standard requirements, the measurement results may be useful at estimating the influence of screened cable types on the emission of radiated disturbances of converter drives. The view of the measuring stand of the tested converter drive system is shown in Fig. 3.



Fig. 3. The view of the measuring stand of the tested converter drive system

3. Results of cables' screening attenuation tests

The measurement of screening attenuation for two types of cable was conducted in frequency range from 1 MHz to 1 GHz with division of given range into subranges: 1–100 MHz, 100–500 MHz, 500 MHz–1 GHz. Owing to the fact, we can gather information about screening attenuation in a particular frequency bandwidth and more precise similarity of the tested parameter than during measurement for the whole range.

The above plots present a comparison of the screening attenuation measurement results for a single screened cable and a double screened cable. Through an analysis of particular bandwidths, the obtained results show that, in all frequency bandwidths, the double screened cable has a higher level of screening attenuation. An evident difference of the tested parameter can be noticed for the compared cables. Both cables reach maximal attenuation value in the frequency range from 500 MHz to 1 GHz (Fig. 6). Minimal attenuation value for both tested cables occurs in the frequency range from 100 MHz to 500 MHz (Fig. 5). Taking

into consideration the whole frequency range from 1 MHz to 1 GHz, the minimal value from all subranges (obtained for bandwidth 100 MHz to 500 MHz) was assumed as resultant screening attenuation for both cables. Screening attenuation for the single screened cable amounts to 30 dB and 40.5 dB for the double screened one. It needs to be mentioned that, besides applying a double screen to cable, other parameters, e.g. screen thickness, coverage density and conductance of screen's material, have a significant impact on screening effectiveness.

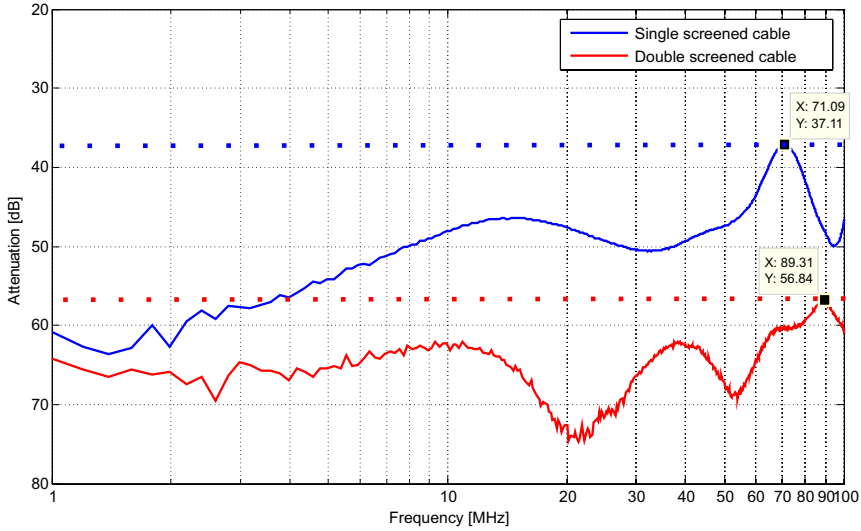


Fig. 4. Screening attenuation in frequency range 1–100 MHz

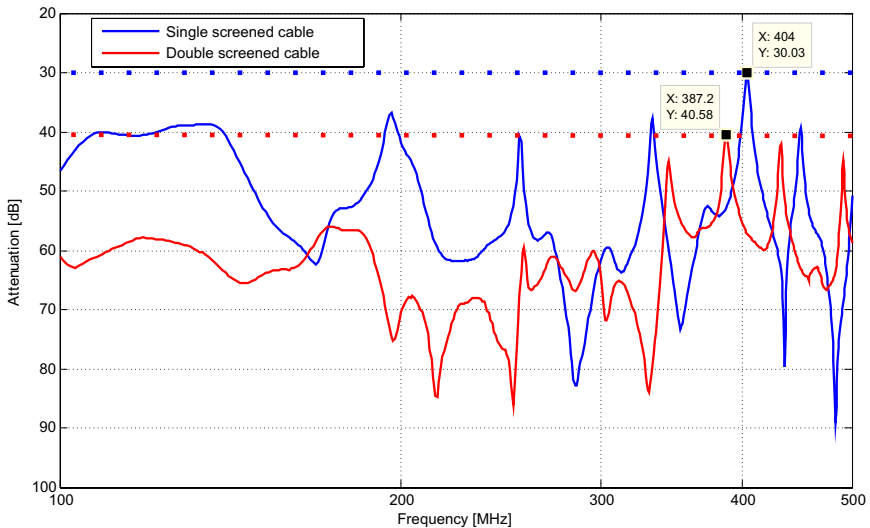


Fig. 5. Screening attenuation in frequency range 100–500 MHz

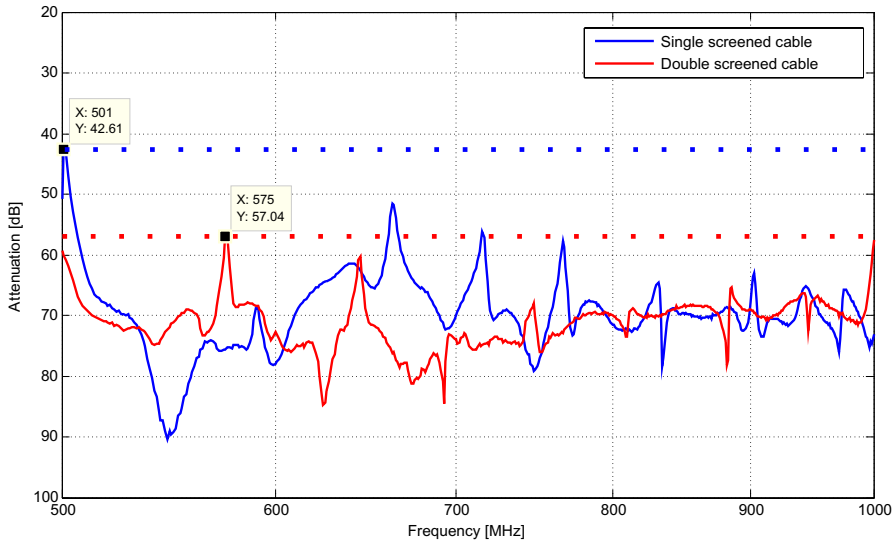


Fig. 6. Screening attenuation in frequency range 500–1000 MHz

4. Results of radiated electromagnetic disturbances tests

Laboratory tests of radiated electromagnetic disturbances for a standard frequency bandwidth from 30 MHz to 1 GHz were carried out due to the significant contribution of the investigated system in the disturbance emission in that frequency bandwidth [1]. The frequency subrange was chosen for analysis after considering the whole bandwidth. In the chosen range, the radiated disturbances definitely exceeded background signals (investigated drive switched off). The analyzed emission levels concern the standard subrange from 30 MHz to 80 MHz.

The results obtained for that bandwidth show noticeable difference in the emission of radiated electromagnetic disturbances. Higher levels of disturbance emission for the analyzed frequency bandwidth occur for the converter drive system working with a single screened cable. It shows the influence of the cable screen's parameters on the radiated emission. Investigation of the converter system with double screened cable showed disturbance emission decrease of maximally 14 dB (peak detector) and 9 dB (quasi-peak detector) for the frequency range 61 MHz to 77 MHz (Fig. 7 and 8). Limit quasi-peak values for measuring distance of 10 m according to standard PN-EN 61800-3 have been marked on standard bandwidth disturbance charts with green. The measured emission levels of radiated disturbances for the quasi-peak detector exceeded the limit values, especially for PDS (power drive system) category C1 (Limit 1). It speaks in favour of using double screened cables, especially in a situation, when radiated emission of the tested system may be reduced only with outer methods. It will allow thereafter to fulfil the requirements of the system's electromagnetic compatibility.

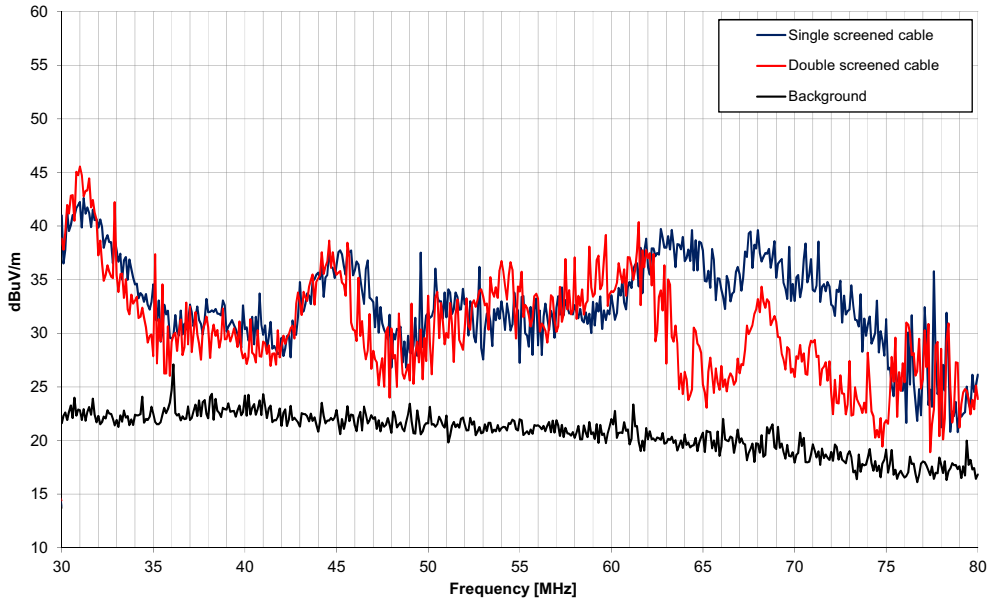


Fig. 7. Comparison of radiated electromagnetic disturbances for single and double screened cable (peak detector)

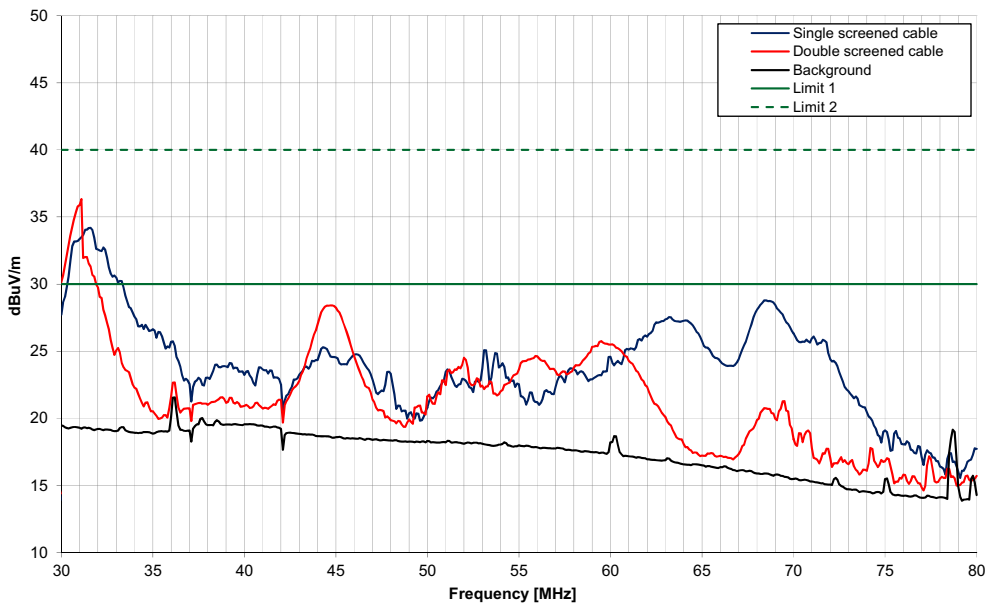


Fig. 8. Comparison of radiated electromagnetic disturbances for single and double screened cable (quasi-peak detector, Limit 1 – category C1, Limit 2 – category C2 to PN-EN 61800-3)

5. Summary

The conducted research on converter cables' screening attenuation and emission of radiated electromagnetic disturbances of laboratory converter drive may be a basis for evaluating the influence of screened cables' parameters on system's electromagnetic compatibility. The article presents the methodology and exemplary results for determining one of the parameters defining the electromagnetic properties of cables applied in converter drive systems. Screening attenuation of cables was determined and analyzed. The stand was made according to measuring method description and advices included in the standard. The stand was also verified through measurements. The obtained screening attenuation results for two cable types with a different screen construction allowed us to determine the level of this parameter for converter cables. The division of the conducted tests into subranges allows us to indicate frequency bandwidths where screening effectiveness is the highest and where it is the lowest.

The conducted measurements of radiated electromagnetic disturbances' emission had an engineering and comparative character. Despite the fact that the obtained differences in the emission levels were not significant, they confirmed a positive influence of double screened cable's higher attenuation on the radiated emission of the tested system. It should be noted that laboratory measurements were carried out for relatively short cables (4 m). The influence of the screened cable's attenuation may be by far more evident for considerably longer cables used in real systems.

When comparing the obtained results, we can notice a significant advantage of screening attenuation for cables with double screen in all the frequency bandwidths. On the basis of the conducted measurement and analysis, we can confirm the correctness of applying double screened cables in converter systems. It will result in the limitation of the emitted electromagnetic disturbances and provide an electromagnetic compatibility of a system.

References

- [1] Standard PN-EN 61800-3:2008 – Adjustable speed electrical power drive systems – Part 3: EMC requirements and specific test.
- [2] Czuchra W., Jakubas W., Zając W., *Disturbances in track circuit from magnetic fields of traction vehicles*, Technical Transactions, vol. 1-E/2011, 31–39.
- [3] Czuchra W., Zając W., *Investigation of electromagnetic interference generated by a tram and a trolley-bus with inverter drives*, International Conference on ship propulsion and railway traction systems, Bologna, Italy, 4.5.6 October 2005.
- [4] Czuchra W., Mysiński W., Zając W., *Modelling and testing of RFI filter for a trolleybus transistor inverter*, EPE 2009 13th European Conference on Power Electronics and Applications, Barcelona, Spain, 8–10 September 2009.

- [5] Akcam N., Karatas M.H., *Measurement of Transfer Impedance and Screening Attenuation Effects on Cables Using Tri-axial Method*, International Journal on Technical and Physical Problems of Engineering (IJTPE), Issue 10, Vol. 4, No., March 2012.
- [6] Kreisch K., Kubitzek S., Hofmeister Ch., Barenfanger J., Schugt M., *Transfer Impedance Measurements and Simulations on perforated Fully-Rigid Coaxial Cables with the Line Injection and the Traxial Method*, Proc. of the 2014 International Symposium on Electromagnetic Compatibility (EMC Europe 2014), Gothenburg, Sweden, September 1–4, 2014.
- [7] Mustaq A., Frei S., Siebert K., Barenfanger J., *Analysis of Shielding Effectiveness os HV Cable and Connectors Systems used for Electric Vehicles*, Proc. of the 2013 International Symposium on Electromagnetic Compatibility (EMC Europe 2013), Brugge, Belgium, September 2–6, 2013.
- [8] Standard PN-EN 50289-1-6:2009: Communication cables – Specifications for test methods. Part 1–6: Electrical test methods – Electromagnetic performance.

TOMASZ LERCH, MICHAŁ RAD*

INFLUENCE OF HIGHER HARMONICS ON LOSSES IN INDUCTION MACHINES

WPLYW WYŻSZYCH HARMONICZNYCH NA STRATY W MASZYNI INDUKCYJNEJ

Abstract

The paper summarizes the power loss results in induction machines supplied with distorted voltage. The voltage waveform contained the fifth and seventh harmonics components of adjustable level in the range of 0% to 30%. The influence of the harmonic content on the core and windings losses is of particular interest. The paper investigates the additive impacts of basic and additional losses resulting from distorted power supply conditions.

Keywords: induction machine losses, efficiency standards, power quality

Streszczenie

Artykuł przedstawia wyniki pomiarów strat silnika indukcyjnego zasilanego ze źródła napięcia odkształconego. Napięcie zawierało, prócz składowej podstawowej, także piątą i siódmą składową harmoniczną w zakresie od 0% do 30% w stosunku do składowej podstawowej. Badany był wpływ zawartości składowych na straty w rdzeniu i straty w wirniku silnika. Sprawdzono również czy straty powodowane zawartością poszczególnych składowych są addytywne.

Słowa kluczowe: maszyna indukcyjna, normy sprawności, jakość energii

* Ph.D. Eng. Tomasz Lerch, Assoc. Ph.D. Eng. Michał Rad, Department of Power Electronics and Energy Control Systems, Faculty of Electrical Engineering, Automatics, Computer Science and Biomedical Engineering, AGH University of Science and Technology.

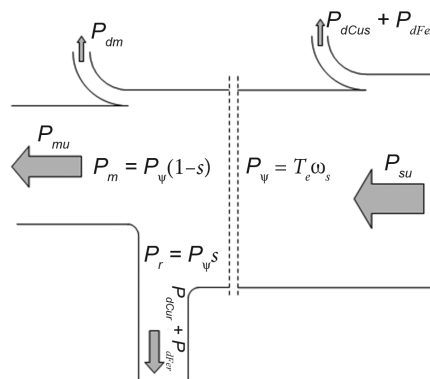
1. Introduction

The new standard IEC 60034–30 (International Electrotechnical Commission), published in 2011, introduces the method of assessing the efficiency ranges of all motors launched to the European market. In the light of the current standard, the class IE2 is required. Efficiency figures provided by manufacturers should be achieved at rated sinusoidal voltage supply conditions [1]. It can be expected that the declared standards may not be fulfilled when machines are supplied from poor-quality power sources. Efficiency standards may not be met by the very same machine operated in the conditions of poor-quality energy supply [2–4]. The quality of energy supply is a complex issue, beyond the scope of the present study, which focuses on the contribution of harmonics only.

The problem of iron losses and the impact of power quality on these losses have been discussed in a number of publications. The causes of losses in soft magnetic materials are described in the works [9, 10]; they also specified the methods of calculating these losses. The same author as in publication [3] describes the method of calculating the losses in rotating machines. The problem of losses increased due to the distorted power was discussed in work [12]. Modeling of losses in rotating machinery was also described in the works [2, 13]. All cited publications focus on modeling and calculating the iron losses caused by sinusoidal or distorted power. This article is a continuation of these studies, presenting the results of laboratory measurements of this problem.

2. Losses in Induction Machine

Typical energy flows and classes of energy losses of induction motors are well known [5, 6]. The flow of active power in an induction machine during a positive rotor slip, involving individual losses, is shown in the diagram in Fig. 1.



P_{su} – stator power; P_{ψ} – rotating field power; T_e – electromagnetic torque; ω_s – rotating field pulsation;
 P_m – mechanical power; P_{mu} – mechanical usable power; s – slip; P_r – rotor power (slip power);
 P_{dCus} – stator winding losses; P_{dCur} – rotor winding losses; P_{dFes} – stator core losses; P_{dFer} – rotor core losses; P_{dm} – mechanical losses

Fig. 1. The flow of active power in an induction machine

Harmonic distortions have a major impact on core and winding losses [6, 7]. The model of core losses is quite complicated and therefore loss prediction is not easy [8–15]. The Authors therefore undertook to directly measure the impacts of the higher harmonics on the loss results. This study is restricted to no-load tests and measurements were taken under varied conditions.

3. Measurements

During the idle run, all energy that is supplied becomes wasted on losses. The supplied energy is quite easy to measure. Voltage and currents are sampled and measured by an analog to digital (A/D) converter card. Voltage is supplied from a programmable AC source, allowing almost any shape of voltage waveform to be generated. A diagram of the measurement system is shown in Fig. 2. For each operating point of the machine, the waveform portion was recorded, with a 20 kHz sampling frequency, and calculations of the active power were performed accordingly [16]. For each case, the full ‘no load test’ was performed, involving power measurements for voltage being varied from 0.2 to 1.2 U_N . All testing was done on a wound-rotor induction machine type SUDg 132M-4A, $U_N = 400$ V, $I_N = 13.0$ A, $n = 1400$ rpm, $P_N = 6.3$ kW.

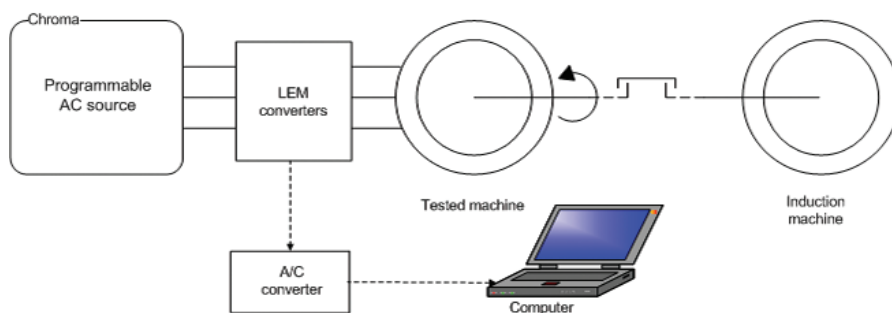


Fig. 2. Diagram of the measurement system

Four cases were considered in the test:

- Case 1: rotor windings are open and rotor is immobile, the fifth harmonic is added
- Case 2: rotor windings are open and rotor is immobile, the seventh harmonic is added
- Case 3: rotor windings are shorted, rotor is in motion, the fifth harmonic is added
- Case 4: rotor windings are shorted, rotor is in motion, the seventh harmonic is added

Seven tests were performed in each case, for 0, 5, 10, 15, 20, 25, 30% of added harmonics amplitude.

3.1. Case 1

The first set of tests was performed on a machine with open rotors windings and with the contribution of the fifth harmonic. Under these conditions, the active power of the supply source is wasted on stator winding losses and iron losses. Figure 3 shows iron losses only. It can

be seen that there is a set of characteristic curves for different levels of harmonics contribution. In the range of 0.2–1 U_n , the differences between curves are very small, indicating that the influence of the fifth harmonic on iron losses is rather minor. Fig. 4 shows a zoomed section of Fig. 3. It appears that the losses are even smaller for higher harmonic contents, which may be because the harmonic component changes the total RMS voltage value. Fluctuations of RMS value of voltage are therefore bigger than loss variations. One has to bear in mind, however, that the chart shows only the loss results obtained for the total RMS value of voltage.

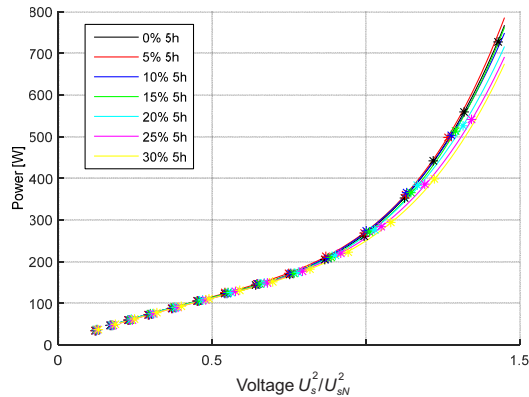


Fig. 3. Iron losses, for voltage with various amount of 5 harmonic added (with winding losses subtracted), open rotor

3.2. Case 2

The results of measurements taken for Case 2 and involving the seventh harmonic contribution were very similar. The zoomed section of the graph near the nominal voltage value is shown in Fig. 5. The losses turned out to be similar to those reported in Case 1.

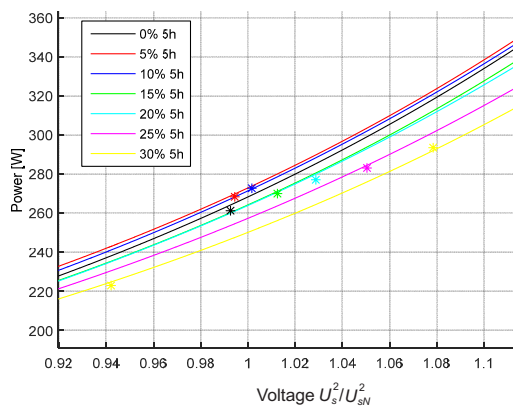


Fig. 4. Iron losses, for voltage with various amount of 5 harmonic added (with winding losses subtracted), zoomed section

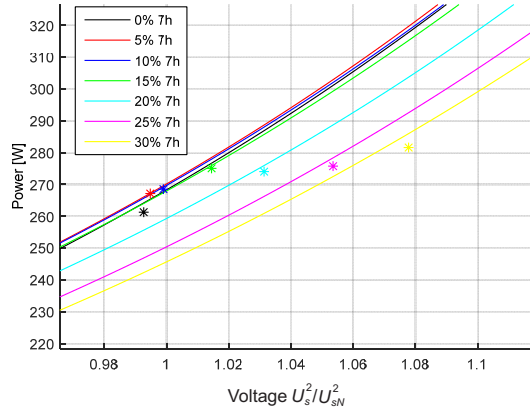


Fig. 5. Iron losses, for voltage with various amount of 7 harmonic added (with winding losses subtracted), zoomed section

3.3. Case 3

During this test, the rotor windings were shorted so the total losses of the machine should involve the core losses and rotor winding losses. Mechanical losses and stator winding losses were subtracted after the measurements. The resistance of the stator windings was measured by the technical method, the same for all tests. It is worthwhile to mention that, in the first and second case, the magnetic field pulsation in the stator and rotor remained the same. Now, when the rotor speed is nearing the synchronous speed, the magnetic field pulsation of the rotor caused by fundamental harmonic is close to zero, whilst the pulsation due to higher harmonics will be nonzero. The fifth harmonic is a positive sequence component and therefore the rotor's magnetic field pulsation due to this component is increased by the rotational speed, giving the rotor current a frequency of 300 Hz. Waveform measurement data seem to corroborate this view (Fig. 6). Fig. 7 shows the characteristics obtained for the

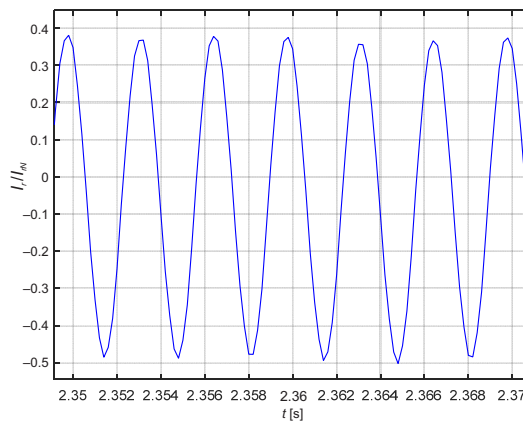


Fig. 6. Rotor current waveform

fifth harmonic contribution. In contrast to Case 1, the losses are clearly dependent on the harmonic contribution. It can be assumed that it is so because of the losses from the rotor's current. The loss increase can be well seen in Fig. 8.

It is readily apparent that the contribution of 30% of the fifth harmonic produces a 30% increase of the losses in relation to those registered for the clear sine waveform.

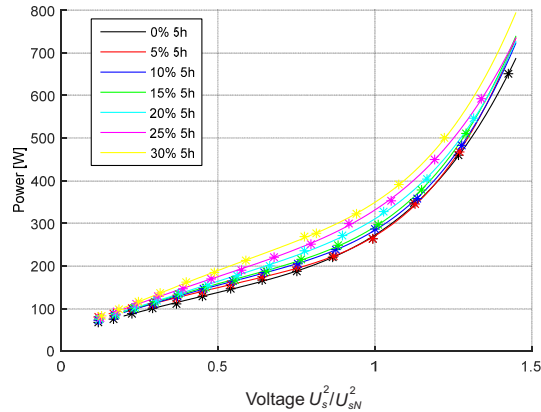


Fig. 7. Idle run losses, for voltage with various amount of 5 harmonic added (with winding and mechanical losses subtracted) shorted rotor

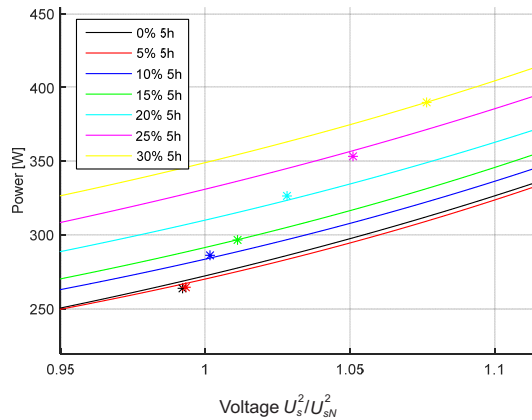


Fig. 8. Idle run losses, for voltage with various amount of 5 harmonic added (with winding and mechanical losses subtracted) shorted rotor, zoomed section

3.4. Case 4

Similar measurements taken for the seventh harmonic reveal a decidedly smaller increase of rotor winding and rotor core losses. It may seem unexpected, as the magnetic field pulsation in the rotor was identical. One has to bear in mind, however, that pulsation is the same because the seventh harmonic is a negative sequence component, and therefore

the magnetic field pulsation in the rotor due to this component is decreased by the rotational speed. Fig. 9 gives a zoomed section of the characteristic showing the contribution of the seventh harmonic.

In the case of the seventh harmonic, the maximal loss increase is about 12% compared to the purely sine waveform supply conditions. The difference between losses registered with the fifth and seventh harmonic contribution is attributable to the damping of higher frequencies by the stator windings.

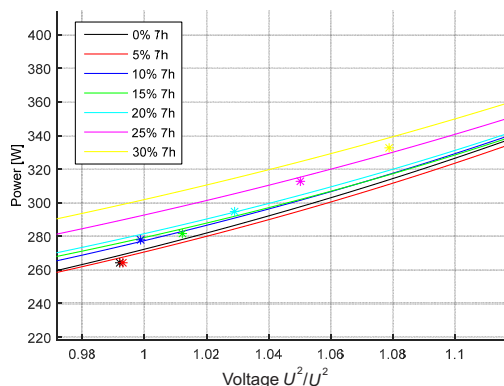


Fig. 9. Idle run losses, for voltage with various amount of 7 harmonic added (with winding and mechanical losses subtracted) shorted rotor, zoomed section

For clarity of presentation, let us consider another characteristic. Fig. 10 plots the losses under nominal voltage versus the level of harmonic contribution. In Case 1 and Case 2, (open rotor) we only obtain iron losses, whereas in Case 3 and Case 4 (shorted rotor), the rotor winding losses are also involved.

The dashed lines in Fig. 10 denote core losses in the rotor and stator due to the fifth and seventh harmonics. Solid lines denote losses registered in Case 3 and Case 4, when the losses

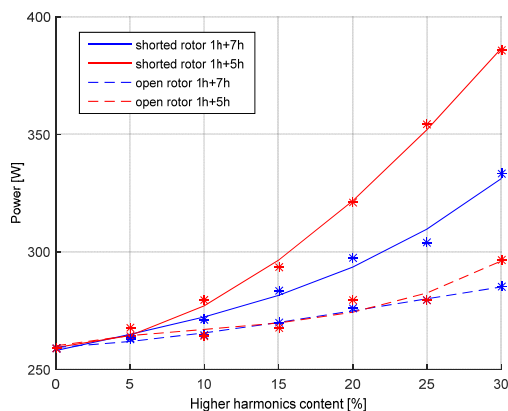


Fig. 10. Losses under idle run, with open and shorted rotor

are further increased by rotor currents. For practical purposes, only the results obtained for harmonic contribution of up to 15% will be relevant. Higher harmonics contributions are rather unusual in real-life conditions, which is why the measurements taken of higher harmonics provide the framework for comparison only. Test results reveal that major loss increases are caused only by the rotor current. Iron losses are increased slightly, and in the same extent for both harmonics (the fifth and seventh).

4. Additivity of losses

Further experiments were performed to check whether the losses due to the fundamental harmonic and higher harmonics would simply add up. Having already measured the loss due to the pure fundamental harmonic, we proceeded to measure losses due to higher harmonics only. The frequency of the applied voltage supply was 250 Hz as well as 350 Hz and the amplitude fell in the range of 0–30% of the nominal value.

As in the previous cases (Case 1 and Case 2), we measured losses while rotor windings were open and the rotor was stalled, and while rotor windings are shorted and the rotor was rotating (Case 3 and 4). To ensure the required rotating speed, the rotor was driven by another induction machine (Fig. 2).

Figure 11 shows experimental results obtained when the rotor windings were open. Upper lines denote results for the distorted supply conditions (fundamental and higher harmonics); lower lines denote the power supply conditions with the contribution of higher harmonics only. The graph reveals the power after deducting losses in stator windings, so iron losses can be clearly seen.

When the losses due to the contribution of fundamental harmonic and higher harmonics are simply added (dashed line in Fig. 12), we obtain values nearing those obtained for the distorted supply conditions (solid lines in Fig. 12).

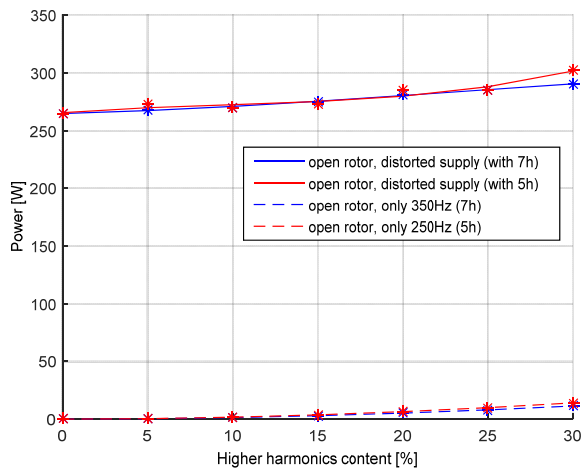


Fig. 11. Study of the additivity of losses. Iron losses

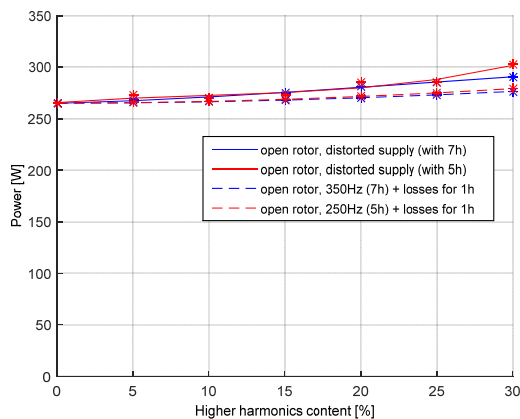


Fig. 12. Study of the additivity of losses. Iron losses, comparison

For a harmonics contribution of 15% or less, the values are very close, while for higher harmonics contributions, the power values tend to differ slightly because of the saturation effect. In other words: voltage supply conditions with higher harmonics contribution tend to shift to the nonlinear area on the iron core magnetization curve.

The results of experiments with shorted rotor windings are presented in Fig. 13. To ensure the same test conditions as in Case 3 and 4, the rotor had to be driven by an additional machine. Therefore, pulsation of higher flux density harmonics in the rotor was the same as in the previous tests. The results are represented by a dashed line in Fig. 13, providing the comparison to Case 3 and 4 (solid lines).

Loss increase is more considerable than in the tests with open rotor windings because of additional losses in rotor windings. Higher harmonics contribution causes the current flow at a frequency of 300 Hz in the rotor windings, as it was discussed before.

The summarized results (see Fig. 14) reveal that losses due to distorted supply conditions are quite similar to those registered for the contributing fundamental harmonic summed with higher harmonics.

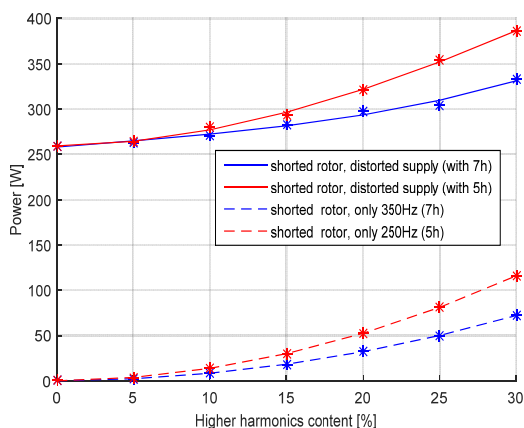


Fig. 13. Study of the additivity of losses. Losses under idle run (P-Pdcu-Pdm)

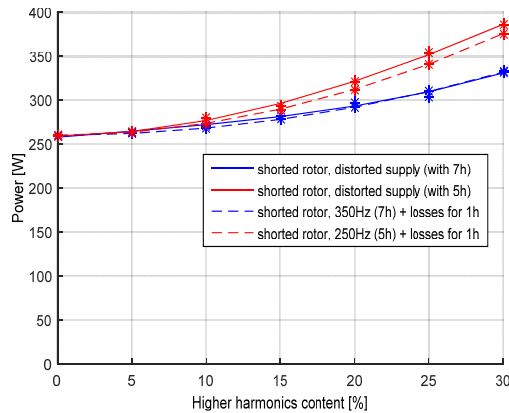


Fig. 14. Study of the additivity of losses. Losses under idle run ($P-P_{dcu}-P_{dm}$), comparison

5. Conclusion

Iron losses depend on higher harmonics in a minor degree only. For harmonics contribution of up to 15%, they practically remain on the same level and they are nearly the same for both the fifth and seventh harmonics.

The loss increased during the tests with shorted rotor windings. This is a normal state of work for the induction machine. Higher losses are attributable to currents induced by higher harmonics in the rotor windings. Here, the fifth harmonic gives rise to higher losses due to the damping of the seventh (and higher) harmonic in stator windings. Besides, it appears that losses due to higher harmonics and the fundamental harmonic tend to add up. The effects they produce in the core and windings of machines are the same, no matter whether contributing jointly or separately.

However, losses caused by higher harmonics seem not to be comparable, almost all of them affect the rotor, not the stator. In some cases, it could be a problem, because of the fact that heat transfer from the rotor is much more difficult than from the stator.

The investigations presented in the article do not cover work under the load, and the influence of the higher harmonics on the rated parameters of the machines was not tested as well.

References

- [1] Wenping C., *Assessment of induction machine efficiency with comments on new standard IEC 60034-2-1*, International Conference on Electrical Machines, Vilamoura, Algarve, Portugal 6–9 Sept. 2008, 1–6.
- [2] Cummings P., *Estimating effect of system harmonics on losses and temperature rise of squirrel-cage motors*, IEEE T IndAppl, 22, 1986, 1121–1126.

- [3] Gała M., Jagieła K., Kepinski M., Rak J., *Influence of high power dc converter drives on operating parameters of induction machines*, ZeszytyProblemowe – Maszyny Elektryczne, 76, 2007, 35–40.
- [4] Polak A., *Additional parasitical effects appearing in induction motors supplied with distorted voltage*, Prace Naukowe Instytutu Maszyn, Napędów i Pomiarów Elektrycznych Politechniki Wrocławskiej, 48, 2000, 21–28.
- [5] Corino S., Romero E., Mantilla LF., *How the efficiency of induction motor is measured?*, International Conference On Renewable Energies And Power Quality ICREPQ'08, Santander, Spain, 12–14 March 2008, 352–354.
- [6] Debruyne C., Desmet J., Derammelaere S., Vandeveld L., *Derating factors for direct online induction machines when supplied with voltage harmonics: a critical view*, IEEE International Electric Machines & Drives Conference (IEMDC), Niagara Falls, ON, Canada 14–17 May 2011, IEEE, 1048–1052.
- [7] Knight A.M., Zhan Y., *Identification of flux density harmonics and resulting iron losses in induction machines with nonsinusoidal supplies*, IEEE T Magn, 44, 6, 2008, 1562–1565.
- [8] Manyage M.J., Mthombeni T.L., Pillay P., Boglietti A., *Improved prediction of core losses in induction motors*, Electric Machines & Drives Conference, IEEE, Antalya, Turkey, 3–5 May 2007, 531–536.
- [9] Bertotti G., *General properties of power losses in soft ferromagnetic materials*, IEEE T Magn, 24, 1988, 621–630.
- [10] Bertotti G., *Dynamic generalization of the scalar Preisach model of hysteresis*, IEEE T Magn, 28, 1992, 2599–2601.
- [11] Bertotti G., Boglietti A., Chiampi M., Chiarabaglio D., Fiorillo F., Lazzari M., *An improved estimation of iron losses in rotating electrical machines*, IEEE T Magn, 27, 1991, 5007–5009.
- [12] Fiorillo F., Novikov A., *An improved approach to power losses in magnetic laminations under nonsinusoidal induction waveform*, IEEE T Magn, 26, 1990, 2904–2910.
- [13] Yamazaki K., Fukushima N., *Iron-loss modeling for rotating machines: comparison between bertotti's three-term expression and 3-D eddy-current analysis*, IEEE T Magn, 46, 8, 2010, 3121–3124.
- [14] Sadowski N., Lajoie-Mazenc M., Bastos J.P.A., Ferreira da Luz M.V., Kuo-Peng P., *Evaluation and analysis of iron losses in electrical machines using the rain-flow method*, IEEE T Magn, 36, 4, 2000, 1923–1926.
- [15] Krings A., Soulard J., *Overview and comparison of iron loss models for electrical machines*, Ecologic Vehicles Renewable Energies EVER, Monte Carlo, Monaco, 25–28 March 2010, 113–119.
- [16] Czarnecki L.S., *Currents' physical components (CPC) concept: a fundamental of power theory*, International School on Nonsinusoidal Currents and Compensation ISNCC, Lagow, Poland, 10–13 June 2008, 1–11.
- [17] McClay C., Williamson S., *The variation of cage motor losses with skew*, IEEE T IndAppl, 36, 6, 2000, 1563–1570.
- [18] Yamazaki K., Kuramochi S., *Additional Harmonic Losses of Induction Motors by PWM Inverters: Comparison between Result of Finite Element Method and IEC/TS*

60034, International Conference on Electrical Machines (ICEM), Marseille, France, 2–5 September 2012, 1552–1558.

- [19] Gnaciński P., Pepliński M., Szweđa M., *Influence of subharmonics and interharmonics voltage on currents in windings of an induction machine*, Zeszyty Problemowe – Maszyny Elektryczne, 92, Katowice 2011, 67–71.

ILJA BOGUSLAWSKY*, IRINA KRUCHININA*,
ALEXANDER LIUBIMTCEV**, LYUBOV SHTAINLE**

METHOD OF EMF TOTAL HARMONIC DISTORTION
CALCULATION OF THE SALIENT
POLE SYNCHRONOUS GENERATOR
(using 2D simulation package)

METODA OBLICZENIA WSPÓŁCZYNNIKA ZAWARTOŚCI
HARMONICZNYCH W SILE ELEKTROMOTORYCZNEJ
DLA WYDATNOBIEGUNOWEGO GENERATORA
SYNCHRONICZNEGO
(z użyciem pakietu symulacyjnego 2D)

Abstract

This paper presents the method of total harmonic distortion factor calculation, which could be applied for the salient pole synchronous generator with electromagnetic or permanent magnet excitation. The method takes into account the saturation of the magnetic circuit and actual winding scheme (including winding with fractional value of slots per pole and phase Q). The calculations are based on 2D FEM simulation that produces the radial (normal to stator surface) component of the magnetic flux density in the air gap. Total harmonic distortion factor is determined as a function of the shape of the pole shoe. The analysis is performed at a constant value of equivalent air gap. The task is to find the shape of the pole shoe that guarantees the minimal value of the distortion factor K_{DIST} .

Keywords: voltage harmonics, salient pole synchronous generator, total harmonic distortion

Streszczenie

W artykule przedstawiono metodę obliczania współczynnika zawartości harmonicznych, która może być stosowana dla wydatnobięgunowego generatora synchronicznego ze wzbudzeniem elektromagnetycznym lub z magnesami trwałymi. Metoda uwzględnia nasycenie obwodu magnetycznego i rzeczywisty schemat uzwojenia (łącznie z uzwojeniem o ułamkowej wartości liczby zębów na biegun i fazę Q). Obliczenia są oparte na symulacji MES 2D, przy założeniu promieniowego przebiegu (normalnego do powierzchni stojana) składowej indukcji magnetycznej w szczelinie powietrznej. Współczynnik zawartości harmonicznych jest określony jako funkcja kształtu nabiegunkownika. Analizę prowadzi się przy stałej wartości zastępczej szczeliny powietrznej. Celem jest znalezienie kształtu nabiegunkownika, gwarantującego minimalną wartość współczynnika odkształcenia K_{DIST} .

Słowa kluczowe: harmoniczne napięcia, wydatnobięgunowy generator synchroniczny, współczynnik zawartości harmonicznych

* Ilja Boguslawsky, Prof. of chair “Electrical Machines”, TU “Politech”, St-Petersburg, PEL¹, Inst. Silic. Chem. of RAS², St-Petersburg, collaborator, senior member of IEEE, Irina Kruchinina – Dr. of sc. (engineering), deputy director of Inst. Silic. Chem. of RAS², St-Petersburg, head of base chair “Nanomaterials in electromechanical and electrotechnical devices” in the TU “Aerospace Instrumentation”, St-Petersburg, senior lecturer of base chair “Nanomaterials in microelectronics” in the TU “LETI”, St-Petersburg, member of IEEE**.

** Alexander Liubimtcev – PEL¹ of Inst. Silic. Chem. of RAS², St-Petersburg, engineer, Lyubov Shtainle – PEL¹ of Inst. Silic. Chem. of RAS², St-Petersburg, researcher.

¹ PEL: Power and ecology laboratory of Inst. Silicon Chemistry, St-Petersburg.

² RAS: Russian Academy of Sciences.

1. Introduction

Total harmonic distortion (THD) factor K_{DIST} is the measure of the line-to-line voltage wave deviation from the sinusoidal form in no-load state. The THD is limited (in accordance with GOST and IEC [1]) for generators with rated power above 100 kVA: $K'_{\text{DIST}} \leq 5\%$, for generators with rated power from 10 kVA to 100 kVA: $K'_{\text{DIST}} \leq 10\%$. This includes generators of various types: hydro generators operating in power lines, large low-speed diesel generators (10–50 MW, 100–250 rpm), working both independently and in power grid, high-speed generators with permanent magnet excitation driven by gas turbines and others.

The restriction of the THD is related to the fact that the higher harmonics in the electromotive force (EMF) generator curve cause:

- Noise in communication lines, located near power network,
- Resonance and overvoltage in power transmission lines [2],
- Additional losses in the windings and stator core of the generators,
- Vibration of the windings and the stator core; higher noise level.

Many factors affect THD, including the form of mutual magnetic flux in the air gap, the number Q of slots per pole and phase of the stator winding. To create high-speed generators and generators with very low speed, it is often necessary to design the stator winding with the number of Q , close to unity, in some cases, for $Q < 1$. This requires a thorough analysis of the higher harmonics of the EMF [3–5]. Investigation of the distortion factor for non-salient generators is discussed in [6].

The distortion factor K_{DIST} estimation is included in the procedure of electrical generator testing in practice [1]. The line-to-line EMF of generator in no-load state is recorded in time. If the winding scheme is symmetrical, the EMF value is measured between any two line terminals; for example, between phase A and phase B terminals. The Fourier transform decomposes EMF (*time*) in a series of frequencies, which are used to calculate the total harmonic distortion factor K_{DIST} by the methods described in GOST and IEC [1].

To determine the distortion factor K_{DIST} , it is required to:

- Calculate magnetic flux (radial component) distribution in the air gap and the amplitudes of its harmonics,
- Calculate frequencies and amplitudes of the harmonics in the generator output EMF waveform.

The method presented solves both these problems using 2D FEM simulation package.

2. Calculation of the magnetic flux (radial component) distribution in the air gap and the amplitudes of its harmonics

The waveform of magnetic flux in the air gap at no-load state depends on the shape of the pole shoe (its width b_p and gap under the pole), the shape of the stator tooth zone and the saturation of the generator magnetic circuit.

2.1. Shape of the pole shoe account

The pole shoe has a circular shape. The center of the circle lays on the pole axis of the symmetry. The radius of the circle is calculated from the relation [2]:

$$R_p = D_{IN} / [2 + 8 \cdot D_{IN} \cdot (\delta_{MAX} - \delta_{MIN}) / b_p^2] \quad (1)$$

where:

- D_{IN} – stator inner diameter,
- $\delta_{MIN}, \delta_{MAX}$ – the minimum and maximum value of the air gap under the pole,
- b_p – pole shoe width.

The circle segment to the pole pitch τ ratio is $\alpha = b_p / \tau$, where τ is the pole pitch. In power generators, the value of α is usually [2]: $0.55 \leq \alpha \leq 0.8$.

It is convenient to define new variables: the air gap ratio is $\Lambda_{GAP} = \delta_{MAX} / \delta_{MIN}$ and the value of equivalent (average) air gap δ_{EQ} under the pole [2]:

$$\delta_{EQ} = \delta_{MIN} [1 + (\Lambda_{GAP} - 1)/3] \quad (2)$$

The ratio Λ_{GAP} is usually lays within [2]: $1.2 \leq \Lambda_{GAP} \leq 2$.

Taking into account (2) the relation (1) becomes:

$$R_p = D_{IN} / \{2 + 8 \cdot D_{IN} \cdot \delta_{EQ} \cdot (\Lambda_{GAP} - 1) / [1 + 0.333 \cdot (\Lambda_{GAP} - 1)] b_p^2\} \quad (3)$$

The equivalent air gap δ_{EQ} and the fundamental harmonic of the radial component of the magnetic flux provides the data for the rotor magneto-motive force (MMF) calculation in no-load state [2].

If the stator inner diameter D_{IN} and the equivalent air gap δ_{EQ} are considered to be pre-defined parameters, then the pole shoe curvature radius R_p is a function of the air gap ratio Λ_{GAP} and the pole shoe width b_p : $R_p = f(b_p, \Lambda_{GAP})$.

Therefore, the problem is to find the ratio Λ_{GAP} , which provides near sinusoidal magnetic flux distribution along the pole pitch. This problem is discussed in [7], but the saturation of the magnetic circuit is estimated approximately there, and the stator teething is represented only by the Carter factor [8, 9]. In fact, Carter factor does not reveal the teeth harmonics' influence on the distortion factor K_{DIST} . These harmonics are determined by the value Q of slots per pole and phase of the stator winding.

2.2. Stator tooth zone geometry. Generator magnetic circuit saturation level

It is a common solution for the stator tooth zone that the ratio of the slot width b_{SL} to the tooth pitch t_{ST} is: $b_{SL} / t_{ST} \approx 0.5$ (for rectangular slots). There is guidance [2] on the typical value of the magnetic flux density in stator elements. For example, for electrical steels used for powerful salient-pole machines, the magnetic flux density in the tooth usually does not exceed $B_z \leq 1.8$ T (measured at 65% of the tooth height, counting from the bottom of the slot).

2.3. Method of the magnetic flux linkage calculation at no-load state

Initial data for magnetic flux calculation are:

- Stator/rotor cross-section dimensions in a cylindrical coordinate system:

$$G = f(\rho, \theta),$$

where:

- ρ – radius-vector,
- θ – central angle.

- Rotor MMF at no-load state of the generator or rotor permanent magnet parameters.

The problem is to find (optimize) geometric dimensions $G = f(\rho, \theta)$, including the pole shoe radius $R_p = f(\Lambda_{\text{GAP}}, b_p)$ so that the factor K_{DIST} value is minimal (or less than specified limit).

This optimization problem is solved numerically. 2D FEM simulation software [10] is used to calculate magnetic field in generator cross section (Fig. 1). The software solves Maxwell's equations in the differential form [11] operating with vector magnetic potential \mathbf{A} ($\mathbf{B} = \text{curl } \mathbf{A}$) [12].

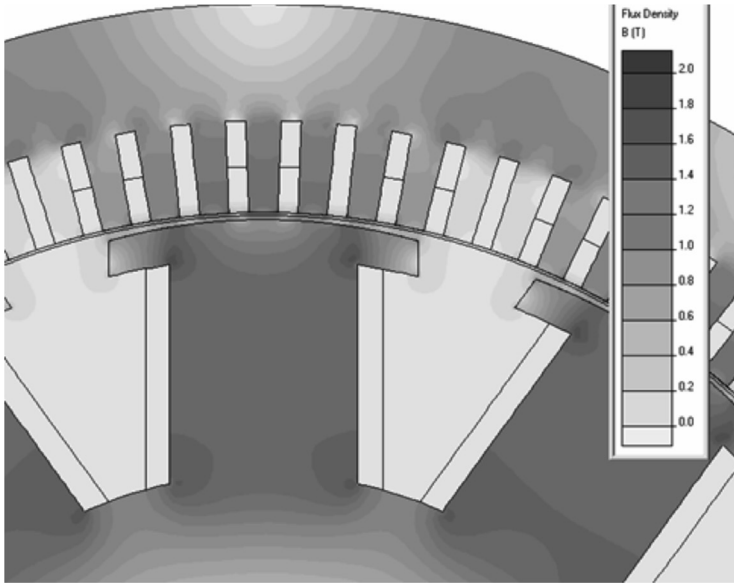


Fig. 1. Magnetic flux density distribution in the cross-section of the 2D model of the synchronous salient-pole generator (see Appendix 2) in no-load state. $\Lambda_{\text{GAP}} = 1.6$, $b_p/\tau = 0.70$

2.4. Harmonics spectrum of the magnetic flux (radial component) in the air gap

The magnetic flux radial (normal) component is used to calculate the stator winding EMF at no-load state. The flux is measured along the circular arc with radius $\rho = D_{\text{IN}} - \delta_{\text{EQ}}$. The results post-processing (from calculated magnetic field distribution to EMF value) include several stages:

- Extracting the magnetic flux density $b(\theta)$ in the air gap along the circular arc with radius $\rho = D_{\text{IN}} - \delta_{\text{EQ}}$ (fully automated in simulation package [10]) and θ is the angular coordinate.
- Calculation of the radial component the magnetic flux density $b_r(\theta)$ along the same circular arc (see Fig. 2).
- Decomposition of the $b_r(\theta)$ in the harmonic series.

For windings with integer Q (slots per pole and phase), the $b_r(\theta)$ is periodic in interval $T_{\text{INT}} = \pi \cdot (D_{\text{IN}} - 2 \cdot \delta_{\text{EQ}}) / p$. For windings with fractional number Q , the periodic interval should include the full circle length [13–18]:

$$T_{\text{FR}} = \pi \cdot (D_{\text{IN}} - 2 \cdot \delta_{\text{EQ}}) \quad (4)$$

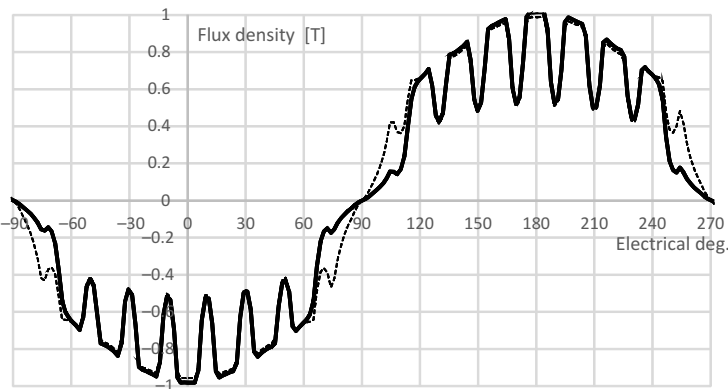


Fig. 2. Flux density distribution in the air gap of the synchronous salient-pole generator (see Appendix 2) in no-load state. $\Lambda_{\text{GAP}} = 1.6$. Solid line corresponds to the $b_p/\tau = 0.70$ case, dashed line corresponds to the $b_p/\tau = 0.80$ case

In some types of the machines (especially for slow-speed electrical machines with a large number of pole pairs), the winding scheme could be constructed as unsymmetrical on purpose: to reduce the length of the balance connectors between the phase zones [2]. In such stator windings (even with integer Q), the output EMF is not balanced between phase zones [2].

It is recommended to use the full circle length as a periodic interval T_{FR} for both types of the winding schemes: with fractional number Q (especially for $Q < 1$) and for integer Q . This allows to find not only the harmonics of the output EMF, but also its phase unbalance.

The result of the decomposition of the magnetic flux density radial component $b_r(\theta)$ in harmonics series in the interval T_{FR} can be represented as a sum of N of harmonics:

$$b_r(\theta) = \sum \underline{B}_N \cdot \exp(j \cdot \Psi_N) \quad (5)$$

where:

$\underline{B}_N = |B_N| \cdot \exp(j \cdot \Theta \cdot N)$ is a complex amplitude (phasor) of the N th-harmonic,
 Ψ_N – phase angle of the N th-harmonic.

These values are stored in Table 1 and used for the harmonics calculation of the stator phase winding output EMF. The decomposition in harmonics is an automated simulation package [10] and is not discussed in this paper.

Table 1

Harmonics of the magnetic flux density radial component: complex amplitudes (phasor) \underline{B}_N and phase angles Ψ_N . The periodic interval is chosen according to (4)

\underline{B}_N	\underline{B}_1	...	\underline{B}_R	\underline{B}_S	\underline{B}_U	...	\underline{B}_W	\underline{B}_K	...	\underline{B}_M
Ψ_N	Ψ_1	...	Ψ_R	Ψ_S	Ψ_U	...	Ψ_W	Ψ_K	...	Ψ_M

Indices of 1... $R, S, U...$ $W, K...$ M in Table 1 denote the harmonics numbers. Following groups of harmonics could be distinguished:

- from 1 to R are harmonics of “low” order,
- $S = p$ is fundamental harmonic,
- from U to W are “high” harmonics (with order below than tooth harmonics order),
- from K to M are “high” harmonics (with order higher than tooth harmonics order).

3. Harmonics of the generator output EMF

The generator stator winding EMF calculation based on the results of harmonics calculation of the magnetic flux radial component (Table 1) is the second stage of the distortion factor K_{DIST} estimation.

First, the EMF harmonics related to the stator teething are calculated. Then, the equations are derived for EMF harmonics calculation of any particular order N , and finally, the distortion factor is evaluated.

3.1. EMF “tooth” harmonics

3.1.1. EMF “tooth” harmonics of the winding with integer value of Q (slots per pole and phase)

Typically, salient-pole generators with torque value below 20 tonne-force·meter (for example, a series of high-speed diesel generators with rated power of 0.5–10 MW and speed of 500–1500 rpm) are usually constructed with windings with integer value of Q [2, 7–11].

EMF tooth harmonics’ order that has maximum amplitude is calculated from the relation [13] for windings with an integer value of Q as:

$$N_1 = 2 \cdot m_{\text{PH}} \cdot Q - 1, \quad N_2 = 2 \cdot m_{\text{PH}} \cdot Q + 1 \quad (6)$$

where:

m_{PH} – is the number of phases of the generator.

3.1.2. EMF harmonics of the winding with fractional value of Q

Typically, powerful salient-pole generators (such as hydro and low speed diesel generators) with torque value above 20 tonne-force·meter (tf·m) are constructed with windings with fractional value of Q .

Such windings feature higher tooth harmonics order (and therefore lower amplitude [8, [13]. EMF tooth harmonics' order that has maximum amplitude is calculated from the relation [16] for windings with the fractional value of Q as:

$$N_1 = 2 \cdot m_{\text{PH}} \cdot Q \cdot F - 1, \quad N_2 = 2 \cdot m_{\text{PH}} \cdot Q \cdot F + 1 \quad (7)$$

where:

$F > 1$ – the smallest integer that makes the term $(2 \cdot m_{\text{PH}} \cdot Q \cdot F)$ an even number.

Example

For $m_{\text{PH}} = 3$, $Q = 2$, according to (2) the tooth harmonics orders are: $N_1 = 11$, $N_2 = 13$.

For $m_{\text{PH}} = 3$, $Q = 2.5$, according to (4) at $F = 2$, the tooth harmonics orders are: $N_1 = 29$, $N_2 = 31$.

Thus, the utilization of the winding with a fractional value $Q = 2.5$ (instead of $Q = 2$) increases the tooth harmonics order/ frequency (N_1 , N_2) more than two times. Respectively, with an increase of the harmonics order, the harmonics amplitude decreases. Unfortunately, the windings with fractional Q not only reduce the higher harmonics, but also at the same time, induce the lower harmonics in the output EMF. If a generator operates in load state, the lower harmonics cause additional vibration of stator core and housing. In some cases, the vibration force exceeds the permissible level, despite the fact that the EMF harmonics amplitudes are significantly less than the fundamental harmonic amplitude [17]. To reduce the vibration level, it is usually necessary to increase the size and weight of the housing (this way to increase its rigidity). That solution is often implemented in average power generators (20 tf·m $< M < 200$ tf·m, where M is the torque on the shaft).

3.1.3. Ways of reducing the stator winding EMF tooth harmonics amplitude and the distortion factor K_{DIST}

There are several ways to reduce the EMF harmonics amplitude and the distortion factor K_{DIST} [8, 9, 15]. These solutions could be applied for the windings with integer Q . For the windings with fractional Q , it is recommended to try to adjust the Q value.

Generators with outer stator diameter of 990 mm or less [2] are often designed with the stator slot skewing. The stator slots skewing is difficult to construct for the generators of larger size, the rotor poles skewing [2, 7] in the axial direction or rotor poles shift in tangential direction is then used. You can find the basic equations of the EMF tooth harmonics calculation in [15], including the case of the stator slot skewing by the tooth pitch value t_{ST} . The effects of possible technological deviations of the skewing value on the K_{DIST} were studied. Specific cases $0.5 \cdot t_{\text{ST}}$, $0.75 \cdot t_{\text{ST}}$, $1.1 \cdot t_{\text{ST}}$ were analyzed (see Table 3) for the generator featuring winding with integer Q . Generator data are listed in Appendix 2.

In case Q is a fractional number, the harmonics have low magnitude (see p. 3.1.2) and the slot skewing is not required. Nevertheless, it still could be applied to mitigate winding asymmetry or rotor eccentricity effects.

3.1.4. EMF tooth harmonics calculation

In [15] the EMF amplitudes ratio of the tooth harmonic (order $N \neq p$, according to (6) or (7)) to the fundamental harmonic (order $N = p$) is presented. For example, for the phase A the equation is:

$$E_{A,(N \neq p)} = (2/\pi) \cdot [B_{(N \neq p)}/B_{(N=p)}] \cdot E_{A,(N=p)} \quad (8)$$

where:

$B_{(N \neq p)}, B_{(N=p)}$ – are magnetic flux harmonics amplitudes shown in the Table 1.

The equation for the EMF $E_{A,(N=p)}$ calculation is presented in the section 3.2.

For phases B, C , there will be similar equations. Sometimes, the first factor is replaced with 1 yielding a bit higher tooth harmonics magnitude (with positive margin).

3.2. EMF harmonics of arbitrary order calculation

3.2.1. Representation of the stator winding (bars or coils)

The EMF of the phase is the sum of the EMF of phase' bars (coils) that are distributed in Q_s slots. In section 2.3.3, it is mentioned that the windings are not always constructed to be symmetrical [13, 14, 16]. For example, the phase zone A may include a few bars (coils) from the nearest phase zone, e.g. C . It is done to reduce the length of the balance connectors between the phase zones, and eventually this leads to phase EMF unbalance. The degree of asymmetry can be estimated if EMF of bars (coils) located in all Q_s stator slots of the winding is calculated. This also allows to find possible errors in the winding scheme design, which is important for the windings of multi-pole machines, and for the windings with a fractional value of Q (including $Q < 1$).

Appendix 1 contains the scheme of bar (coil) connections of the stator winding. It provides the sequence of slots for each phase of each of the six zones of the three-phase windings. For phase zone A , it has the form: $A'_1, A'_2, A'_3, A'_4, \dots, A'_L$. For example, consider the winding of the generator with $Q_s = 66, p = 4$. For this winding, the phase zone corresponding sequence of bars (coils) is [13, 14, 16]: 10, 11, 26, 27, 28, 42, 43, 44, 59, 60, 61. The difference between any two slots numbers determines the phase angle between the EMF of their bars (coils). The order of the slots in the sequence is arbitrary, for example, this would be a correct sequence, too: 28, 11, 43, 27, 10, 61, 26, 44, 59, 60, 42.

For a two-layer winding, it is sufficient to present a sequence of bars (coils) only for one layer, e.g., the upper. The sequence for the second layer can be obtained by shifting on the chording (β). The value of (β) should be specified in the Appendix 1.

3.2.2. EMF harmonics calculation

a) EMF of the winding phase calculation.

The complex amplitude of the electromotive force' N th-harmonic for the phase zone A is:

$$E_{A,N}^{\text{PH}} = \left\{ b_{R,N} \cdot \left[\begin{array}{l} \exp(j \cdot A_1 \cdot \Theta_{\text{ST}} \cdot N) + \exp(j \cdot A_2 \cdot \Theta_{\text{ST}} \cdot N) + \\ + \exp(j \cdot A_3 \cdot \Theta_{\text{ST}} \cdot N) + \dots + \\ + \exp(j \cdot A_Q \cdot \Theta_{\text{ST}} \cdot N) \end{array} \right] \right\} \cdot \Pi = \quad (9)$$

$$= |E_{A,N}| \cdot \exp(j \cdot \varphi_{A,N})$$

where:

$b_{R,N} = |B_N| \cdot \exp(j \cdot \psi_N)$ – according to (5) and Table 1,
 $\Theta_{\text{ST}} = 2 \cdot \pi / Q_s$ – angle between slots,

$$\Pi = \frac{1}{2} \cdot \omega_1 \cdot \left(\frac{2}{\pi} \cdot \tau \cdot L \cdot S \right) \cdot K_{SK} - \text{coefficient that takes into account stator dimensions and slot zone parameters (see equation 9a),}$$

ω_1 – EMF circular frequency of network,
 L – the length of the core,
 S – number of effective conductors of the coil,
 K_{SK} – skew factor [2].

Notes:

1. The meaning of the Π coefficient could be derived from the known expression for the phase EMF of the stator winding:

$$E_{A,N}^{PH} = \omega_1 \cdot \Phi \cdot w \cdot K_w \cdot K_{SK} = \omega_1 \cdot \left(\frac{2}{\pi} \cdot \tau \cdot L \cdot S \cdot \underline{B}_N \right) \cdot w \cdot K_w \cdot K_{SK} \quad (9a)$$

where:

- w – number of turns of the phase zone winding,
 K_w – winding factor [8].
2. In the general case, the phase zone EMF is calculated using equation (9). In case of symmetrical winding construction, the more simple equation (9a) can be used. The difference in results calculated by (9) and (9a) for symmetrical winding is less than 1%. For the phase zone A' , the equation of EMF N th-harmonic is as follows:

$$E_{A',N}^{PH} = \left\{ b_{R,N} \cdot \left[\begin{array}{l} \exp(j \cdot A'_1 \cdot \Theta_{ST} \cdot N) + \exp(j \cdot A'_2 \cdot \Theta_{ST} \cdot N) + \\ \exp(j \cdot A'_3 \cdot \Theta_{ST} \cdot N) + \dots + \\ \exp(j \cdot A'_L \cdot \Theta_{ST} \cdot N) \end{array} \right] \right\} \cdot \Pi = \quad (9')$$

$$= |E_{A',N}| \cdot \exp(j \cdot \phi'_{A',N})$$

In case of the two-layer winding ($S_{LR} = 2$, Appendix 1), the value of $E_{A,N}$ and $E_{A',N}$ should be multiplied by the value:

$$T = 1 - \exp(j \cdot \beta \cdot \pi \cdot N / p),$$

where:

β – chording.

The equations for the complex amplitudes (phasor) of the EMF for the phase zones B , B' , C and C' would be similar to the (9), (9') and are not presented here.

- b) Line-to-line EMF calculation.

The complex amplitude (phasor) of the N th-harmonic of line-to-line EMF A - B is:

$$E_{A,B(N)} = (E_{A,N}^{PH} - E_{B,N}^{PH}) = |E_{A,B(N)}| \cdot \exp(j \cdot \phi_{A,B(N)}) \quad (10)$$

This equation is based on the results obtained in (9), (9'). The equations for the complex amplitudes of the line-to-line EMF A - C and B - C would be similar to the (10) and are not presented here.

4. Stator windings asymmetry

The line-to-line terminal voltage asymmetry tolerances are regulated by standards GOST, IEC [1]. The voltage asymmetry could be caused by the errors in winding connection scheme or by the rotor eccentricity. The developed algorithm allows to take into account both these factors. The winding asymmetry is dealt with in p. 3.2.1, the rotor eccentricity is dealt with by the simulation package [10].

5. Total harmonic distortion factor K_{DIST}

The calculation is based on the results shown in the Table 1. It is assumed (see Section 2.3.3) that the harmonic order $S = p -$ is fundamental, the harmonic orders of $1 \dots R -$ are lower, and orders of $U \dots W, K \dots M -$ are higher. Also see Table 1.

For the line-to-line EMF $A-B$, the total harmonic distortion factor K_{DIST} can be calculated as:

$$K_{\text{DIST}} = \sqrt{\frac{\left| \frac{E_{A,B(1)}}{E_{A,B(S)}} \right|^2 + \dots + \left| \frac{E_{A,B(R)}}{E_{A,B(S)}} \right|^2 + \frac{\left| \frac{E_{A,B(U)}}{E_{A,B(S)}} \right|^2 + \dots + \left| \frac{E_{A,B(W)}}{E_{A,B(S)}} \right|^2}{\left| \frac{E_{A,B(K)}}{E_{A,B(S)}} \right|^2 + \dots + \left| \frac{E_{A,B(M)}}{E_{A,B(S)}} \right|^2}} \quad (11)$$

The equations of distortion factor K_{DIST} for the line-to-line EMF $A-C$ and for the line-to-line EMF $B-C$ would be similar to the (11) and are not presented here.

6. Example

Table 2 shows the result of the distortion factor calculation $K_{\text{DIST}} = f(\Lambda_{\text{GAP}}, b_p)$ for the generator (see Appendix 2), which have winding with integer number Q of slots per pole and phase. The factor K_{DIST} is calculated for the two cases $\alpha = b_p/\tau$: when $\alpha = 0.70$ (*) and $\alpha = 0.8$ (**), with skew factor $K_{sk} = 1$ (the skew is done by one tooth-pitch).

These results indicate that for the $1.2 \leq \Lambda_{\text{GAP}} \leq 2.0$ the distortion factor K_{DIST} satisfies GOST [1] requirements.

Variation of $\alpha = b_p/\tau$ in more than 5 – 7% drastically changes the magnetic flux density in the air gap. The air gap value δ_{EQ} and the rotor MMF should be adjusted then. This could lead to the full re-design of the geometry of the active part of the machine and requires new electromagnetic analysis to be carried out.

Table 2

Harmonic distortion factor K_{DIST} as a function of Λ_{GAP} (keeping the equivalent air gap δ_{EQ} a constant value) for generator with integer number Q and $K_{sk} = 1$

Λ_{GAP}	1.2	1.4	1.6	1.8	2.0
$K_{\text{DIST}} (*)$	0.0148	0.0140	0.0135	0.0131	0.0131
$K_{\text{DIST}} (**)$	0.0108	0.0109	0.0112	0.0114	0.0116

(*) – at $b_p/\tau = 0.70$, (**) – at $b_p/\tau = 0.8$

It is important to know the tolerances on the skew step value t . The dependency $K_{\text{DIST}}(t)$ is calculated for the case of $\Lambda_{\text{GAP}} = 1.6$ and $b_p/\tau = 0.7$. Table 3 contains the results for the skew step t equal to stator tooth pitch t_{st} (nominal value, 100%) and for the t equal to 50%, 75% and 110% of the t_{st} .

Table 3

Harmonic distortion factor K_{DIST} as a function of skew step t , calculated for $\Lambda_{\text{GAP}} = 1.6$ and $b_p/\tau = 0.70$ for generator with integer number Q

Stator slot skew step, t/t_{st}	50%	75%	100%	110%
K_{DIST}	0.13	0.064	0.0135	0.02

Table 3 data indicates that skew step tolerances are very strict.

7. Implementation of the distortion factor calculation method in a general design process

It is possible to implement the discussed calculation method in the generator design process. The generator design process consists of several stages. In the first stage, the geometrical dimensions of the active part and winding machine data are determined, which would satisfy basic requirements (generator weight, efficiency, winding temperature) of the Technical Specification and Russian State Standards. The results obtained at the first stage of calculation do not often satisfy additional requirements. So in the second stage, the special requirements are examined. In order to comply with special requirements, the related basic parameters could be corrected as well.

One of these special requirements could be the limitation of the distortion factor K_{DIST} . It depends on basic parameters (3): b_p , Λ_{GAP} at $\delta_{\text{EQ}} = \text{const}$, and Q (number of slots per pole and phase).

8. Conclusions

1. The proposed method of synchronous salient-pole generator no-load state line-to-line EMF THD calculation is distinguished by its ability to take into account: actual magnetic field distribution (2D FEM simulation [10]), harmonic spectrum of radial

(normal) magnetic flux density distribution in the air gap, saturation of ferromagnetic materials, winding scheme (both with integer or fractional number Q of slots per pole and phase). The method could also be used to find the dependency of the THD factor on the different factors, for example – pole shoe shape and Q . It is found that the pole shoe radius is a function of three parameters: $R_p = f(D_{IN}, \Lambda_{GAP}, b_p)$.

2. In case of the winding constructing with fractional value Q of slots per pole and phase, the Fourier decomposition periodic interval should be taken according to (4). In this case, the fundamental harmonic of the magnetic flux distribution in the air gap and of the winding electromagnetic force is of the order $N = p$, and we get not only higher, but also lower harmonics. The possible errors in the winding scheme could be revealed using harmonic analysis (which is actual for multi-pole machines with the fractional value Q). Equation (9) supports EMF calculation for non-symmetrical winding as well. The analysis allows to determine the unbalance of phase and line-to-line EMF also.
3. The method could answer some questions arising in the manufacturing practices of synchronous generators with electromagnetic excitation:
 - What are the tolerance limits on the slot skew angle?
 - Is the stator slot skew necessary?

Appendix 1. Input data sheet

1. The scheme of three-phase six-zone winding of the stator (in this example: Q – integer).

A_1	A_2	A_3	...	A_Q	C'_1	C'_2	C'_3	...	C'_Q	B_1	B_2	B_3	...	B_Q
A'_1	A'_2	A'_3	...	A'_Q	C_1	C_2	C_3	...	C_Q	B'_1	B'_2	B'_3	...	B'_Q

2. The geometrical dimensions.

D_{IN}, D_A – the stator inner and outside diameters, β – chording,
 b_{SL}, h_{SL} – the width and height of stator slot, Q_s – the number of stator slots,
 b_M, h_M – the width and height of pole core, D_0 – the rotor inner diameter,
 S_{LR} – the type of stator winding: for one-layered winding $S_{LR} = 1$, for two-layered winding
 $S_{LR} = 2$,
 $\delta_{MAX}, \delta_{MIN}, p, b_p, h_p$ – see description in the text.
 3. F_{EX} – MMF of the rotor winding at no load state.

Appendix 2. The synchronous generator data

Power rating	1250 kW
Rated line voltage	6300 V
Number of rotor poles	10
Frequency	50 Hz
Stator outer diameter	1195 mm
Stator inner diameter	922 mm
Stator core length	600 mm
Steel grade	2412
Equivalent air gap	4.5 mm
Slot dimensions	13.1 × 60 mm
Number of effective conductors in the slot	12
Number of parallel paths	1
Chording	0.78
Phase connection type	star

References

- [1] Russian State Standards GOST 52776 – 2007 (IEC 60034-1-2004). Rotating Electrical Machines Nominal Data and Characteristics (In Russian).
- [2] Mueller G., Vogt. K., Ponick B., *Berechnung elektrischer Maschinen*, Springer, 2007, 475 (in German).
- [3] Danilevich Ya.B., Kruchinina I.Yu., Shtainle L.Yu., *Air gap magnetic field spectrum calculation method*, St. Petersburg State Polytechnical University Journal, No. 117, 2011, 221–226 (in Russian).
- [4] Kruchinina I.Yu., Shtainle L.Yu., *Magneto-motive Force of Stator Multiphase Windings with Fractional Number of Slots Q per Pole and Phase*, Allerton Press, Inc. Distributed worldwide by Springer, Russian Electrical Engineering, Vol. 81, No. 8, 2010.
- [5] Kruchinina I.Yu., *Electrical machines for small power engineering: some design problems of stator slots*, Proceedings of RAS, Power Engineering Journal, No. 1, 2012, 113–119 (in Russian).
- [6] Balovnev D.I., *An investigation of the shape of the curve of synchronous generator voltage*, Russian Electrical Engineering, Vol. 86, Issue 2, February 2015, 58–60.
- [7] Mueller G., Ponick B., *Grundlagen elektrischer Maschinen*, Springer, 2005 (in German).

- [8] Mueller G., Ponick B., *Elektrische Maschinen*, John Wiley, New York 2009, 375 (in German).
- [9] Voldek A.I., Popov V.V., *Electrical Machines*, vol. 2, L. Piter, 2007, 540 (In Russian).
- [10] QuickField – finite element analysis system, Version 6.0, User’s guide, Tera-Analysis Ltd., Svendborg, Denmark 2013, 295 (in English).
- [11] Demirchan K.S., Neiman L.R., Korovkin N.V., Chechurin V.L., *The Theoretical Foundation Of The Electrical Engineering – L. Piter*, 2004 (in Russian).
- [12] Korn G., Korn T., *Mathematical Dictionary*, M. Nauka, 1970, 720 (in Russian).
- [13] Boguslawsky I.Z., *Motors and Generators of Alternating Current: The Theory and investigation Methods Working in Networks with Nonlinear Elements*, SPbSTU, Vol. 1, 2, 2006 (in Russian).
- [14] Boguslawsky I.Z., Kuss H., *The investigations of multiphase stator winding structure with fractional number Q* , Russian Electrical engineering, № 1, 2000.
- [15] Arseniev I.A., Boguslawsky I.Z., Korovkin N.V., *Research Method for the Slot-Ripple EFM in Polyphase Integral Slot Winding*, Proc. 2012 of the IEEE Russia North West Section, Vol. 4, 36–45.
- [16] Berger A.Ya., *Synchronous Machines*, L.-M. GONTI publishing, 1938 (in Russian).
- [17] Detinko F.M., Zagorodnaya G.A., Fastovskiy V.M., *The Strength and Vibrations of Electrical Machines*, L. Energy, 1964 (in Russian).
- [18] Boguslawsky I.Z., *Generators for independent power plants: performance and design*, Electrical Engineering (Archiv fuer Elektrotechnik), Springer, № 5, Berlin 2006 (in German).

MAREK DUDZIK*, SŁAWOMIR DRAPIK*, JANUSZ PRUSAK***

APPROXIMATION OF OVERLOADS FOR A SELECTED TRAM TRACTION SUBSTATION USING ARTIFICIAL NEURAL NETWORKS

APROKSYMACJA PRZECIĄŻEŃ WYBRANEJ TRAMWAJOWEJ PODSTACJI TRAKCYJNEJ Z WYKORZYSTANIEM SZTUCZNYCH SIECI NEURONOWYCH

Abstract

The article presents some of the results of measurements of loads for a selected tram traction substation for a continuous period of time covering sixteen weeks (112 days). Particular attention was paid to overloads occurring in consequent days. The second part of the article presents the analysis of overloads relating to the time interval of 60 minutes in successive days. This analysis was implemented in Matlab using a two-layer feedforward artificial neural network (ANN). The results of the approximation of the analyzed overloads are promising. A continuation of research may lead to the formulation of mathematical equations that might be useful for designers in terms of sufficiently precise calculations of overloads of rectifier units of DC traction substations.

Keywords: loads and overloads of tram traction substation, artificial neural network

Streszczenie

W artykule przedstawiono niektóre wyniki pomiarów obciążenia wybranej tramwajowej podstacji trakcyjnej dla spójnego okresu czasowego obejmującego szesnaście tygodni (112 dni). Szczególną uwagę zwrócono na występujące przeciążenia w kolejnych dniach realizacji pomiarów. W drugiej części artykułu dokonano przetwarzania przeciążeń odnoszących się do przedziału czasowego 60 minut w kolejnych dobach, z wykorzystaniem sztucznej sieci neuronowej (SSN) dwuwarstwowej typu feedforward, zaimplementowanej w środowisku Matlab. Uzyskane wyniki aproksymacji analizowanego przeciążenia wyglądają obiecująco. Oznacza to, że kontynuując badania, będzie można uzyskać zapis matematyczny, użyteczny dla projektantów w zakresie wystarczająco dokładnych obliczeń (oszacowań) przeciążeń zespołów prostownikowych podstacji trakcyjnych prądu stałego (DC).

Słowa kluczowe: obciążenia i przeciążenia tramwajowej podstacji trakcyjnej, sztuczne sieci neuronowe

* Ph.D. Eng. Marek Dudzik, Ph.D. Eng. Janusz Prusak, Institute of Electrical Engineering and Computer Science, Faculty of Electrical and Computer Engineering, Cracow University of Technology.

** M.Sc. Sławomir Drapik, ELECTREN S.A.

1. Introduction

Variability of loads of rectifier units and other elements of the main circuits of traction substations is no surprise to specialists. The reasons behind this phenomenon are known [3, 8, [12]. Researches and analyses of such loads, which have been conducted for many years both for train and tram traction substations [4, 5, 9, 10], show that the powers of used rectifier units are designed with considerable excess. Reserves in power supply systems are indispensable, exactly because of the variability of traction loads, but as well due to the adjustable structure of these systems, which enables active customization, e.g. adaptation of the number of rectifier units to currently acting loads [2, 7].

Problems relating to the variable nature of the traction loads are confirmed by publications and specialists from other research centers [15–24].

Excessive reserves in power supply systems, compared to actual or diagnosed currents (powers), generate unnecessary investment and operating costs. A reduction of these costs will undoubtedly strengthen the competitiveness of electric rail transport and will also downscale the negative ecological impacts due to lower energy consumption [6].

The article presents research results on the approximation of 60-min overloads for traction loads determined on the basis of measurements for a working tram traction substation [14].

The aim of the research is the improvement of computational methods in terms of the determination of traction overloads, in particular the overloads, which are taken into consideration when designing the number and power of rectifier units for traction substations.

2. Load characteristics of the analyzed traction substation

Registered loads, which were analyzed and are partially presented below, relate to a tram traction substation located in the central part of a big city, on a complex rail and road junction with considerable traffic [4–6].

2.1. Examples of instantaneous traction loads

In order to give the idea of what measured magnitudes are taken into account, Fig. 1 shows examples of the waveforms of instantaneous values of traction currents, which constitute loading of rectifier units of the above mentioned tram traction substation. Waveforms for a weekday (23.10.2013 – Wednesday) and a holiday (27.10.2013 – Sunday) are presented. These test results apply to 2 days, which is approx. 0.55% of the calendar year. The currently used design methods base on the assessment of the annual energy consumption. Following subsections of the article include much longer periods.

Based on these results, it could be concluded that, on the analyzed days, the traction substation „Czyżyny” was not fully loaded [6]. For example, on a weekday, the occurring load was corresponding to the continuous power of four rectifier units, which build the substation, only for approx. 6 minutes (in total). Also, for almost 5 hours in total, the substation (rectifiers) were not under load at all. During this time, all four transformers of the rectifier units took energy from the power supply system just to cover no-load state losses.

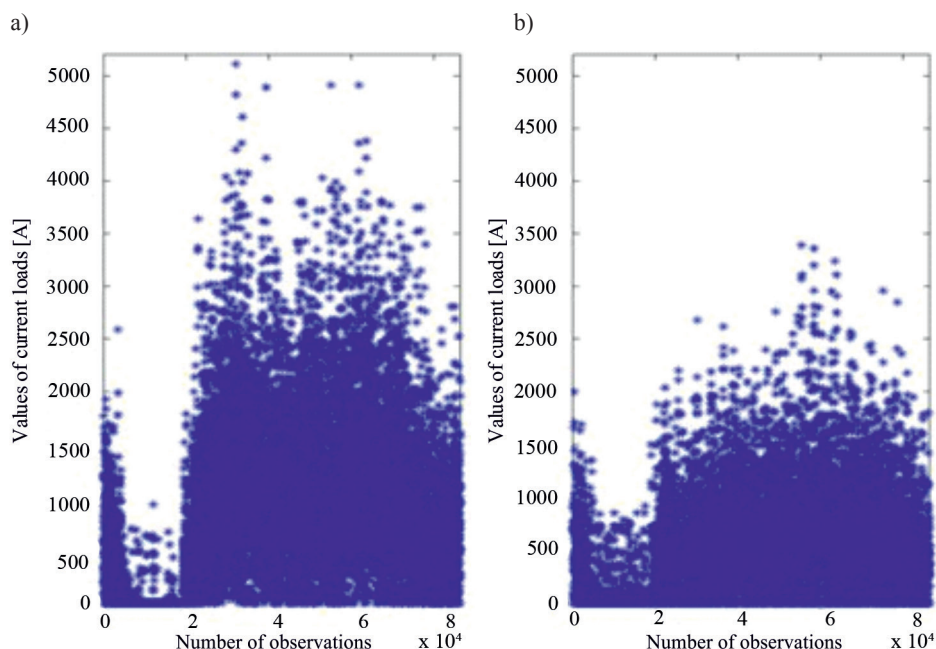


Fig. 1. Registered instantaneous values of current loads of the traction substation „Czyżyny” on: a) 23.10.2013 (Wednesday), b) 27.10.2013 (Sunday). From: [6, 14]

2.2. Traction loads and overloads for a longer time period

This subsection presents measurement results and selected aspects of their analysis [4, 14] for a time period of 16 consecutive weeks in autumn and winter (from 09.01.2014 to 12.21.2014). Some of the presented results were then analyzed using an artificial neural network (Section 3).

Fig. 2 shows the average values of current traction loads in individual weeks of the studied period.

From the above figure, it can be inferred that the substation was bearing different loads with respect to individual weeks. The highest average value of current (the greatest energy consumption) occurred in the 14th week and was equal to 778.74 A, which is 1.25 times more than the average for the period, which in turn is equal to 621.61 A.

Fig. 3a depicts average values of current traction loads in individual days (for a full span of 24 h). On the other hand, Fig. 3b gives the ordered graph of these loads: from the highest value (965.38 A) to the smallest one (304,11 A).

The overload (the overload factor α) is defined as the ratio of the highest load (the highest average current value) lasting for a certain period of time, e.g. 5 min or 60 min, in a given 24-hour period, to the average current value for the same 24 hrs.

Fig. 4a shows 5-minute overload values in individual 24-hour periods. These factors are presented in an ordered manner, that is, from the highest ($\alpha_5 = 3.11$) to the smallest ($\alpha_5 = 2.08$). Fig. 4b depicts the diagram of ordered 60-min overloads. One can observe that here the highest value is $\alpha_{60} = 2.08$ and the lowest value is $\alpha_{60} = 1.35$.

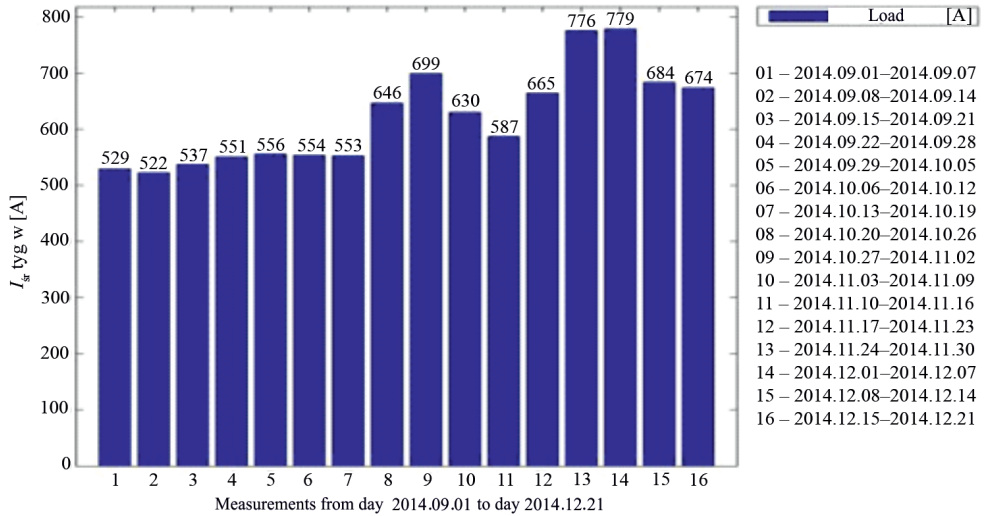


Fig. 2. Average values of current traction loads in individual weeks. From: [4]

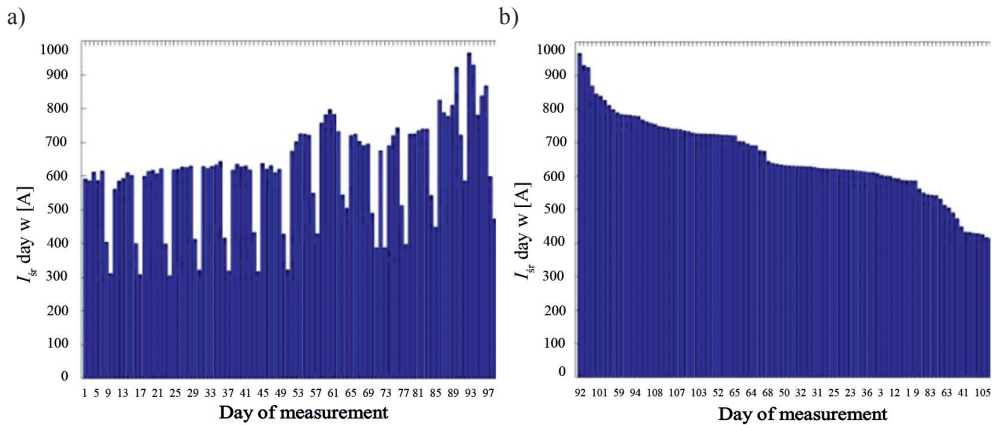


Fig. 3. Average values of current loads of the traction in individual days: a) chronologically, b) ordered. From: [4]

Fig. 5 presents two polylines created by joining the points corresponding to 5-min and 60-min overloads with straight line sections. The points were linked chronologically: from day 1 (01.09.2014), to the last, 112th, day (21.12.2014).

In the above figure, one can see that the overloads in succeeding days assume different values and that 5-min overloads are higher compared to 60-min ones. This observation is not surprising, particularly among specialists. The data in Fig. 5 also easily leads to getting a grasp on the extent to which these values differ.

Fig. 6 depicts the whole range of possible overload changes (overload factors changes), depending on different time periods of the highest load taken for the calculation of the factors. The chosen time periods start from 10 seconds up to 3 hours. The calculations were

performed for the measurement data for the above-mentioned 112 days. The abscissa axis refers to time periods of overloads taken for calculations (acc. to Tab. 1); the vertical axis refers to overloads (overload factors). The upper curve is plotted for maximum values, while the bottom one – for minimum values. The area between these curves is the range in which other values of overload factors can occur.

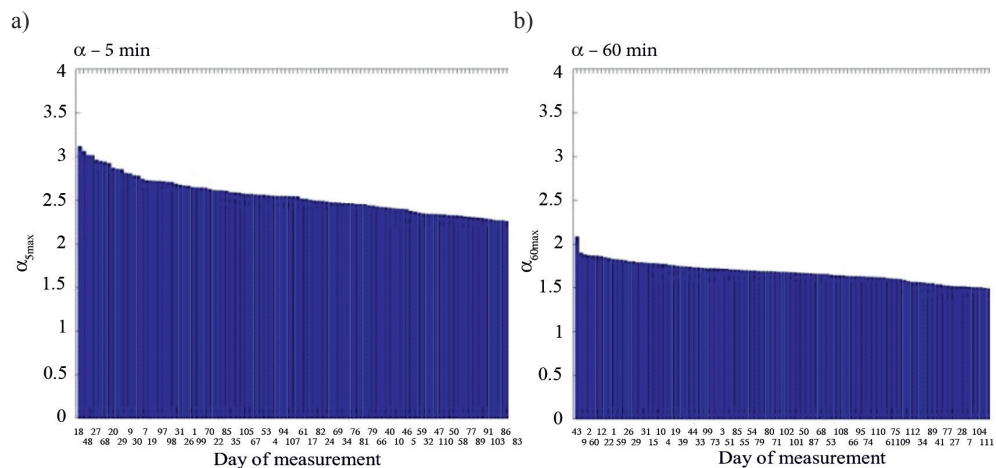


Fig. 4. Maximum overloads ordered from the highest to the smallest value (for 112 days); for time periods: a) 5 min, b) 60 min. From: [4]

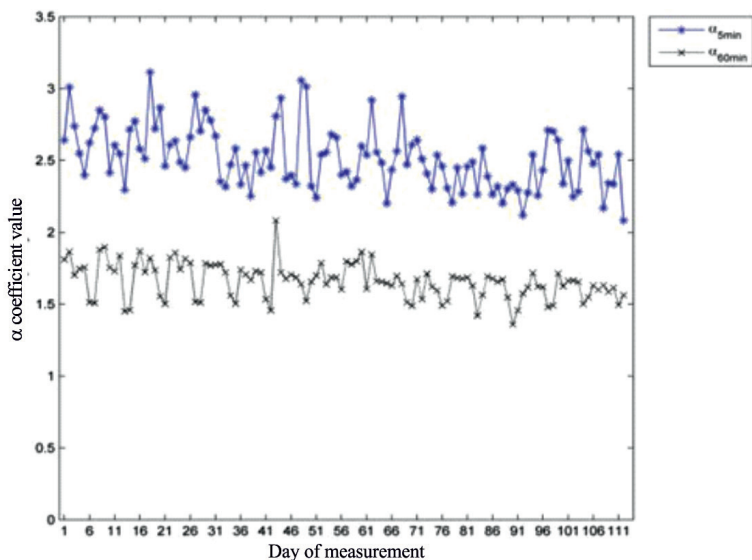


Fig. 5. Changes of 5-min and 60-min overload factors, presented chronologically. Own work

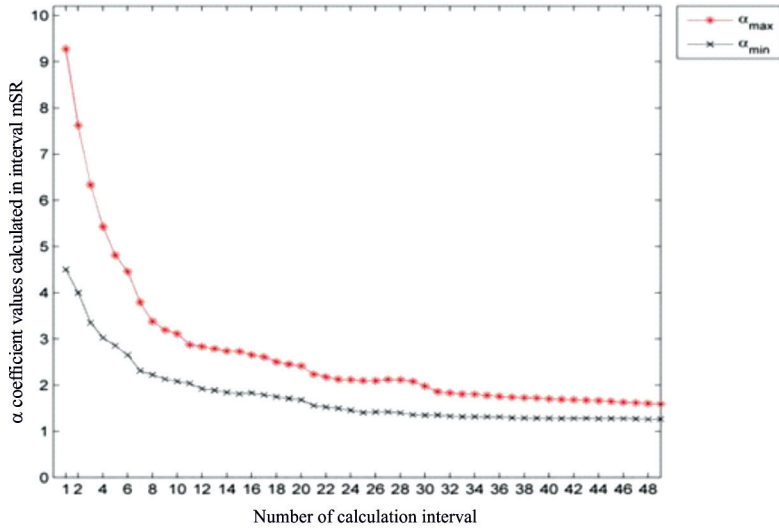


Fig. 6. Values (maximum and minimum) of overload factors for selected time periods. Own work

Table 1

Lengths of time periods taken for calculations to determine changes of overloads (overload factors). Own work

Time period	Lengt [h]												
1	2	3	4	5	6	7	8	9	10	11	12	13	14
1.	10 sec	8.	3 min	15.	10 min	22.	25 min	29.	60 min	36.	165 min	43.	270 min
2.	20 sec	9.	4 min	16.	11 min	23.	30 min	30.	75 min	37.	180 min	44.	285 min
3.	30 sec	10.	5 min	17.	12 min	24.	35 min	31.	90 min	38.	195 min	45.	300 min
4.	40 sec	11.	6 min	18.	13 min	25.	40 min	32.	105 min	39.	210 min	46.	315 min
5.	50 sec	12.	7 min	19.	14 min	26.	45 min	33.	120 min	40.	225 min	47.	330 min
6.	60 sec	13.	8 min	20.	15 min	27.	50 min	34.	135 min	41.	240 min	48.	345 min
7.	2 min	14.	9 min	21.	20 min	28.	55 min	35.	150 min	42.	255 min	49.	360 min

3. The use of an artificial neural network in the analysis of a selected overload

Artificial neural network (ANN) is a general name for mathematical structures and their software or hardware models, which perform calculations or signal processing by rows of elements called artificial neurons. Artificial neurons realize some basic operations on their input. The original inspiration for ANNs was the structure of natural neurons, synapses connecting the neurons and nervous systems, especially a brain [11, 13].

3.1. Introductory information and input data

The calculations were performed using Matlab R2011B version. The input data for the ANN analysis were in this case 112 pairs of numbers. In each pair one of the numbers (Input) was the average value of current on a given day (Fig. 3) and the other number (Output) was the corresponding 60-min overload (the overload factor) for the same day (Fig. 4b).

Measurement data processing was performed using a two-layer feedforward neural network implemented in Matlab. Fig. 7 shows the neural network block created in the Simulink environment.

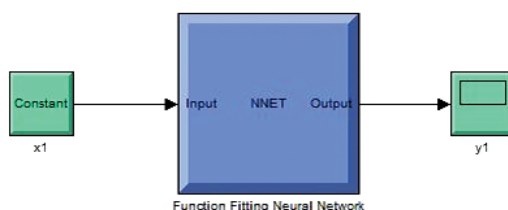


Fig. 7. The neural network block created in the Simulink environment. Own work

Fig. 8 depicts the created neural network structure. This structure had one hidden layer consisting of four neurons. There were no delays implemented on the input for this layer. The activation function for the hidden layer was tangensoidal (tansig). The output layer had a linear activation function.

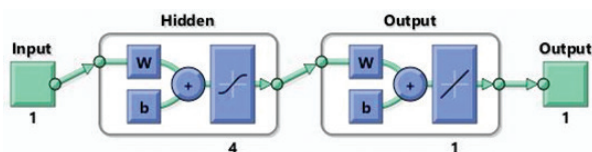


Fig. 8. The created neural network structure. Own work

The aim of the study was to approximate the function that would relate the average load value for a traction substation in a given day with the overload factor – in this case for the time period of 60 minutes.

The results shown below in Subsection 3.2. were obtained for the following ANN training settings [1]:

- maximum number of epochs to train: 1000;
- performance goal: 0;
- learning rate: 0,01;
- maximum validation failures: 12;
- momentum: 0,9;
- minimum performance gradient: 10^{-10} ;
- epochs between displays: 25;
- maximum time to train in seconds: infinite.

In order to teach the designed artificial neural network, the one-way network (up to 3 layers) training was used according to the Levenberg-Marquardt algorithm.

3.2. Computation

Fig. 9 depicts results obtained from the training, validation and test of the ANN in the form of an error histogram.

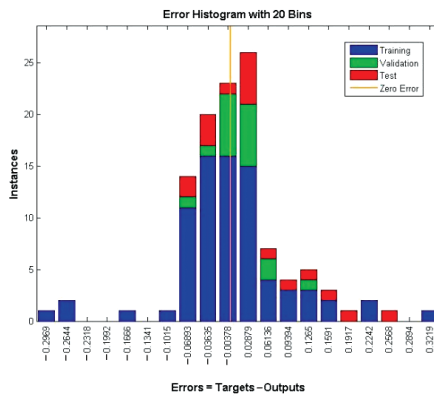


Fig. 9. Error histogram. Own work

Fig. 10 shows the illustration of performance of the ANN for successive learning epochs.

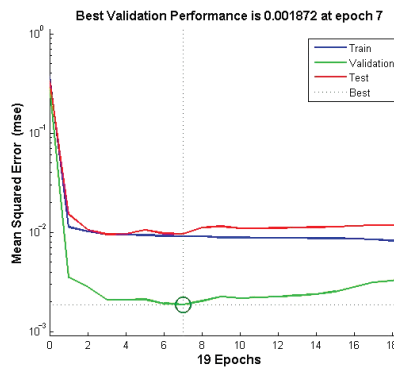


Fig. 10. Performance of the ANN. Own work

Fig. 10 presents the artificial neural network performance graph during its learning. The ordinate axis refers to the ANN performance function values. Mean square error (mse) was chosen as the performance function. The horizontal axis corresponds to learning epochs. The system reached the best neural network validation of the ANN performance for the 7th epoch and it was equal to 0.001872. One can observe that the neural network system continued the learning algorithm for another 12 epochs in order to confirm the alleged local minimum for the goal set for the created network structure (Fig. 8). From epoch 1 to 7, a downward trend in validation tests of the ANN learning can be seen.

Fig. 11 depicts the regression results for the training, validation and test and the regression for all data assigned to the ANN learning with a supervisor. Here, the ordinate axis represents the neural network output for the given input data. The abscissa axis shows values from the actual measurements (targets), to which the values returned by the ANN should be convergent.

The $R = 1$ regression result means that there is an unequivocal relation between the actual value (target; from measurement or simulation) and the neural network output value.

The regression results for the discussed case are as follows. The regression for the data assigned to the training reached $R = 0.65986$. The data constituted about 70% of all data assigned to the ANN learning with a supervisor. The regression for the validation was equal to $R = 0.9113$. The data used for this step were about 15% of all data. Lastly, the regression for the test was $R = 0.69163$. Consequently, the data used in this stage was about 15% of all data. One more regression value was calculated, for all data, and it was equal to $R = 0.68304$.

The training, validation and test are performed during the procedure of the neural network learning.

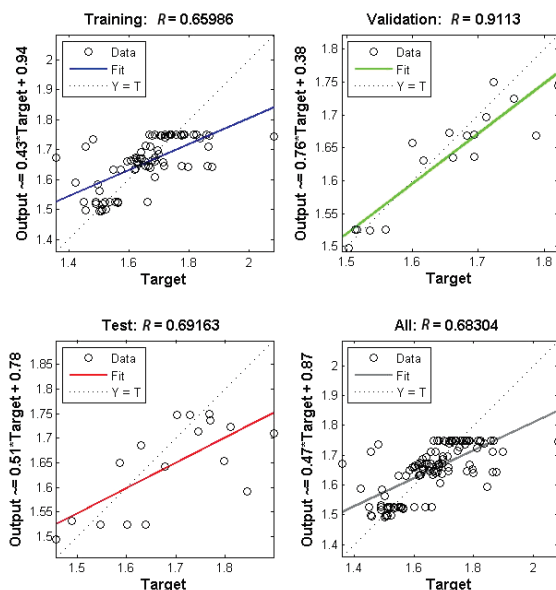


Fig. 11. Regression results for the training, validation and test and the regression for all data assigned to the ANN learning with a teacher. Own work

Fig. 12 presents the results obtained from the approximation process (function fitting process) performed by the artificial neural network learning. In this figure dots represent actual values of the factor α obtained from measurements (targets), while cross marks represent results of the approximation. Vertical lines are absolute errors between actual values and the corresponding results obtained by the function fitting process. The solid line is the plot of the resulting approximating function.

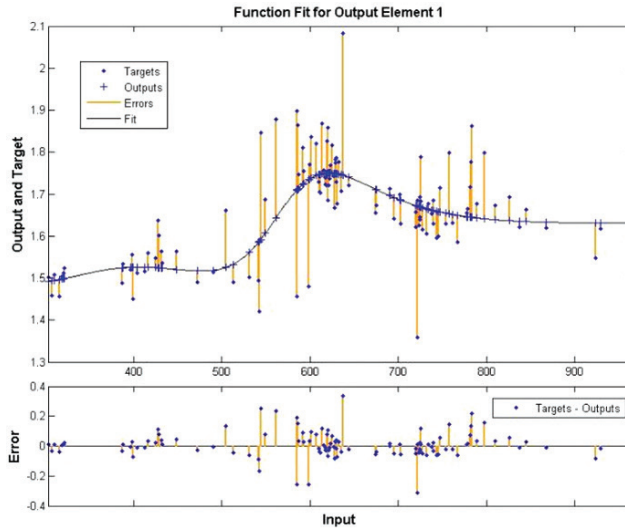


Fig. 12. Results of function fitting with the use of the ANN. Output – the overload factor, input – the average value of current on a given day. Own work

4. Conclusions

The calculation results are promising. Getting to know the possibilities (specificity) of neural networks applied for studies of variability parameters of traction loads should contribute to the formation of conceptual solutions for qualitative changes in the design and construction of power supply systems for railway and tram lines. In effect, this should lead to the reduction of energy consumption and, in particular, to the reduction of various kinds of losses in the power system. Other positive results should be: the improvement of economic competitiveness of electric rail transport and the reduction of the emission of harmful agents into the atmosphere. In further studies, the authors are going to analyze the relation of hidden neurons' impact on the result.

References

- [1] Bartman J., *Podstawowe funkcje biblioteki narzędziowej "Neural Network Toolbox. Version 5" pakietu MATLAB v.6*, Uniwersytet Rzeszowski, Zakład Elektrotechniki i Informatyki, materiały zamieszczone w sieci.
- [2] Chrabąszcz I., Drapik S., Dudzik M., Kaczmarczyk A., Prusak J., *Analiza obciążeń zespołów prostownikowych, dla „inteligentnych” kolejowych podstacji trakcyjnych DC – wstępne badania symulacyjne wybranych przypadków*, *Logistyka* 6/2015, 990–999.
- [3] Chrabąszcz I., Prusak J., Drapik S., *Trakcja elektryczna prądu stałego. Układy zasilania*. Podręcznik INPE dla elektryków, Zeszyt nr 27, Kraków–Bełchatów, 2009.
- [4] Drapik S., Kuzniecowa W., Markowski P., Prusak J., Woszczyzna B., *Badanie skali zmienności obciążeń wybranej tramwajowej podstacji trakcyjnej na podstawie rzeczywistych wyników pomiarowych dla spójnego okresu czasowego obejmującego szesnaście tygodni*, *Logistyka* 6/2015, 1026–1035.
- [5] Drapik S., Markowski P., Prusak J., Woszczyzna B., *Analiza obciążeń zespołów prostownikowych przed i po wystąpieniu przeciążenia na przykładzie wybranej tramwajowej podstacji trakcyjnej*, *TTS Technika Transportu Szynowego*, 12/2015, 427–434.
- [6] Drapik S., Markowski P., Prusak J., Woszczyzna B., *Tramwajowe podstacje trakcyjne – wybrane problemy bezpieczeństwa ekologicznego w świetle oceny ich obciążeń*, *Logistyka* 4/2015, 3017–3027.
- [7] Jagiełło A.S., Chrabąszcz I., Drapik S., Dudzik M., Kobielski A., Prusak J., *System do aktywnej regulacji obciążenia zespołów prostownikowych kolejowej podstacji trakcyjnej. Sposób aktywnej regulacji obciążenia zespołów prostownikowych kolejowej podstacji trakcyjnej*, Rozwiązanie zarejestrowane w Urzędzie Patentowym RP na rzecz Politechniki Krakowskiej pod numerem P.511511, objęte ochroną prawną od dnia 10.03.2015.
- [8] Kałuża E., Bartodziej G., Ginalski Z., *Układy zasilania i podstacje trakcyjne*, Skrypty uczelniane Politechniki Śląskiej nr 1220, Gliwice 1985.
- [9] Kobielski A., Drapik S., Dudzik M., Prusak J., *Time Series as an Aid to Research of traction Substation Load*, *JEPE Journal of Energy and Power Engineering*, Vol. 7, Number 5, May 2013 (Serial Number 66), David Publishing Company, El Monte, USA, 979–986.
- [10] Kobielski A., Drapik S., Dudzik M., Prusak J., *Wstępne studium efektywności zastosowania sieci neuronowych w badaniach obciążeń kolejowych podstacji trakcyjnych*, *TTS Technika Transportu Szynowego*, 10/2014, 40–43.
- [11] Korbicz J., Obuchowicz A., Uciński D., *Sztuczne sieci neuronowe. Podstawy i zastosowania*, Akademicka Oficyna Wydawnicza PLJ, Warszawa 1994.
- [12] Mierzejewski L., Szelaąg A., Gałuszewski M., *System zasilania trakcji elektrycznej prądu stałego*, Wydawnictwo Politechniki Warszawskiej, Warszawa 1989.
- [13] Tadeusiewicz R., *Sieci neuronowe*, Akademicka Oficyna Wydaw. RM, Kraków 1992.
- [14] Wyniki pomiarów prądów obciążeń trakcyjnych kabli zasilających podstacji tramwajowej nr „01” („Czyżyny”), materiały udostępnione przez ZIKiT w Krakowie, 2015.
- [15] Cejtlin S.J., *Operatywne prognozowanie rozchoda elektroenergii na tiagu po danym monitoringu i informacyjnym modelowaniu procesów gruzowych żelaznodod-*

- rożnych pieriewozog, [w:] Cejtin S.J., Kuzniecowa W.G., *Transport. Matematycznie modelowania w inżynierynych ta ekonomicznych zadaczach transportu: Zb. nauk. pr.*, 1999, 133–139.
- [16] Domanski W.T., *Awtomatizirowannaja sistema kontrola i uciota elektroenergii na distancjach elektrosnabrzenia*, [w:] Donskij W.T., Kuzniecowa W.G., Karpjenko S.J., *Zalicznij transport Urkainy*, Nr. 4, 2002, 33–36.
- [17] Dżuman W.G., *Issliedowanie raboty sistemy elektrosnabrzenia postojannogo toka pri propuskie sdwojennych pojezdow*, [w:] Dżuman W.G., Sczenko W.G., Kuzniecowa W.G., Kiriluk T.I., *Elektrotechnika i elektromechanika*, Nr 3, 2011, 74–76.
- [18] Iwanow A.P., *Stoimostnaja optimizacija režimow wiedienia gruzowych pojezdow s uciotom zatrat aktiwnoj i reaktiwnoj elektroenergii*, [w:] Iwanow A.P., Kuzniecowa W.G., *Tezy dopowidiej VI Miżnarodnoj naukowo konferenciji „Proglemy ekonomiki transportu”*, DNUZT, Dniepropietrowsk 2007, 175.
- [19] Kuznetsov V.G., *Elaboration of methodology for calculation of traction power-supply system with the help of renewal stream theory*, [w:] Kuznetsov V.G., Vaiciunas G., *Transbaltica 2009*, Proceedings of the 6-th international scientific conference, Vilnius Gediminas Technical University, Vilnius 2009, 123–128.
- [20] Kuznetsov V.G., *Problemy uciota i kontrola elektroenergii na distancii elektrosnabrzenia*, [w:] Kuznetsov V.G., Domanski W.T., *Trudy merzdunar. simp. „Elektrifikacija i Razwidje rzelieznodorożnogo transporta Rossii, Tradicii cowriemiennost, perspektiwy (Eltrans 2001)*, 2011, 79–80.
- [21] Kuznetsov V.G., *Statisticzieskij podchod k opriedielienju potier elektroenergii w transformatorach diagowych podstanciji pieriemienogo toka*, [w:] Kuznetsov V.G., *Wisnig Dnipropietrowskowo nacjonalnogo uniewersitetu zalicznogo transportu imieni akademika W. Łazariana*, Nr. 6, 2005, 124–126.
- [22] Kuznetsov V.G., *Ocenka potier elektroenergii w tiagowej sietji magistralnych żelaznych dorog*, [w:] Kuznetsov V.G., Micko R.S., Bosyj D.O., *Wisnig Dnipropietrowskowo nacjonalnogo uniewersitetu zalicznogo transportu imieni akademika W. Łazariana*, Nr 12, 2006, 36–40.
- [23] Kuznetsov V.G., *Optimizacija grafika dwirzenia pojezdow s uciotą energeticzieskoj sostawjusciej*, [w:] Kuznetsov V.G., Kałasznikow K.A., *Trudy mieżdnarodnoj nauczno-practiczeskoj konferenciji „Problemy i perspektiwy razwikja transportnogo kompleksa: obrazowanje nauka, proizwoctwo”*, G. Roztowna Domu: RGUPS, 2009, 362–363.
- [24] Skałozup W.W., *Optimizacija režimow wiedienia pojezdow pa kriteriu minimuma stoimosti patriebloņnoj aktivnoj i reaktivnoj elektroenergii*, [w:] Skałozup W.W., Bosyj D.O., Iwanow A.P., *Informacijno-kierujuczi sistemy na zalicznom transporti*, Nr 4, 2008, 111–114.

DARIUSZ BORKOWSKI*

VOLTAGE AND FREQUENCY CONTROL OF A STAND-ALONE INDUCTION GENERATOR USING SVPWM CONVERTER IN A SMALL RESERVOIR HYDROPOWER PLANT

STEROWANIE CZĘSTOTLIWOŚCI I NAPIĘCIA AUTONOMICZNEGO GENERATORA INDUKCYJNEGO PRZEZ PRZEKSZTAŁTNIK SVPWM W ZBIORNIKOWEJ ELEKTROWNI WODNEJ

Abstract

Induction generators are widely used to generate electrical power in small hydraulic applications. The main disadvantage of stand-alone induction generators is the problem of regulating the voltage magnitude and voltage frequency under load variation. This paper investigates a three-phase self-excited induction generator (SEIG) operating under varying load, utilizing the water energy in a small reservoir hydropower plant. The generator excitation is provided by a three-phase capacitor bank and an inverter with Space Vector Pulse Width Modulation (SVPWM). Furthermore, the inverter with a battery controls the active power flow between the generator and the load in order to provide a constant frequency of voltage. The proposed control scheme consists of two PI controllers. The first controls the voltage magnitude by regulating the inverter reactive power, while the second one adjusts the guide vanes of the turbine according to the DC voltage of the battery. The proposed control system has been tested under load step changes. The simulation results of the system, obtained using the Matlab/Simulink software, have demonstrated good control performance.

Keywords: self-excited induction generator, SVPWM inverter, small hydropower plant, control algorithm

Streszczenie

Generatory indukcyjne są szeroko stosowane do produkcji energii elektrycznej w elektrowniach wodnych małej mocy. Główną wadą samowzbudnych generatorów indukcyjnych są problemy z regulacją amplitudy i częstotliwości napięcia podczas zmian obciążenia. W artykule przedstawiono wyniki badań układu generacji autonomicznej z maszyną indukcyjną przetwarzającą energię mechaniczną turbiny w zbiornikowej małej elektrowni wodnej. Moc bierna niezbędna do wzbudzenia maszyny dostarczana jest zarówno przez baterię kondensatorów oraz falownik napięcia sterowany z zastosowaniem metody modulacji wektorowej (SVPWM). Ponadto, falownik wyposażony jest w bufor energii (baterię) przez co może sterować przepływem mocy czynnej, a w rezultacie sterować częstotliwością napięcia. Proponowany system sterowany jest za pomocą dwóch regulatorów PI. Pierwszy steruje wartością napięcia poprzez dostarczanie mocy biernej, podczas gdy drugi reguluje kierownicą turbiny wodnej na podstawie napięcia w obwodzie DC. Zaprezentowany system został przetestowany podczas skokowej zmiany obciążenia. Przedstawiono symulacje pochodzące z modelu stworzonego w aplikacji Matlab/Simulink, które prezentują właściwości systemu.

Słowa kluczowe: samowzbudny generator indukcyjny, falowniki SVPWM, mała elektrownia wodna, algorytmy sterowania

* Ph.D. Eng. Dariusz Borkowski, Institute of Electromechanical Energy Conversion, Faculty of Electrical and Computer Engineering, Cracow University of Technology.

1. Introduction

Squirrel-cage induction generators are widely used in various applications, for instance: hydropower, wind turbines, biomass sources, fuel engine driven generation systems etc., especially in small-scale systems. This is caused by their low price, simple construction, robustness, ease of maintenance, and no separate excitation source [1].

The on-grid operation is simple and does not require any special synchronization procedure like synchronous generators. The induction machine starts generating active power when the rotor speed is greater than the synchronous speed defined by the frequency of the grid voltage. However, there is the need of reactive power compensation, which is often provided by the capacitor bank.

Induction generators can also be used in off-grid applications for supplying isolated areas. The voltage may be built-up either by the residual flux or by pre-charged capacitors connected in parallel to the machine. The main disadvantage of the self-excited induction generator (SEIG) is poor regulation of the frequency and magnitude of the generator stator voltage [2]. The frequency is affected by the load level due to the machine slip, while the magnitude depends mainly on the value of excitation capacitor, magnetization characteristics as well as electrical load and its power factor.

Induction generators may be operated at a constant speed or variable speed. The variable speed operation is often used in the systems where speed regulation may provide higher energy conversion efficiency of the turbine under changeable conditions, for instance in wind systems. However, it requires using a full-scale AC/DC/AC converter consisting of two back-to-back PWM inverters, which increases the control complexity, costs and decreases the overall system efficiency. Moreover, the induction generator efficiency is significantly affected by the power and speed variations [3].

In the recent literature, many control methods providing voltage and frequency regulation of the constant speed SEIG are presented. The basic voltage controllers use Thyristor Switched Capacitors (TSC) to adjust the terminal voltage [4], while other solutions employ a power electronic converter, such as Static Var Compensator (SVC) that provides voltage regulation [5] with an assumption of the constant speed operation. The simple speed governor controls the input mechanical torque in order to keep a constant frequency [6]. This solution characterizes poor regulation capabilities under dynamic transients due to the large mechanical time constants. Other structures, called ungoverned-speed-based systems, also employ the PWM inverters, but do not control the speed. The voltage regulation is done by consuming all exceeding energy of the generated power (not consumed by the load) by the controlled resistance acting as an electronic load controller [7] or sending it to the grid by a single-phase line [8]. The surplus energy may also be utilized by a controlled load like the variable frequency induction motor drive (VFIMD) [9]. New methods use two separate modules, known as a distribution static compensator and VFIMD, which control the voltage and the frequency separately [10]. The stabilization of the stator voltage amplitude of an induction generator can also be achieved using the field-orientation control strategy for PWM voltage source inverter [11]. This method ensures voltage amplitude stabilization even at high dynamic load changes and changes of rotor speed of the generator; however it requires a large number of processing signals to estimate the rotor flux space vector.

Very promising solutions use the voltage source inverter (VSI) with the battery energy storage system (BESS) [12, 13]. The battery is used to control the active power and thus adjusts the voltage frequency. The significant load variations require providing a large-size energy buffer. Moreover, these solutions are appropriate for the energy source systems that are suitable to operate under narrow speed variations also called the “constant-frequency systems”. It means that the almost-constant speed cannot affect the energy conversion efficiency under changeable conditions. Taking into account turbine performance, this solution is rather suitable for hydropower than for wind turbines.

In this paper, the VSI with the BESS is employed to control the magnitude and frequency of the load voltage in a small hydropower plant. In order to minimize the battery size, power governor (input torque governor), in the form of the guide vane regulator, is implemented. The active power provided by the converter is used only in the dynamic transients, while the power governor is adjusting. The system model containing a squirrel-cage induction generator, converter with batteries and variable load is prepared in the Matlab/Simulink software using the power system blockset (PSB) toolboxes.

2. Description of the energy conversion system

The configuration of the analyzed energy conversion system is presented in Fig. 1. The induction generator is driven by the water turbine via a gearbox. A hydro-set also contains guide vanes, which control the amount of water flowing through the turbine. The excitation is provided by the capacitor bank and the voltage controller (VC), which consists of the VSI, the battery and a reactor. The VC acts as the bidirectional source of active and reactive power and controls the voltage in magnitude and frequency that are perturbed by the variable three-phase load.

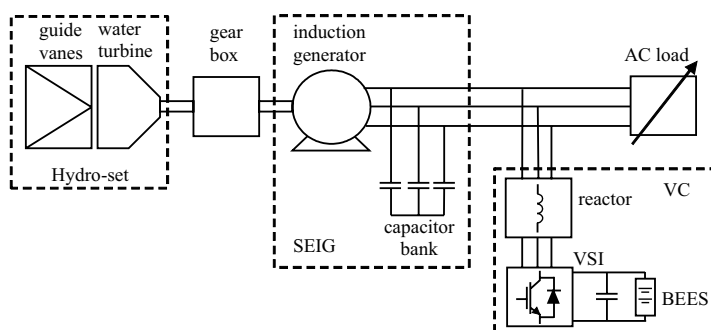


Fig. 1. Schematic diagram of the system configuration of the energy conversion system

3. Hydro-set model

In the paper, the reservoir hydropower plant is investigated, where stored water can be used when it is the most convenient. The main operation target is to utilize the water energy according to the energy demand of the load. This function is performed by guide

vanes, which control the turbine discharge. Assuming a constant water head, defined as the difference between the upper and the lower water level, the discharge corresponds to the water power potential. The output power of the water turbine is additionally affected by its efficiency (1).

$$P_t = 9.81 \cdot \rho_w \cdot Q \cdot H \cdot \eta \quad (1)$$

where:

- ρ_w – water density [kg/m³],
- Q – water flow (turbine discharge) [m³/s],
- H – difference of water level between the upstream level and the downstream level (water head) [m],
- η – turbine efficiency.

The turbine performance is usually visualized on the water discharge – speed plane, the so-called hill chart. It also presents the efficiency isolines that connect the operation points with the same efficiency. This chart is obtained from mathematical modelling or it is identified on the site after turbine installation. Using formula (1) and the hill chart, it is possible to approximate the relative torque of the turbine by a polynomial function of relative speed (2) with constants that are guide vane angle functions [14].

$$T_t^r = C_H \cdot (a(\alpha) \cdot n_t^{r^2} + b(\alpha) \cdot n_t^r + c(\alpha)), \quad C_H = \left(\frac{H}{H_N} \right)^{3/2}, \quad n_t^r = \frac{n_t}{n_{tN}} \left(\frac{H}{H_N} \right)^{1/2} \quad (2)$$

where:

- n_t^r – relative water turbine velocity,
- C_H – water level coefficient,
- $a(\alpha), b(\alpha), c(\alpha)$ – function coefficients,
- α – guide vane angle [%].

The function coefficients were identified in the real hydropower plant with a propeller turbine. Taking the nominal parameters: $Q_N, H_N, \eta_N, \alpha_N, n_{tN}$ as reference values, the function coefficients can be approximated by the following functions [14].

$$\begin{aligned} a(\alpha) &= -0.44423\alpha^3 + 2.32343\alpha^2 - 3.12\alpha \\ b(\alpha) &= 3.6548\alpha^5 - 13.585\alpha^4 + 15.256\alpha^3 - 5.552\alpha^2 + 2.094\alpha \\ c(\alpha) &= -2.4484\alpha^5 + 10.09\alpha^4 - 13.493\alpha^3 + 5.872\alpha^2 + 0.347\alpha \end{aligned} \quad (3)$$

The shape of the turbine torque at different guide vane angles under constant water head is presented in Fig. 2.

The hydro-set model should include the dynamics of the water mass that is contained in the pipeline and the turbine. It is usually defined by the water inertia time constant (4) [15].

$$T_w = \frac{Q_N}{gH_N} \frac{L}{A} \quad (4)$$

where:

- g – gravity acceleration,
- L – pipeline length,
- A – cross section area of the pipeline.

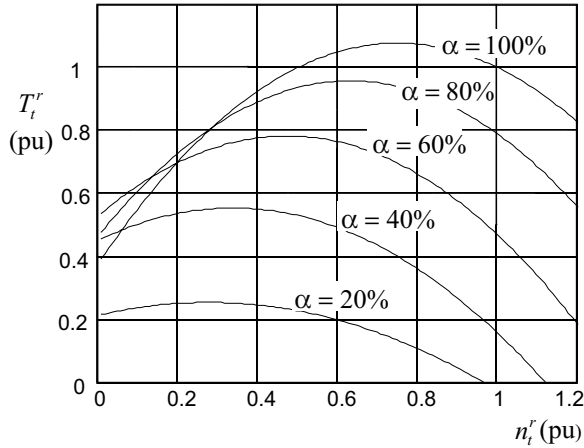


Fig. 2. Propeller turbine torque curves at different guide vane angles and nominal head in the per-unit system

The guide vane governor often operates based on the fluid drive system, where the movement is controlled by the electrically operated spool valve. The movement speed is determined by the fluid pressure and it is constant. Therefore, the model of the guide vane governor should include the speed limiter (R_s – raising and failing slew rate). The governor time constant is very small in comparison to the water inertia time constant, so it may be neglected.

The resulting hydro-set model containing the steady state relation of torque (2) with coefficients (3), water inertia time constant (4) and the governor speed limiter is presented in Fig. 3.

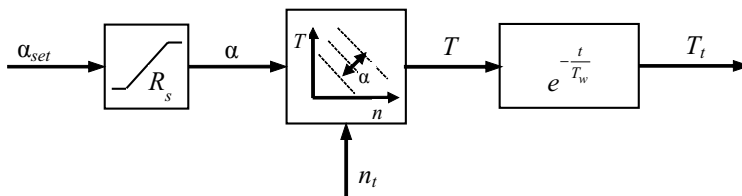


Fig. 3. Block diagram of the hydro-set model

4. SEIG model

The model of a three-phase squirrel-cage asynchronous machine is taken from the SimPowSys library. The model with a reference frame of rotor and Park transformation is used. The electrical part is represented by the four order state space model, while the mechanical part by the second order system [16]. The saturation of the mutual flux is specified by the curve of the stator voltage versus the stator current in the no-load state. The curve points are approximated by the piecewise linear relationship.

The capacitance value of the capacitor bank is assigned to the generator parameters in order to provide the excitation and may be obtained from the principle of L - C resonance according to the value (5).

$$C_g = \frac{1}{2\pi f (X_{\sigma s} + X_m)} \quad (5)$$

where:

- f – voltage frequency,
- $X_{\sigma s}$ – stator leakage reactance,
- X_m – magnetizing reactance.

5. VC model

The VC is controlled using the space vector (SV) technique. The SV based modulation gives better voltage utilization and reduces the harmonics of output signals more than the conventional sinusoidal PWM technique [17]. The block diagram of the SV generator is presented in Fig. 4. The sector selector indicates one of the six sectors, depending on the actual voltage angle. Then, the duration time block calculates the time duration of two adjustment active vectors (T_i , T_j) for a given sector from the sector number, voltage angle, reference line voltage U_{ref} , actual DC voltage U_{dc} and switching period T_s . The modulation index m is defined by (6).

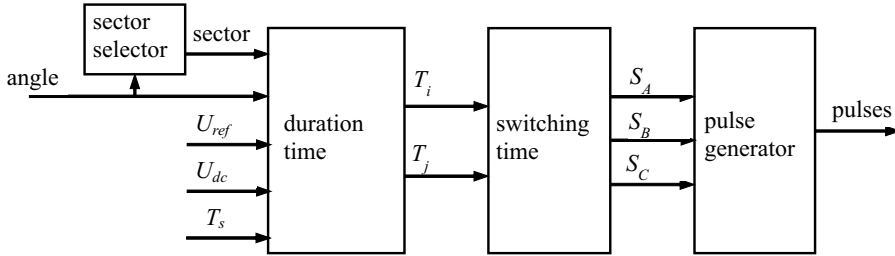


Fig. 4. Block diagram of the space vector generator.

$$m = \sqrt{3} \frac{U_{ref}}{U_{dc}} \quad \text{where: } 0 \leq m \leq \sqrt{2} \quad (6)$$

The timing sequence for each transistor (S_A , S_B , S_C) is estimated by the SVPWM switching patterns at each sector in the switching time block. Pulses for IGBT transistors are generated in the pulse generator block by comparing the switching timing signals with a triangle wave signal.

The presence of the capacitor bank decreases the VC reactive power necessary to regulate the voltage magnitude. It also constitutes with the VC inductance (reactor) the low pass filter. The inductance value L_{vc} can be calculated depending on the cut off frequency f_c (7). Furthermore, the minimum cost, losses and weight criteria should be taken into consideration [18].

$$L_{vc} = \frac{1}{(2\pi f_c)^2 C_g} \quad (7)$$

The battery model is characterized by the following parameters: nominal voltage U_{batt} , rated capacity Q_{batt} and the shape of the discharge characteristics. The discharge characteristics depend on the battery type. The battery used in the BEES is a Lithium-Ion battery because of the low internal resistance. The battery parameters have to be set mainly depending on the load value and guide vane governor. The maximal discharge current is determined by the load value for the minimal possible DC voltage, while the dynamics of the guide vane governor define the battery capacity and the discharge curve shape. The main condition is enough to keep the high DC voltage for the VSI to provide AC voltage higher

than the nominal load voltage according to the formula: $U_{dc} > \sqrt{\frac{3}{2}} U_l$. The battery should

maintain a DC voltage higher than 500 V under the maximal discharge current I_{batt}^{max} for the specific time. This time, defined by the hydro-set slew rate $T_{batt} \geq 1/R_s$, is enough to change the guide vane angle from 0 to 100% by the governor. The battery parameters are given in the Appendix and the battery discharge curve is presented in Fig. 5.

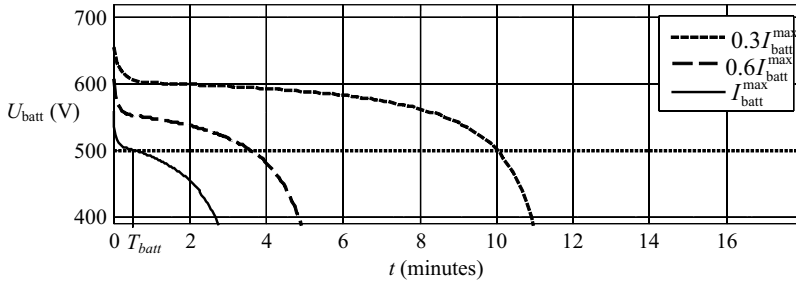


Fig. 5. Discharge curve of the Lithium-Ion battery (parameters given in the Appendix) under different discharge currents

6. Control strategy

The VC aim is to control the voltage of the load in magnitude and frequency. A simplified equivalent circuit of the VC connected to the load line through the impedance Z_{vc} is presented in Fig. 6.

The power flow at the connection point is described as follows [19].

$$\begin{aligned} \underline{S}_{vc} &= P_{vc} + jQ_{vc} = \underline{U}_l \underline{I}^* = \underline{U}_l \left(\frac{\underline{U}_l - \underline{U}_{vc}}{\underline{Z}_{vc}} \right)^* = \underline{U}_g \left(\frac{\underline{U}_l - \underline{U}_{vc} e^{j\varphi_0}}{\underline{Z}_{vc} e^{-j\vartheta}} \right) = \\ &= \frac{U_l^2}{Z_{vc}} e^{j\vartheta} - \frac{U_l U_{vc}}{Z_{vc}} e^{j(\vartheta + \varphi_0)} \end{aligned} \quad (8)$$

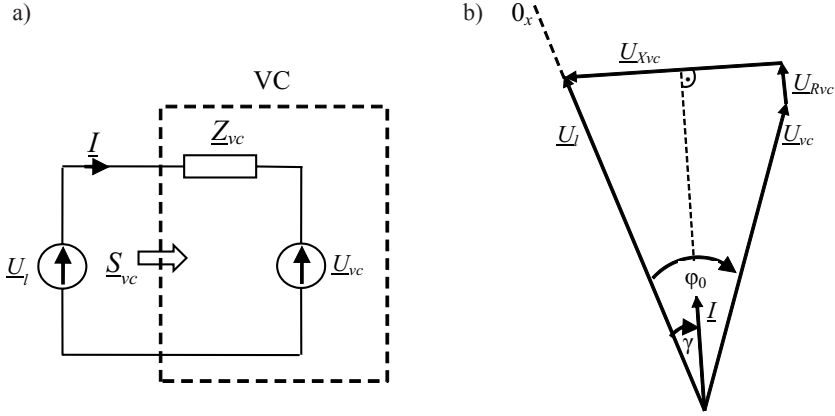


Fig. 6. VC connected to the load line: a) equivalent circuit, b) phasor diagram

The active and reactive power component can be calculated by separating the real and imagined part.

$$P_{vc} = \frac{U_l^2}{Z_{vc}} \cos(\vartheta) - \frac{U_l U_{vc}}{Z_{vc}} \cos(\vartheta + \varphi_0) \quad Q_{vc} = \frac{U_l^2}{Z_{vc}} \sin(\vartheta) - \frac{U_l U_{vc}}{Z_{vc}} \sin(\vartheta + \varphi_0) \quad (9)$$

Introducing $\vartheta = \arctg\left(\frac{X_{vc}}{R_{vc}}\right)$, these formulas may be presented as:

$$P_{vc} = \frac{U_l}{Z_{vc}^2} \left[R_{vc} (U_l - U_{vc} \cos(\varphi_0)) + X_{vc} U_{vc} \sin(\varphi_0) \right]$$

$$Q_{vc} = \frac{U_l}{Z_{vc}^2} \left[-R_{vc} U_{vc} \sin(\varphi_0) + X_{vc} (U_l - U_{vc} \cos(\varphi_0)) \right] \quad (10)$$

Assuming that the inductance is dominant, $X_{vc} \gg R_{vc}$ the resistance can be neglected. Moreover, considering the small value of the phase φ_0 ($\varphi_0 < 10^\circ$), which results in $\sin(\varphi_0) \approx \varphi_0$ and $\cos(\varphi_0) \approx 1$, the equations (10) may be simplified.

$$P_{vc} = \frac{U_l U_{vc}}{X_{vc}} \varphi_0, \quad Q_{vc} = \frac{U_l}{X_{vc}} (U_l - U_{vc}) \quad (11)$$

The above formulas (11) mean that the active power depends mainly on the voltage phase φ_0 of the VC, while the reactive power depends on the voltage difference $U_l - U_{vc}$.

The frequency control is provided by the voltage phase of the VC. The voltage angle is set in the SVM generator and defined by the system frequency and the phase $\varphi = \omega_{vc} t + \varphi_0 = 2\pi f_{vc} t + \varphi_0$. In the situation when the active power of the load equals the generated power, the voltage phases of the load and the VC are equal, then $\varphi_0 = 0$ and $P_{vc} = 0$. Any disturbances of the system frequency (phase), caused by the surplus or deficiency of the active power in the system, is compensated by the active power provided

by the VSI. The surplus energy charges the battery, while the deficiency of active power discharges it.

The voltage magnitude of the SEIG depends on the reactive power value. The VC can provide additional reactive power in order to maintain the magnitude at the constant level. This is done with the value of the reference voltage, which is set in the SVM generator. The reference voltage is related to the modulation index (6) by the DC voltage, which value can vary according to the battery charge. The reference voltage is adjusted by the PI controller in the closed loop control based on the actual error (Fig 7). The PI error is calculated based on the RMS value of the line voltage. The line voltage can be estimated from the 3- instantaneous line voltages using formula (12) and it is filtered by the low pass filter (f_n – natural frequency, ζ – damping ratio).

$$U_{\text{RMS}} = \sqrt{\frac{1}{3}(u_a^2 + u_b^2 + u_c^2)} \quad (12)$$

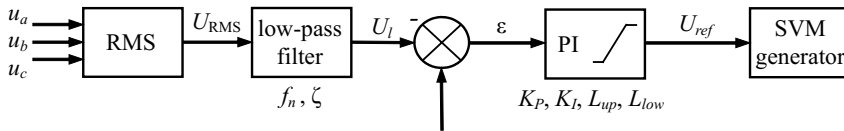


Fig. 7. Controller of the voltage magnitude (reactive power controller)

The state of the battery charge has to be controlled in order to provide the minimum DC voltage value necessary to obtain the fundamental line-voltage amplitude at about 400 V. This is the task of the guide vane controller (Fig. 8). The fully charged battery voltage is the set point. The PI regulator adjusts the set angle of the guide vanes, which is the input of the hydro-set model (Fig. 3). The Hydro-set model calculates the actual turbine torque that is transferred by the gearbox of the gear ratio R_g which matches the generator and turbine speeds.

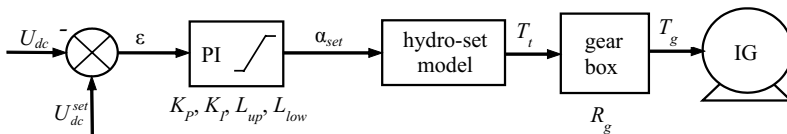


Fig. 8. Guide vane controller (battery charge controller)

7. Simulation results

The simulations have been performed in the Matlab/Simulink software with parameters and rated data given in the Appendix. The ready elements: induction motor, battery, universal bridge are taken from the SimPowerSys toolbox. The prepared model is solved in a discrete mode with $1 \cdot 10^{-6}$ s of sample time using the Tustin method. The initial conditions concern the generator slip (0.01) and the capacitor bank voltages (50 V, -25 V, -25 V).

The simulation presents time domain signals of the system disturbed by the changing load. The step changes of the load that affects the magnitude and frequency of the load voltage have been analyzed. The simulation sequence is as follows.

At the beginning the voltage build-up process with no load, that takes about 1 s, is visible (Fig. 9). After 4 seconds when the line voltage equals 400 V the three-phase load ($P_l = 3.5 \text{ kW}$, $Q_l^{ind} = 1 \text{ kVar}$) is connected. A small dip of the voltage and frequency at this time is visible; however, the voltage controller reaches the set point within 1s after the disturbance. In order to keep the frequency constant, the VC supplements the active power of the load, while the guide vane governor is adjusting (Fig. 10). Initially, it covers all of the load power demand. This process takes time due to the long hydro-set time constants. In the steady state, the total active power of the load is provided by the induction generator.

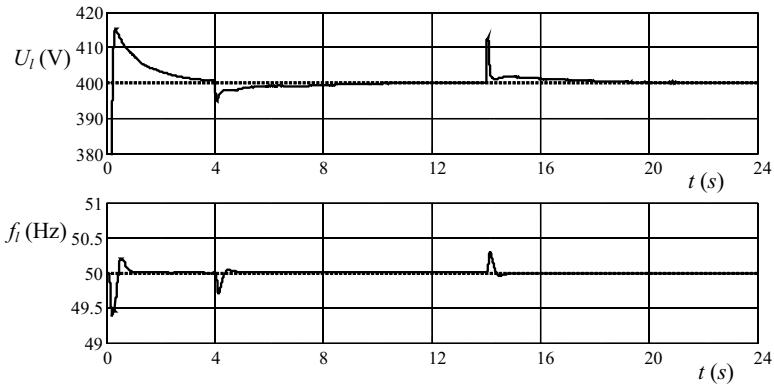


Fig. 9. Variations of the voltage in magnitude and frequency of the load

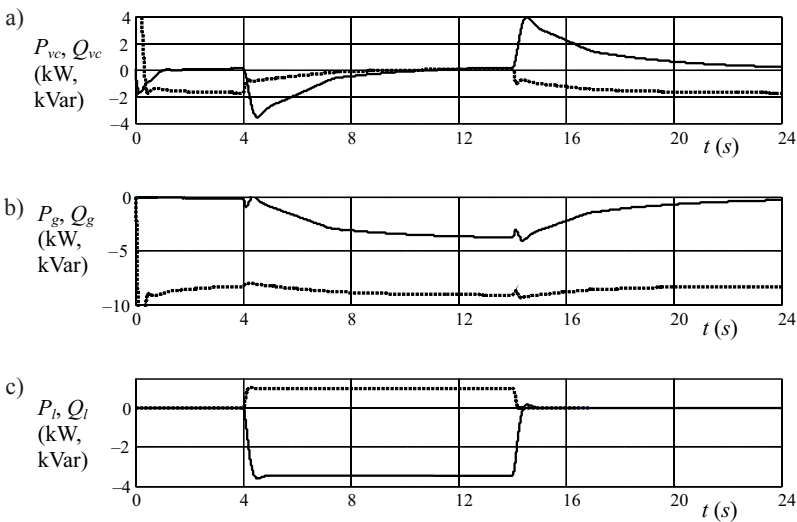


Fig. 10. Active (solid line) and reactive (dotted line) power flow: a) VC, b) generator, c) load

At $t = 14$ s the load is switched off what causes the voltage and frequency increase. These perturbations are quickly eliminated by the VC which absorbs the surplus power in the battery. The battery current (Fig. 11) which corresponds to the charging process indicates the battery contribution in the control process for about 8 seconds after the load disturbance. At this time the battery energy is compensated to its nominal capacity by the guide vane controller which monitors the battery voltage.

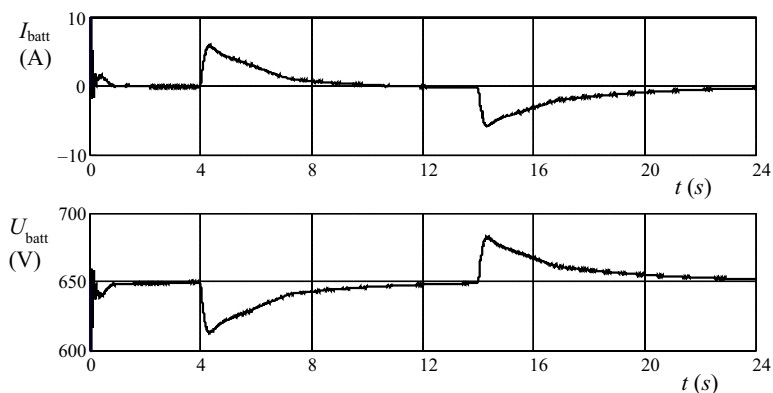


Fig. 11. Current and voltage of the battery

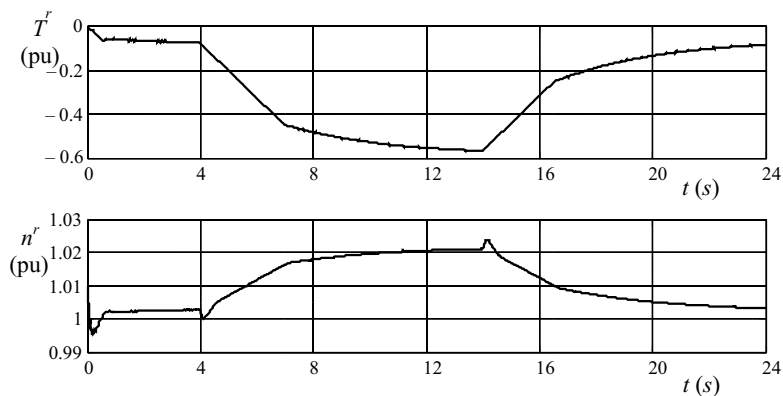


Fig. 12. Relative values of torque and speed of the generator

The turbine governor adjusts the generator's torque through the guide vane angle according to the battery voltage (Fig. 12). This affects the generator speed, which is additionally disturbed by the load variations.

The aim of the control system in the form of the voltage in magnitude and frequency stabilization is achieved with the satisfactory static and dynamic results. The SEIG in cooperation with the VC provide the active and reactive energy, according to the load demand (Fig. 10c).

8. Conclusions

The presented test shows the system dynamic performance under step changes of the electrical load. The voltage and frequency variations are minimized by using the VC, which acts as a controllable active and reactive power source. The energy buffer (battery) provides the active power necessary to maintain a constant frequency. The presented system uses the guide vane governor that controls the DC voltage of the battery. This solution minimizes the size of the battery of which energy is utilized only for a short time after the load disturbance when the guide vane governor is adjusting. Moreover, the VC decreases the negative dynamic stress of the hydro-set during the load disturbance. The presented frequency stabilization with variations of less than 0.5 Hz is not achievable by conventional speed governors due to the large turbine time constants. The VC can also compensate the reactive power of the load. By adding the VC to the conventional small reservoir hydropower plant with an induction generator and a guide vane governor, it is possible to achieve an autonomous generating system, which provides voltage and frequency stabilization.

Acknowledgment

The presented results of the research, which was carried out under the theme No. E-2/580/2016/DS, were funded by the subsidies on science granted by Polish Ministry of Science and Higher Education.

Appedndix

Hydro-set model	SEIG model	VC model	Voltage controller	Guide vane controller
$Q_N = 1 \text{ m}^3/\text{s}$ $H_N = 1 \text{ m}$ $\eta_N = 0.75$ $\alpha_N = 100\%$ $n_{iN} = 600 \text{ rpm}$ $g = 9.81 \text{ m/s}^2$ $L = 5 \text{ m}$ $A = 0.24 \text{ m}^2$ $T_w = 2.12 \text{ s}$ $R_s = 20\%/s$	$P_N = 7.5 \text{ kW}$ $U_N = 400 \text{ V}$ $n_N = 1440 \text{ rpm}$ $X_{as} = 0.226 \Omega$ $X_m = 13.04 \Omega$ $C_g = 480 \mu\text{F}$ $R_g = 2.6$	$T_s = 0.0002 \text{ s}$ $L_{vc} = 1 \text{ mH}$ $U_{batt} = 600 \text{ V}$ $U_{batt} = 1 \text{ Ah}$ $I_{batt}^{\max} = 15 \text{ A}$ $T_{batt} = 25 \text{ s}$ $\omega_{vc} = 100 \pi \text{ rad/s}$ $C_{dc} = 2 \text{ mF}$ $f_c = 112 \text{ Hz}$	$f_n = 20 \text{ Hz}$ $\zeta = 1$ $U_l^{set} = 400 \text{ V}$ $K_p = 1$ $K_I = 8$ $L_{up} = 420 \text{ V}$ $L_{low} = 370 \text{ V}$	$U_{dc}^{set} = 650 \text{ V}$ $K_p = 0.003$ $K_I = 0.02$ $L_{up} = 1.1$ $L_{low} = 0$

References

- [1] Singh G.K., *Self-excited induction generator research – a survey*, Electric Power Systems Research, vol. 69, 2004, 107–114.
- [2] Bansal R., *Three-phase self-excited induction generators an overview*, IEEE Transactions on Energy Conversion, vol. 20(2), 2005, 292–299.
- [3] Alnasir Z., Kazerani M., *Performance comparison of standalone SCIG and PMSG-based wind energy conversion systems*, IEEE 27th Canadian Conference on Electrical and Computer Engineering (CCECE), Toronto, 4–7 May 2014, 1–8.

- [4] Haque M.H., *Voltage regulation of a stand-alone induction generator using thyristor-switched capacitors*, IEEE International Conference on Sustainable Energy Technologies, Singapore, 24–27 Nov. 2008, 34–39.
- [5] Ahmed T., Noro O., Nakaoka M., *Terminal voltage regulation characteristics by static var compensator for a three-phase self-excited induction generator*, IEEE Transactions on Industry Applications, vol. 40(4), 2004, 978–988.
- [6] Suarez E., Bortolotto G., *Voltage-frequency control of a self excited induction generator*, IEEE Trans. on Energy Convers., vol. 14(3), 1999, 394–401.
- [7] Marra E., Pomilio J., *Self-excited induction generator controlled by a VS-PWM bidirectional converter for rural applications*, IEEE Transactions on Industry Applications, vol. 35(4), 1999, 877–883.
- [8] Marra E.G., Pomilio J.A., *Induction-generator-based system providing regulated voltage with constant frequency*, IEEE Transactions on Industrial Electronics, vol. 47(4), 2000, 908–914.
- [9] Chilipi R.R., Singh B., Murthy S., *A new voltage and frequency controller for standalone parallel operated self excited induction generators*, Int. J. Emerg. Elect. Power Syst., vol. 13(1), 2012, 1–17.
- [10] Chilipi R.R., Singh B., Murthy S.S., *Performance of a Self-Excited Induction Generator With DSTATCOM-DTC Drive-Based Voltage and Frequency Controller*, IEEE Transactions on Energy Conversion, vol. 29(3), 2014, 545–557.
- [11] Jakubowski B., Pieńkowski K., *Analysis and synthesis of converter control system of autonomous induction generator with field oriented control*, Archives of Electrical Engineering, vol. 62(2), 2013, 267–279.
- [12] Singh B., Kasal G.K., *Voltage and Frequency Controller for a Three-phase Four-wire Autonomous Wind Energy Conversion System*, IEEE Transaction on Energy Conversion, vol. 23(2), 2008, 509–518.
- [13] Barrado J., Grino R., Valderrama-Blavi H., *Power-quality improvement of a stand-alone induction generator using a statcom with battery energy storage system*, IEEE Trans. Power Del., vol. 25(4), 2010, 2734–2741.
- [14] Borkowski D., *Performance analysis of the Single-Phase Grid-Connected Inverter of a photovoltaic system in water and wind applications*, E3S Web of Conferences, SEED, vol. 10, 2016, no. 00004.
- [15] Zoby M.R.G., Yanagihara J.I., *Analysis of the primary control system of a hydropower plant in isolated model*, Journal of the Brazilian Society of Mechanical Sciences and Engineering, vol. 31, 2009, 5–11.
- [16] Boldea I., *The Electric Generators Handbook, Volume II: Variable speed generators*. CRS Press, Boca Raton USA 2006.
- [17] Mohan N., Undeland T.M., Robbins W.P., *Power Electronics: Converters, Applications and Design*, Wiley, New York 1996.
- [18] IEEE Standard 519-1992: IEEE Recommended Practices and Requirements for Harmonic Control in Electrical Power Systems, New York, USA, 1993.
- [19] De Brabandere K., Bolsens B., Van den Keybus J., Woyte A., Driesen J. and Belmans R., *A Voltage and Frequency Droop Control Method for Parallel Inverters*, IEEE Transactions on Power Electronics, vol. 22(4), 2007, 1107–1115.

VASYL I. HUDYM*, PIOTR DROZDOWSKI**, DOMINIK MAMCARZ**

INFLUENCE OF A PASSIVE CONTROLLED L-C FILTER ON HIGHER VOLTAGE AND CURRENT HARMONICS IN THE POWER SUPPLY NETWORK FOR ELECTRIC ARC DEVICES

WPLYW STEROWANEGO FILTRA PASYWNEGO NA WYŻSZE HARMONICZNE NAPIĘCIA I PRĄDU W SIECIACH ZASILAJĄCYCH URZĄDZENIA ŁUKOWE

Abstract

Electrical machines, such as welding arc devices, negatively affect the quality of electric power in a supply network, which in turn affects the operation of loads connected in parallel. The aim of this paper is to present the results of research confirming the positive effect of a passive L-C filter dedicated for welding devices. The paper demonstrates the effectiveness of the filter, which not only helps to reduce the total voltage distortion, but the reactive power compensation as well. The results confirm that installing a passive controlled L-C filter significantly reduces power losses in elements of the power supply network. The conducted research leads the authors to recommend using such filters in electrical arc devices.

Keywords: voltage distortion, current distortion, welding arc devices, passive controlled L-C filter, higher harmonics

Streszczenie

Urządzenia elektryczne, takie jak spawalnicze urządzenia łukowe, negatywnie oddziałują na jakość energii elektrycznej w sieci zasilającej, co wpływa na pracę równoległe podłączonych odbiorników. Celem artykułu jest przedstawienie wyników badań, które potwierdzają pozytywny wpływ pasywnego filtra sterowanego przeznaczonego do urządzeń spawalniczych. Pokazano efektywność działania filtra, który nie tylko wpływa na obniżenie całkowitego współczynnika zniekształcenia przebiegu napięcia, ale i również kompensację mocy biernej. Wyniki potwierdzają, że instalacja pasywnego filtra sterowanego pozwala na istotne obniżenie strat mocy w elementach sieci zasilającej. Na podstawie otrzymanych wyników autorzy rekomendują stosowanie takich filtrów do urządzeń łukowych.

Słowa kluczowe: odkształcenie napięcia, odkształcenie prądu, spawalnicze urządzenia łukowe, pasywny filtr sterowany, wyższe harmoniczne

* Prof. D.Sc. Ph.D. Eng. Vasyl I. Hudym, Institute of Electromechanical Energy Conversion, Faculty of Electrical and Computer Engineering, Cracow University of Technology, Lviv State University of Life Safety.

** D.Sc. Ph.D. Eng. Piotr Drozdowski, M.Sc. Eng. Dominik Mamcarz, Institute of Electromechanical Energy Conversion, Faculty of Electrical and Computer Engineering, Cracow University of Technology.

1. Introduction

Many branches of industry use welding arc devices, which negatively affect the power supply network in terms of voltage fluctuations and the generation of higher harmonics. Loads connected in parallel, such as digital circuits and microprocessors, are vulnerable to distortions generated by active arc devices within the same network. One of the effects of arc devices is an unstable operation of power inverters. A majority of arc devices are powered with a low-voltage (0.4 kV) network and connected directly to it, with the electric arc constituting the source of process heat and a non-linear element of the electric circuit. The negative effect of these devices on the supply network depends on the parameters of the network and the device itself as well as on the short-circuit impedance of the electric power system [1, 5].

Numerous studies investigating the operation of arc devices in networks with different parameters showed that these devices are the sources of both even and uneven harmonics. During arc burning, however, the amplitude values of even harmonics depend on the material that the electrodes are made from and the welded material, while uneven harmonics depend on the voltage and current characteristics of the arc. Thus, it is extremely important to analyze the effect of arc devices on the power supply network and develop a method for limiting this effect [3, 6–8, 11–15].

2. Effect of arc devices on current and voltage waveforms in the power supply network

Welding arc devices using a jacketed fusible metal electrode (manual arc welding, MMA) are most commonly employed for minor welding works. They usually operate in objects with a connected load of 6 kW for a single-phase connection point and 16 kW for a three-phase connection point. The generated distortions and a low power factor of arc devices affect the distribution transformer located in a substation, leading to a pre-magnetization of the transformer, which in turn leads to increased voltage distortion, increased load of the transformer and, ultimately, to increased power losses [1, 7, 8, 11–15].

The waveform of the registered voltage (Fig. 2) in the power supply line during the operation of the analyzed arc device is asymmetrical about the *time*-axis and not

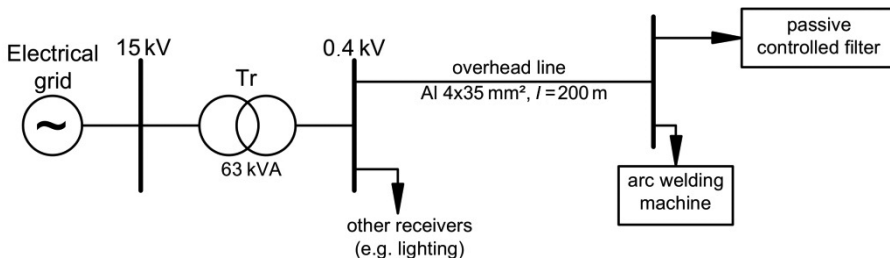


Fig. 1. Concept diagram of the power supply system

sinusoidal. This negative effect indicates the presence of a constant component in the frequency spectrum of voltage harmonics. This constant component causes undesirable pre-magnetization in the core of the transformer, which leads to increased distortion. The asymmetry results from differences in the characteristics of electron emissions between the metal and the electrode in the welded material. The analyzed arc device draws reactive power from the supply network, as indicated by the phase shift between the current and voltage waveforms.

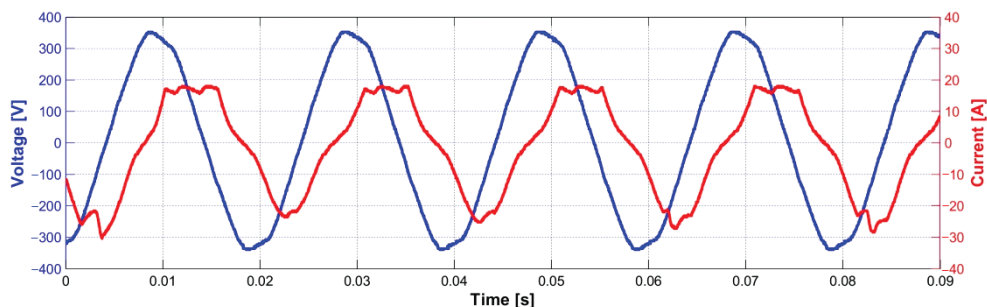


Fig. 2. Waveforms of voltage and current in the power supply line

The low value of the power factor (0.39) resulted in high reactive power consumption, which is highly undesirable from the viewpoint of an electric network, as it leads to increased values of operational currents, which in turn lead to increased power losses and voltage drops at individual elements of the transmission network and an increased temperature of the wires. On the other hand, from the viewpoint of the technological process and electric arc stability, the same state is beneficial and, indeed, necessary [1, 3, 9, 10].

The results in Fig. 3 and 4 are not presented in the discrete form, because not only multiples of the fundamental harmonic are existent. The total harmonic distortion of the voltage (THD_U), calculated based on the obtained spectrum of higher voltage harmonics, amounted to 13.08% (Fig. 3). According to the Polish Standard No. [9], THD_U should not exceed 8%, which means that the obtained result exceeds the allowable level by over 5% and is thus unacceptable [9, 10].

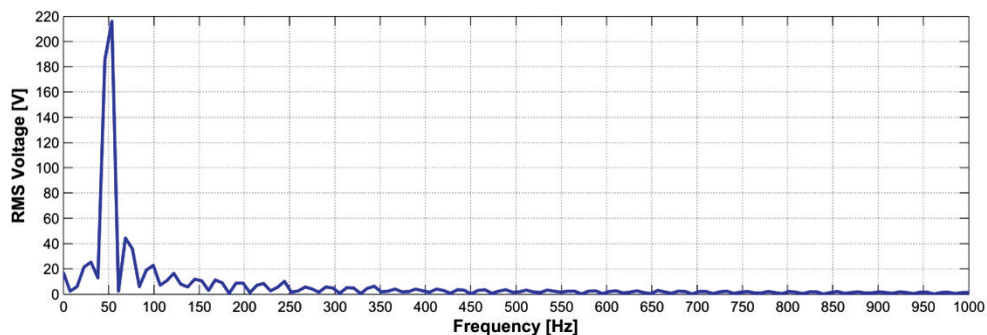


Fig. 3. Harmonic voltage spectrum

Even though [9] does not specify the allowable levels of current distortion, the total harmonic distortion of the current THD_1 was calculated. THD_1 amounted to 25.22%. The obtained frequency spectrum of higher current harmonics (Fig. 4) constitutes a reference point and will enable the assessment of the effect of a passive controlled L-C filter on reactive power compensation [9, 10].

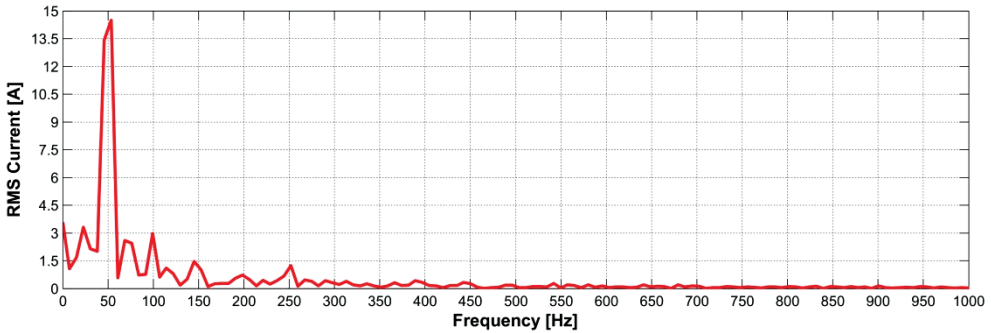


Fig. 4. Harmonic current spectrum

Passive resonant filters are usually used to reduce voltage distortion. However, due to changes in the amplitudes of harmonics over time and the occurrence of signals that are not whole-numbered multiples of the fundamental harmonic, filters with constant parameters can hardly improve the situation. A solution to these limitations may involve a passive controlled L-C filter, shown in Fig. 5.

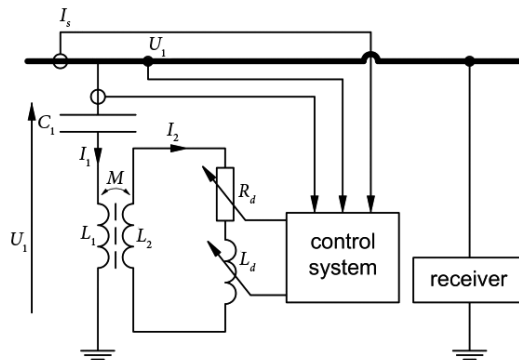


Fig. 5. Passive controlled L-C filter

The benefit of a passive controlled L-C filter is that its parameters can be adjusted during operation, i.e., without the need to detach the filter system from the supply voltage. The possibility to adjust the damping band and resonance frequency enables better filtration than in the case of ordinary passive filters with constant parameters. The filter is equipped in a solid-state relays (SSR) to changing values of the elements R_d and L_d . Systems of this type cause losses in active power. This, however, is acceptable in view of the benefits provided by the filter [2, 6, 15].

The filter system has capacitor properties for the frequency of the fundamental harmonic. This means that reactive power is generated, i.e., the system enables reactive power compensation. As the frequency increases, the system begins to function as a band-stop filter. The individual parts of the passive controlled L-C filter are selected to ensure that the total reactance for the resonance frequency between the connection points is equal to zero [2, 6, 15].

The System of Equations (1) was written based on the equivalent circuit shown in Fig. 5 to determine the values of resistance and inductance entering the main circuit of the filter [4].

$$\begin{cases} R_1 I_1 + j\omega L_1 I_1 + j\omega M I_2 = U_1 \\ R_2 I_2 + j\omega L_2 I_2 + R_d I_2 + j\omega L_d I_2 + j\omega M I_1 = 0 \end{cases} \quad (1)$$

After transformation it is obtained:

$$I_1 = \frac{U_1}{R_1 + R_{w1} + j\omega(L_1 - L_{w1})} \quad (2)$$

where:

$$R_f = R_1 + R_{w1} \quad (3)$$

$$L_f = L_1 - L_{w1} \quad (4)$$

$$R_{w1} = \frac{(\omega M)^2 (R_2 + R_d)}{(R_2 + R_d)^2 + (\omega L_2 + \omega L_d)^2} \quad (5)$$

$$L_{w1} = -\frac{(\omega M)^2 (L_2 + L_d)}{(R_2 + R_d)^2 + (\omega L_2 + \omega L_d)^2} \quad (6)$$

$$M = k\sqrt{L_1 L_2} \quad (7)$$

- f – frequency,
 k – coil coupling coefficient,
 L_1, L_2 – choke coil inductance,
 R_1, R_2 – choke coil resistance,
 R_{w1}, L_{w1} – resistance and inductance introduced into the primary circuit of the filter,
 R_d, L_d – resistance and inductance connected to the secondary coil of the choke,
 U_1, I_1, I_2 – have been explained in the Fig. 5.

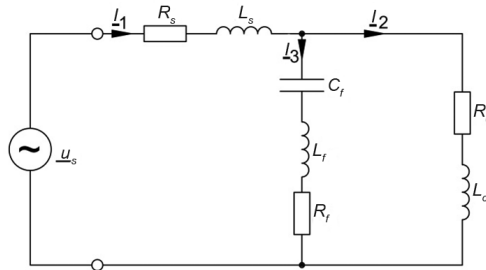


Fig. 6. Simplified diagram used for system analysis

To enable a more detailed analysis of the passive L-C filter and its effect on the power supply network, the impedance characteristics of the system shown in Fig. 6 were established. This analysis helps to determine the frequencies for which an undesirable parallel resonance can occur. The calculated equivalent impedance is given by Equation (8) [4].

$$\underline{Z}_z(j\omega) = R_s + j\omega L_s + \frac{(R_o + j\omega L_o) \left(R_f + j\omega L_f - j \frac{1}{\omega C_f} \right)}{R_o + j\omega L_o + R_f + j\omega L_f - j \frac{1}{\omega C_f}} \quad (8)$$

where:

- R_s, L_s – resistance and inductance of the power supply network,
- R_f – resistance representing losses in the filter,
- C_f, L_f – capacitance of the capacitor and inductance of the choke in the L-C filter,
- R_o, L_o – resistance and inductance of the load – measured for quasi steady-state.

Waveforms were established for the following parameters:

$$R_o = 240 \text{ m}\Omega, L_o = 0.120 \text{ mH},$$

$$R_f = 110 \text{ m}\Omega, C_f = 100 \text{ }\mu\text{F}$$

$$R_f = 110 \text{ m}\Omega, C_f = 100 \text{ }\mu\text{F},$$

For the resonance frequency, the impedance of the filter should be lower than the impedance of the power supply network to ensure appropriate damping of the filtered harmonic. The impedance characteristics presented in Fig. 7 show that, for certain frequencies, an undesirable resonance with the power supply network may occur, which strengthens the current harmonics and may thus lead to distortions in the waveform of the current flowing through the load and the network.

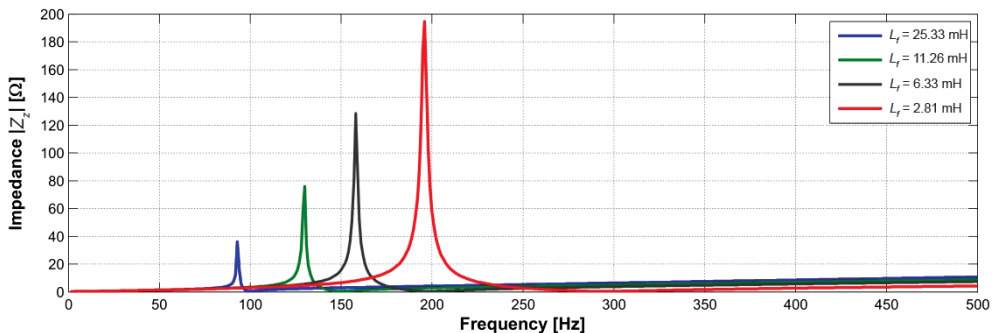


Fig. 7. Impedance characteristic of system

The phase characteristics shown in Fig. 8 indicate that changes to the inductance of the choke, with other elements of the filter remaining at constant values, correlate with a decrease in the Q factor of the system. As a result, the damping band increases.

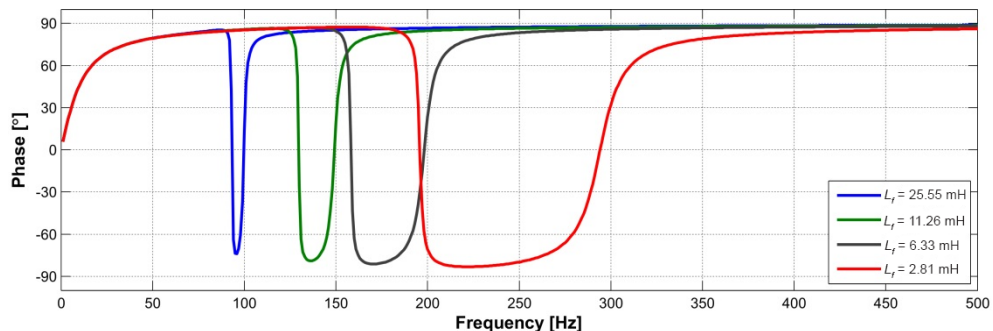


Fig. 8. Phase characteristic of system

When appropriate elements are added to the secondary circuit of the choke, a change in the parameters of the passive L-C filter allows the width of the damping band and the resonance frequency to be adjusted. Thus, filters of this type can extend their damping band over a large range of frequencies, eliminating not only the harmonics, but other constituents that are not whole-numbered multiples of the fundamental harmonic as well.

3. Effect of passive controlled filter on the quality of electric power

Connecting the passive L-C filter to the analyzed load in parallel helped to improve the waveform of the voltage in the power line, decreasing distortion to 4.57%. Fig. 9 shows the voltage waveform for the arc device with the filter introduced to the input. The applied filtration method also allowed the phase shift angle between current and voltage waveforms to be reduced, which indicates that the reactive power taken by the load from the supply network was compensated for. This means that the power factor $\cos\alpha$ has been improved, which led to the decrease in the current flowing in the power line and to the decrease in power losses.

The advantage provided by L-C filters, i.e., the ability to adjust the parameters of the system by introducing appropriately selected elements into the secondary coils of the filter

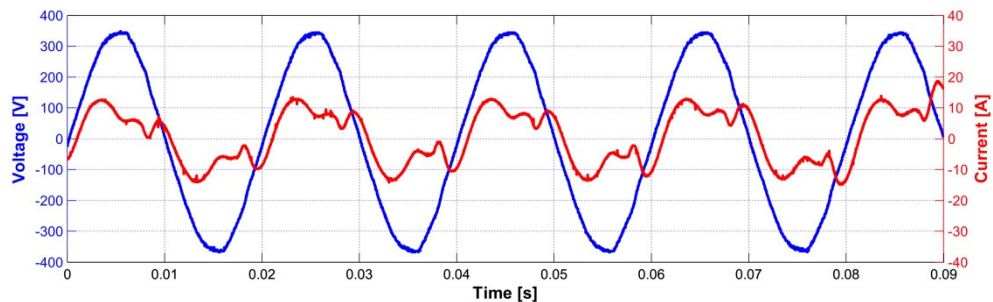


Fig. 9. Waveform of current and voltage in the power supply line (filter on)

choke, helped to improve the voltage waveform in the power supply line. The registered waveform was subjected to FFT. Fig. 10 shows the full range of obtained spectra of higher harmonics.

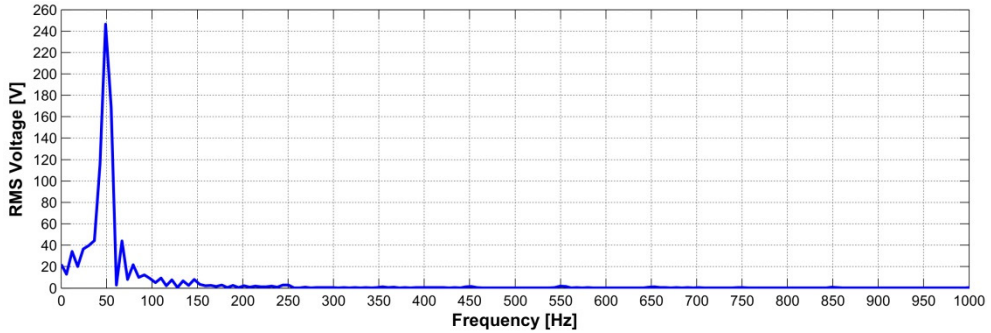


Fig. 10. Harmonic voltage spectrum (filter on)

A comparison between the spectra of higher voltage harmonics for two cases, i.e., a filter-less load and a load with a passive L-C filter introduced to the input, indicates a decrease in the amplitudes of higher harmonics for a certain range of frequencies. The voltage distortion coefficient has been decreased by over 10%. The new value falls within the allowable range stipulated by the Standard [9].

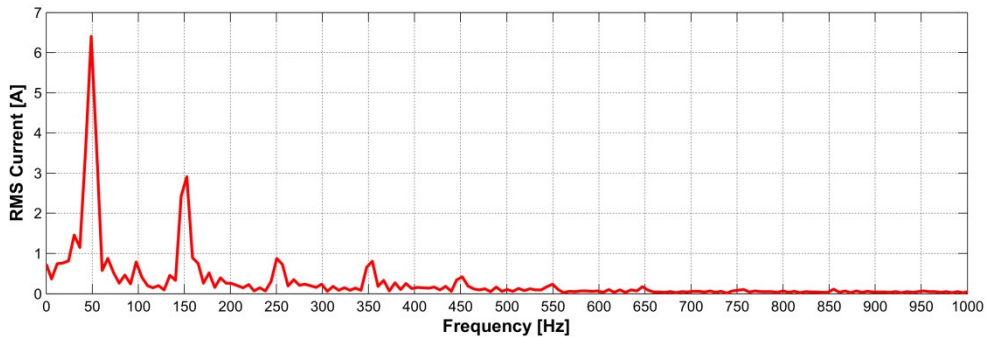


Fig. 11. Harmonic current spectrum (filter on)

The current distortion coefficient has been doubled. This was caused by the fact that the amplitude of the fundamental harmonic of the current has been decreased 2 times. In addition, the amplitudes of higher harmonics also has been decreased: the second harmonic has been decreased by approx. 23.5%, and the fifth by 52.3%. On the other hand, the value of the third harmonic increased, but because the required value of THD_U (stipulated by the [9] Standard) had been reached, the damping band of the filter was not raised. The current flowing through the power line decreased due to reactive power compensation. Consequently, the power factor increased from 0.39 to 0.96.

Important parameters related to the quality of electric power are the true mean square of voltage in the power supply network, the true mean square of current flowing in the power supply network, the reactive power, and the power factor $\cos\alpha$ (all measurements were taken using True RMS gauges). Table 1 shows the values of these parameters for a load with a filter and without one.

Table 1

Measured parameters

Parameter	filter off		filter on	
	Value	Unit	Value	Unit
Voltage U	242.6	[V]	247.38	[V]
Current I	15.0	[A]	8.7	[A]
Active power P	1419.2	[W]	2074.1	[W]
Reactive power Q	3350.8	[VAr]	574.4	[VAr]
Apparent power S	3639.0	[VA]	2152.2	[VA]
$\cos\alpha$	0.39	[-]	0.96	[-]
THD_U	13.08	[%]	4.57	[%]
THD_I	25.22	[%]	51.76	[%]

The obtained results indicate that the passive controlled L-C filter not only helps to decrease voltage distortions, but can also be used to compensate reactive power. Furthermore, installing the filter helped to reduce the current flowing in the power supply line, leading to decreased power losses. The previous observations confirm these arguments.

4. Summary

The analysis of literature and research results concerning arc loads allowed to determine the negative effect of these devices on the power supply network. This negative effect involves a dynamic process of changes to the arc discharge, which affects the current and voltage waveforms of the devices.

Using a passive controlled L-C filter helped to eliminate the disadvantage of passive filters adjusted to a single frequency, i.e., the risk of detuning due to changes in the frequency of the supply voltage and allowed the damping band to extend to constituents that were not whole-numbered multiples of the fundamental harmonic.

The obtained results indicate that the installed passive L-C filter operated correctly, as indicated by the decrease in THD_U by over 8% to 4.13%, which fell within the standard [9].

Arc loads have a low power factor. The power factor in the analyzed device amounts to 0.39, which negatively affects the power supply network. Thanks to the application of the passive controlled L-C filter, not only did the voltage waveform improve, but reactive power compensation also dropped from 3350.8 VAr to 574.4 VAr, improving the power factor to 0.96.

References

- [1] Dobaj E., *Maszyny i urządzenia spawalnicze*, WNT, Warszawa 1998, 52–60.
- [2] *Zagadnienia energetyczne wybranych urządzeń elektrycznych systemów stalowniczych*, pod red. Antoniego Sawickiego, Wydawnictwo Politechniki Częstochowskiej, Częstochowa 2010, 98–101.
- [3] Žeželenko I.V., *Vysšie garmoniki v sistemah elektroposnabženiâ prompredpriätij*, 4-e izd., M: Energoatomizdat, 2000.
- [4] Bolkowski S., *Teoria obwodów elektrycznych*, WNT, Warszawa 2008, 187–194.
- [5] Dugan R.C., McGranaghan M.F., Satoso S., Wayne Beaty H., *Electrical Power Systems Quality*, McGraw-Hill Companies, 2004.
- [6] Gudim V.I., *Tehnični zasobi znižennâ garmonik v elektropostaćalnih sistemah*, Tehn. Elektrodinamika, No 3/1996, 67–72.
- [7] Hanzelka Z., *Rozważania o jakości energii elektrycznej (IV)*, Elektroinstalator, No. 2/2001, 10–17.
- [8] Hanzelka Z., *Rozważania o jakości energii elektrycznej (V)*, Elektroinstalator, No1/2002, 26–31.
- [9] PN-EN 50160: Parametry napięcia zasilającego w publicznych sieciach elektroenergetycznych.
- [10] Rozporządzenie Ministra Gospodarki z dnia 4 maja 2007 r. w sprawie szczegółowych warunków funkcjonowania systemu elektroenergetycznego (Dz.U. Nr 93 z 2007 r., poz. 623).
- [11] Kusko A., *Power Quality in Electrical Systems*, McGraw-Hill Professional, 2007.
- [12] Vedam R. Sastry, Sarma M.S., *Power Quality: VAR Compensation in Power Systems*, CRC Press, 2008.
- [13] *Power Quality*, Edited by A. Eberhard, InTech, 2011.
- [14] Chattioadhyah S., Mitra M., Sengupta S., *Electric Power Quality*, Springer, 2011.
- [15] Fuchs E., Masoum M.A.S., *Power Quality in Power Systems and Electrical Machines*, AcademicPress, 2015.

WOJCIECH MYSIŃSKI, NATALIA PRAGŁOWSKA-RYŁKO*

USE OF MIDDLEBROOK'S METHOD IN FREQUENCY ANALYSIS OF POWER ELECTRONIC CIRCUITS

WYKORZYSTANIE METODY MIDDLEBROOK'A DO ANALIZY CZĘSTOTLIWOŚCIOWEJ UKŁADÓW ENERGOELEKTRONICZNYCH

Abstract

The article presents Middlebrook's method, which allows one to obtain the frequency analysis of power electronic circuits based on time analysis. The authors carried out their simulations in LTspice. The article discusses selected examples of circuits, such as an active filter, a resonant RLC circuit and a Buck-Converter with a correction circuit. An important advantage of Middlebrook's method is that it allows for the determination of the amplitude and phase characteristics for nonlinear circuits, as opposed the common .AC method. Simulation tests of non-linear circuits indicate that, in order to obtain correct results using Middlebrook's method, the values of input signals need to be selected very carefully.

Keywords: Middlebrook's method, AC analysis, Buck-Converter

Streszczenie

W artykule przedstawiono metodę Middlebrook'a, która umożliwia otrzymanie charakterystyki częstotliwościowej, np. układów energoelektronicznych na podstawie analizy czasowej. Autorzy przeprowadzili badania symulacyjne w programie LTspice, aby sprawdzić zalety i wady tej metody. Wzięto pod uwagę kilka układów, takich jak filtr aktywny, obwód rezonansowy RLC oraz przekształtnik DC/DC obniżający napięcie z torem korekcyjnym. Zaletą metody Middlebrook'a jest możliwość wyznaczania charakterystyki amplitudowej i fazowej w przypadku obwodów nieliniowych w porównaniu do zwykłej metody .AC. Badania symulacyjne układów nieliniowych pokazują, że należy bardzo starannie dobrać wartości sygnału wymuszającego, aby uzyskać poprawne wyniki w metodzie Middlebrook'a.

Słowa kluczowe: Metoda Middlebrook'a, analiza częstotliwościowa, Buck-Converter

* Ph.D. Eng. Wojciech Mysiński, M.Sc. Eng. Natalia Pragłowska-Ryłko, Institute of Electrotechnics and Computer Science, Faculty of Electrical Engineering and Computer Science, Cracow University of Technology.

1. Introduction

AC analysis is widely used in the case of electronic devices. One of the methods used to obtain frequency characteristics is Middlebrook's method. The significant advantage of this method is the retention of non-linear element characteristics, as compared with the classic AC analysis, which linearizes non-linear circuits, causing errors.

Middlebrook's method was published by R. David Middlebrook in 1975 in "Measurement of Loop Gain in Feedback Systems" [4]. Middlebrook's method determines frequency responses by employing time analysis (.TRAN analysis). The authors have added to the circuit a voltage sine source [2] which generates signals with the same amplitude but a different frequency for each iteration (for each .TRAN). The number of iterations is defined by a frequency step change. All sine signals have the same period number, but different duration and the stop time for each .TRAN analysis is different. The amplitude of sine signals determines the noise level [7].

In order to determine the frequency response of circuits, Middlebrook's method uses measured time-dependent values, frequency step changes and signal recalculations from the time domain to the field of complex. To obtain the frequency characteristics, the authors defined two measurement points *a* and *b* (as in Fig. 1) [3]. The location of the points depends on the location of circuit elements influencing the frequency characteristics.

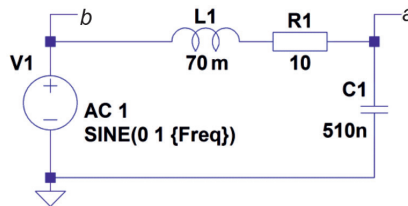


Fig. 1. Simple RLC resonant circuit

2. Middlebrook's method in LTspice

In Middlebrook's method frequency characteristics are based on the .TRAN analysis. Voltage values in points *a* and *b* are saved using the LTspice formula `.save V(a) V(b)`.

The LTspice uses the following formulas, described below [1, 4, 5].

$$\begin{cases} \text{.tran 0 } \{5 / \text{Freq} + 0.1 \text{ m}\} 0.1 \text{ m} \\ \text{.step dec param Freq 10 10k 10} \end{cases} \quad (1)$$

The analysis declaration defines the .TRAN analysis and frequency step change of input signal using the global parameter „Freq”.

$$\begin{cases} \text{.measure Aavg avg } V(a) \\ \text{.measure Bavg avg } V(b) \end{cases} \quad (2)$$

The first two above formulas allow us to measure mean voltage values in points a and b (3) for each. TRAN analysis.

$$\begin{cases} A_{avg} = \bar{V}(a) \\ B_{avg} = \bar{V}(b) \end{cases} \quad (3)$$

where:

A_{avg}, B_{avg} – mean voltage values in points a and b ,
 $V(a), V(b)$ – output and input voltage.

The next formulas eliminate the DC component from voltage signals (subtracting the mean voltage signal value from the current voltage value).

$$\begin{cases} .measure Are avg (V(a) - Aavg) \cdot \cos(360 \cdot \text{time} \cdot \text{Freq}) \\ .measure Aim avg - (V(a) - Aavg) \cdot \sin(360 \cdot \text{time} \cdot \text{Freq}) \\ .measure Bre avg (V(b) - Bavg) \cdot \cos(360 \cdot \text{time} \cdot \text{Freq}) \\ .measure Bim avg - (V(b) - Bavg) \cdot \sin(360 \cdot \text{time} \cdot \text{Freq}) \end{cases} \quad (4)$$

In the same step, the following equations transform the signals from the time domain to the field of complex (5). The LTSpice formulas convert the signals in points a and b to location vector with defined real and imaginary part, as shown below:

$$\begin{cases} A_{re} = \overline{(V(a) - \bar{V}(a)) \cos(2\pi tf)} \\ A_{im} = -\overline{(V(a) - \bar{V}(a)) \sin(2\pi tf)} \\ B_{re} = \overline{(V(b) - \bar{V}(b)) \cos(2\pi tf)} \\ B_{im} = -\overline{(V(b) - \bar{V}(b)) \sin(2\pi tf)} \end{cases} \quad (5)$$

where:

A_{re}, B_{re} – real parts of signals in points a and b ,
 A_{im}, B_{im} – imaginary parts of signals in points a and b ,
 f – input signal frequency,
 t – time,
 $\bar{V}(a), \bar{V}(b)$ – voltage in point a and b .

The last two formulas determine amplitude and phase characteristics. In order to define the final equations, the authors defined module (6) and argument – phase shift (7) of the spectral transfer function as:

$$|G(\omega)| = \frac{A(\omega)}{B(\omega)} \quad (6)$$

$$\varphi(\omega) = \arg G(j\omega) = f_A(\omega) - f_B(\omega) \quad (7)$$

where:

$A(\omega), B(\omega)$ – voltages in points a and b in function of pulsation ω ,
 $f_A(\omega), f_B(\omega)$ – phase shift of signals in points a and b in function of pulsation ω .

The transfer function can be also defined by the equation:

$$G(j\omega) = G_{re}(\omega) + jG_{im}(\omega) \quad (8)$$

where:

$$\begin{cases} G_{re}(\omega) = \text{Re}(G(j\omega)) \\ G_{im}(\omega) = \text{Im}(G(j\omega)) \end{cases} \quad (9)$$

The module of transfer function can be also defined as:

$$|G(j\omega)| = \sqrt{G_{re}^2(\omega) + G_{im}^2(\omega)} \quad (10)$$

The following equations are the final definition for amplitude and phase characteristics:

$$\begin{cases} |G(\omega)| = 20 \log |G(j\omega)| \\ \varphi(\omega) = \text{arctg} \frac{G_{im}(\omega)}{G_{re}(\omega)} \end{cases} \quad (11)$$

The LTspice formulas using the equations from (7) are presented below:

$$\begin{cases} \text{.measure GainMag param } 20 \cdot \log_{10}(\text{hypot}(A_{re}, A_{im}) / \text{hypot}(B_{re}, B_{im})) \\ \text{.measure GainPhi param mod}(\text{atan2}(A_{im}, A_{re}) - \text{atan2}(B_{im}, B_{re}) + 180, 360) - 180 \end{cases} \quad (12)$$

In the case of amplitude characteristic (GainMag), the authors used the hypot function to define the magnitude of A and B vectors. The final result is given in [dB].

Based on (7)–(11), the authors determined the phase characteristics (GainPhi). They also used the modulo function (mod) to move all values to one period (remainder from division by 360). What is more, in order to obtain the positive value in mod function, one should add 180 degrees (subtracting it later to obtain proper conditions), thus arriving at the final results.

2. Simulation results

Simulations were carried out for three different circuits: an RLC resonant circuit, an active filter, and the power stage of a Buck-Converter. Determining the open loop gain from a closed loop switch mode power supply is best accomplished using Middlebrook's method.

2.1. Resonant circuit

The first example shows the results for the simple linear RLC circuit from Fig. 1 – capacitor voltage in relation to input voltage. In order to compare the classic. AC analysis with Middlebrook's method, the authors made a frequency analysis using both methods. The results for 1000 measurement points per decade for. AC analysis and Middlebrook's method are presented in Fig. 2. and Fig. 3.

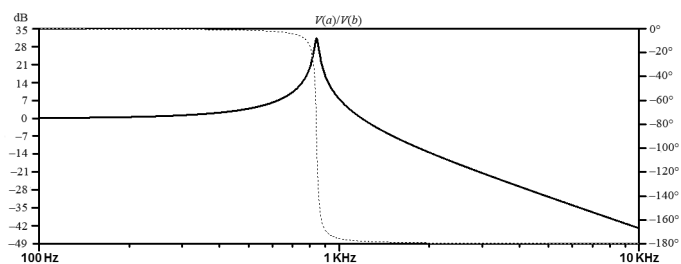


Fig. 2. Resonant circuit – classic .AC analysis

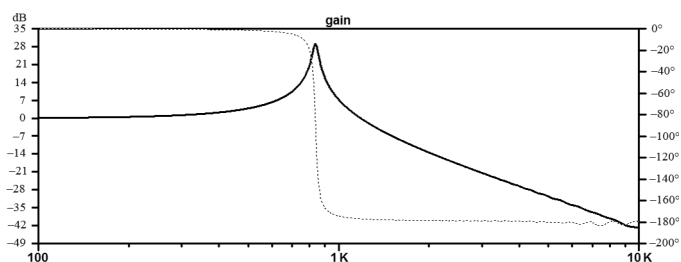


Fig. 3. Resonant circuit – Middlebrook's method

As can be seen in Fig. 2 and Fig. 3, in respect of the simple linear resonant circuit, the results from the classic .AC analysis and from Middlebrook's method are the same. The resonant frequency from calculations is ca. 842.33 Hz. The results from Middlebrook's method depend on the number of frequency changes. This simple exercise was designed to verify whether the mathematical equations and instructions in LTSpice are correct and allow for the determination of the frequency characteristics of the circuit using Middlebrook's method.

2.2. Active filter

The second analysis was carried out for the active low pass filter presented in Fig. 4.

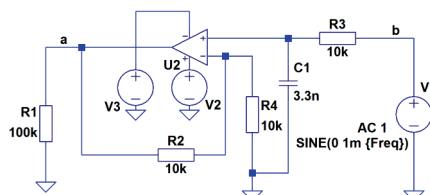


Fig. 4. Low-pass active filter

The frequency characteristics for the above circuit, determined using Middlebrook's method, are presented in Fig. 5.

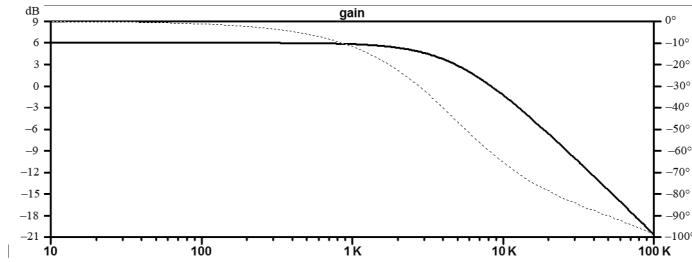


Fig. 5. Low-pass active filter – Middlebrook’s method

The frequency characteristics of the filter are same as the ones obtained from classic .AC analysis. These two simple examples demonstrate that the results obtained using Middlebrook’s method are the same as the ones produced in .AC analysis. However, the time taken to make the calculations with the classic .AC analysis is significantly shorter than the time taken by the other method. This is due to the fact that in order to obtain frequency characteristics of a circuit using Middlebrook’s method, it is necessary to carry out ca. 100. TRAN analyses, which is far more time-consuming.

2.3. Buck converter with a correction circuit

In this part, the authors analyzed a step-down converter with a correction circuit to show Middlebrook’s method for nonlinear circuits (with a transistor switch and a PWM regulator). The authors carried out the following simulations for three cases of additional voltage source locations and amplitudes. All the simulations were done for 100 measurement points per decade. The element values in correction circuit were selected to obtain a visible resonant frequency. In the first case (Fig. 6), the additional voltage signal amplitude was defined as 1 mV (because of significant damping of the amplifier) and the step frequency from 10 Hz to 5 kHz.

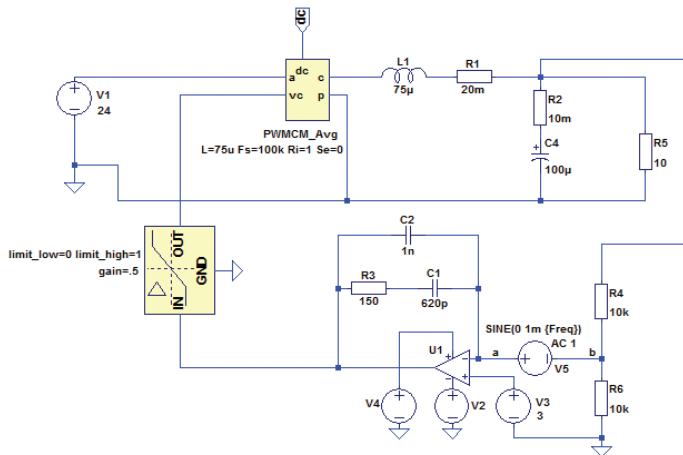


Fig. 6. Step-down converter with a correction circuit – case I

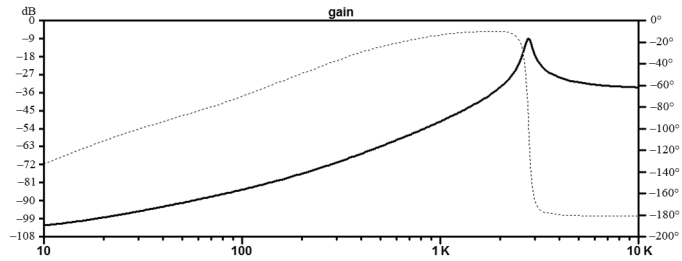


Fig. 7. Frequency analysis result for Step-Down Converter – Middlebrook's method

The analysis of the case shown in Fig. 6 shows the effect of element values from the correction circuit on the frequency characteristics.

In the second case of a buck converter, the voltage signal amplitude was defined as 100 mV in order to show the analysis for changing load current.

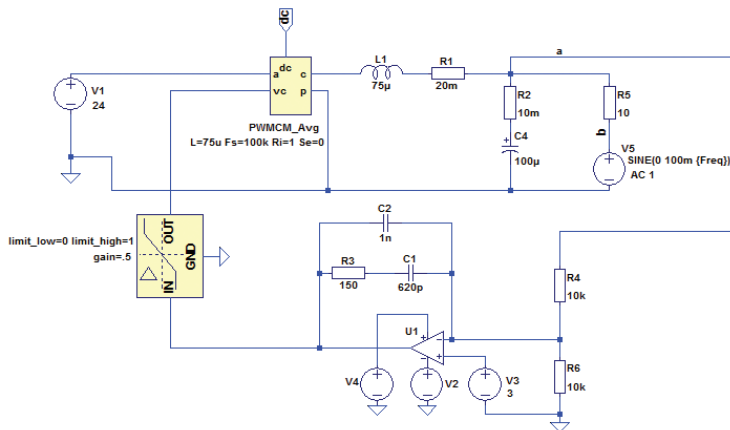


Fig. 8. Step-down converter with a correction circuit – case II

Fig. 9 presents the frequency analysis for the circuit from Fig. 8.

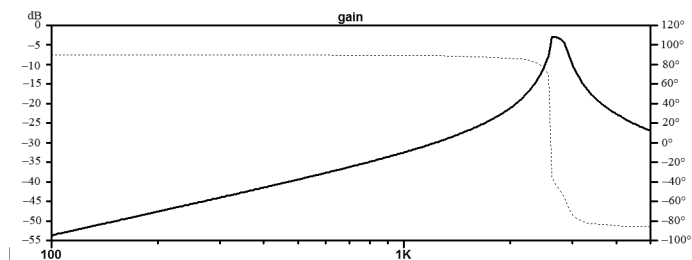


Fig. 9. Frequency analysis result for step-down converter – Middlebrook's method

In order to verify Middlebrook’s method, the authors carried out a dozen or so individual. TRAN analyses (the frequency of V5 ranged from 100 Hz to 5 kHz) and manually determined the frequency characteristics of the circuit, which is shown in Fig. 10.

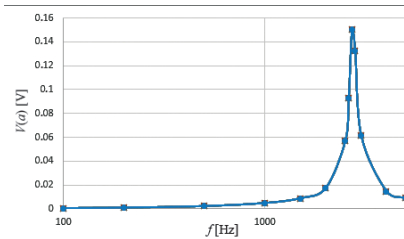


Fig. 10. Output voltage (AC component) for frequency step changes, $f_r = 2.65$ kHz

Comparing the results from Fig. 9 and Fig. 10, one can see that the resonant frequency 2.65 kHz is identical. This confirms the correctness of Middlebrook’s results. Low frequencies of load current have only slight impact output voltage. The oscillations of output voltage appear around the resonant frequency.

The circuit from Fig. 11 has an additional point defined (b1) to obtain the changes of additional voltage signal (V5). The signal amplitude was 10 V to show the effect of the input voltage changes on the output voltage.

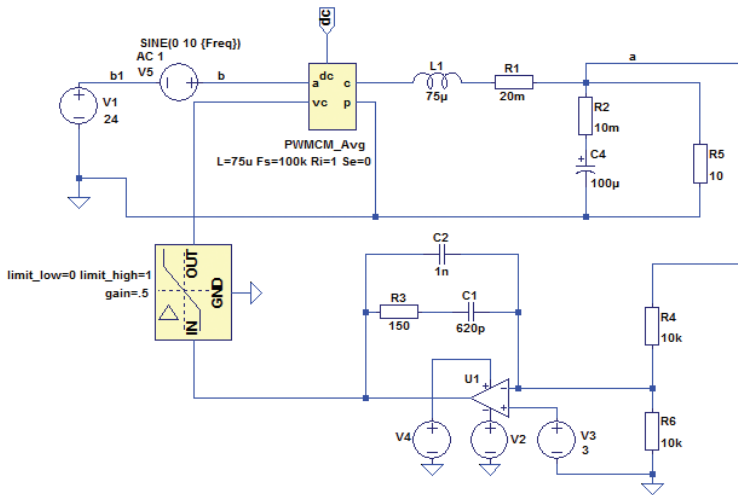


Fig. 11. Step-down converter with a correction circuit – case III

In Fig. 12, one can see a small effect of the input voltage AC component on output voltage. The pulsation of output voltage occurs for resonant frequency about 150 Hz (the damping about 30 dB).

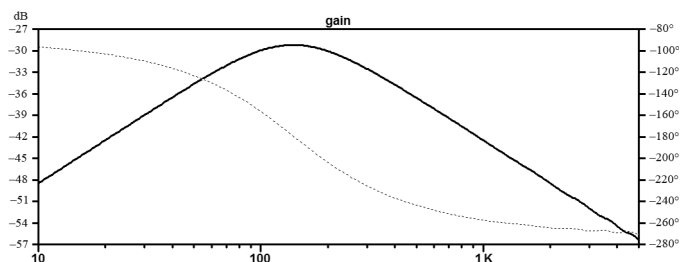


Fig. 12. Frequency analysis result for a step-down converter – Middlebrook's method

2.4. Power stage of a buck converter

In order to show incorrect results from Middlebrook's method, the authors carried out a simulation for the power stage of a buck converter (Fig. 13) with an additional signal amplitude of 1 mV.

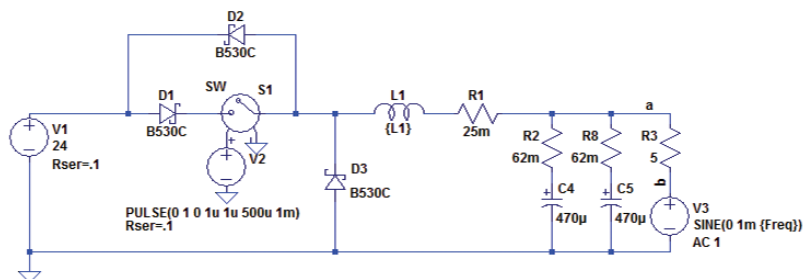


Fig. 13. Frequency analysis result for a step-down converter – Middlebrook's method

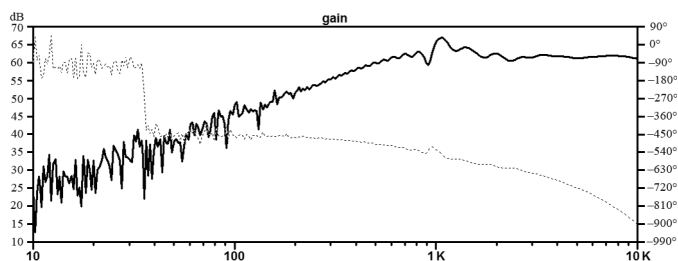


Fig. 14. Frequency analysis result for a step-down converter – Middlebrook's method

The results from Fig. 14 show that the wrong selection of voltage amplitude of the additional source in the Middlebrook's method gives the wrong results: phase shift up to 90° and inaccurate amplitude characteristic.

3. Advantages and disadvantages of Middlebrook's method

Middlebrook's method has both advantages and disadvantages, depending on the analyzed circuit. In this method, it is important to choose enough measurement points to obtain correct results (sufficient number of frequency steps). If the number of points is too small, the frequency characteristics are imprecise. Incorrect results can also be produced when a sine signal in a measurement point (output point) is distorted. This can result from defining an incorrect input signal amplitude. The value of an additional source amplitude varies in the case of different circuits and should be determined separately for each circuit. Another important parameter is the range of input signal frequencies. For example, in switched power supply circuits, power transistor control frequency is found. In order to ensure that frequency analysis results in the method presented are as accurate as possible, the maximum input signal frequency has to be much lower than the power transistor control frequency. An important disadvantage is the simulation time. Because of many iterations, the analysis lasts much longer than in the case of the classic .AC analysis (the duration of Middlebrook's method analysis is tens of seconds, whereas the classic method only takes tens of *milliseconds* to complete – depending on circuit complexity). That is why it is not recommended to use Middlebrook's method for simple, linear circuits.

In order to determine frequency characteristics, it is necessary to carry out .TRAN time analysis many times. The time taken to do that should be added to the time needed by the user to select (find) the right input signal amplitude. Based on the numerous simulation tests on the step-down converter, the authors conclude that, in order to obtain reliable results using Middlebrook's method, simulations have to be performed many times.

The main advantage becomes apparent when comparing Middlebrook's method with classic .AC analysis is that the former involves nonlinear element characteristics (classic .AC analyses linearize circuits in an unknown way, which gives unreal results). It is important to bear this mind in the case of power converters with PWM regulators and transistor switches in their power stage. The results from Middlebrook's method are more real. The frequency characteristics of a circuit are mainly determined in order to verify the gain of a circuit versus frequency, in other words, how the amplitude of an input signal changes relative to the input signal frequency. Middlebrook's method and the capabilities of LTspice allow the user to verify the effect of changes in an input parameter as a function of frequency (this can be e.g. current, voltage, a parameter of an element) on a selected output parameter from the circuit (e.g. voltage or current). This allows engineers to verify the behavior of power circuits, such as DC/DC converters within a given frequency range.

4. Summary

This paper is a development of the considerations made in [6]. The authors presented three types of circuits: a resonant circuit, a low-pass filter and a buck converter. As shown in Fig. 2 and 3, in respect of simple circuits, Middlebrook's method produces the same results as classic .AC analysis. In this case, it is more advantageous to use .AC analysis because it is much faster.

For more complex circuits, such as buck converters (Fig. 6, Fig. 8 and Fig. 11), which contain a nonlinear element, it is recommended to use Middlebrook's method. This technique is precise because it involves nonlinear characteristics of components, but it is important to define the appropriate number of frequency changes.

Middlebrook's method can be very useful while designing the power stages of DC/DC or AC/DC converters, analyzing the effect of elements from correction circuits on output voltage, and testing stability of more complex circuits.

References

- [1] Alonso G., *Basic steps in generating a bode plot of SMPS*, <http://www.linear.com/solutions/4673> (access: 01.07.2016).
- [2] Choi H., *Practical Feedback Loop Design Considerations for Switched Mode Power Supplies*, Fairchild Semiconductor Power Seminar, 2010, 1–14.
- [3] Engelhardt M., *Extracting Switch Mode Power Supply Loop Gain in Simulation and Why You Usually Don't Need To*, <http://www.linear.com/solutions/4672> (access: 01.07.2016).
- [4] Middlebrook R.D., *Measurement of loop gain in feedback systems*, Int. J. Electronics, vol. 38, 1975, 485–512.
- [5] Paperno E., *Simulating Return Ratio in Linear Feedback Networks by Middlebrook's Method*, 2012 http://www.ee.bgu.ac.il/~paperno/Lecture_notes_2012_2013/%20%28not%20for%20exam%29%20Additional%20reading%20on%20feedback/Simulating%20return%20ratio.pdf (access: 01.07.2016).
- [6] Prąglowska-Ryłko N., Mysiński W., *Comparison of frequency analysis methods for correction circuits in Step-Down Converters*, Poznan University of Technology Academic Journals, 2016, 323–332.
- [7] Zhang Henry J., *Modeling and Loop Compensation Design of Switching Mode Power Supplies*, Linear Technology, Application Note 149, 2014.

WOJCIECH CZUCHRA*, WOJCIECH MYSIŃSKI*, BARTOSZ WOSZCZYNA**

ELECTROMAGNETIC COMPATIBILITY OF SiC TECHNOLOGY POWER CONVERTER

KOMPATYBILNOŚĆ ELEKTROMAGNETYCZNA PRZEKSZTAŁNIKA ENERGOELEKTRONICZNEGO WYKONANEGO W TECHNOLOGII SiC

Abstract

Producers of power electronics components are currently introducing silicon carbide (SiC) to their products and MOSFET transistors made with this technology, working at a wide voltage and current range, are affordable. They are distinguished by high frequency of operation, reaching 100 kHz and low switching losses. Silicon carbide technology allows to build power converters, which are characterized by high efficiency, smaller dimensions, smaller passive components and higher thermal tolerance in comparison with traditional technology (Si). The aspect of the electromagnetic compatibility of SiC technology converter was analyzed in the article. Determined levels of interferences generated by the converter into the supply grid in the range of harmonics and inter-harmonics were presented. Measurement results of electromagnetic conducted disturbances were presented. Increased levels may make it difficult to fulfil standard requirements and may adversely affect the operation of devices connected to the same supply network. Additionally, conducted disturbance levels at converter output have also been analyzed, of which increase may lead to problems in providing the so-called inner compatibility of the tested circuit or may be a source of radiated electromagnetic emission. The results of tests and analysis, presented in the article, conducted for wide frequency range, allow to evaluate the silicon carbide (SiC) technology application for a converter in the EMC scope.

Keywords: power electronics, transistors SiC electromagnetic compatibility

Streszczenie

Producenci komponentów energoelektronicznych wprowadzają obecnie do swoich produktów węgiel krzemu (SiC) a tranzystory MOSFET wykonane w tej technologii, pracujące w szerokim zakresie napięciowym i prądowym są dostępne na rynku. Charakteryzują się one wysoką częstotliwością pracy sięgającą 100 kHz i niskimi stratami przełączania. Technologia węgla krzemu umożliwia budowę przekształtników energoelektronicznych, które charakteryzują się w porównaniu z tradycyjną technologią (Si), wysoką sprawnością, mniejszymi gabarytami, mniejszymi elementami pasywnymi oraz większą tolerancją termiczną. W artykule przeanalizowano aspekt kompatybilności elektromagnetycznej przekształtnika wykonanego w technologii SiC. Zaprezentowano wyznaczone poziomy zakłóceń generowanych przez przekształtnik do sieci zasilającej w zakresie harmonicznych i interharmonicznych. Przedstawiono wyniki zaburzeń elektromagnetycznych przewodzonych generowanych do sieci zasilającej, których zwiększone poziomy mogą utrudniać spełnienie przez przekształtnik odpowiednich wymogów normatywnych oraz mogą wpływać niekorzystnie na pracę urządzeń przyłączonych do tej samej sieci zasilającej. Dodatkowo przeanalizowano poziomy zaburzeń elektromagnetycznych przewodzonych również na wyjściu układu przekształtnikowego, których zwiększone poziomy mogą doprowadzić do problemów w zapewnieniu tzw. kompatybilności wewnętrznej badanego układu lub być źródłem emisji elektromagnetycznej promieniowanej. Przedstawione w artykule wyniki badań i analiz przeprowadzone w szerokim paśmie częstotliwości umożliwiając ocenę zastosowania technologii węgla krzemu (SiC) w układzie przekształtnika w zakresie EMC.

Słowa kluczowe: energoelektronika, tranzystory SiC, kompatybilność elektromagnetyczna

* Ph.D. Eng. Wojciech Czuchra, M.Sc. Eng. Bartosz Woszczyzna, Department of Traction and Traffic Control, Faculty of Electrical and Computer Engineering, Cracow University of Technology.

** Ph.D. Eng. Wojciech Mysiński, Institute of Electrical Engineering and Computer Science, Faculty of Electrical and Computer Engineering, Cracow University of Technology.

1. Introduction

The electromagnetic compatibility of converter drive systems includes the system's emissivity and immunity issues. In the scope of the system's emission, among others, harmonics in the frequency range below 9 kHz and conducted electromagnetic disturbances for a bandwidth from 150 kHz to 30 MHz are considered [1, 2].

Harmonics content in voltage and current signal is an important issue related to the energy quality. There are many calculative analytical methods of harmonics content, determining distorted signals. Those methods are also indicated in appropriate standard documents. Those calculations are conducted with a view to energy quality and in view of safety, e.g. influence of harmonics in the supply current of traction vehicles on railway traffic control circuits [3].

Harmonics, as sinusoidal signals of frequency equal to whole times of signal's basic frequency, may be evaluated individually by the relative value of the signal amplitude related to the signal value of the basic component or altogether by total harmonics distortion factor [1]. Spectrum components, of which frequency is non-whole times of signal's basic frequency, are called inter-harmonics. They can appear as discrete frequencies or as a broadband spectrum and they are generated as a result of signal amplitudes' or phase angles' alteration or switching semiconductor elements in static converters unsynchronized with the supply network frequency.

High operating frequency together with high signal steepness at output of converters made with silicon carbide technology may be associated with the increase of electromagnetic disturbance levels generated by the system [4]. The generated disturbances, depending on the system's parameters and switching method, and resulting from energy conversion, occur technically in the whole considered frequency bandwidth. High switching frequency of power electronics components leads to a shift of those disturbances into the conducted disturbances bandwidth (from 9 kHz (150 kHz) to 30 MHz), which may also require a reduction of the conducted disturbances emission or even a reduction of the radiated disturbances with filtering methods [5]. The conducted research of the EMC phenomenon in SiC converter drives, both individual and comparative with Si technology systems, are the subject of many scientific articles, which indicates a topicality of that matter [6, 7]. Propositions of new methods and means of limiting problems related to EMC are also a subject of considerations [8, 9].

2. Tested system and research methodology

The converter system with a voltage-source pulse width modulation (PWM) inverter built on the basis of silicon carbide technology components (SiC-MOSFET, SCT2160KEC, Rohm) was constructed in order to conduct laboratory tests in the scope of electromagnetic compatibility. The constructed converter unit, working as a drive for an asynchronous squirrel-cage motor (SZJe 340), was tested in the scope of electromagnetic compatibility. During the tests, the system was operating at identical supply, load and switching conditions, without the use of filtering devices. The measurement of frequency characteristics was

conducted according to the basic requirements of standard PN-EN 61800-3 [1]. Current probe HAMEG HZ56 was used as a current transducer and A/C transducer Dewetron 43 was used as a recording device for harmonics and inter-harmonics measurements. Spectrum analyzer Rohde&Schwarz FSL3, voltage probe SCHWARZBECK MESS – ELEKTRONIK TK9420 and current probe TESEQ CSP 9160A were used for carrying out measurements of conducted electromagnetic disturbances. The measured characteristics were determined with a peak detector. A simplified measurement setup of the converter drive is shown in Fig. 1., and a view of the measurement stand is shown in Fig. 2. Additionally, a measurement of magnetic induction was conducted with magnetic field measuring coil EMCO 7604 and with spectrum analyzer Rohde&Schwarz FSL3.

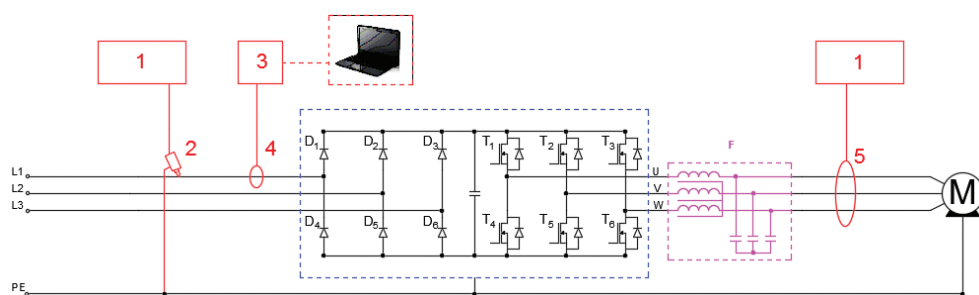


Fig. 1. A simplified measurement setup of converter drive, 1 – spectrum analyzer, 2 – voltage probe, 3 – A/C transducer, 4 – current probe HZ56, 5 – current probe CSP9160A, F – sinusoidal filter



Fig. 2. A view of the measurement stand for tested converter drive system

3. Harmonics and inter-harmonics tests

In the case of electrical drive systems with varying speed, the requirements concerning harmonics' emission are included in standard PN-EN 61800-3. According to the standard, harmonics should be determined at nominal load as the percentile content related to the basic component of current, up to at least order 25. THD current factor (up to order 40) and high-frequency component PHD should be determined.

Considering a device supplied from public low voltage network, the above standard refers to the limit values included in standard PN-EN 61000-3-2 [10], which lists four device classes – A, B, C and D. The considered converter drive system, due to the 3-phase power supply, is assigned to class A.

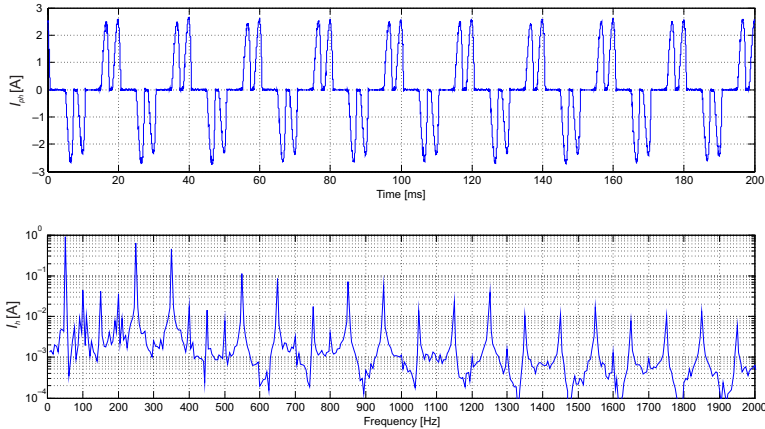


Fig. 3. Varying component of input phase current (I_{ph}) and current harmonics spectrum (I_h) for $f = 6.5$ kHz

Harmonics content and time waveform of the input phase current of the tested system is shown in Fig. 3 (carrier frequency $f = 6.5$ kHz) and Fig. 4 (carrier frequency $f = 82$ kHz). A results summary, concerning odd harmonics, with permissible values according to standard [10], is shown in Table 1 and Fig. 5. The comparison is shown with limit to order 19, due to very low values of higher orders harmonics (below 10 mA) and accuracy of measuring equipment. Because of the very low content of even harmonics in the considered signal (about 10 mA and less), the comparison of results with permissible values is not presented.

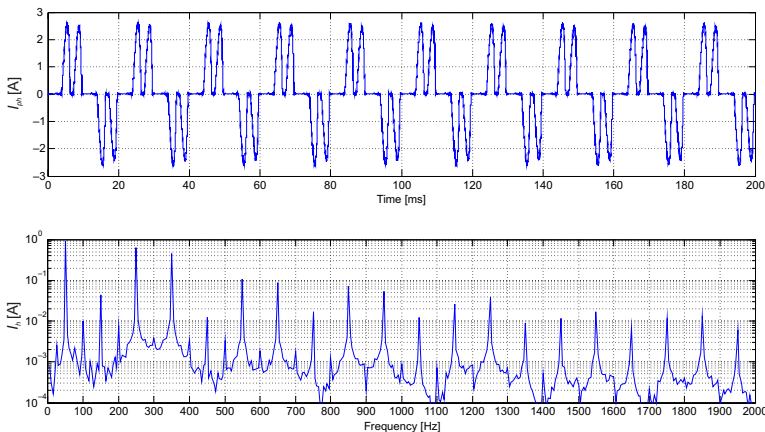


Fig. 4. Varying component of input phase current (I_{ph}) and current harmonics spectrum (I_h) for $f = 82$ kHz

Table 1

Harmonics content in supply current of tested system

Harmonics order	f_h [Hz]	I _{hperm} [A]	I_h [A]	I_h [%]	I_h [A]	I_h [%]
			for $f=6.5$ kHz	for $f=6.5$ kHz	for $f=82$ kHz	for $f=82$ kHz
3	150	2.300	0.041	4.6	0.044	4.8
5	250	1.140	0.636	70.6	0.640	69.9
7	350	0.770	0.455	50.5	0.451	49.3
9	450	0.400	0.015	1.7	0.012	1.3
11	550	0.330	0.111	12.3	0.106	11.6
13	650	0.210	0.085	9.4	0.088	9.6
15	750	0.150	0.018	2.0	0.017	1.9
17	850	0.132	0.071	7.9	0.073	8.0
19	950	0.118	0.057	6.3	0.055	6.0

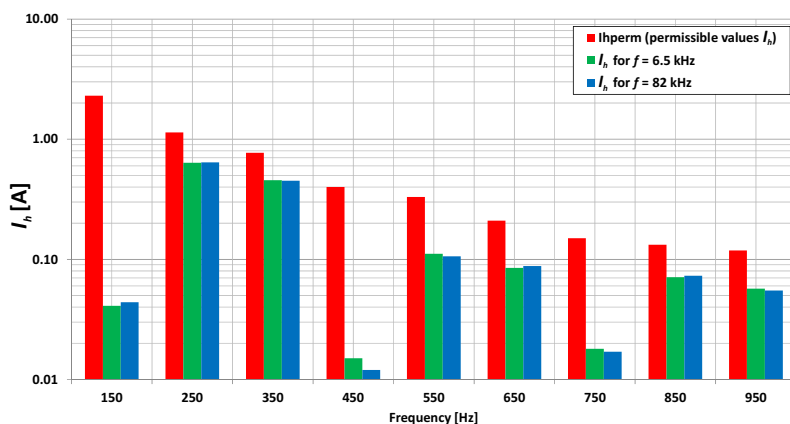


Fig. 5. Comparison harmonics content in supply current with permissible values according to standard PN-EN 61000-3-2 for $f=6.5$ kHz and $f=82$ kHz

Factors describing the total harmonics content in the converter's supply current were calculated based on determined levels of individual harmonics. They are presented in Table 2. Total Distortion Ratio (TDR), Total Distortion Factor (TDF), Total Harmonic Distortion (THD), Total Harmonic Factor (THF) and Partitive Harmonic Distortion (PHD) factors were determined. The above factors are defined as:

- Total Distortion Ratio TDR taking inter-harmonics into account:

$$\text{TDR} = \frac{\sqrt{I^2 - I_1^2}}{I_{1N}} \quad (1)$$

where:

- I – total root mean square,
- I_1 – root mean square of basic component,
- I_{1N} – nominal root mean square of basic component,

- Total Distortion Factor TDF taking inter-harmonics into account:

$$\text{TDF} = \frac{\sqrt{I^2 - I_1^2}}{I_N} \quad (2)$$

where:

- I – total root mean square,
- I_1 – root mean square of basic component,
- I_N – nominal total root mean square,

- Total Harmonic Distortion THD omitting inter-harmonics:

$$\text{THD} = \frac{\sqrt{\sum_{h=2}^{h=40} I_h^2}}{I_{1N}} \quad (3)$$

where:

- I_h – root mean square of h-order harmonic,
- I_{1N} – nominal root mean square of basic component,

- Total Harmonic Factor THF omitting inter-harmonics:

$$\text{THF} = \frac{\sqrt{\sum_{h=2}^{h=40} I_h^2}}{I_N} \quad (4)$$

where:

- I_h – root mean square of h-order harmonic,
- I_N – nominal total root mean square,

- Partitive Harmonic Distortion PHD omitting inter-harmonics:

$$\text{PHD} = \frac{\sqrt{\sum_{h=14}^{h=40} I_h^2}}{I_{1N}} \quad (5)$$

where:

- I_h – root mean square of h-order harmonic,
- I_{1N} – nominal root mean square of basic component.

Table 2

Factors describing the harmonics content in the tested system

	$f= 6.5$ kHz	$f= 82$ kHz	Notes:
TDR [%]	90	88	with inter-harmonics
TDF [%]	67	66	with inter-harmonics
THD [%]	89	88	without inter-harmonics
THF [%]	67	66	without inter-harmonics
PHD [%]	12	12	without inter-harmonics

The determined distortion factors of tested converter drive's supply current show a significant influence of higher harmonics on current waveform. The presented comparisons show no influence of current inter-harmonics on factors describing the total harmonics content. Primarily higher harmonics influence the converter's supply current distortion. Calculations also confirmed that there is a difference between THD and THF factors in current analysis, which is not so evident in voltage analysis. The obtained results for the PHD factor, which shows influence of higher order harmonics (14–40), confirmed their small contribution to supply current distortion. A comparison of all factors determined for two carrier frequencies of inverter ($f = 5.6$ kHz and $f = 82$ kHz) allows us to deduce that there is no significant influence (difference of 1%) of this parameter on current distortion in the considered frequency range.

4. Conducted electromagnetic disturbances and magnetic fields research

As a result of the carried out laboratory tests for the conducted disturbances in the frequency range from 150 kHz to 30 MHz, a number of findings were obtained. Based on them, it was noticed that there are possible issues of electromagnetic compatibility scope with SiC inverters.

Measurements of frequency characteristics were conducted for the converter system. Signals at input (from supply side) and output (from motor side) of the inverter were chosen. The inverter was operating at identical supply and load condition, carrier frequency 6.5 kHz and 82 kHz and 50 Hz output frequency. The first comparisons shown in Fig. 6 and 7 concern the influence of SiC inverter's carrier frequency on the conducted disturbance level. Voltages and currents of the conducted disturbances at $f = 6.5$ kHz are shown in blue, while at $f = 82$ kHz are shown in green. Additionally, limit values (Limit 1 – category C1 and Limit 2 – category C2) for the conducted disturbances, according to standard PN-EN 61800-3 for quasi-peak value, are marked in Fig. 6. Despite presenting the results for the peak value of disturbances, it can be assumed, with high probability, that the limit levels of input non-symmetrical disturbance voltage would also be exceeded for the quasi-peak detector.

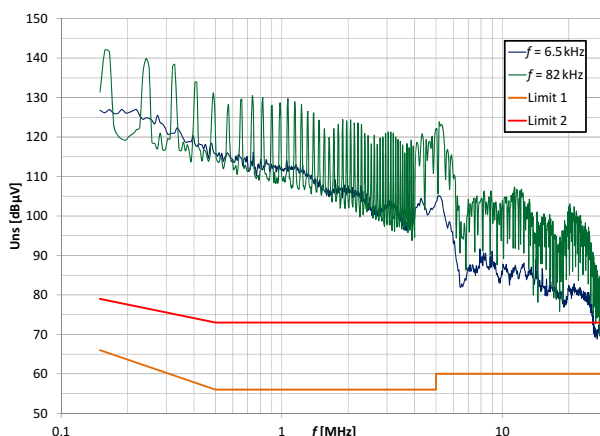


Fig. 6. Comparison of non-symmetrical voltages of conducted disturbances for different carrier frequencies

The obtained measurement results of spectrums clearly show that an inverter working with carrier frequency increased to 82 kHz generates higher levels of conducted disturbances in the whole frequency bandwidth at the supply side as well as from the load side. Level increment of both input and output disturbance voltage and current reaches a maximum of about 20 dB. Using the possibility of SiC semiconductors working with significantly higher carrier frequencies may cause difficulties with providing the electromagnetic compatibility.

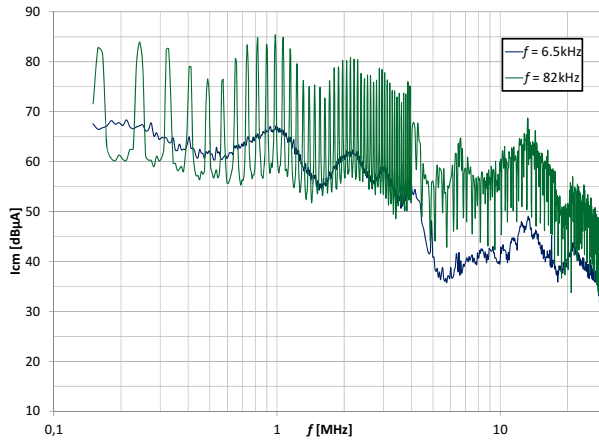


Fig. 7. Comparison of output asymmetrical currents of conducted disturbances for different carrier frequencies

A increased level of electromagnetic conducted disturbances may result in increased levels of electromagnetic fields in the converter system's surroundings. Measurements of magnetic induction at 30 cm from the tested system were carried out in order to investigate fields emission. Measurements were carried out for frequency the bandwidth from 150 kHz to 1 MHz. Results' comparison for carrier frequencies 6.5 kHz and 82 kHz is presented in Fig. 8.

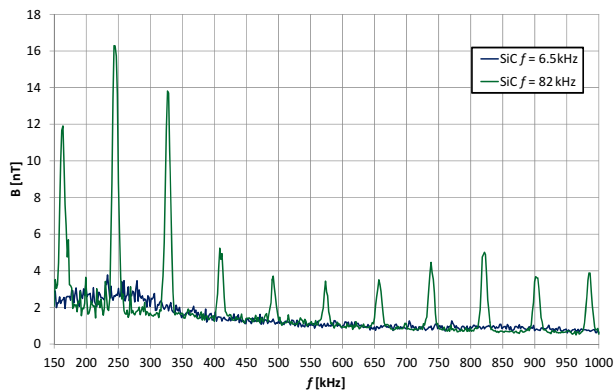


Fig. 8. Comparison on magnetic induction in converter's surroundings for different carrier frequency

The presented comparison confirms that increased levels of conducted disturbances of SiC converter operating at higher carrier frequencies result in higher levels of outer electromagnetic fields. That issue should be also considered when designing converter systems using semiconductors made with the silicon carbide technology.

5. Limiting the EMC problems

Manufacturers of converter drive systems often resign of additional inductive elements or complete input filters, which may easily improve the EMC situation of the system. Those components reduce the harmonics emission into the supplying grid, reduce the emission in the scope of electromagnetic conducted and radiated disturbances, but also protect the system from a number of phenomena, which may damage the system's elements.

Paying attention especially to EMC problems, the converter system output results from the possibility of additional costs caused by e.g. damage of motor cable or motor alone. Control measurements and potential use of means improving converter drive's reliability, such as: dv/dt chokes and filters, filters, motor chokes or sinusoidal output filters, are often required. The task of a typical sinusoidal filter working as a low-pass filter is to convert the inverter's (PWM) output signal to a smoothed sinusoidal signal. Fragmentary pulsations may be adjusted by the choice of LC elements. Additional tests were conducted in the article using the FN5010 sinusoidal filter, of which parameters are: nominal operating voltage: 3 x 400 Vac, motor frequency 0 to 70 Hz, switching frequency 4 to 16 kHz, rated currents 13A and $L = 4.2$ mH, $C = 1.5$ μ F.

The waveform of phase-to-phase voltage and phase current before sinusoidal filter are shown on Fig. 9. The presented results were obtained for a converter drive system working with a fundamental frequency of 50 Hz. The shape of output voltage corresponds to typical PWM inverter's output voltage waveform, with high voltage steepness and a big contribution of pulsations being noticeable in current waveform.



Fig. 9. Phase-to-phase voltage (CH4) and phase current (CH1) waveform before sinusoidal filter from inverter side

The waveform of phase-to-phase voltage and phase current after sinusoidal filter from motor side are shown on Fig. 10.

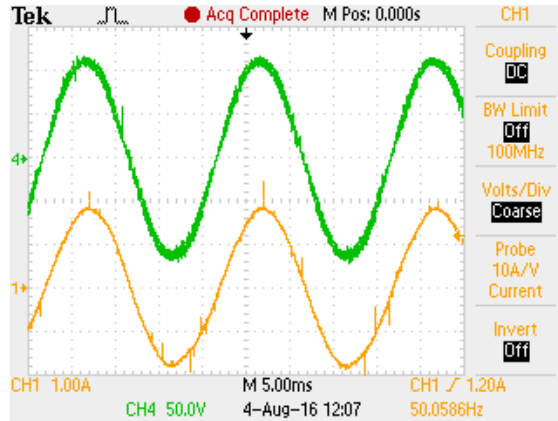


Fig. 10. Phase-to-phase voltage (CH4) and phase current (CH1) waveform after sinusoidal filter from motor side

The used filter formed the phase-to-phase voltage into sinusoidal wave, reduced the steepness of voltage pulses and minimized the pulsation of phase current.

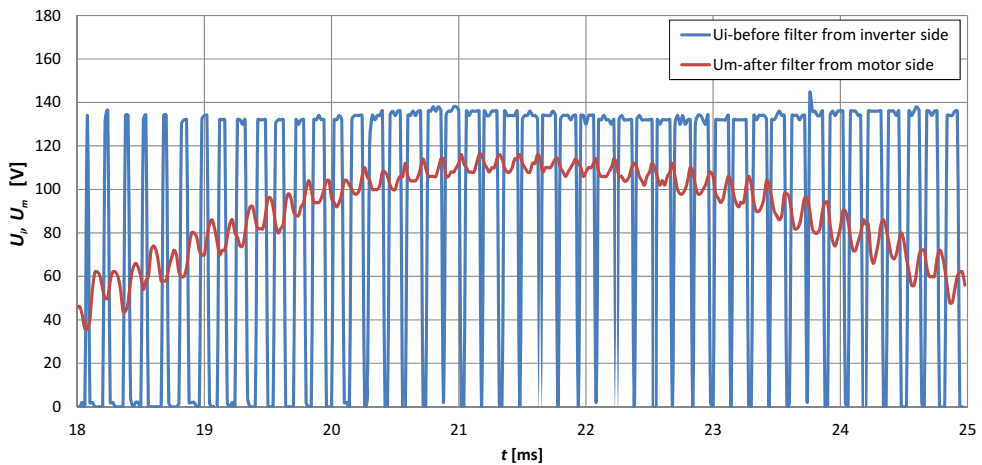


Fig. 11. Phase-to-phase voltage waveform (U_p) before filter from inverter side and (U_m) after sinusoidal filter from motor side (zoom)

A deep analysis of results showed that the sinusoidal input filter used in the tested system has also reduced the motor's phase current pulsations thrice from $p(I_i) = 15\%$ to $p(I_m) = 5\%$ (Fig. 12). Higher harmonics in the motor's phase current related to inverter's switching frequency have also been reduced. The reduction of harmonics levels is about 10 times.

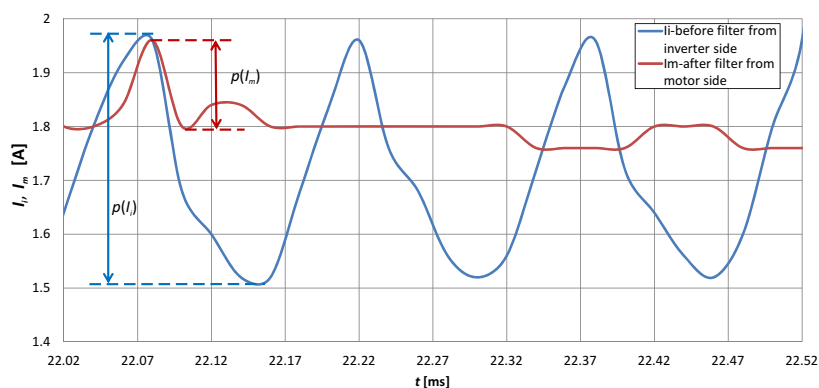


Fig. 12. Phase current waveform (I_i) before filter from inverter side and (I_m) after sinusoidal filter from motor side (zoom)

As shown by test conducted in time domain, the used sinusoidal filter formed a motor's supply voltage waveform with limited pulsations and reduced voltage steepness (Fig. 10, Fig. 11). It will provide the motor and the cable protection from high dv/dt and overvoltage, magnetic losses reduction, acoustic interferences reduction and increase of the whole system's reliability. The modified sinusoidal filter may be required to solve the remaining problems like high frequency line-to-ground current, bearing currents or the possibility of using very long non-screened cables. It comprises a connection of typical symmetrical sinusoidal filter and an asymmetrical filter with additional connection with intermediate DC circuit.

6. Summary

The conducted investigation of laboratory converter drive constructed with transistors made with SiC technology may be a base to a preliminary evaluation of the silicon carbide (SiC) technology application in the aspect of electromagnetic compatibility. The conducted tests in the frequency range below 9 kHz, including the bandwidth of harmonics and inter-harmonics emission, did not show increased emission levels. The results of individual analysis and group evaluation factor showed that signals dominating in that range include a group of odd harmonics, and the contribution of inter-harmonics and higher order harmonics is relatively low. Based on the obtained results, the possible side effects of the application of the SiC technology in converter drive systems was indicated. It may cause difficulties with providing system's electromagnetic compatibility. During analysis of electromagnetic disturbance levels in the bandwidth from 150 kHz to 30 MHz, it has been established that, for a SiC converter system, the carrier frequency increase from 6.5 kHz to 82 kHz brought significant an increase of the conducted disturbance levels. In further consequence, it results in, what was proved, that inverter with SiC transistors working with higher carrier frequencies is a source of an increased level of outer magnetic fields. The silicon carbide technology allows to build power converters, which are characterized by high efficiency (low losses in transistors), smaller dimensions, smaller passive components

and higher thermal tolerance in comparison with traditional technology (Si). However, those elements are a bigger threat for the electromagnetic environment in respect of electromagnetic compatibility, which was confirmed by the conducted research. Increased levels of conducted disturbances at inverter's supply side may make it difficult to fulfil appropriate standard requirements and may be harmful for devices connected to the same supply network. On the other hand, increased disturbance level at system's output may result in troubles with providing the so-called inner compatibility. Then, a requirement of using output components appears, e.g. sinusoidal filter, which was a subject of research. Test results showed that it will be necessary to use many methods of electromagnetic disturbances reduction in order to make the tested converter drive fulfil the standard requirements in the EMC scope and in order to increase system reliability. Research results showed that there will be a necessity of using systems lowering electromagnetic disturbance levels in order to fulfil standard requirements in the EMC scope by a converter drive.

References

- [1] Standard PN-EN 61800-3:2008 – Adjustable speed electrical power drive systems – Part 3: EMC requirements and specific test.
- [2] Czuchra W., Zajac W., *Electromagnetic Conducted Interferences in Laboratory Converter Drive*, Technical Transactions, vol. 1-E/2007, 23–30.
- [3] Skarpetowski G., Zajac W., Czuchra W., *Analytical Calculation of Supply Current Harmonics Generated by Train Unit*, 12th International Power Electronics and Motion Control Conference EPE-PEMC 2006, Portoroz 2006.
- [4] Czuchra W., Zajac W., *Investigation of Electromagnetic Interference Generated by a Tram and a Trolley-bus with Inverter Drives*, International Conference on ship propulsion and railway traction systems, Bologna, Italy, 4.5.6 October 2005.
- [5] Czuchra W., Mysinski W., Zajac W., *Modelling and Testing of RFI Filter for a Trolleybus Transistor Inverter*, EPE 2009 13th European Conference on Power Electronics and Applications, 8–10 September. Barcelona, Spain.
- [6] Gong X., Ferreira J.A., *Comparison and Reduction of Conducted EMI in SiC JFET and Si IGBT-Based Motor Drives*, IEEE Transactions on Power Electronics, vol. 29, no. 4, April 2014, 1757–1766.
- [7] Czuchra W., Mysinski W., Woszczyna B., *Analysis of the use Transistors Based on SiC Technology in Inverters in the context of Electromagnetic Compatibility*, Technical Transactions, 1-E/2016, 2016, 33–43.
- [8] Gong X., Josifovic I., Ferreira J. A., *Comprehensive CM Filter Design to Suppress Conducted EMI for SiC-JFET Motor Drives*, Proc. IEEE 8th International Conference on Power Electronics, ECCE Asia, 2011, 720–727.
- [9] Akagi H., Shimizu T., *Attenuation of Conducted EMI Emissions From an Inverter-Driven Motor*. IEEE Transactions on Power Electronics, vol. 23, no. 1, January 2008, 282–290.
- [10] Standard PN-EN 61000-3-2: Electromagnetic compatibility (EMC)-Part 3-2-Limits. Limits for harmonic current emissions (equipment input current ≤ 16 A per phase).

JAROSŁAW TULICKI, JANUSZ PETRYNA, MACIEJ SUŁOWICZ*

FAULT DIAGNOSIS OF INDUCTION MOTORS IN SELECTED WORKING CONDITIONS BASED ON AXIAL FLUX SIGNALS

DIAGNOSTYKA SILNIKA INDUKCYJNEGO W WYBRANYCH STANACH PRACY NA PODSTAWIE SYGNAŁU STRUMIENIA POOSIOWEGO

Abstract

The article presents the possibility of using axial flux signals in the fault diagnosis of low-power induction machines working under varying load conditions. The study involved cases of asymmetrical rotors and stators in steady state and transient conditions during start-up. The laboratory measurements were performed on a modified induction motor, which was equipped with a special coil built into the bearing shield allowing the measurement of the voltage proportional to the motor axial flux. Examples of the obtained waveforms and numerical data were supplemented by conclusions and a review of current knowledge concerning the application of the axial flux signal for the purpose of the fault diagnosis of squirrel cage induction motors.

Keywords: asymmetry induction motor, axial flux, diagnostics

Streszczenie

Artykuł przedstawia możliwość zastosowania sygnału strumienia poosiowego w diagnostyce maszyn indukcyjnych małej mocy, pracujących przy zmiennych warunkach obciążenia. Badaniom poddano przypadki niesymetrii wirnika i obwodu stojana dla stanu ustalonego oraz przejściowego. Pomiar laboratoryjny zostały wykonane na zmodyfikowanym silniku, przystosowanym do pomiaru napięcia wprost proporcjonalnego do strumienia unipolarnego, za pomocą wbudowanej cewki w tarczy łożyskowej. Przykłady uzyskanych przebiegów oraz danych liczbowych uzupełniono o wnioski i przegląd dotychczasowej wiedzy z zakresu zastosowania sygnału strumienia poosiowego w diagnostyce maszyn klatkowych.

Słowa kluczowe: asymetria silnika indukcyjnego, strumień osiowy, diagnostyka

* M.Sc. Eng. Jarosław Tulicki, Ph.D. Eng. Janusz Petryna, Ph.D. Eng. Maciej Sułowicz, Department of Electrical and Computer Engineering, Institute of Electromechanical Conversion, Cracow University of Technology.

1. Introduction

The basic diagnostic signals in the induction motor are the voltage and current signals of the stator circuit. In addition to the values of the currents in the windings of the stator and the rotor, the level of the magnetic flux is another distinctive feature of induction motors. In symmetrical induction machines, flux linkages have a component only in a radial direction. For any asymmetry of induction motors, flux linkages decompose themselves additionally into an axial component. The axial component causes not only additional losses in the stator end-windings, but it also acts as a carrier of diagnostic information contained in the electromagnetic field time harmonics available by the measurement [1, 6, 7]. As it was proved in articles [2, 9, 10, 11, 13, 14, 19], an analysis of the axial flux course allows an effective identification of damage to the stator circuit in the form of coil turn short-circuits and rotor asymmetry. The article presents selected results of the authors' research on the application of the axial flux in the fault diagnosis of low-power induction motors [17, 18]. In the article, a comparison to the stator current analysis was made under similar conditions to those under which the axial flux waveforms were analysed.

1.1. Method of measurement of the axial flux

The main element used for detecting changes of the axial flux in time is the coreless coil. The coil acts as a secondary winding in which a voltage, whose actual value is the time derivative of flux, is induced by the action of the alternating axial flux.

As it can be seen, the main metrological feature of the air coil is lack of nonlinear distortions and its characteristic similar to that of a band-pass filter.

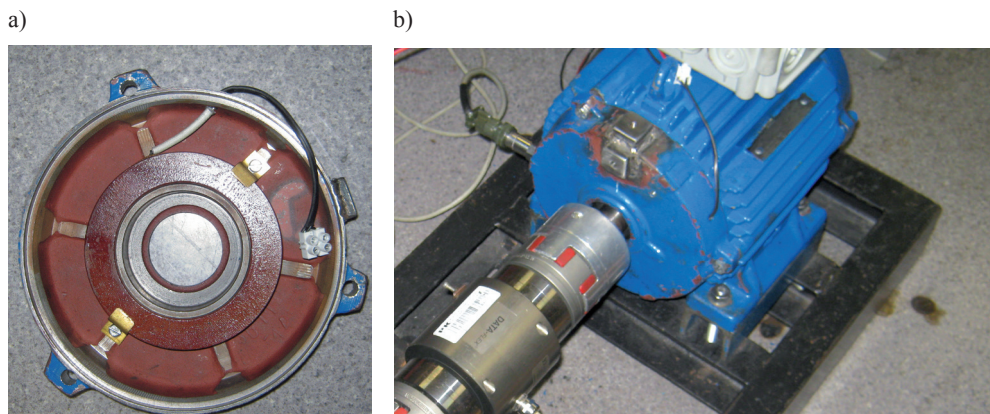


Fig. 1. View of measuring coil: a) inside the bearing shield, b) mounted inside the motor housing

In terms of mechanical structure, the diameter of the carcass is a very important parameter. The diameter of the carcass cannot be either less than the diameter of the rotor or greater than the diameter of the stator [7, 10]. Typically, the measuring coil is mounted on the

fan cover or inside the bearing shield [6] – it is rarely mounted on the motor body [3]. Fig. 1 shows a view of the measuring coil used in the laboratory and its assembly inside the motor housing.

2. Measuring system

The subject of the study was the induction motor type Sg-112M-4. The motor was mechanically connected to a separately-excited DC generator by means of the Rotex flexible claw coupling and the DataFlex 22/50 measuring shaft with integrated measuring speed system. The DC generator provided a mechanical load to the induction motor.

The load torque was adjusted by changing the generator excitation current – an autotransformer with a rectifier was used for this purpose. The DC generator output was loaded by 4 kW set of resistive heating elements. The NI USB 6259 multifunctional measuring card was used for the acquisition of measurement signals. The duration of data recording for a single measurement was 10 seconds – the signals were recorded with a sampling frequency of 10 kS/s per channel. In addition to measuring the coil voltage and the shaft speed and torque, the phase voltage and current waveforms were recorded with the use of the transducers LEM LV 25-P and HY15-P.

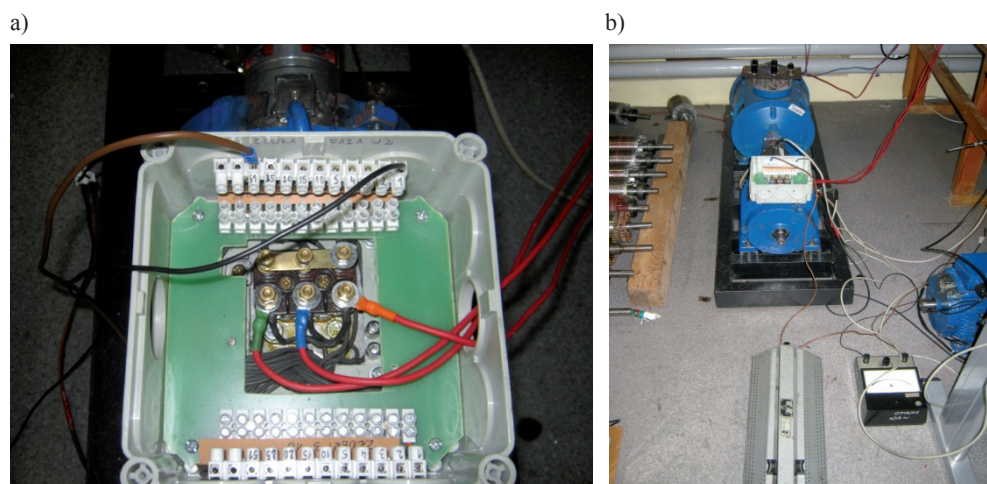


Fig. 2. Laboratory view of: a) modified terminal box, b) induction motor with measuring instruments

Several simulated damages to the rotor were realized by the use of rotors with different degrees of asymmetry. In the research, a symmetrical rotor and other two damaged rotors: one with one broken bar and the other one with two broken bars, were used.

For the purposes of the research, some modifications to the stator windings and the terminal box were required. The stator winding modification allowed the short-circuiting of a selected number of turns in phase ‘W’ by the use of the 6–40 Ω control resistor and an

ammeter to limit the short-circuit current. During the measurements, the induction motor phases were connected in the star configuration. The motor was supplied from the rigid network and operated without its cooling fan. The fan was removed because of the possible generation of additional rotary components in the frequency spectrum related directly to the number of fan blades. Before the measurements session, the drive system was aligned. All calculations and measurements were performed using the Matlab software. Fig. 2 shows views of the laboratory stand together with the measuring instruments.

3. Diagnostic signals

3.1. Asymmetry of the rotor cage

In the case of rotor asymmetry (as damaged bars or dynamic eccentricity), the spectrum of the voltage proportional to the axial flux contains noticeable components described by the following equation [6, 7]:

$$f_r = f_0 [s + k(1 - s)] \quad (1)$$

where:

f_r – frequency associated with the asymmetrical rotor;

f_0 – fundamental frequency;

s – slip;

k – 3, 5, 7... .

Additionally, regardless of the rotor condition, from among the spectrum components, besides the mains frequency and its odd multiples, the first slip component can be identified [6, 11] as:

$$f_{s1} = f_0 s \quad (2)$$

where:

f_{s1} – primary slip frequency.

Based on equation (2) and design parameters of an induction motor as demonstrated in [9, 19], it is possible to reproduce courses of the torque and rotor speed in time domain.

Among additional frequencies related to the rotor asymmetry described by equation (1), in the spectrum of the measuring coil voltage, the following components described by equation (3) can be observed:

$$f_{sw} = k f_0 s \quad (3)$$

where:

f_{sw} – another successive odd slip frequency.

Also in the case of analysis of the axial flux signal, the diagnostic signal (commonly used to analyse the stator current and to detect rotor cage asymmetry and dynamic eccentricity [6, 7, 15, 19]) described by the equation (4), was applied:

$$f_b = f_0 (1 - 2s) \quad (4)$$

where:

f_b – left sideband slip frequency.

It should be noted that on the basis of equations (3) and (4), a damage to the joint rings of the rotor cage can be detected. However, in the case of the stator current analysis, the distinction between the damage to the rotor bars and to the joint rings is not possible in practice [6, 15].

3.2. Asymmetry of the stator

A common cause of asymmetry of the stator circuit are inter-turn short-circuits inside a single phase of the winding or inter-phase short-circuits leading to the rapid failure of the induction motor [3, 6]. As indicated in the introduction, the analysis of voltage proportional to the axial flux allows the detection of inter-turn short-circuits already in the initial stage of damage. The main diagnostic signal in the form of spectrum components for the short-circuits detection in the stator winding can be described by the following formula [3, 6, 7]:

$$f_k = k f_0 + [n_s(1 - s) m]/60 \quad (5)$$

or

$$f_k = k f_0 + n m/60 \quad (6)$$

where:

f_k – frequency appearing when short-circuiting;

n_s – synchronous speed;

m – $-2, -1, +1, +2, \dots$

n – motor speed.

As it can be seen, the frequencies of the spectrum components depend on design parameters of the induction motor as the number of pole pairs and supply frequency.

4. Measurement results and analysis

4.1 Stationary analysis

Spectral analysis of the steady state signal [4, 15, 16] is one of the basic methods for assessing the condition of a rotor and stator. When attempting to identify the characteristic signs of damage within the spectrum of stator current, it is necessary to provide and maintain the specified measurement conditions. When testing a low- and medium-power induction motor, it should be loaded at least half the nominal torque [15].

Furthermore, the drive system should be free of defects in mechanical connections, such as a misalignment for example, while the rotor unbalance influences the quality of the measurements slightly less. Failure to meet these conditions regarding the tested induction motor leads to disorder in the readability of the current spectrum, making proper separation of diagnostic components impossible. It should also be mentioned that a direct spectral analysis of the stator phase current does not allow to detect the stator asymmetry caused by an insignificant number of shorted turns inside a single stator phase.

The axial flux signal (expressed in an intermediate form of the voltage waveform where influence of load torque values and supply frequency [6, 7] on readability of the spectrum voltage is minimal) is free of the above drawbacks [17, 18]. In addition, as it will be shown later in this article, the axial flux signal shows high sensitivity to any asymmetries of electrical origin. Below, some chosen measurements and the FFT spectrum calculations results for an induction motor with rotor and stator asymmetry are presented. The amplitude spectrum was limited to a band of 200 Hz. The resulting diagrams were produced on a linear scale (Fig. 4–6). Some selected examples were obtained for an induction motor running in the steady state with the stator load current 4.5 amps.

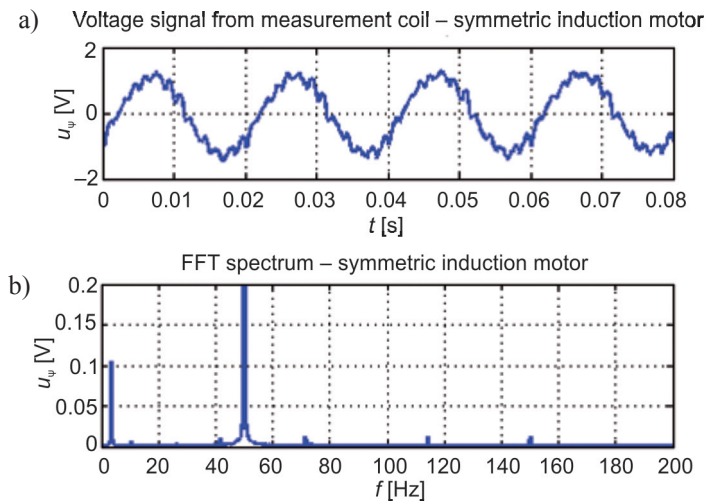


Fig. 3. Symmetrical induction motor: a) voltage signal from measurement coil, b) FFT spectrum

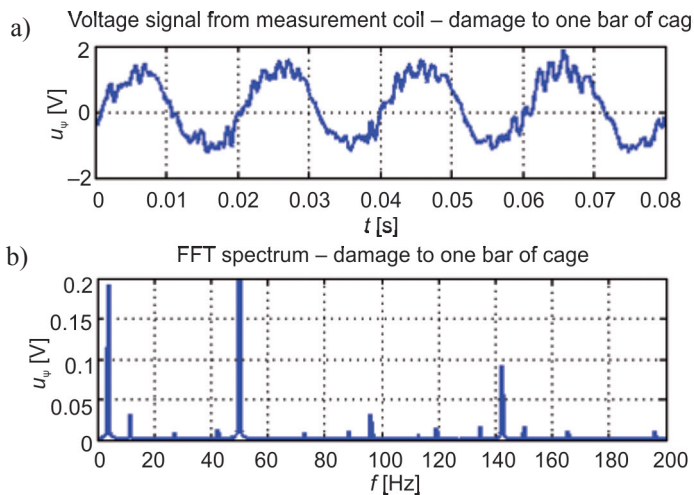


Fig. 4. Damage to one bar of cage: a) voltage signal from measurement coil, b) FFT spectrum

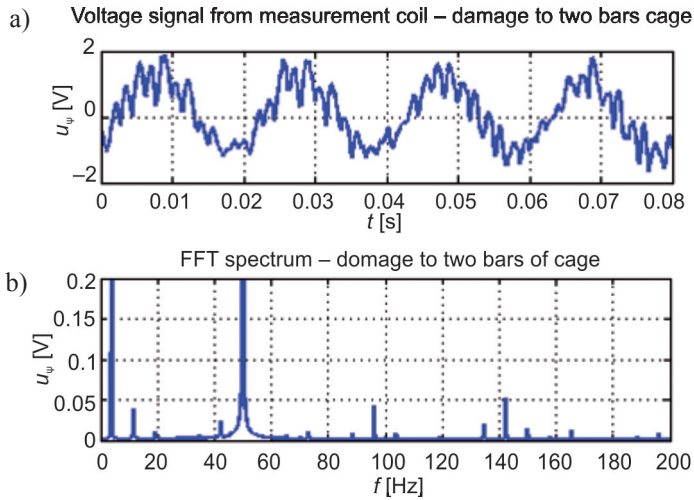


Fig. 5. Damage to two bars of cage: a) voltage signal from measurement coil, b) FFT spectrum

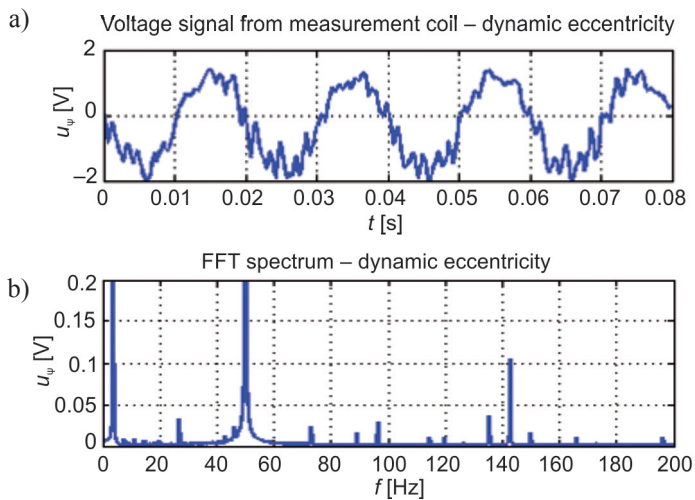


Fig. 6. Dynamic eccentricity 40%: a) voltage signal from measurement coil, b) FFT spectrum

In the case of an induction motor damage resulting in an asymmetry of the rotor cage, it can be shown that the damages to the cage bars cause a significant increase in component amplitudes described by formulas (1) to (4), while at the same time, they cause a decrease of the supply fundamental component amplitude (Tab. 1). For dynamic eccentricity, like in the case of the damages to the bars, the growth of the amplitudes of the components (1) and (4) can be observed, in the absence of changes in the component (3) as compared with a symmetrical induction motor. Based on the conclusions made, it can be stated that the preliminary assessment of dynamic eccentricity is possible on the basis of odd multiple components of slip frequency (3) and seems to be an important supplement to the method based on searching slot harmonics in the band of mid-frequency spectrum [19].

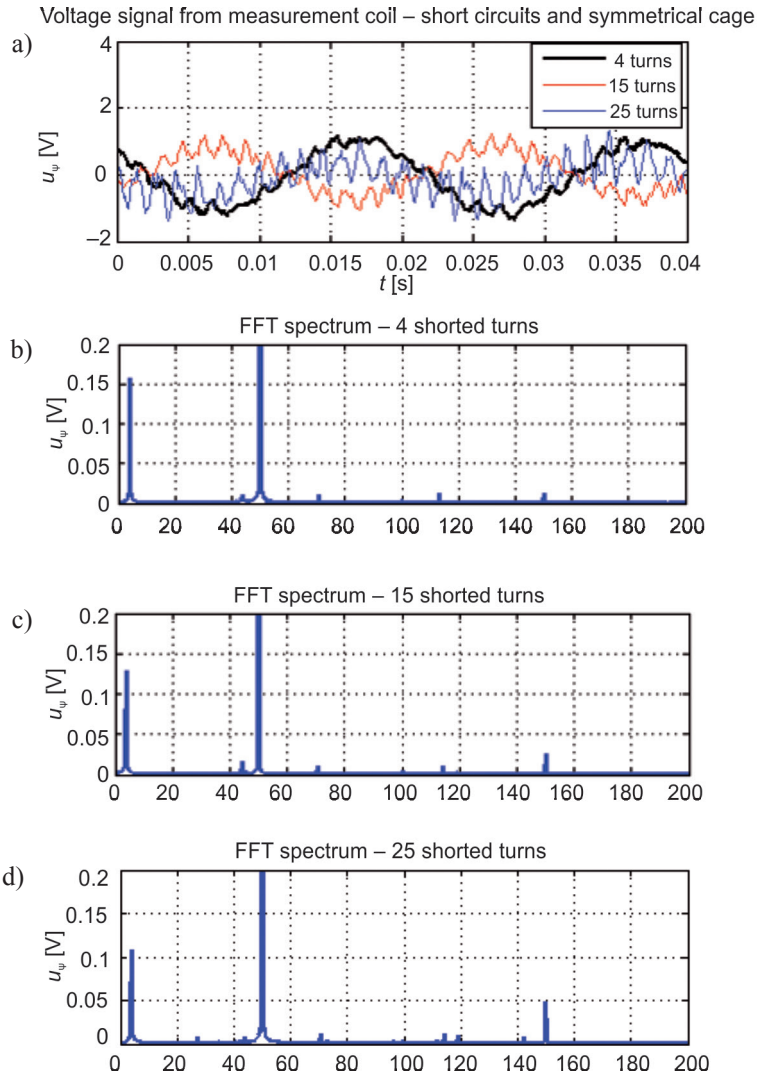


Fig. 7. Short circuits and the symmetrical cage: a) voltage signal from measurement coil, b), c), d) FFT spectrum for different number of shorted turns

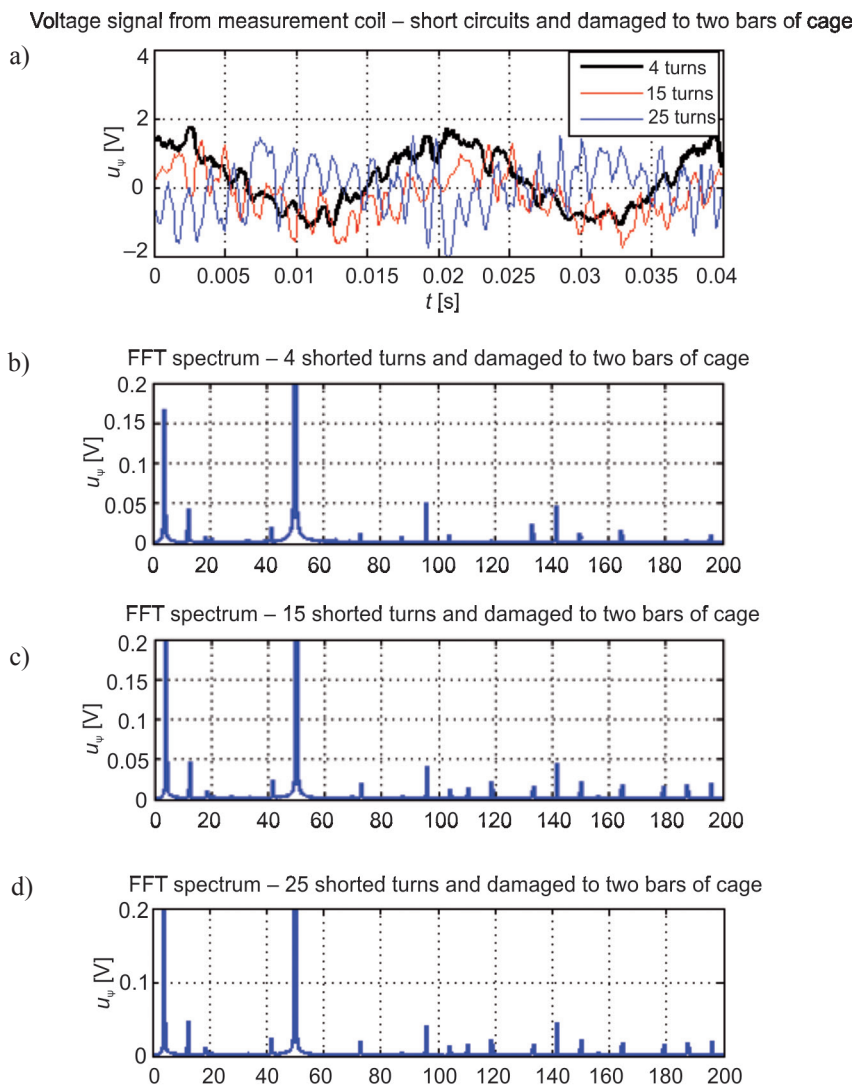


Fig. 8. Short circuits and two bars of cage damaged: a) voltage signal from measurement coil, b), c), d) FFT spectrum – shorted turns and two bars of cage damaged

Values of the diagnostic signals from FFT spectrum

Type of damage	Diagnostic signals [V/Hz]					
	$f_0 s$	$3f_0 s$	$5f_0 s$	$f_0 (1 - 2s)$	f_0	$f_0[s + 3(1 - s)]$
					$3f_0$	
Symmetric motor	0.104/3.5	0.006/10.5	0.00046/24.5	0.0046/43	1.35/ 50 0.14/150	0.0006/143
One bar of cage	0.192/3.8	0.032/11.4	0.002/19.3	0.012/42.4	1.20/ 50 0.15/150	0.092/142.4
Two bars of cage	0.208/3.8	0.04/11.4	0.010/19.3	0.022/42.3	0.94/ 50 0.16/150	0.052/142.3
Dynamic Eccentricity	0.202/3.6	0.008/10.8	0.0064/19.5	0.014/42.3	1.24/ 50 0.16/150	0.104/142.6
4 shorted turns and 2 bars	0.166/4.2	0.044/12.6	0.006/21.0	0.02/41.7	0.98/ 50 0.14/150	0.046/141.6
15 shorted turns and 2 bars	0.202/4.2	0.046/12.6	0.0042/21.0	0.026/41.7	0.68/ 50 0.02/150	0.046/141.6
25 shorted turns and 2 bars	0.224/4.2	0.046/12.6	0.0072/21.0	0.018/41.7	0.56/50 0.12/150	0.054/141.6
Type of damage	f_0	$3f_0$	$3f_0 + [n_s(1 - s) m]/60$			
			$m = 2$	$m = -1$	$m = -2$	$m = -3$
4 shorted turns and 2 bars	1/ 50	0.013/ 150	0.0108/195.8	0.0012/127.1	0.0106/104.2	0.00112/81.3
15 shorted turns and 2 bars	0.66/ 50	0.022/ 150	0.020/195.8	0.0012/127.1	0.0126/104.5	0.00024/81.3
25 shorted turns and 2 bars	0.54/ 50	0.06/ 150	0.022/195.8	0.0024/127.1	0.0114/104.5	0.02/ 81.3
4 shorted turns	1.10/ 50	0.012/ 150	0.00074/196.2	0/252.2	0/207.4	0.0004/80.7
15 shorted turns	0.76 /50	0.026/ 150	0.00144/196.2	0.0010/126.1	0/207.4	0.00030/80.7
25 shorted turns	0.42/ 50	0.048/ 150	0.0024/ 196.2	0.0004/126.1	0.0004/103.8	0.0004/80.7
For: $R = 21.5 \Omega$, 4 shorted turns – 0.1 A, 15 shorted turns – 0.3 A, 25 shorted turns – 0.65 A						

According to the presented measurements and calculation results from Fig. 7 and 8, the occurrence of slight inter-turn short circuits in the stator phase produces a growth in the amplitude of the third supply harmonic, while at the same moment, a weakness of the flux of the supply frequency can be observed. Upon a combined damage to rotor and stator circuits, an interaction of the rotor and the stator magnetic fields can be observed, expressed by the occurrence of sums and differences of the components as described (5) and equal to twice the slip fundamental frequency (2). The basic feature of the combined damage to rotor and stator circuits is the lack of significant differences in the amplitudes of the components associated with the asymmetry of the rotor (1), (3) and (4) relative to an induction motor with the rotor circuit damage only.

4.2. Non-stationary analysis

The operating states of an induction motor in transient conditions [7, 8] can be divided into electrodynamic and electromechanical transient states. In the first case, the waveforms of electromagnetic and mechanical quantities vary with comparable speed. In the above operating condition, extraction of the diagnostic signal (which is an electrodynamic quantity) from the total current waveform is considerably more difficult or even impossible.

Therefore, the most often considered transient state in the diagnostics of induction motors is an electromagnetic transient state, where it is assumed that the electromagnetic quantities change as a function of time at a constant speed. In this case, the preferred option is a long duration of the electromagnetic transient state, a typical example of this is the heavy start-up of an induction motor.

As shown in [9, 11], also in the case of the voltage waveform proportional to the axial flux in the transient state and the dynamic state, similarly as in the analysis of the stator current, the low-frequency methods can be applied successfully in the comparative analysis of diagnostics signals' fluctuation. As it will be proven later in the article, a precise observation of changes in selected diagnostic signals is only possible when using the time-frequency methods.

Below, one can find some examples of spectrograms made with the use of the short-time Fourier transform [15, 20] during the start-up of the symmetrical motor and the motor with one damaged bar of the cage. The below examples were selected for the induction motors operating in steady states and loaded at 7 amps stator currents. In the analysis, a short-time Hanning window with a duration of 0.2 seconds was applied. The frequency band under observation was limited to the frequency range 0–150 Hz, where the amplitudes of diagnostic signals associated with the rotor circuit achieved the greatest values. The obtained spectrograms were supplemented by the theoretical waveform of the diagnostic signals during the start-up (Fig. 9).

According to the spectrograms presented in Figs. 10 and 11, a common feature is the presence of the supply fundamental component and primary slip frequency (2). For an induction motor with one damaged cage bar, one can observe the change in time of the components described by formulas (1) – [for $k = 3, 5, 7$] and (3) – [for $k = 3$]. Despite the short time of the motor start, the basic diagnostic signals remain clearly visible, which does not happen in the case of the stator current analysis, where it is required that the starting time of the induction motor is at least 1.5s.

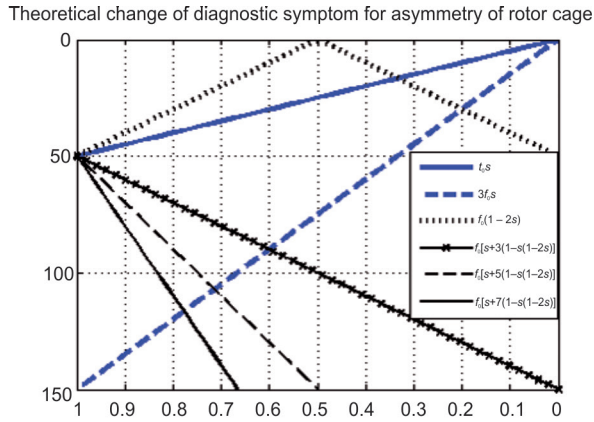


Fig. 9. Theoretical change of diagnostic symptoms for the asymmetry of the rotor cage for different motor loads

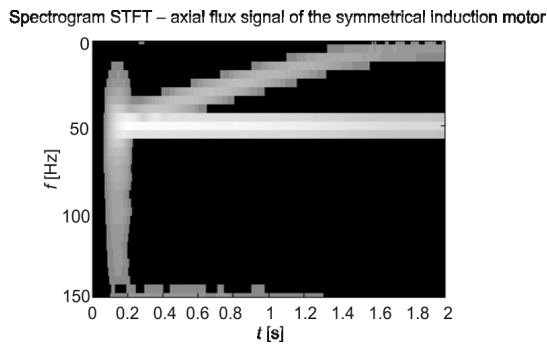


Fig. 10. Spectrogram STFT – axial flux signal of the symmetrical induction motor

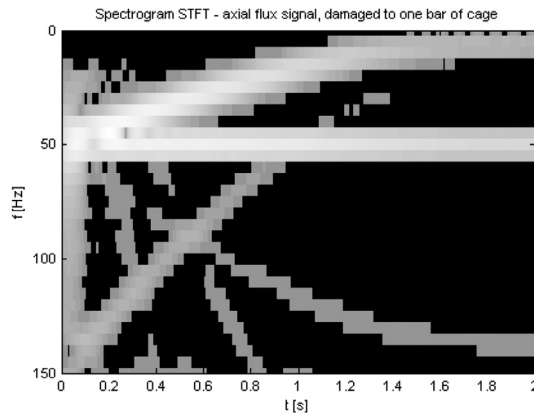


Fig. 11. Spectrogram STFT – axial flux signal, one damaged bar of the cage

Fig. 12 presents the course of observed diagnostic signals in the time domain for the frequency of 125 Hz. The observed frequency was selected in view of the possibility to observe all relevant diagnostic signals associated with the cage rotor circuit, with the exception of the signal (2). The frequency band in the range of 100–150 Hz should be considered universal to evaluate the technical condition of the cage rotor during the start-up because the pattern of the diagnostic signals remains constant regardless of the design parameters of the induction motor.

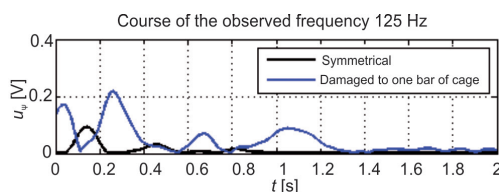


Fig. 12. Change of the observed frequency 125 Hz

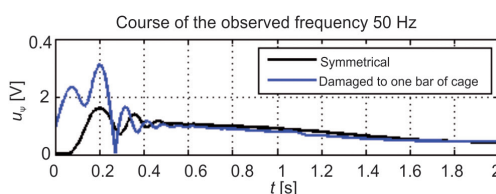


Fig. 13. Course of the observed frequency 125 Hz

5. Conclusions

Among the most important advantages of using the signal of the axial flux as a diagnostic signal, one should point the lack of significant influence of such physical quantities as the torque and supply frequency on the readability of the spectrum.

As it was shown, the greatest benefit from the axial flow analysis can be obtained in the initial stage of development of any asymmetry of electrical origin in the form of damage to the rotor and the stator. In addition, the analysis of the flux axial signal requires less effort than the calculations for the purposes of the stator current analysis.

One of the disadvantages of using the axial flux as a diagnostic signal seems to be the lack of measurement of the operational quantities in the form of voltage or current as well as the need to use measuring coils of different diameters customized to the mechanical size of the induction motor, in the case of the coil location inside or outside the bearing shield.

In the future research concerning the use of the axial flux, the authors plan to create a database of measurements for high-power induction motors and the detailed elaboration of the statistical data for different duties and mechanical loads – this is required to develop a reliable indicator of technical condition of a wide range of power of induction motors.

Acknowledgment

Presented results of the research, which was carried out under the theme No. E-2/581/2016/DS, were funded by the subsidies on science granted by Polish Ministry of Science and Higher Education.

References

- [1] Biernat A., Góralski P., *Zastosowanie pomiaru strumienia osiowego do okresowej diagnostyki silników indukcyjnych w zakładach przemysłowych*, Zeszyty Problemowe – Maszyny Elektryczne nr 4/2014 (104), wyd. BOBRME Komel, 247–252.
- [2] Duda A., Petryna J., Sułowicz M., Guziec K., *Metoda wstępnej oceny stanu wirnika silnika indukcyjnego przy pomocy dedykowanego przyrządu opartego na pomiarze strumienia poosiowego*, Zeszyty Problemowe – Maszyny Elektryczne nr 2/2015 (106), wyd. BOBRME Komel, 59–63.
- [3] Frosini L., Borin A., Girometta L., Venchi G., *A novel approach to detect short circuits in low voltage induction motor by stray flux measurement*, Electrical Machines (ICEM), 2012 XXth International Conference on Marseille.
- [4] Glinka T., *Maszyny elektryczne i transformatory. Podstawy teoretyczne, eksploatacja i diagnostyka*, Instytut Napędów i Maszyn Elektrycznych KOMEL 2015.
- [5] Gołębiowski L., Gołębiowski M., Noga M., Skwarczyński J., *Strumień osiowy w modelu 3D MES maszyny indukcyjnej*, Elektrotechnika i Elektronika, Tom 25, Zeszyt 2, 2006.
- [6] Kokko V., *Condition Monitoring of Squirrel-Cage Motors by Axial Magnetic Flux Measurements*, Department of Electrical Engineering, Optoelectronics and Measurement Techniques Laboratory, University of Oulu, Oulu 2003.
- [7] Kowalski Cz.T., *Diagnostyka układów napędowych z silnikiem indukcyjnym z zastosowaniem metod sztucznej inteligencji*, Oficyna Wydawnicza Politechniki Wrocławskiej, Wrocław 2013.
- [8] Paszek W., *Stany nieustalone maszyn elektrycznych prądu przemiennego*, WNT, Warszawa 1986.
- [9] Petryna J., Sułowicz M., Duda A., *Wykorzystanie strumienia poosiowego do badania stanów dynamicznych maszyn indukcyjnych małej i dużej mocy*, Zeszyty Problemowe – Maszyny Elektryczne nr 2/2014 (102), wyd. BOBRME Komel, 165–171.
- [10] Petryna J., Sułowicz M., Puzio Ł., Dziechciarz A., *Wykrywanie zwarć zwojowych w maszynach elektrycznych na stacji prób z wykorzystaniem cewki do pomiaru strumienia poosiowego*, Zeszyty Problemowe – Maszyny Elektryczne nr 2/2015 (106), wyd. BOBRME Komel, 185–190.
- [11] Petryna J., Sułowicz M., Duda A., Guziec K., *Wykorzystanie strumienia unipolarnego w diagnostyce maszyn prądu przemiennego*, Zeszyty Problemowe – Maszyny Elektryczne nr 2/2013 (99), wyd. BOBRME Komel, 85–90.
- [12] Pietrowski W., *Zastosowanie radialnej sieci neuronowej w diagnostyce uszkodzeń uzwojenia stojana maszyny indukcyjnej klatkowej*, Zeszyty Problemowe – Maszyny Elektryczne nr 88/2012, wyd. BOBRME Komel, 93–96.

- [13] Pole G.O., *Application of Magnetic Fields To Aid The Detection and Diagnosis of Induction Motor Drive Faults*, University of Wales Institute Cardiff, January 2009.
- [14] Pusca R., Romary R., Fireteanu V., Ceban A., *Finite Element Analysis and Experimental Study of The Near-Magnetic Field for Detection of Rotor Faults in Induction Motors*, Progress in Electromagnetics Research B, Vol. 50, 2013, 37–59.
- [15] Swędrowski L., *Pomiary w diagnostyce silników indukcyjnych klatkowych*, Wydawnictwo Politechniki Gdańskiej, Gdańsk 2013.
- [16] Szymaniec S., *Badania, eksploatacja i diagnostyka zespołów maszynowych z silnikami indukcyjnymi*, Oficyna Wydawnicza Politechniki Opolskiej, Opole 2013.
- [17] Tulicki J., Sułowicz M., *Zastosowanie strumienia poosiowego do oceny stanu technicznego silnika klatkowego w trakcie rozruchu. Część I: Niesymetria wirnika*, Zeszyty Problemowe – Maszyny Elektryczne nr 2/2016 (110), wyd. BOBRME Komel, 147–154.
- [18] Tulicki J., Sułowicz M., *Zastosowanie strumienia poosiowego do oceny stanu technicznego silnika klatkowego w trakcie rozruchu. Część II: Zwarcia zwojowe, łączna asymetria obwodu stojana i wirnika*, Zeszyty Problemowe – Maszyny Elektryczne nr 2/2016 (110), wyd. BOBRME Komel, 155–162.
- [19] Weinreb K., Duda A., Petryna J., Sułowicz M., *Diagnostyka ekscentryczności silnika indukcyjnego w oparciu o pomiar strumienia poosiowego*, Zeszyty Problemowe – Maszyny Elektryczne nr 2/2015 (106), wyd. BOBRME Komel, 13–20.
- [20] Zieliński T.J., *Cyfrowe przetwarzanie sygnałów. Od teorii do zastosowań*, Wydawnictwa Komunikacji i Łączności, 2007.
- [21] Pietrowski W., *Wavelet analysis of axial flux in an induction machine on no-load test*, Przegląd Elektrotechniczny, Vol. 7b, 2012, 20–23.
- [22] Pietrowski W., *Application of Radial Basis Neural Network to diagnostics of induction motor stator faults using axial flux*, Przegląd Elektrotechniczny, Vol. 6, 2011, 190–192.
- [23] Głowacz A., *Diagnostics of direct current machine based on analysis of acoustic signals with the use of symlet wavelet transform and modified classifier based on words*, Eksploatacja i Niezawodność – Maintenance and Reliability, Vol. 16, no. 4, 2014, 554–558.
- [24] Ludwinek K., *Measurement of momentary currents by Hall linear sensor*, Przegląd Elektrotechniczny, Vol. 85, Issue 10, 2009, 182–187.
- [25] Głowacz A., Głowacz Z., *Diagnostics of induction motor based on analysis of acoustic signals with application of FFT and classifier based on words*. Archives of Metallurgy and Materialsvol, 55, issue. 3, 2010, 707–712.

WITOLD MAZGAJ, ADAM WARZECHA*

ANISOTROPIC PROPERTIES OF DYNAMO STEEL SHEETS

ANIZOTROPOWE WŁAŚCIWOŚCI BLACH PRĄDNICOWYCH

Abstract

The paper deals with the anisotropic properties of typical dynamo steel sheets. The cause of the magnetic anisotropy is the occurrence of certain textures in the dynamo sheets. The most frequently occurring types of textures in these sheets are briefly described. For a few selected dynamo sheets, values of the typical magnetic parameters for different directions of magnetization processes are presented. The paper proposes a method, which allows us to take into account the anisotropic properties of dynamo sheets in calculations of flux density changes during both the axial and rotational magnetization. A specially selected function of the grain distribution in the given dynamo sheet allows taking into consideration the anisotropic properties. Examples of the flux density changes during the axial and rotational magnetization are presented in the end part of the paper.

Keywords: dynamo steel sheet, hysteresis loop, magnetic anisotropy

Streszczenie

Artykuł dotyczy anizotropowych właściwości typowych blach prądnicowych. Przyczyną anizotropii magnetycznej takich blach jest występowanie w nich pewnych tekstur. Krótko scharakteryzowano typy tekstur najczęściej występujące w tych blachach. Dla kilku wybranych blach prądnicowych przedstawiono wartości typowych parametrów magnetycznych dla różnych kierunków magnesowania. Zaproponowano metodę uwzględnienia anizotropowych właściwości blach prądnicowych w obliczeniach zmian indukcji podczas przemagnesowania osiowego i obrotowego. Specjalnie dobrana funkcja rozłożenia ziaren w danej blasze pozwala uwzględnić anizotropowe właściwości w obliczeniach zmian indukcji. Przykłady zmian indukcji podczas przemagnesowania osiowego i obrotowego przedstawiono w końcowej części artykułu.

Słowa kluczowe: anizotropia magnetyczna, blachy prądnicowe, pętla histerezy

* D.Sc. Ph.D. Eng. Witold Mazgaj, D.Sc. Ph.D. Eng. Adam Warzecha, Institute of Electromechanical Energy Conversion, Faculty of Electrical and Computer Engineering, Cracow University of Technology.

1. Introduction

Dynamo steel sheets are mainly applied in magnetic circuits of rotating machines, but quite often they are also used in magnetic cores of small power transformers. Therefore, these sheets should have the same magnetic properties in each direction on the sheet plane. Grains in the dynamo steel sheets are very small, their average size is in the range from about 20 μm to about 100 μm , and the distribution of grains in isotropic (non-oriented) sheets should be the same with respect to all directions. However, magnetic measurements carried out by means of both the RSST device and the Epstein frame have shown that the majority of the dynamo steel sheets have certain anisotropic features. As a result, the anisotropic properties of the dynamo sheets have a certain influence on the magnetic flux distribution in the magnetic cores of electrical machines and transformers [1, 2]. Crystallographic research, performed for several typical dynamo sheets with the use of the X-ray diffractometer, has shown that an amount of the sheet grains has a certain texture (privilege crystallographic orientation). The volume part of the individual texture is in the range from a few to over twenty percent of the whole sample volume of the given dynamo sheet.

Changes of the flux density in electrical steel sheets depend not only on the field strength value, but they also depend on the texture types, which can occur in these sheets. Various technological procedures in the manufacturing process of dynamo steel sheets are designed to achieve texture-free (non-oriented) materials, but these sheets have not been produced so far on an industrial scale.

Textures in dynamo sheets are also the reason of the anisotropy, which refers to power losses during magnetization processes. Due to the occurrence of certain crystallographic orientations, hysteresis loops measured along different directions on the sheet plane differ from each other. As a result of this, the hysteresis losses depend on the direction of the magnetization process; this problem is discussed in [3–6].

Dynamo steel sheets can be magnetized in different directions. First of all, it refers to the magnetic cores of the rotational machines, although in magnetic circuits of transformers the magnetic flux can also change its direction. For example, this case can occur during a current overload when the permeability of the magnetic circuit decreases strongly. So, in many cases it is necessary to calculate the magnetic field distribution for different directions of the magnetic flux. This is possible using an appropriate model of the magnetization process, which allows us to take into account anisotropy properties of the dynamo steel sheets. The method of the modelling of magnetization processes in soft magnetic materials is widely presented in [7].

The anisotropic properties of the dynamo steel sheets are discussed on the basis of four selected sheets coming from different manufacturers. In order to assess the anisotropy of these dynamo sheets, special crystallographic studies were carried out; they have shown an occurrence of certain textures in these sheets. Additionally, magnetic measurements of the axial magnetization along some directions on the sheet plane were performed. Results of the texture analysis were used in order to take into account the anisotropic properties in the author's model of the rotational magnetization.

2. Typical textures of dynamo steel sheets

Studies concerning textures in dynamo sheets were carried out for some typical sheets with the thickness of 0.5 mm by means of the X-ray diffractometer [8]. The textures were determined by the interpretation of X-ray diffraction patterns, which were obtained for the radiation with an energy of 30 keV passing through the dynamo sheets¹. In this research, the stereographic projections are performed and the reflections from the selected crystallographic plane of the given dynamo sheet sample are counted. Points with the same intensity of reflections are connected by lines. It allows obtaining the so-called pole figures, which make possible the description of the texture type in electrical steel sheets. The intensity of reflections in the pole figures gives the possibility to estimate the volume of a privileged crystallographic orientation.

The diffraction patterns concerning the lattice planes type $\{100\}$, $\{110\}$ and $\{111\}$ of the iron crystal allow interpretation of the six known fibres of the rolling and the recrystallization texture of the ferritic steel. All six fibres are involved in creation of diffractions from the plane $\{110\}$. However, diffractions from the planes $\{100\}$, $\{111\}$ do not have complete information about textures and these diffractions have a secondary meaning. For texture tests, the following dynamo sheets were selected: M400-50A, M800-50A (both produced in Sweden), M530-50A (Czech Republic), and M530-50A (South Korea). Figure 1 presents, for example, the pole figures of the dynamo sheets M400-50A and M530-50A (Czech Republic). The pole figures of the sheet M800-50A and of the Korean sheet M530-50A are similar to the pole figures presented in Figure 1a and 1b, respectively.

It is obvious that all grains in any dynamo sheet should be distributed evenly. However, texture studies have shown that in these sheets a certain amount of grains has a privilege crystallographic orientation. The analysis of the diffraction patterns indicates that in the sheets type M400-50A and M800-500 the following textures occur first of all: $\{100\}\langle 056 \rangle$, $\{100\}\langle 049 \rangle$, $\{111\}\langle 11\bar{2} \rangle$, $\{111\}\langle 3\ 4\bar{7} \rangle$. These symbols indicate which crystallographic planes and directions of the cubic-shaped iron crystals are parallel to the sheet plane and to the rolling direction [8]. The two first crystallographic orientations refer to the so-called cubic texture in which two of six walls of the iron crystal are arranged parallel to the sheet plane. It causes the same magnetization properties in two mutually perpendicular directions on the sheet plane; however, these orientations usually differ with respect to the rolling direction. Other types of the mentioned textures indicate that all three easy magnetization axes of the iron crystal are inclined to the sheet plane at an angle of 45 degrees, and the planes $\{111\}$ are parallel to the sheet plane. These planes are determined by three points of the cubic-shaped iron crystal, which do not belong to the same crystal wall. In this case, the same magnetization properties occur every 120 degrees on the sheet plane. It should be stressed that flux density changes on the sheet plane depend on all texture types and on remaining randomly distributed grains in the given dynamo sheet. In the other two tested sheets type M530-50A (Czech Republic and South Korea) the texture type $\{110\}\langle 1\bar{1}1 \rangle$ occurs in addition to the above-mentioned textures. It means that two of six easy

¹ Crystallographic research was performed in the Institute of Non Ferrous Metals in Gliwice, Light Metal Division in Skawina (Poland).

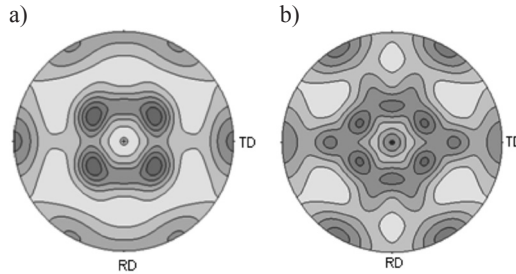


Fig. 1. Pole figures $\{110\}$ of the dynamo sheet: a) M400-50A, b) M5300-50A (Czech Republic); intensity scale is linear, RD – rolling direction, TD – transverse direction

magnetization axes of the cubic-shaped iron crystal are parallel to the sheet plane, but these two axes are usually not parallel to the rolling direction.

Determination of the volume fraction of the given texture in the sheet sample is not an easy task in crystallography. Special software for the analysis of the pole figures, developed in the research centres, allows estimation of the volumetric amount of individual textures occurring in the given dynamo sheet. The share of individual textures is not high (in comparison to the transformer sheets), but in some cases this share is even over twenty percent of the total volume of the given sheet sample. It is worth underlining that research concerning textures indicates that grains are distributed symmetrically relative to both the rolling and the transverse directions [9, 10].

The occurrence of different textures in the dynamo steel sheets is the main cause of their anisotropic properties. These properties are different for particular dynamo sheets and have a significant impact on the magnetic parameters of these sheets that strongly depend on the magnetization direction. Magnetic measurements have allowed the authors to present dependences of the flux densities on the magnetization direction; it is presented in detail in the next Chapter. Determination of the volume fraction of a dominant texture in the given tested dynamo sheet was used by the authors to take into account the sheet anisotropy in the model of the rotational magnetization (Chapter 4).

3. Magnetic anisotropy in typical dynamo steel sheets

Measurements of magnetization curves were carried out by means of the Epstein frame². Hysteresis loops were measured in different directions at every 15 degrees with respect to the rolling direction. The measurement results have shown that all tested dynamo sheets have anisotropic properties, although in various degrees. Characteristic magnetic parameters measured for three angles between the magnetization and the rolling direction are presented in Table 1. In turn, Figure 2 presents the dependence of the flux density maximum values on the angle between the given direction on the sheet plane and the rolling direction. The

² Measurements were carried out in the Laboratory of Magnetic Measurements (Stalprodukt S.A.) in Bochnia (Poland).

influence of the magnetic anisotropy on the flux density maximum value is lesser when the value of the field strength increases. This is because the process of the domain wall motion ends and the resultant flux density vectors of the particular grains begin to rotate towards the direction of the field strength [11, 12].

Table 1

Characteristic magnetic parameters of selected dynamo sheets for three assumed maximum values of the flux density

Type of sheet		M120-27S			M110-23S			M120-30S			
Conductivity [($\Omega \cdot \text{m}$) ⁻¹] * 10 ⁶		2.13			1.64			2.38			
Flux density [T]		1.0	1.5	1.7	1.0	1.5	1.7	1.0	1.5	1.7	
Eddy current losses 100 Hz 0.360		50 Hz	0.090	0.202	0.259	0.041	0.092	0.118	0.115	0.259	0.333
		0.808	1.036	0.164	0.368	0.472	0.460	1.036	1.332		
Excess losses	0°	meas. 50 Hz	0.140	0.295	0.385	0.136	0.288	0.409	0.104	0.222	0.260
		estim. 50 Hz	0.139	0.296	0.373	0.144	0.310	0.392	0.106	0.226	0.285
		meas. 100 Hz	0.448	0.948	1.159	0.464	0.950	1.229	0.310	0.664	0.775
		estim. 100 Hz	0.410	0.852	1.066	0.499	0.982	1.207	0.326	0.695	0.876
	15° measured 100 Hz	50 Hz	0.203	0.474	0.681	0.168	0.456	0.734	0.187	0.424	0.613
		0.624	1.362	1.862	0.548	1.359	2.002	0.551	1.188	1.635	
	30° measured 100 Hz	50 Hz	0.365	1.049	1.349	0.252	0.816	1.361	0.310	0.889	1.585
		1.051	2.663	4.094	0.783	2.205	3.501	0.899	2.317	3.906	
	45° measured 100 Hz	50 Hz	0.678	2.039	1.924	0.554	1.831	1.401	0.638	2.088	1.998
		1.796	5.011	4.989	1.536	4.555	3.676	1.671	4.954	4.304	

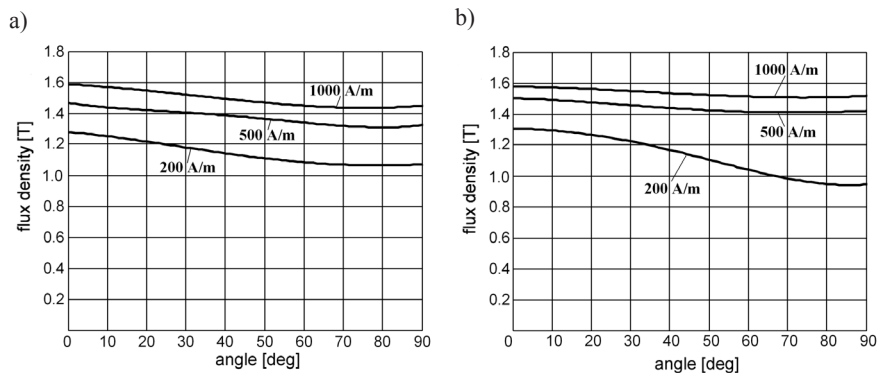


Fig. 2. Maximum values of the flux density as the dependence on the angle of the field strength direction: a) M530-50A (Czech Republic), b) M800-50A

The influence of the anisotropy on the magnetic properties is more noticeable when we present the remanence (residual flux density) as the dependence on the angle of the field strength direction. Similarly, as previously, Figure 3 shows the remanence values as a function of the angle between the given direction and the rolling direction for some values of the field strength.

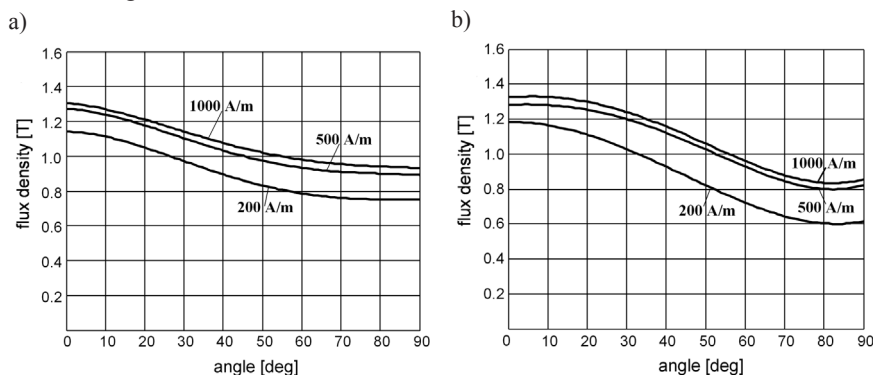


Fig. 3. Remanence values as the dependence on the angle of the field strength direction: a) M530-50A (Czech Republic), b) M800-50A

The highest values of the remanence occur along the rolling direction. However, in the range close to the transverse direction the remanence values are even 50 per cent lesser with respect to the rolling direction. It has an impact on the flux density values, especially when the field strength is lesser than 100 A/m for typical dynamo sheets.

4. Inclusion of the magnetic anisotropy in magnetization process model

Methods allowing engineers to take into calculations the anisotropy of the electrical steel sheets have been already presented in several papers. About 20 years ago, the so-called elliptical model of the magnetic anisotropy [13] and the model based on the co-energy density [14, 15] were proposed, however, these proposals concerned non-hysteresis materials. Sometimes the magnetic anisotropy of electrical steel sheets is taken into calculation using the reluctivity or permeability tensor [16, 17]. Quite often, this problem is being solved by appropriate modification of a chosen vector hysteresis model. A proposal how to take the magnetic anisotropy of electrical steel sheets is described in [18], but the presented method is based on an artificial change of the field strength with respect to the different directions on the given sheet plane.

The method which allows us to take into account the magnetic anisotropy of the dynamo steel sheets was presented by the authors in a simplified form in Proceedings of the Conference EPNC'2012, whereas the extended version of this method is described in [10]. This paper presents how to take into calculations the texture types which occur in the given dynamo sheet.

In order to take into calculations the anisotropy, the author's model of the rotational magnetization described in [7] is used. In this model, the plane of a sample of an anisotropic

sheet is divided into an assumed number of specified directions. For engineering purposes, the anisotropic properties can be taken into account with the assumption that all grains are the same and they have one easy magnetization axis, as it was suggested in [19]. Due to the magnetic anisotropy, to each individual direction a different number of grains (whose easy magnetization axis is parallel to the given direction) is assigned (Fig. 4). Assuming that the sample of the given dynamo sheet is divided on 12 directions, the distribution of the grains can be described by means of the so-called grain distribution function $d(k)$:

$$d(k) = d_1, d_2, \dots, d_k, \dots, d_{11}, d_{12} \quad (1)$$

where:

d_k – relative amount of grains that are assigned to the k -th direction.

The sum of all function values must be equal to 1. For the example which is shown in Figure 4, the grain distribution function has the following values:

$$d(k) = 0.01 \cdot (6, 7, 7, 7, 10, 10, 12, 10, 10, 7, 7, 7) \quad (1a)$$

The determination of the values of the grain distribution function is not easy. These values are estimated with the use of special software applied in crystallography, which enables us to determine the volumetric amount of this texture in the given dynamo sheet sample [8].

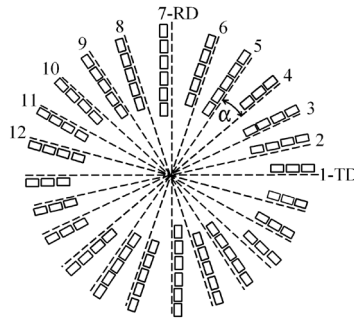


Fig. 4. Simplified distribution of grains in a certain sheet: RD, TD – rolling, transverse direction, respectively

Usually it is assumed that the grains of the most privileged orientation are arranged in accordance with the Gaussian distribution, and remaining grains are distributed randomly. However, it should be noted that quite often the final correction of these values is carried out by means of the trial-and-error method.

In the used model of the magnetization process, a certain hysteresis loop (the so-called direction hysteresis) is assigned to each specified direction on the dynamo sheet plane (Fig. 5). These direction hysteresees are described by such parameters as: saturation flux density b_{sk} , remanence (residual flux density) b_{rk} , and coercive force h_c . It is necessary to underline that these parameters and direction hysteresees cannot be measured and they differ from the hysteresis of the whole sheet sample. The parameters of the direction hysteresees are calculated on the basis of measurements of the limiting and some partial hysteresis loops. In numerical calculations, the hysteresis model based on an exponential function has been used [20].

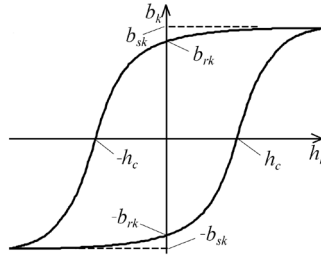


Fig. 5. Example of the direction hysteresis

Determination of the direction hysteresis parameters is presented in detail in [7]; this paper presents only the basic formulas. In the saturation state, the resultant flux density B_s of the whole sheet sample is an algebraic sum of the saturation flux densities of all direction hystereses. The saturation flux density b_{sk} for the given k -th direction equals:

$$b_{sk} = d_k B_s \quad (2)$$

where:

B_s – saturation flux density (determined by measurements) of the dynamo sheet.

When the field strength is decreased from the saturation state to zero, then the resultant flux density of the given sheet sample is equal to the remanence B_r of the given dynamo sheet. The flux density vectors of the direction hysteresis lie along individual directions and the lengths of these vectors are equal to the remanences b_{rk} of the direction hysteresis. The remanence b_{rk} of the individual direction hysteresis is equal to the $b_{rk} d_k$ product:

$$b_r = \frac{B_r}{d_2 \cos 5\alpha + d_3 \cos 4\alpha + \dots + d_7 + \dots + d_{12} \cos 5\alpha} \quad (3)$$

where:

B_r – remanence measured with respect to the rolling direction,

α – angle between two neighbouring directions (Fig. 4).

When the field strength H changes in the opposite direction to the saturation state then the flux densities b_k of the direction hysteresis decrease, and the points with the coordinates (h_k, b_k) move along the left curves of the direction hysteresis loops. If we assume that the dependence between the flux density b_k and the field strength h_k is linear in a quite wide range we can prove that the coercive force h_c of the direction hysteresis equals:

$$h_c = H_c \frac{b_{r2} \cos^2 5\alpha + b_{r3} \cos^2 4\alpha + \dots + b_{r7} + \dots + b_{r12} \cos^2 5\alpha}{b_{r2} \cos 5\alpha + b_{r3} \cos 4\alpha + \dots + b_{r7} + \dots + b_{r12} \cos 5\alpha} \quad (4)$$

where:

H_c – coercive force of the dynamo sheet with respect to the rolling direction.

The values of the grain distribution function have not occurred in the last relation. However, the coercive force h_c depends on this function because the remanences of the direction hystereses are dependent on the d_k values.

It is necessary to underline that for relatively low values of the field strength only domain wall movements occur in the grains of the dynamo sheets. For higher values of the field strength, the flux density vectors rotate towards the field strength direction. New positions of the flux density vectors can be determined on the basis of the energy minimum condition. However, numerical calculations have shown that the angles of these rotations are not greater than two to three degrees if the amplitudes of the field strength are not higher than 500 A/m. Thus, the rotations of the flux density vectors can be neglected in the considered cases of the magnetization process in the dynamo steel sheets.

In numerical algorithm, for the given vector of the field strength the vector projections on the specified directions are calculated. In the next step, the flux densities in the individual directions are determined on the basis of the direction hystereses. The resultant flux density in the elementary sheet sample is the vector sum of the flux densities in the specified directions. For the next field strength vector (with a new value and position), the projections of this vector of the individual directions are determined again. Then the flux density changes in the specified directions and new resultant values of the flux density in the given sheet sample can be calculated.

5. Influence of the anisotropy on flux density changes

As it was previously mentioned, dynamo steel sheets are applied also in magnetic circuits of small power transformers. In some parts of the given transformer sheet the magnetic flux is parallel to the rolling direction, but in other parts, the same magnetic flux is parallel to the transverse direction. It is worth underlining that in the corners of the transformer magnetic circuits, the magnetic flux has usually a different angle with respect to both the rolling and transverse directions. Additionally, in the *T*-points of three-phase transformer cores, the magnetization process can have a rotational character with a certain small elliptical degree. Therefore, the calculations of the magnetic field distribution in magnetic circuits, which are made from anisotropic dynamo sheets, should be carried out using the model of the rotational magnetization. The previously described model allows us to obtain correct calculation results independently of the field strength direction. The experimental verification of this model was presented in [21]. It is necessary to stress that the model of the rotational magnetization can also be used in calculations of the axial magnetization.

Numerical calculations were performed for two selected dynamo sheets. The first one was the sheet M800-50A with the following parameters: saturation flux density – 1.98 T, remanence – 1.15 T, and coercive force – 80 A/m, and the second one was the sheet M530-50A (produced in Czech Republic) with the parameters, which are equal to 1.95 T, 1.10 T, and 70 A/m, respectively. The values of the grain distribution function for the first sheet were equal to: 6, 6, 7, 7, 8, 12, 14, 12, 8, 7, 7, 6 and for the second sheet: 6, 5, 6, 7, 9, 13, 13, 13, 9, 8, 6, 5 respectively. The calculated hysteresis loops were compared with the hysteresis loops obtained on the basis of the measurements (Fig. 6). Differences between hysteresis loops are the result of the magnetic anisotropy which is caused by the occurrence of the privileged orientations of a certain amount of grains in the majority of typical dynamo steel sheets.

The magnetic anisotropy influences the flux density changes also during the rotational magnetization. When the given dynamo sheet has anisotropic properties then the hodographs of flux density changes during rotational magnetization (with a constant value of the field strength) do not have a circular shape. For example, the calculated hodographs of the flux density for three values of the field strength are presented in Figure 7. For increasing values of the field strength, these hodographs are more and more similar, because the rotations of the resultant flux density vectors of the individual grains begin to have the major contribution to the magnetization process.

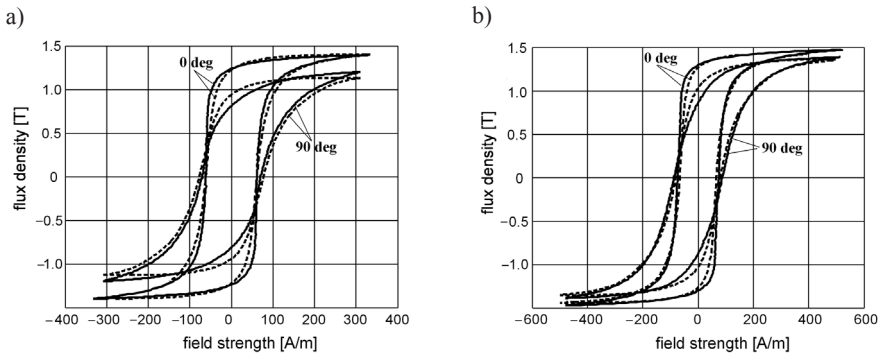


Fig. 6. Hysteresis loops for the rolling direction (0 deg) and transverse direction (90 deg): a) M530-50A (Czech Republic), b) M800-50A; continuous lines – measured loops, dashed lines – calculated loops

It should also be noted that the lag angle of the flux density depends on the field strength value. Figure 8 shows hysteresis loops measured and calculated with respect to the rolling direction (RD), and transverse direction (TD) during the rotational magnetization [22].

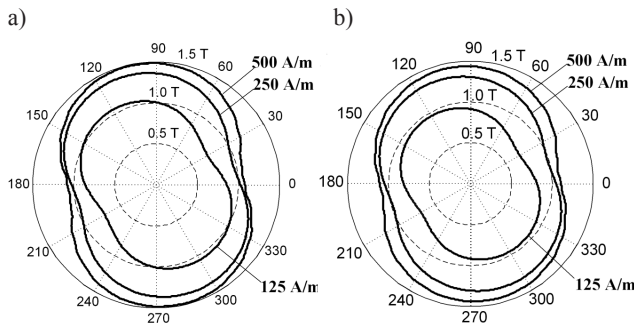


Fig. 7. Hodographs of the flux density during the rotational magnetization for three assumed values of the field strength: a) M530-50A (Czech Republic), b) M800-50A

It is worth mentioning that the shape of these loops differs significantly from the well-known shape of the hysteresis loop during the axial magnetization. Due to the anisotropic properties, the maximum values of the flux density are higher than the corresponding values of the flux density determined in the transverse direction.

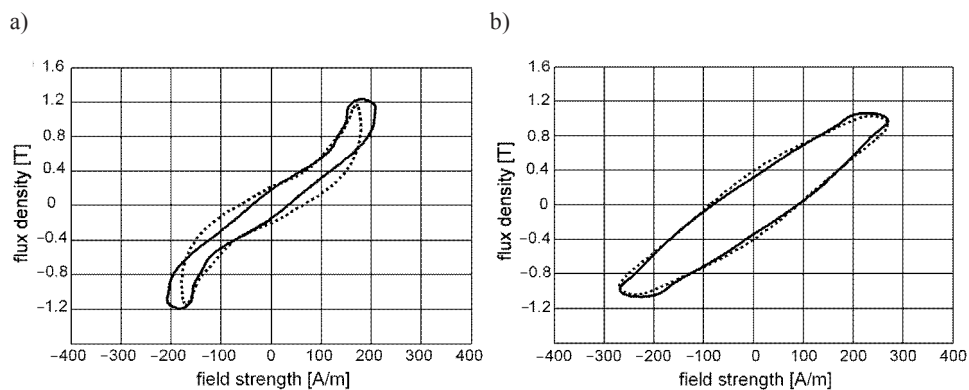


Fig. 8. Hysteresis loops during the rotational magnetization of the dynamo sheet M530-50A (Czech Republic) along: a) the rolling direction RD, b) transverse direction TD; continuous lines – measured loops, dotted lines – calculated loops

6. Conclusions

This paper briefly presents the influence of the magnetic anisotropy on the magnetization processes in typical dynamo sheets. This anisotropy can cause quite significant differences between magnetization processes, which occur in different directions on the sheet plane. Changes of the flux density depend not only on the value and direction of the field strength, but also they depend on the occurrence of the privileged orientations of grains in the given dynamo sheets. It has a significant meaning when the field strength can change its direction on the sheet plane, especially during the rotational magnetization.

The magnetic anisotropy of the dynamo sheets is taken into account with the use of the grain distribution function. Thus, the parameters of the direction hystereses depend on this function values. For simplification, it was assumed that all grains in dynamo sheets have only one easy magnetization axis. However, the cube-shaped grains of iron have three easy magnetization axes; therefore, the comprehensive model of the magnetization process should consider three easy magnetization axes, and magnetization processes occurring along these axes.

Acknowledgements

The research presented in this paper was funded by subsidies on science granted by Polish Ministry of Science and Higher Education under the theme No. E-2/581/2016/DS “Modelling of magnetization processes in magnetic circuits of electrical machines and devices for diagnostics and loss estimation”.

References

- [1] Soiński M., Moses A.J., *Handbook of Magnetic Materials*, Vol. 8, Elsevier Science B.V., 1994.
- [2] Tumański S., *Handbook of magnetic measurements*, CRC/Taylor & Francis, Boca Raton 2011.

- [3] Banach A., Mazgaj W., *Specific power loss of typical dynamo steel sheets*, Technical Transactions 1-E/2015, 291–299.
- [4] Banach A., Mazgaj W., Szular Z., *Estimation of power losses in dynamo steel sheets during axial magnetization*, Przegląd Elektrotechniczny, Vol. 91, No. 12, 2015, 276–280.
- [5] Pluta A.W., *Core loss model in electrical steel sheets with different orientation*, Przegląd Elektrotechniczny, Vol. 87, No. 9b, 2011, 37–42.
- [6] Paltanea V., Paltanea G., Gavrilă H., *Magnetic Anisotropy in Silicon Iron Alloys*, Electrical and Electronic Engineering, Vol. 2(6), 2012, 383–388.
- [7] Mazgaj W., *Modelling of rotational magnetization in anisotropic sheets*, COMPEL, Vol. 30, No. 3, 2011, 957–967.
- [8] Kelly A., Groves G.W., *Crystallography and crystal defects*, Longman, London 1970.
- [9] Wohlfarth E.P., *Ferromagnetic materials. A handbook on the properties of magnetically ordered substances*, Vol. 2, North-Holland Publishing Company, Amsterdam–New York–Oxford 1980.
- [10] Mazgaj W., Warzecha A., *Influence of electrical steel sheet textures on their magnetization curves*, Archives of Electrical Engineering, Vol. 62 (245), No. 3, 2013, 425–437.
- [11] Bozorth R.M., *Ferromagnetism*, IEEE Press, New York 1978.
- [12] Jiles D., *Introduction to magnetism and magnetic materials*, Chapman & Hall, London 1998.
- [13] Dedulle J.M., Meunier G., Foggia A., Sabonnadiere J.C., *Magnetic fields in nonlinear anisotropic grain-oriented iron-sheet*, IEEE Transactions on Magnetics, Vol. 26, No. 2, 1990, 524–527.
- [14] Mekhiche M., Péra T., Maréchal Y., *Model of the anisotropy behaviour of doubly oriented and non-oriented materials using coenergy: application to a large generator*, IEEE Transactions on Magnetics, Vol. 31, No. 3, 1995, 1817–1820.
- [15] Dupre L.R., Van Keer R., Melkebeek J.A., *Numerical evaluation of the influence of anisotropy on the eddy currents in laminated ferromagnetic alloys*, IEEE Transactions on Magnetics, Vol. 38, No. 2, 2002, 813–816.
- [16] Vande Sande H., Boonen T., Podoleanu I., Henrotte F., *Simulation of a three-phase transformer using an improved anisotropy model*, IEEE Transactions on Magnetics, Vol. 40, No. 2, 2004, 850–855.
- [17] Lin D., Yhou P., Badics Z., *A new nonlinear anisotropic model for soft magnetic materials*, IEEE Transactions on Magnetics, Vol. 42, No. 4, 2006, 963–966.
- [18] Kuczmann M., Stoleriu L., *Anisotropic vector Preisach model*, Journal of Advanced Research in Physics 1(1), 011009, 2010, 1–5.
- [19] Shi Y.M., Jiles D.C., Ramesh A., *Generalization of hysteresis modelling to anisotropic and textured materials*, Journal of Magnetism and Magnetic Materials, Vol. 178, Iss. 1, 1998, 75–78.
- [20] Mazgaj W., *Application of an exponential function for description of flux density changes in ferromagnetic materials*, Archives of Electrical Engineering, Vol. LV, No. 3–4, 2006, 223–235.
- [21] Mazgaj W., Sobczyk T.J., Warzecha A., *Inclusion of the model of rotational magnetization into equations of magnetic field distribution*, Proc International Conference on the Computation of Electromagnetic Fields COMPUMAG 2013, Budapest, Hungary, 2013, paper PA5.
- [22] Warzecha A., Mazgaj W., *Magnetization measurements in circle-shaped samples of typical dynamo steel sheets*, Przegląd Elektrotechniczny, No. 6, 2015, 96–99.

PAWEŁ SZCZUREK*, WITOLD MAZGAJ**, AGNIESZKA BANACH**

INFLUENCE OF THE MAGNETIZATION DIRECTION ON POWER LOSSES IN TRANSFORMER STEEL SHEETS

WPŁYW KIERUNKU MAGNESOWANIA NA STRATY MOCY W BLACHACH TRANSFORMATOROWYCH

Abstract

Calculation of power losses in transformer steel sheets is still a significant problem. In some places of cores of a three-phase transformer the flux density is not parallel to the rolling direction; it especially refers to the so-called T-points of the transformer cores. In these places magnetization curves differ from the curve measured for the rolling direction. The paper deals with hysteresis losses, eddy current and excess losses and their dependences on the direction of magnetization processes. Analysis is performed for several frequencies of the magnetization process. Measured power losses of the selected transformer steel sheets are compared with results obtained on the basis of the analytical formulas.

Keywords: eddy current losses, excess losses, hysteresis losses, transformer sheets

Streszczenie

Wyznaczanie strat mocy blach transformatorowych jest nadal istotnym problemem. W pewnych obszarach rdzenia transformatorów trójfazowych linie pola magnetycznego nie są równoległe do kierunku walcowania; szczególnie odnosi się to do tak zwanych T-punktów rdzeni transformatorów. W tych obszarach charakterystyki namagnesowania różnią się od charakterystyki wyznaczonej do kierunku walcowania. Artykuł dotyczy strat histerezy i wiroprądowych oraz ich zależności od kierunku procesu magnesowania. Analizę przeprowadzono dla kilku częstotliwości procesu magnesowania. Zmierzone straty mocy wybranych blach transformatorowych porównano z wynikami uzyskanymi na podstawie wzorów analitycznych.

Słowa kluczowe: blachy transformatorowe, straty histerezy, straty wiroprądowe nadmiarowe

* M.Sc. Eng. Paweł Szczurek, Laboratory of Magnetic Measurements, Stalprodukt SA Bochnia.

** D.Sc. Ph.D. Eng. Witold Mazgaj, M.Sc. Eng. Agnieszka Banach, Institute of Electromechanical Energy Conversion, Faculty of Electrical and Computer Engineering, Cracow University of Technology.

1. Introduction

Magnetic circuits of transformers are often made from amorphous and nanocrystalline materials, particularly for low power rating transformers. However, it seems that for a long time, magnetic cores of medium and high power rating transformers will be constructed with the use of “classical” 3% Fe-Si transformer (grain-oriented) steel sheets, whose magnetic properties are continually improved. This refers to obtaining higher values of the flux densities as well as reduction of both hysteresis and eddy current losses.

Magnetic fields that occur in the transformer cores are usually considered as one-dimensional fields, and magnetization processes are treated as the axial magnetization. Lines of the magnetic fields are parallel to the rolling direction in the most part of the transformer cores. This note applies to low power rating transformers, whose cores are made usually of dynamo steel sheets, which have almost the same properties in any magnetization direction. For this aim, the E and U sheet shapes are cut out from these sheets. Thereby, the permeability is the same in each point of the given transformer core. However, the permeabilities of the dynamo sheets have lower values with respect the transformer sheets. In the cores which are constructed using the transformer sheets, the magnetic lines are almost always parallel to the rolling direction of these sheets. However, in core corners or in T-joint points (connections between columns and yokes) of medium and high power rating transformer, the magnetic lines have different directions with respect to the rolling direction. It is necessary to stress that around the T-joint points the magnetization has rotational character of varying degrees of ellipticity [1, 2].

The transformer steel sheets are produced as grain-oriented sheets and the Goss texture is their characteristic feature. It causes that these sheets are most easily magnetized along the rolling direction [3–6]; in other directions the magnetization properties are significantly worse. Therefore, this fact should be taken into account in predicting of the power losses in the transformer cores, especially when estimation of the losses refers to the corners or T-joint points of the three-phase transformer. It is worth underlining that lines of the magnetic field may not be parallel to the rolling direction in transformer columns in overload or short-circuit states due to the occurrence of a leakage flux. Grains and thus domains of the transformer steel sheets can have an area of several square centimeters in contrary to the dynamo steel sheets whose average size is in the range from 60 to 100 μm .

The total power losses in electrical steel sheets are a sum of the hysteresis losses, the “classical” eddy current losses, and the excess losses whose reason are the so-called domain eddy currents occurring in transformer sheets [5, 7–9]:

$$P_{\text{tot}} = P_h + P_{ed} + P_{\text{exc}} \quad (1)$$

where:

- P_h – hysteresis losses,
- P_{ed} – “classical” eddy current losses,
- P_{exc} – excess losses.

Losses in steel sheets are determined per mass unit and they are called the specific power loss. These losses can be estimated with the use of some analytical formulas, however, these formulas do not taken into account the influence of the magnetization direction on

the loss value. Despite the large number of scientific studies, the estimation of power losses in transformer sheets is not completely solved. In some cases, calculated hysteresis losses differ significantly in comparison to the measured hysteresis losses; it also concerns the total eddy current losses due to the occurrence of the excess losses caused by domain eddy currents [10–12]. Differences between measured and calculated losses may also occur when winding currents are distorted with respect to the sinusoidal shape [13, 14].

The purpose of this paper is a comprehensive discussion of the power losses occurring in the transformer steel sheets (especially their dependence on the magnetization direction) on the basis of the magnetic measurements performed by the authors. The total power losses were separated on the aforementioned loss components, and the measured losses were compared with values of the particular losses obtained using analytical formulas. The magnetic measurements were carried out for three different transformer sheets and have shown that the power losses determined for directions other the rolling direction are significantly higher than the losses in the rolling direction. Taking into account the magnetic field distribution in the core of a typical transformer, the considered directions on the sheet plane can have angles not bigger than 45° with respect to the rolling direction. The magnetic measurements and the loss analysis were carried out for following transformer sheets: M120-27S, M110-23S, and M120-30S (sheets were received from several manufacturers).

2. Hysteresis losses in transformer steel sheets

The hysteresis power losses are usually estimated using the well-known Steinmetz formula or the Richter formula [3, 15]:

$$P_h = \eta f B_m^p \quad (2)$$

where:

- η – constant whose value depends on the given electrical steel sheets,
- f – frequency of magnetic field changes,
- B_m – maximum value of the flux density during the magnetization process,
- p – exponent which is equal to 1.6 in the Steinmetz formula or 2.0 in the Richter formula.

The coefficient η depends on the given electrical steel sheet, so the same coefficient value should not be used for any transformer steel sheet. Determination of the value of the exponent p in the formula (2) is a separate problem, and the value of this exponent is usually taken between 1.6 and to 2.0.

The hysteresis losses occurring in the transformer steel sheets are usually determined for two typical value of the flux density 1.5 T and 1.7 T. The hysteresis loops measured by the authors along the rolling direction for these two values of the flux density are shown in Fig. 1 and Fig. 2. Due to occurrence of the Goss texture, the hysteresis loops measured along other directions differ significantly in comparison to the loops presented in Fig. 1. The explanation of this phenomena is widely presented in [2, 16]. In a demagnetization state, domains whose magnetization vectors are parallel to the rolling direction occur mainly in the transformer

sheets. When the magnetic field strength increases in the direction perpendicular to the rolling direction, the domains which form 180-degree walls transform into domains which form the 90-degree walls. The magnetization vectors of new domains are parallel to the easy magnetization axes [010] and [001] of iron crystals; these axes are inclined to the transformer sheet plane at the angle of 45°. During this process the resultant flux density of the whole sheet sample increases relatively slowly and it begins to increase faster after the end of this process. For example, Figure 2a shows the hysteresis loops for three directions on the sheet plane measured for the transformer sheet M120-27S. These loops refer to the flux density 1.2 T, because above this flux density value the domain wall motions do not occur. Values of the hysteresis losses depend not only on the value of the flux density, but also on the direction of the magnetization process that influences the amount of these losses; this problem was considered among others in [17, 18].

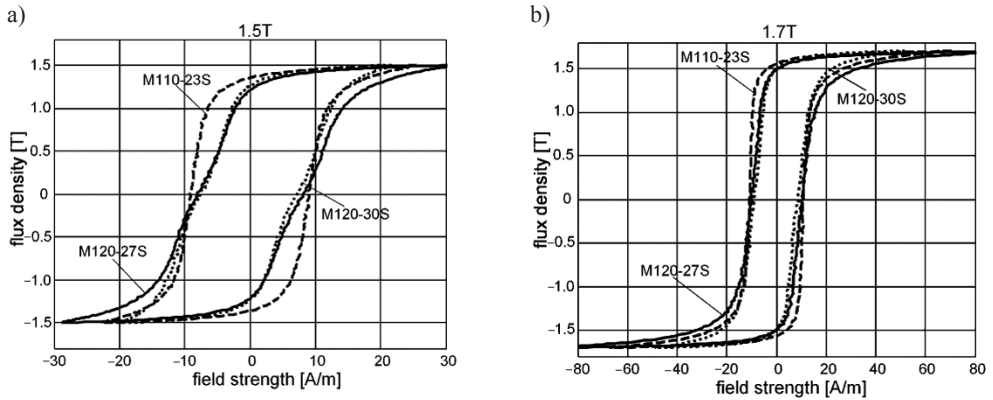


Fig. 1. Hysteresis loops along the rolling direction for the maximum flux density: a) 1.5 T, b) 1.7 T

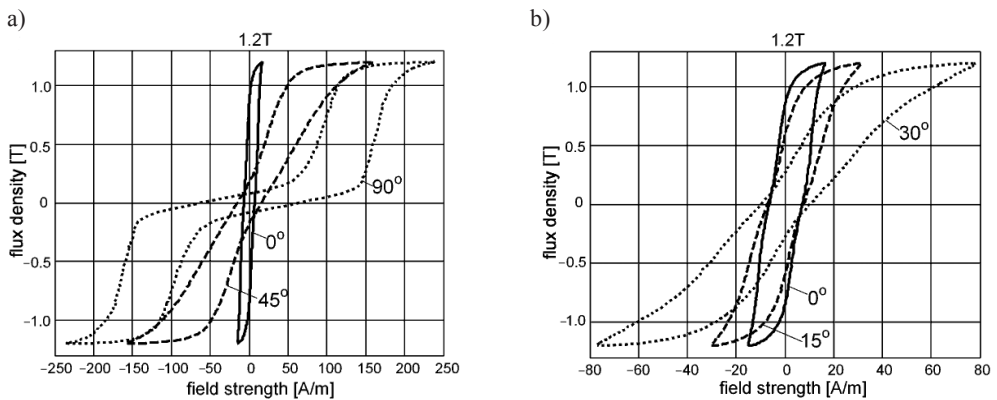


Fig. 2. Hysteresis loops of the transformer sheets M120-27S for the maximum flux density 1.2 T: a) 0° (rolling direction), 45° and 90°, b) 0°, 15° and 30°

As it was earlier mentioned, this is caused by occurrence of the Goss textures in the transformer sheets. The hysteresis losses for an assumed maximum value of the flux density is equal to the surface of the measured hysteresis loop. Magnetic measurements carried out by means of the Epstein frame have shown that the hysteresis power losses depend significantly on the magnetization direction.

The hysteresis losses were determined for each selected magnetization direction on the basis of the static hysteresis loops. These losses measured for angles greater than 15° with respect to the rolling direction can be higher even several times than analogous losses estimated for the rolling direction. For example, Fig. 3a presents hysteresis specific power losses for the sheet M120-27S determined for selected directions on the sheet plane. In turn, the specific power losses of the sheet M110-23S measured for the rolling direction and for three angles 15°, 30° and 45° are included in Fig. 3b. The hysteresis losses for flux densities greater than 1.5 T are not shown in Fig. 3a due to significant saturations of tested transformer sheets and possible measured errors during magnetization along the angles greater than 30° with respect to the rolling direction. It is worth underlining that the Steinmetz formula does not take into account the angle of the magnetization in the estimation of the hysteresis losses. For comparison, values of the hysteresis specific power loss determined on the basis of Steinmetz formula (2) are shown in Fig. 3b. Calculations were performed with the assumption that the parameter η was equal to 0.0032 and the exponent p was equal to 1.6 for the flux density in the range from 0.2 T to 1.3 T and $p = 1.8$ for the flux density higher than 1.3 T.

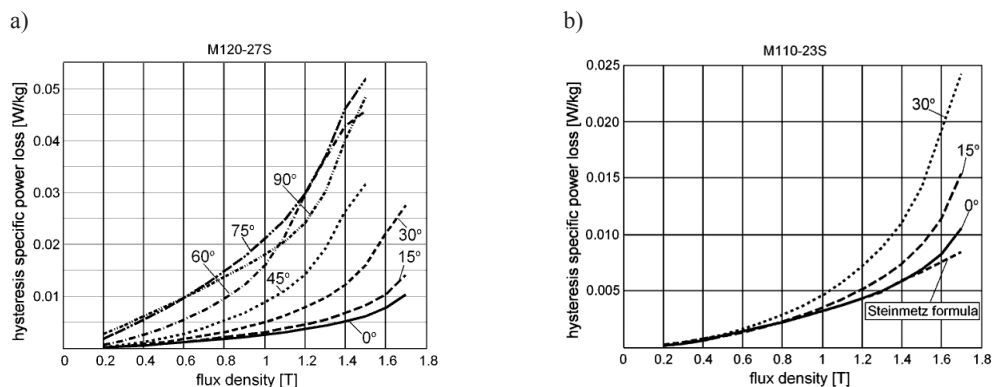


Fig. 3. Hysteresis specific power loss of the transformer sheets: a) M120-27S, b) M110-23S

Dependences of the hysteresis losses on the flux density and the magnetization angle for other two transformer sheets are similar as for the sheet M120-27S. The bigger the angle between the magnetization and the rolling direction is, the faster increases the value of the hysteresis losses. Due to only four measurement points, these dependences were approximated by means of the third degree polynomials; it allows the estimation of the hysteresis power losses for any angle between 0° (the rolling direction) and 45°.

The coercive forces, remanences, characteristic values of the field strength and specific hysteresis power losses of three considered transformer sheets are given in Table 1. These

values are presented for four magnetization direction on the sheet plane. The hysteresis losses determined for other direction than the rolling direction are significantly higher. Thus, the estimation of these losses requires additional magnetic measurements. In some cases, it may be troublesome and even impossible when the width of the tested transformer sheet is smaller than 280 mm in view of tests utilizing the Epstein frame.

Table 1

Magnetic parameters and specific hysteresis loss

Type of sheet	M120-27S			M110-23S			M120-30S			
Flux density [T]	1.0	1.5	1.7	1.0	1.5	1.7	1.0	1.5	1.7	
Coercive force [A/m]	0°	6	8	10	7	9	11	6	7	9
	15°	6	9	12	7	10	12	6	8	10
	30°	9	13	14	8	11	13	7	11	13
	45°	13	17	19	12	16	17	11	16	–
Remanence [T]	0°	0.64	1.21	1.49	0.85	1.36	1.56	0.72	1.24	1.50
	15°	0.44	0.89	1.20	0.50	1.03	1.27	0.51	0.92	1.17
	30°	0.21	0.50	0.65	0.29	0.88	0.98	0.17	0.38	0.61
	45°	0.13	0.24	0.27	0.24	0.43	0.50	0.15	0.30	–
Field strength [A/m]	0°	13	30	90	11	24	69	11	21	50
	15°	23	59	186	23	63	228	21	52	129
	30°	58	225	2500	44	189	2767	54	164	–
	45°	106	3729	12133	114	4025	12312	116	300	–
Hysteresis loss [W/kg]	0°	0.0027	0.0062	0.0104	0.0032	0.0069	0.0106	0.0027	0.0056	0.0083
	15°	0.0032	0.0083	0.0141	0.0035	0.0091	0.0154	0.0032	0.0076	0.0120
	30°	0.0051	0.0161	0.0276	0.0047	0.0142	0.0242	0.0046	0.0139	0.0250
	45°	0.0089	0.0317	0.0283	0.0086	0.0280	0.0234	0.0082	0.0294	–

The magnetization directions in individual points of the T-joint areas are various; so it would be desirable to perform for the given transformer sheet appropriate magnetic measurements, for example, every 5 degrees. Figure 4 shows the ratio (determined by the authors) between the hysteresis losses measured along the assumed magnetization direction and the hysteresis losses determined for the rolling direction (0°) for the transformer sheets M120-27S and M110-23S. Dependences of this ratio on the magnetization angle for the third transformer sheets M120-30S are similar to the curves presented in Figure 4a. It is necessary to stress that studies have been performed only for three transformer sheets which have different thickness. It seems that research carried out for several transformer sheets with the same thickness would be desirable in further studies on the magnetization processes in these sheets.

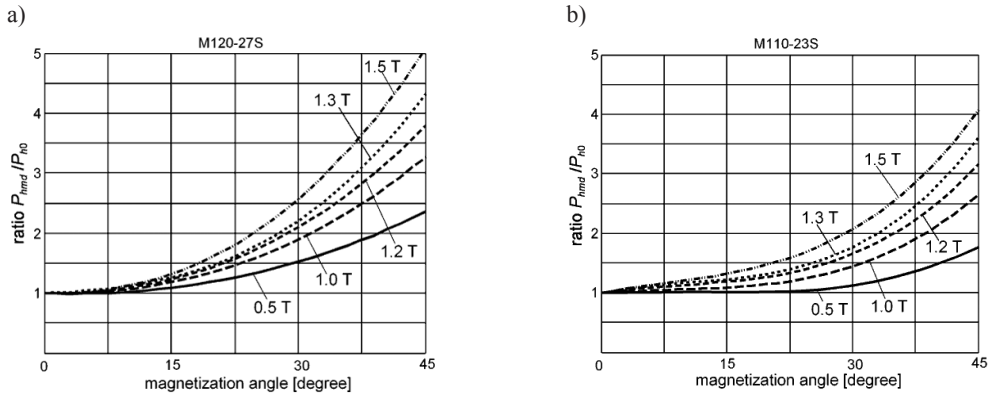


Fig. 4. Ratio between the hysteresis losses P_{hmd} measured along the assumed magnetization direction and the hysteresis losses P_{h0} measured for the rolling direction (0°): a) M120-27S, b) M110-23S

3. Power losses caused by eddy currents

It is well known that measured eddy current losses of the electrical steel sheets are significantly higher than the value of these losses calculated with the use of the analytical formulas. As it is proposed in [11], the measured eddy currents losses for the assumed magnetization direction are differences between the total power losses and the hysteresis losses for the particular frequencies at which magnetic measurements were carried out. Values of these losses for the chosen conditions of the magnetization process are presented in Table 2.

The eddy current losses are usually estimated using the formula [3, 9]:

$$P_{ed} = \frac{\pi^2 \sigma d^2 f^2 B_m^2}{6} \quad (3)$$

where:

- σ – conductivity of the transformer sheet,
- d – thickness of the given transformer sheet.

This relationship was formulated with the assumption that the magnetic permeability has a constant value in a wide range of the flux density changes. However, this assumption can be acceptable when the flux density is not higher than 1.5 T for the rolling direction and not higher than about 1.2 T, when the angle of the magnetization direction is lesser than 45° . It is worth underlining that the value of the eddy current losses calculated with the use of the formula (3) depends also on the accuracy of the parameter determination; this remark refers especially to the value of the conductivity of the tested transformer steel sheet. The conductivities of three tested transformer sheets were determined with the use of the Thomson bridge and by means of the technical methods. Average values of these conductivities are presented in Table 2. Similarly as the Steinmetz formula (2) the relationship (3) does not take into account the angle between magnetization direction and the rolling direction.

As earlier mentioned, the measured eddy current losses are bigger than the eddy current losses calculated with the use of the formula (3). The difference between these losses is treated as the excess losses which are caused by eddy microcurrents occurring around moving domain walls in the transformer sheets. The excess losses occur also in dynamo steel sheets [10, 19], but the share of these losses is relatively smaller in comparison with the transformer sheets.

Measurements performed by the authors for three tested transformer sheets have shown that the excess losses depend significantly on the magnetization direction. The bigger the angle between the magnetization direction and the rolling direction is, the higher are these losses. Figure 5 shows dependences of these losses on the frequency and the magnetization direction for the transformer sheet M120-77S; analogous dependences for two other sheets have similar character.

The estimation of the excess losses is still a valid problem. The first proposal of the estimation of the excess losses in the transformer sheets was proposed by Pry and Bean [12]. In turn, G. Bertotti has proposed a certain statistical method allowing the estimation the excess losses [1, 2, 20]. He has assumed that domain wall movements during the magnetization process consists of random jumps in iron crystals of the transformer sheet. He has treated parts of these walls as n certain magnetic objects which are active simultaneously and behaviour of these objects is associated with the occurrence of a certain magnetic strength which is defined as:

$$H_{\text{exc}} = \frac{P_{\text{exc}}}{4fB_m} \quad (4)$$

Determining of the number of the magnetic objects is made according to [11] for the rolling direction and for two frequencies 50 Hz and 100 Hz. The dependences $n = f(H_{\text{exc}})$ determined for the rolling direction are presented in Figure 6. Different ranges of field strength changes are the result of various values of the excess losses in the assumed magnetization conditions.

The dependences $n = f(H_{\text{exc}})$ are more complex and the number n of the magnetic objects decreases (especially for higher values of the field strength H_{exc}) when the magnetization direction forms an angle greater than about 15° with respect to the rolling direction; it significantly complicates the estimation of the excess losses based on the Bertotti's approach. It is worth underlining that the number n of the magnetic objects depends significantly on the thickness of the given transformer sheet.

For field strengths higher than about 3 A/m for 50 Hz and about 6 A/m for 100 Hz, what corresponds to the flux density value of about 0.5 T, it can be assumed that the amount of n magnetic objects can be approximated as follows [10, 11]:

$$n = n_0 + \frac{H_{\text{exc}}}{V_0} \quad (5)$$

where:

n_0, V_0 – parameters characteristic for the given transformer sheet which are estimated on the basis of dependences $n = f(H_{\text{exc}})$ determined for the assumed frequency.

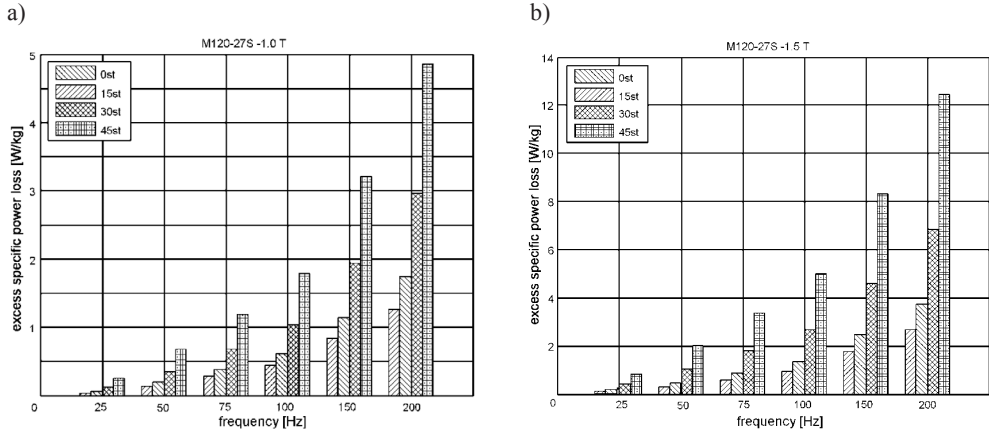


Fig. 5. Excess power losses of the sheet M120-27S measured for the maximum flux density: a) 1.0 T, b) 1.5 T

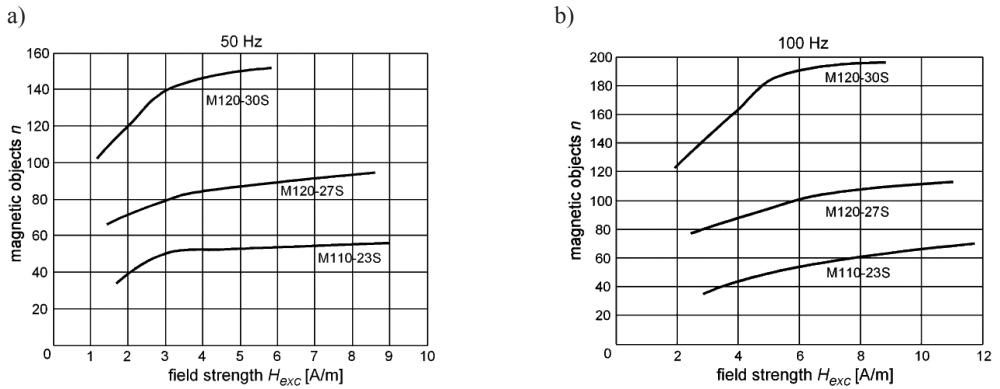


Fig. 6. Number of magnetic objects as dependences on the field strength H_{exc} : a) 50 Hz, b) 100 Hz

According to the Bertotti's approach, the excess losses in the transformer steel sheets can be estimated using the following formula:

$$P_{exc} = 2B_m f \left(\sqrt{16\sigma G S V_0 B_m f + (n_0 V_0)^2} - n_0 V_0 \right) \quad (6)$$

where:

G – constant value which is equal to 0.1356,

S – area of the cross-section of the tested sheet sample.

Values of the excess losses estimated for the frequency 50 Hz and 100 Hz and for three values of the flux density are included in Table 2. In most cases, the relative error of the estimated excess losses is lesser than 10 percent with respect to the measured values.

Table 2

Conductivities and specific eddy current loss in W/kg

Type of sheet		MI20-27S				MI10-23S				MI20-30S			
Conductivity [($\Omega \cdot \text{m}$) ⁻¹] · 10 ⁶		2.13				1.64				2.38			
Flux density [T]		1.0	1.5	1.7	1.0	1.5	1.7	1.0	1.5	1.7	1.0	1.5	1.7
Eddy current losses 100 Hz 0.360	50 Hz	0.090	0.202	0.259	0.041	0.092	0.118	0.115	0.259	0.333			
	0.808	1.036	0.164	0.368	0.472	0.460	1.036	1.332					
	meas.	0.140	0.295	0.385	0.136	0.288	0.409	0.104	0.222	0.260			
	0°	0.139	0.296	0.373	0.144	0.310	0.392	0.106	0.226	0.285			
Excess losses	meas.	0.448	0.948	1.159	0.464	0.950	1.229	0.310	0.664	0.775			
	0°	0.410	0.852	1.066	0.499	0.982	1.207	0.326	0.695	0.876			
	15° measured 100 Hz	0.203	0.474	0.681	0.168	0.456	0.734	0.187	0.424	0.613			
	30° measured 100 Hz	1.362	1.862	0.548	1.359	2.002	0.551	1.188	1.635				
45° measured 100 Hz	50 Hz	0.365	1.049	1.349	0.252	0.816	1.361	0.310	0.889	1.585			
	1.051	2.663	4.094	0.783	2.205	3.501	0.899	2.317	3.906				
	50 Hz	0.678	2.039	1.924	0.554	1.831	1.401	0.638	2.088	1.998			
1.796	5.011	4.989	1.536	4.555	3.676	1.671	4.954	4.304					

4. Conclusions

It has been known that the power losses in the transformer steel sheets depend on the magnetization direction but research carried out for three different transformer sheets has allowed us to assess the quantitative differences between the losses for any magnetization direction and the power losses determined for the rolling direction. This remark refers to both the hysteresis losses and the eddy current losses. The reason of the hysteresis loss increase with the angle between the magnetization direction and the rolling direction is the presence of both the Goss texture and the quite complex process of the domain structure transformation for directions that significantly differ with respect to the rolling direction. It should be stressed once again that the Steinmetz formula does not take into account other magnetization directions than the rolling direction. It is desirable in future research to try to determine the parameters occurring in the Steinmetz formula as functions of the magnetization direction. However, this requires to carry out appropriate magnetic measurements for higher number of tested transformer sheets.

The dependence of the total eddy current losses on the magnetization direction is qualitatively similar to the case of the hysteresis losses. However, the “classical” eddy current losses are calculated without taking into account the microcurrents flowing around the moving domain walls, and these losses do not depend on the magnetization direction. Thus, it can be assumed that the excess losses have significant meaning and their values depend not only on the frequency and the flux density but the magnetization direction influences the excess losses significantly. It is worth underlining that the Bertotti’s approach allows us to estimate the excess losses but the use of this method requires performance of the appropriate magnetic measurements of the given transformer sheet. It can be concluded that in further research the emphasis should be placed on methods allowing the estimation of the excess losses.

Acknowledgment

The research presented in this paper was funded by subsidies on science granted by Polish Ministry of Science and Higher Education under the theme No. E-2/619/2016/DS 144 “Modelling of magnetization processes in magnetic circuits of electrical machines and devices for diagnostics and loss estimation”.

References

- [1] Pfützner H., Mulasalihovic E., Yamaguchi H., Sabic D., Shilyashki G., Hofbauer F., *Rotational magnetization in transformer cores – A review*, IEEE Transactions on Magnetics, Vol. 47, No. 11, 2011, 4523–4533.
- [2] Pfützner H., *Rotational magnetization and rotational losses of grain oriented silicon steel sheets – fundamental aspects and theory*, IEEE Transactions on Magnetics, Vol. 30, No. 5, 1994, 2802–2807.
- [3] Heck C., *Magnetic materials and their applications*, Butterworths, London 1974.

- [4] Soiński M., Moses A.J., *Handbook of magnetic materials*, Elsevier Science B.V., Vol. 8, 1994.
- [5] Tumański S., *Handbook of magnetic measurements*, CRC/Taylor & Francis, Boca Raton 2011.
- [6] Turowski J., *Elektrodynamika techniczna*, WNT, Warszawa 1993.
- [7] Bozorth R.M., *Ferromagnetism*, IEEE Press, New York 1978.
- [8] Bertotti G., *Physical interpretation of eddy current losses in ferromagnetic materials. I. Theoretical considerations*, Journal of Applied Physics 57, (6), 1985, 2110–2117.
- [9] Jiles D.C., *Introduction to Magnetism and Magnetic Materials*, Chapman & Hall, London 1998.
- [10] Bertotti G., *General properties of power losses in soft ferromagnetic materials*, IEEE Transactions on Magnetics, Vol. 24, No. 1, 1988, 621–630.
- [11] Bertotti G., *Hysteresis in magnetism*, Academic Press, San Diego 1998.
- [12] Pry R.H., Bean C.P., *Calculation of the energy loss in magnetic sheet materials using a domain model*, Journal of Applied Physics, Vol. 19, No. 3, 1958, 532–533.
- [13] Lancarotte M., Penteado A., *Estimation of core losses under sinusoidal or non-sinusoidal induction by analysis of magnetization rate*, IEEE Transactions on Magnetics, Vol. 16, No. 2, 2001, 174–179.
- [14] Zakrzewski K., *Overloss coefficient for dynamo sheet during axial magnetization with nonsinusoidal flux*, Archives of Electrical Engineering, XLVI, No. 3, 1997, 355–365.
- [15] Dąbrowski M., *Analiza obwodów magnetycznych. Straty mocy w obwodach*, PWN, Warszawa–Poznań 1981.
- [16] Fiorillo F., Dupré L.R., Appino C., Rietto A.M., *Comprehensive model of magnetization curve, hysteresis loops, and losses in any direction in grain-oriented Fe–Si*, IEEE Transactions on Magnetics, Vol. 38, No. 3, 2002, 1467–1475.
- [17] Pluta A.W., *Core loss model in electrical steel sheets with different orientation*, Przegląd Elektrotechniczny, 87, No. 9b, 2011, 37–42.
- [18] Paltanea V., Paltanea G., Gavrilă H., *Magnetic anisotropy in silicon iron alloys*, Electrical and Electronic Engineering, Vol. 2(6), 2012, 383–388.
- [19] Banach A., Mazgaj W., Szular Z., *Estimation of power losses in dynamo steel sheets during axial magnetization*, Przegląd Elektrotechniczny, R. 91, Nr 12, 2015, 276–280.
- [20] Barbisio E., Fiorillo F., Ragusa C., *Predicting loss in magnetic steels under arbitrary induction waveform and with minor hysteresis loops*, IEEE Transactions on Magnetics, Vol. 40, No. 4, 2004, 1810–1819.

LUCJAN SETLAK*, EMIL RUDA**

ANALYSIS AND SIMULATION OF ADVANCED TECHNOLOGICAL SOLUTIONS IN THE FIELD OF POWER HIGH-VOLTAGE DIRECT CURRENT (HVDC) OF MODERN AIRCRAFT IN LINE WITH THE TREND OF MORE ELECTRIC AIRCRAFT (MEA)

ANALIZA I SYMULACJA ZAAWANSOWANYCH ROZWIĄZAŃ TECHNOLOGICZNYCH W ZAKRESIE ZASILANIA WYSOKIEGO NAPIĘCIA PRĄDU STAŁEGO (HVDC) WSPÓŁCZESNYCH SAMOLOTÓW ZGODNYCH Z TRENDEM SAMOLOTU BARDZIEJ ELEKTRYCZNEGO (MEA)

Abstract

The subject of the paper is to present innovative technological architecture of the power supply system EPS (Electric Power System) in the field of high voltage power HVDC (High Voltage Direct Current) by conducting a critical analysis of the literature as well as an analysis and simulation of its selected component in line with the trend of more electric aircraft MEA (More Electric Aircraft). The considered advanced technologies relate to the architecture of the power supply system HVDC in the high voltage 540V DC (≈ 270 V DC) and 350 V DC, used for advanced aircraft in line with the trend of MEA/ AEA, in particular for military aircraft made by Lockheed Martin (F-22 Raptor, the JSF F-35). Based on the above, the simulation of sample components of the system architecture of high voltage power HVDC has been made, selected from the group of military aircraft in the area of more electric aircraft 'More Electric Aircraft', which is mainly the domain of advanced military aircraft the JSF (Joint Strike Fighter) F-35 and F-22 Raptor. In the final part, the paper presents the main conclusions arising from the analysis and simulation of selected components of HVDC power system architecture in accordance with the concept of a more electric aircraft.

Keywords: MEA, power supply systems of high voltage DC (HVDC), electrical machines

Streszczenie

Przedmiotem niniejszego artykułu jest przedstawienie innowacyjnych rozwiązań technologicznych architektury elektroenergetycznego systemu zasilania EPS (*Electric Power System*) w zakresie zasilania wysokiego napięcia HVDC (*High Voltage Direct Current*) poprzez dokonanie analizy literatury przedmiotu oraz analizy i symulacji wybranego jej komponentu zgodnie z trendem samolotu bardziej elektrycznego MEA (*More Electric Aircraft*). Rozpatrywane zaawansowane rozwiązania technologiczne dotyczą architektury systemu zasilania HVDC w zakresie wysokich napięć 540 V DC (≈ 270 V DC) oraz 350 V DC, stosowanej w zaawansowanych samolotach zgodnych z trendem MEA/AEA, w szczególności samolotach wojskowych koncernu Lockheed Martin (F-22 Raptor, JSF F-35). Dokonano symulacji przykładowych komponentów architektury systemu zasilania wysokiego napięcia HVDC, wybranych z grupy samolotów wojskowych w zakresie samolotu bardziej elektrycznego, będącej domeną głównie zaawansowanych samolotów JSF (*Joint Strike Fighter*) F-35 i F-22 Raptor. W końcowej części referatu przedstawiono główne wnioski wynikające z przeprowadzonej analizy i symulacji wybranych komponentów architektury systemu zasilania HVDC w myśl koncepcji samolotu bardziej elektrycznego.

Słowa kluczowe: MEA, elektroenergetyczne systemy zasilania wysokiego napięcia prądu stałego (HVDC), maszyny elektryczne

* Ph.D. Eng. Lucjan Setlak, Department of Avionics and Control Systems, Deblin, Polish Air Force Academy.

** M.Sc. Emil Ruda, 33. Air Transport Base, Powidz, Poland.

1. Introduction

After analyzing numerous publications and literature, it can be seen that the More Electric Aircraft (MEA) concept has plenty of branches and solutions. One of its aspects – Power Electronics Systems based on the multi-pulse converters – was presented in our previous publication [1]. This paper indicates and considers another advanced solution compatible with MEA concept – High Voltage Direct Current (HVDC).

Both in modern civil (Airbus, Boeing) and military aviation (Lockheed Martin), in terms of aircraft consistent with the concept of the More Electric Aircraft (MEA), you can observe a continuous and dynamic development of the Electric Power System (EPS) architecture. This development can be clearly seen in the field of High Voltage Direct Current (HVDC) and its key component is the Power Electronic System (PES) [1, 2]. Making the introduction to the subject of this paper, it should be noted that modern advanced EPS and PES technology in terms of High Voltage Direct Current (HVDC) relate primarily to the most advanced military aircrafts (F-22 Raptor, JSF F-35). Their domain are high 540 V DC voltages (± 270 V DC) and 350V DC [3, 4]. Advanced technological solutions, which are based on the current widely understood development in the field of electrical machines and their related fields (power electronics, electronics), found application in a variety of advanced aviation, particularly in the field of Power Electronics Systems (PES) [5]. The processing of electrical power based on the technologically advanced multi-pulse transducers (converters, inverters) recently became one of the most dynamically developing trends in aviation technology. This is due to the progressive development of the power semiconductor, so that there are new methods for power management of PMS (Power Management System). Therefore, the transducers of electric energy on board of the advanced aircraft as key components of the PES (Power Electronics System) play a key role in the processing methods of DC, including High Voltage Direct Current (HVDC) [6]. Examples of Power Electronics (PE) application used on board of modern aircraft are presented in the table below (Table 1).

In traditional electrical power systems, the concept of high-voltage DC (HVDC) has been known for many years in the context of the transmission of electricity point-to-point. The growing demand for the transmission of large amounts of electricity in modern aircraft, both civilian (A-380, A-350XWB, B-787), and military (F-22 Raptor, JSF F-35) obliged aviation companies to use advanced aircraft electrical systems, consistent with the trend MEA/AEA, high voltage DC (HVDC). Dictated primarily by the fact that HVDC is characterized by many positive properties, it was also planned in further projection of electrical systems of up to 540 V DC (or ± 270 V DC also called HVDC) [7].

The first such feature is the reduction of the electric wire cross-section obtained by reduced current flow when transferring the same power supply, resulting in lower weight, which is extremely important in aerospace applications. In addition, it should be noted that the voltage levels can be increased in conventional power networks to increase the transmitted electric power. Another advantage of HVDC system is the reduction of electricity losses due to the higher voltage level and the ability to use the DC network that eliminates reactive power consumption. For these reasons, DC links are used for long-distance point-to-point traditional electrical networks. Furthermore, due to the reduction of losses of the electricity network used on modern aircraft air conditioning, ECS (Environmental Control System) has a lower demand for thermal

power (heat). A further advantage of using a DC is the weight cut, as electrical light transducers of AC powering converters must be equipped with passive or active filters, i.e. PFC (Power Factor Correctors), and therefore may be supplied by a sinusoidal current input. This is very important, especially in the case of the high-impedance network, which is onboard aircraft [8, 9].

Table 1

An example application of power electronics on board modern aircraft [7]

Category	Application	Techniques/Circuits
Energy storage	Battery safety	Battery management system: flyback converters
	Charging process	Power factor correction, converter, DC-DC converter
Controlling the movement	Actuator	Engine design, motor drive
	Fuel pump	Electric pump, motor drive, power converter
	Controlling the movement	Power transmitter, vector control, torque control
	Chassis	Engine design, motor drive
Environment control system	Ventilation	Inverter
	Lighting	Electronic ballast, LED
	UPS	Inverter, battery charger
	Adjusted power factor	Capacitor switching
Distribution of electric energy in aviation	Drive	Inverter (DC-AC power converter)
	Production of AC	2-level inverter, resonant converters, phase shift converter
	VFCF	Inverter, power factor corrected converter

2. Overview of high voltage HVDC electrical power supply system architecture solutions

In recent years, the aviation industry resigned from the use of traditional 28 V DC voltage and 115 V AC/ 400 Hz power, in exchange using the system of 230 V AC and 270/ 540 V DC. These changes were necessary due to the requirements dictated by increasing demands for electricity, while minimizing the impact of the power lines weight. From the point of view of power management, this trend poses a challenge in terms of design and use of electronic equipment in terms of ELCUs (Electronic Load Control Units), ‘smart contactors’, SPLS (Smart Programmable Loads and Sources) and BCRU (Battery Charge Regulators Units),

intended to provide 28 V DC voltage and recharge onboard battery, permanently connected to the DC network, according to MEA or AEA trend [10]. The figure below (Fig. 1) [11] shows an example of AC-DC converters, built with a transformer and regulator BCRU, which play a key role in the EPS and PES of advanced aircraft.

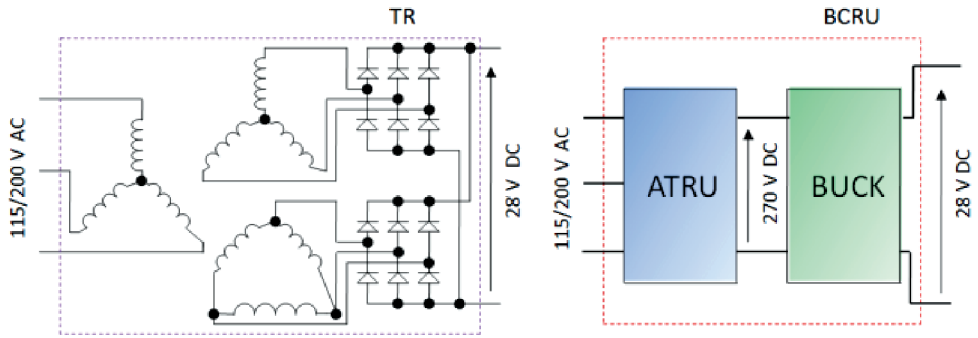


Fig. 1. Example of an advanced technological solution AC-DC converter, used on the Airbus A-380

Electrical Power System (EPS) used on ‘traditional’ airplanes usually comes down to the use of a combination of 115/200 V AC 400 Hz voltage to meet the needs of the high load receivers as well as high power 28 V DC voltage to supply avionic systems, flight control system and other systems powered by DC voltage. However, due to noticeable need for a significant increase in power of on-board power sources and a continuous and dynamic growth in demand for various types of electric power, the adaptation of the advanced systems for producing electric energy of VF (Variable Frequency) requires the use of advanced power supply systems PES (Power Electronics Systems) serving to convert the generator output to a single high voltage transmission and distribution DC system. It should also be mentioned that it is recommended that the voltage of advanced power electronic power systems PES in the range of DC voltage was 270 V, 350 V or even 540 V. Therefore, the use of high voltage in advanced EPS of DC is dictated primarily by advantages, such as: reduced weight, size and energy loss with an increase in the level of power.

Table 2

Example of electricity generation system comparison [8]

		Weight	Performance	Reliability
Constant Frequency System (CFS)	IDG	moderate	lowest	average
	DC-Link	highest	moderate	good
	Cycloconverter	high	moderate	good
VFS		lowest	highest	best
HVDC (270V DC)	Brushless DC Generator	low	moderate	good
	Switched Reluctance Generator (SRG)	high	moderate	good

The above table (Table 2) shows the location of the high voltage 270 V DC system (its benefits) in the context of the currently existing types of electrical power generation systems in today's technologically advanced civil (Airbus, Boeing) and military aircraft (Lockheed Martin) [12, 13].

2.1. Architecture of high voltage 540 V DC (± 270 V DC) power system

Modern aircraft with a high degree of advancement, both civilian Airbus (A-380, A-350XWB) and Boeing (B-787), as well as military Lockheed Martin (F-22 Raptor, the JSF F-35), in line with MEA/AEA have electrical power systems, which, by supplying high voltage DC buses, divide and distribute high-quality electrical power on board modern aircraft. These buses are used to power the DC loads of different purposes, including actuators: electromechanical EMA (Electromechanical Actuation) and electro-hydraulic actuators EHA (Electrohydraulic Actuation). Nowadays, with the developing trend of MEA/AEA and EPS/PES, high-voltage 540 V DC (± 270 V DC) systems are considered as standard. The first generation system applies to 270 V DC, while 540 V DC system is a prospective standard. The most advanced aircraft are characterized by a variety of EPS architecture solutions in the range of HVDC, including ± 270 V DC (2 phases to ground), 270 V DC (1 phase to ground), ± 135 V DC (2 phase to ground) and ± 135 V DC (2 phases without ground) [14].

2.2. Architecture of high voltage 350 V DC power system

The architecture of this kind in the field of high-voltage 350 V DC applies to advanced MEE (More Electric Engine) technology. The engine uses MEE venting fan in order to protect the engine against the phenomenon of icing, as shown in the figure below (Fig. 2).

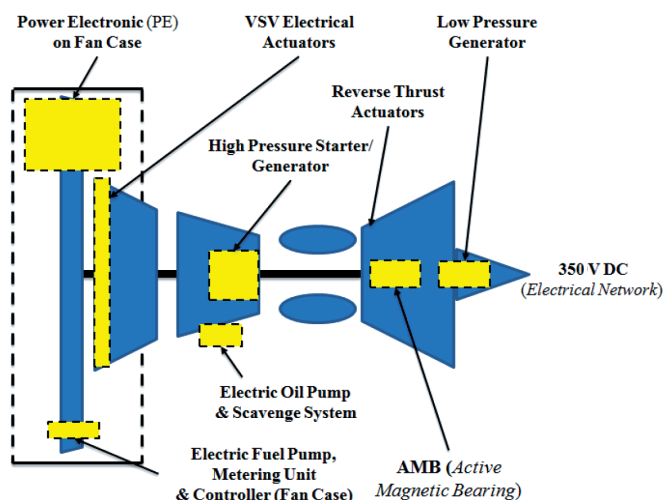


Fig. 2. Arrangement of the basic components of MEE engine Trent 500 [10]

One of these components of the upgraded Trent 500 plus engine, made in the MEE technology, is a bleed air fan used to protect the engine against the phenomenon of icing. The key components of the Trent 500 Rolls-Royce engine are: HPSG (High Pressure Starter/Generator) that provides power of 150 kVA (Permanent Magnet), PEM (Power Electronics Module) providing 350 V DC voltage to the engine and ME (more-electric) components of aircraft, electric fuel pumps, electric motors of VSV (Variable Stator Vanes) and other items, as shown in the Fig. 3.

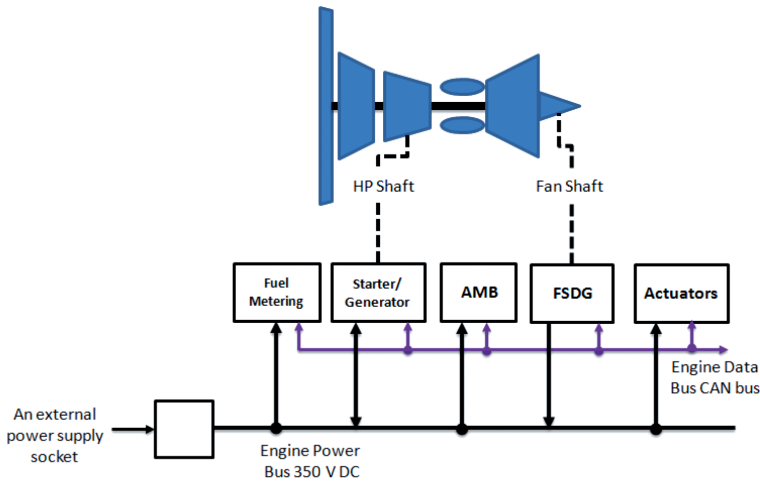


Fig. 3. Main components of the electric MEE engine – Trent 500 Rolls-Royce [10]

In the context of the EPS architecture analysis in the range of high voltage of 350 V DC, the most important component is the electric bus with voltage of 350V DC. On the other hand, starter/generator mounted on the HPSG shaft (High Pressure Starter/Generator), used to start the engine, is powered by 350 V DC from on-board batteries or an external power source. After starting the engine, this unit provides a voltage of 350 V DC to engine bus through PEM (Power Electronics Module) to power subsystems, such as: fuel dosing, AMB (Active Magnetic Bearing) and actuators, which are connected to the data exchange CAN bus (Controller Area Network bus). It should also be noted that in the case of a running engine, the generator operates as a FSDG (Fan Drive Shaft Generator), which also becomes the source of the 350 V DC voltage.

3. Analysis of HVDC electrical power system architecture in line with the MEA trend

The development of current electrical power systems (EPS) in generating, switching and the security of electrical power followed with the development of technological progress in this field. These innovative solutions have an impact on the traditional powering systems that have existed for many years, probably since World War II. These changes have resulted in

the availability of new technologies and equipment, which in turn made advanced concepts of the systems credible, or provided resources for advanced concepts of systems, such as MEA/AEA, EPS/PES, HVDC, etc.

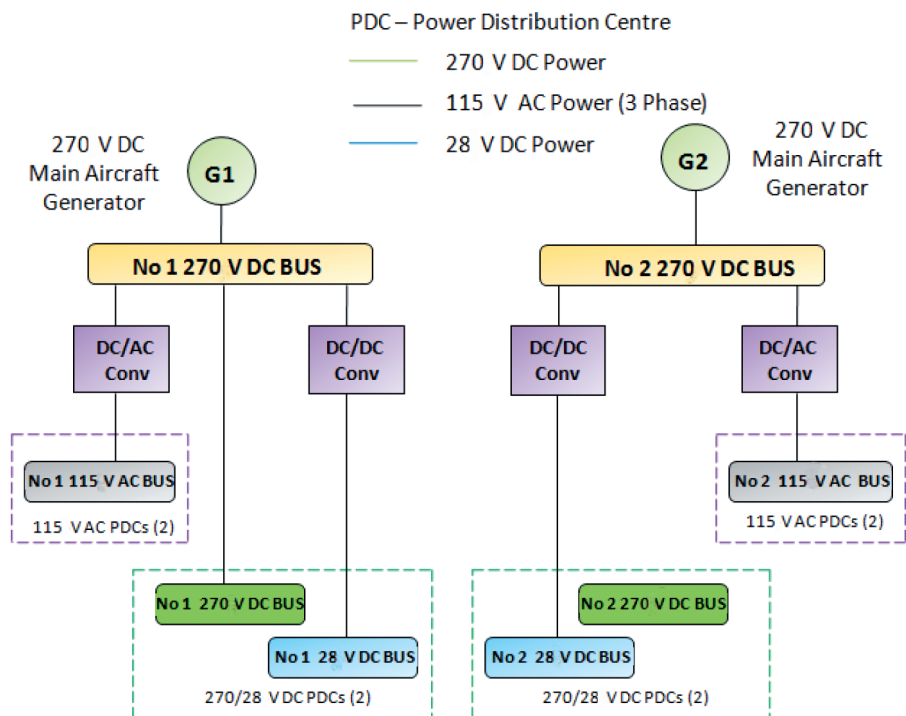


Fig. 4. A simplified EPS system diagram of military aircraft F-22 [12]

Innovative concepts of electrical power system EPS include the following key elements: ELMS (electrical load management system), VSCF (variable speed constant frequency) – Cycloconverter, 270 V DC systems and the MEA [15]. Analyzing the 270 V DC system architecture for a high-voltage HVDC, it should be noted that the system of 270 V DC is used not only as power supply for certain components of an EPS (civilian aircraft), but also it is used as a main power source for advanced military aircraft (F-22 Raptor, the JSF F-35).

Fig. 4 shows a diagram of simplified EPS system diagram of military aircraft F-22 Raptor. US Air Force aircrafts, using 270 V DC EPS in the range of HVDC are: F-22 Raptor and F-35 Lightning II from Lockheed Martin company, which utilize 270 V DC system as the main power system. Application of 270 V DC system is an extrapolation of circumstances to depart the 28 V DC system to the 115 V AC system, namely: reducing the size of the current wires thus minimizing the weight, voltage drop and power dissipation. There are also several disadvantages associated with the usage of the 270 V DC of high voltage HVDC system, which could include: high cost, the usage by the technical staff, in the field of air services, of traditional 28 V DC and 115 V AC voltage, and that the use of higher voltages

extracts greater reliance on techniques and implementation methods of isolation, to avoid power interruption. For this reason, the US military has done a lot of projects, development programs and demonstration. Some of them were designed for greater use of electricity on board of combat aircraft, possibly to replace conventional energy obtainable from secondary sources and hydraulic actuators, or at least to substantially increase them. The determination of these changes is more in line with the trend of More Electric Aircraft (MEA), and therefore may lead to a much larger, if not total use of electrical power in aircraft electrical systems. In addition, the use of HVDC systems in military aircraft poses a threat in the context of the increased possibility of a fire phenomenon, resulting from damage to the aircraft, made of composite materials in the form of carbon (carbon-fiber) during combat operations. In addition, care should be taken to reduce the phenomenon of sparking at high altitudes or in difficult conditions (humidity, salinity, etc.) in tropical and marine environments. It should also be noted that there is also a potential mortal danger to the technical staff during service. Therefore, all these factors must be taken into account during the design stage and the production of advanced aircraft.

4. Simulation of rectifying systems used in aircraft in compliance with ‘More Electric Aircraft’ concept

The below figure (Fig. 5) shows an ATRU (Auto-Transformer Rectifier Unit), which was used, among others, on the Boeing B-787 Dreamliner. It consists of a source of electrical energy in the form of a 230 V AC VF bus, ATU (Auto Transformer Unit) processing voltage from source into 4 voltage groups of 3 phase shifted in phase with each other by 15 degrees, a 24-pulse converter, consisting of four 6-pulse transducers and the system load in the form of resistance [16, 17].

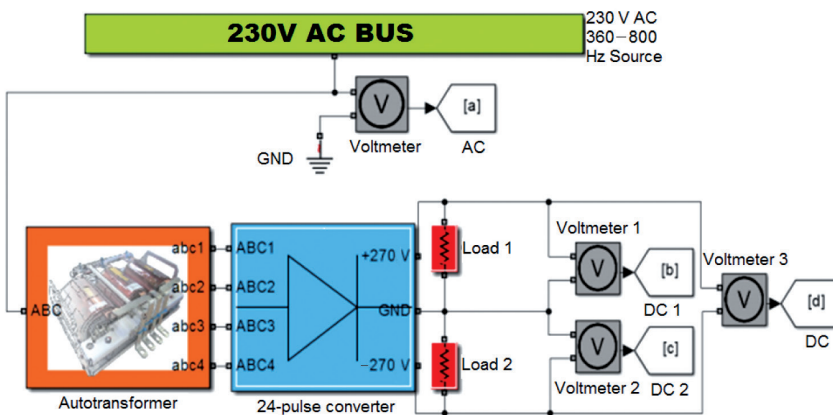


Fig. 5. Block diagram of the auto-transformer rectifier ATRU HVDC ± 270 V DC in the Simulink

The measuring system consists of 4 voltmeters measuring voltage of power source and voltage of output channels: +270 V, -270 V and 540 V, as shown on each graph (Fig. 6–9).

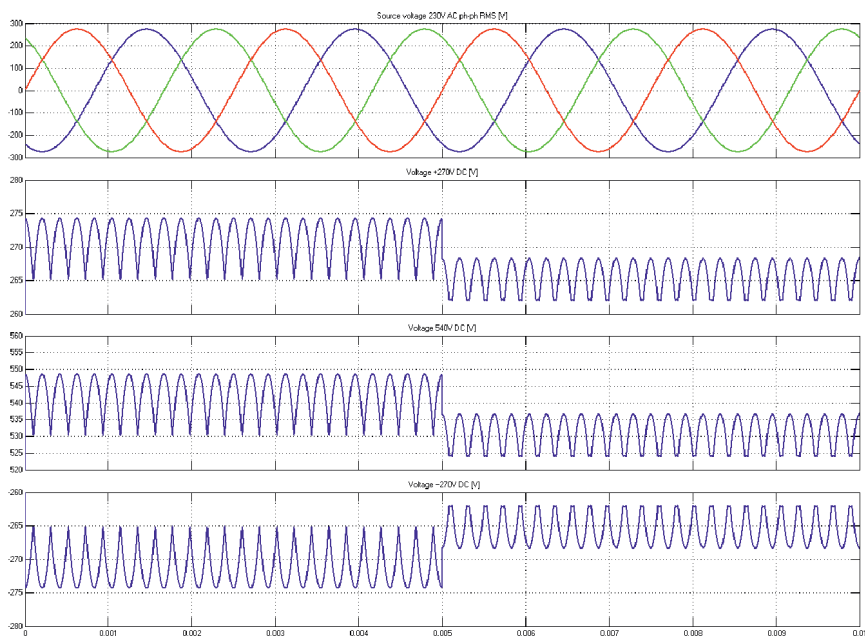


Fig. 6. Chart of source 230 V AC voltage, and output voltages of ATRU (± 270 V DC, 540 V DC)
 $f = 400$ Hz (10 kVA load added in 0.005 s) in the Simulink

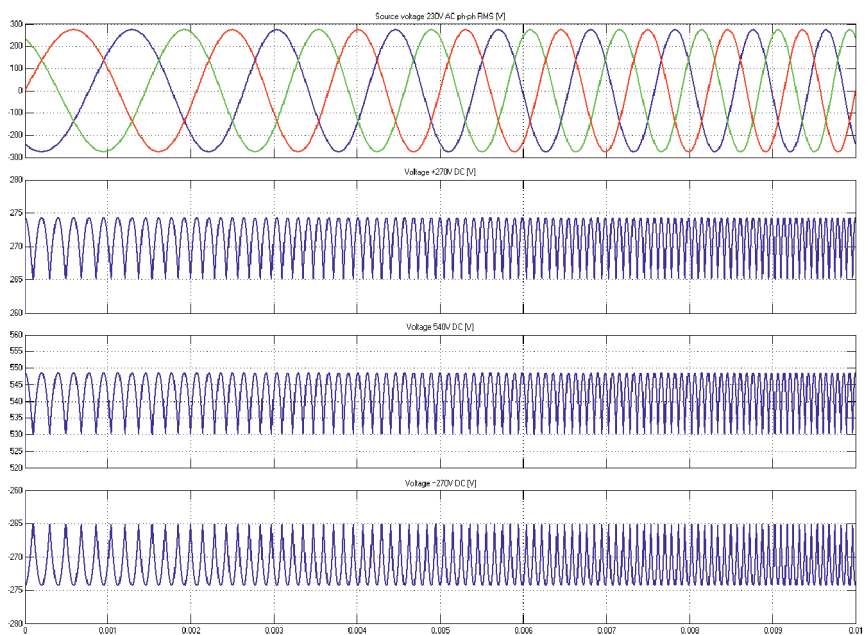


Fig. 7. Graph of source 230 V AC voltage, and output voltages of ATRU (± 270 V DC, 540 V DC)
 $f = 400-800$ Hz in the Simulink

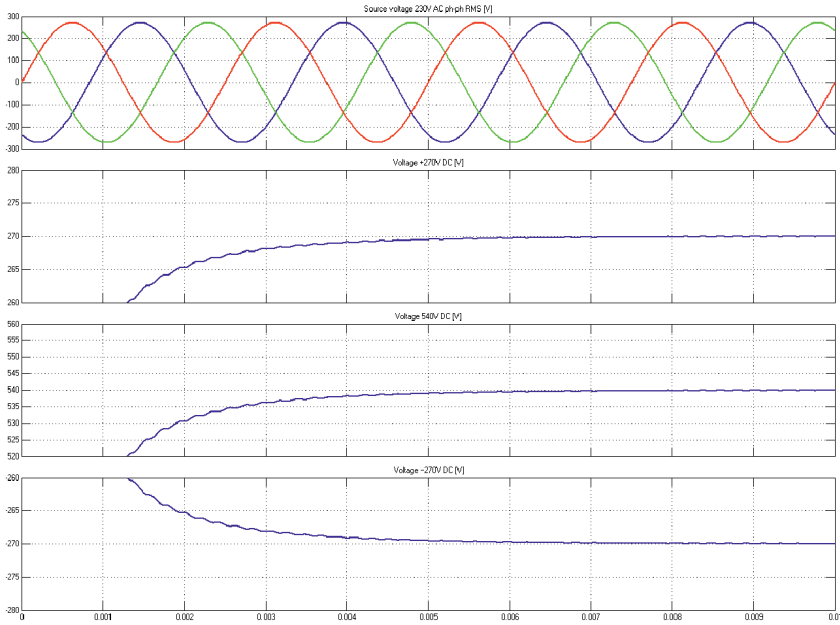


Fig. 8. Chart of source 230 V AC voltage and output ATRU voltages (± 270 V DC, 540 V DC) after adding a capacitance in the Simulink

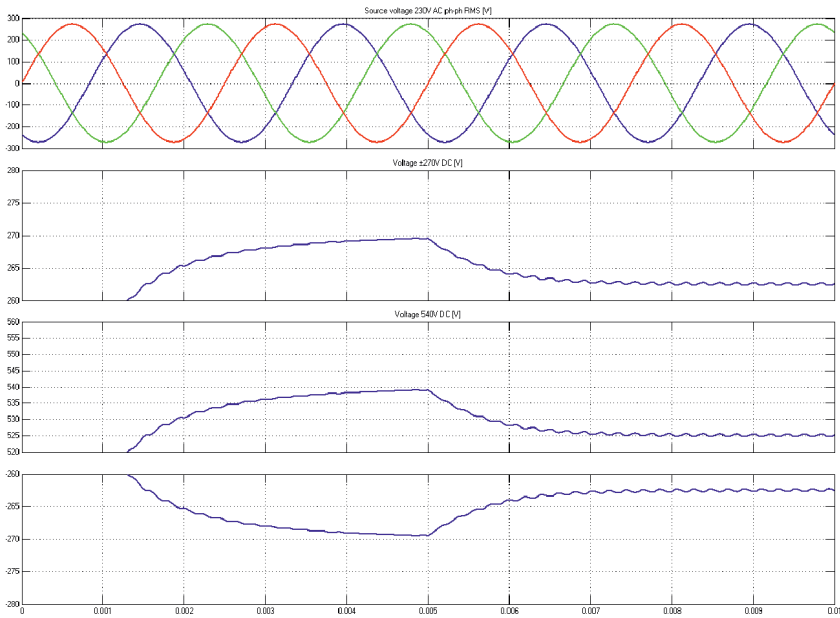


Fig. 9. Chart of source 230 V AC 400 Hz voltage and stabilized output ATRU voltages (± 270 V DC, 540 V DC) with load added in 0.005 s in the Simulink

The three-phase AC source voltage is first processed by the autotransformer to 4 groups of the AC voltage phase-shifted relative to each other at 15 degrees. Each group of the AC voltage goes to one of the four 6-pulse converters, in which the AC voltage is converted into a DC voltage. 6-pulse converters are connected in parallel to form an advanced 24-pulse converter. This solution allows for a significant reduction in output ripple voltage, which in turn feeds the individual instruments and actuators.

The voltage supplied to ATRU is 230 V AC variable frequency in the range of 360–800 Hz, depending on the speed of the motors driving AC alternators. Assuming that the nominal AC frequency is 400 Hz, normal operation of the EPS system was simulated. In the graph (Fig. 6), it can be observed that at this frequency output ± 270 V DC voltage ripple is approx. 9 V (ripple factor approx. 3.3%), while for 540 V DC output voltage ripple is approx. 18 V (ripple factor approx. 3.3%). In the 0.005 s of simulation, there was a 10 kVA load connected to the system. The voltage of all channels dropped by 1.85%.

The operation of the system with increasing AC frequency: from 400 Hz to 800 Hz, was also simulated (Fig. 7). After analyzing the graphs, it can be seen that, despite changes in the frequency, the output voltage is maintained at the nominal values.

The graphs (Fig. 8 and Fig. 9) show working of the system after adding a capacitance. As can be observed, the electrical inertia of the system increased, which allowed to maintain much more precise voltage levels with very small ripples. Also, after adding a load to the system, output voltage value dropped by 2.8%.

5. Summary and conclusions

Based on our review of the literature, the general analysis and examples of ATRU of HVDC ± 270 V DC simulations in the Simulink, it can be assumed that the innovative technological solutions of the HVDC system architecture in the field of high voltage 540 V DC (± 270 V DC) and 350 V DC, used on advanced aircraft (Airbus, Boeing, Lockheed Martin), have the ability to standardize the future aerospace applications. The conducted simulations of selected components of HVDC (+270 V, -270 V and the voltage 540 V) system based on ATRU showed that despite the analysis for different frequencies (from 400 to 800 Hz), the output voltage of HVDC was maintained at nominal values with small ripple level. However, interestingly, a suitable capacitance at the output causes a much smoother voltage level. Adding a load to the system appears in decreased output voltage due to the source internal resistance. It means that this system needs a voltage regulator to keep the voltage at the same level regardless of connected loads. It should also be noted that the analyzed autotransformer rectifier ATRU is characterized by a high density of electrical power, it is designated for transformation of three-phase, variable frequency voltage (230 V AC VF) or three-phase voltage with a fixed frequency (115 V AC 400 Hz) at the input. Its task is to transform to the dual output voltage of ± 270 V DC (i.e. the differential voltage of 540 V DC). Additionally, ATRU converts electrical power of HVDC from the source, using the unregulated AC-DC converters during the process of switching voltage of the autotransformer. Summarizing the above, it should be mentioned that the implementation of the system architecture of the HVDC power supply of the 540 V (± 270 V DC), and 350 V DC voltages plays a key role in the most advanced aircraft in accordance with the current and future trend of the MEA/ MEE and AEA and more AEA.

References

- [1] Setlak L., Ruda E., *Review, Analysis and Simulation of Advanced Technology Solutions in Power Electronics Systems (PES) of More Electric Aircraft*, World Academy of Science, Engineering and Technology, vol. 9 (10), 2015.
- [2] Skvarenina T.L., *The power electronics handbook*, CRC Press LLC, 2002.
- [3] Moir I., Seabridge A., *Design and Development of Aircraft Systems*, Second Edition, John Wiley & Sons, Ltd, 2013.
- [4] Setlak L., Ruda E., *Przegląd, analiza i symulacja wybranych komponentów elektroenergetycznego systemu zasilania EPS samolotu zgodnych z trendem samolotu zelektryfikowanego MEA*, Instytut Napędów i Maszyn Elektrycznych KOMEL, Zeszyty problemowe ZP-ME nr 3/2015 (107), Katowice 2015, 139–144.
- [5] Ronkowski M., Michna M., Kostro G., Kutt F., *Maszyny elektryczne wokół nas*, Politechnika Gdańska 2009/2010.
- [6] Editors Abu-Rub Haitham, Malinowski Mariusz, Al-Haddad K., *Power Electronics for Renewable Energy Systems, Transportation, and Industrial Applications*, First Edition, John Wiley & Sons Ltd., 2014.
- [7] Mohan N., Underland T.M., Robbins W.P., *Power Electronics Converters, Application, and Design*, Book, John Wiley & Sons, 1989.
- [8] Chen J., *Study of 270VDC System Application*, MSc. Thesis, Cranfield University, 2009–2010.
- [9] Guida B., *Modelling, control and supervision strategies for aeronautical electrical networks*, PhD Thesis, Universit di Napoli, 2012.
- [10] Moir I., Seabridge A., *Aircraft Systems: Mechanical, Electrical, and Avionics Subsystems Integration*, John Wiley & Sons, 3rd Edition, 2008.
- [11] Langlois O., Foch E., Roboam X., Piquet H., *From the More Electric Aircraft to the All Electric Aircraft. State of the Art & Prospective*, Presentation, EEA 2004.
- [12] Moir I., Seabridge A., *Military Avionics Systems*, John Wiley & Sons, Ltd, 2006.
- [13] Lockheed M., *Electrical Power Systems (Poland Block 52)*, Customer Training, Lockheed Martin, Fort Worth 2006.
- [14] Lucken A., Brombach J., Schulz D., *Design and protection of high voltage DC on-board grid with integrated fuel cell system on Toward Optimized Electrical Networks electric aircraft*, Electrical Systems for Aircraft Railway and Ship Propulsion (ESARS), Oct. 2010, 1–6.
- [15] Forsyth A., Abdel-Hafez A., *A Review of More-Electric Aircraft*, 13th International Conference on Aerospace Sciences & Aviation Technology, ASAT – 13, Cairo 2009.
- [16] Gong G., Drogenik U., Kolar J.W., *12-Pulse Rectifier for More Electric Aircraft Applications*, ETH Zurich, Power Electronic Systems Laboratory, ICIT 2003.
- [17] Lu Lihan, Sun Jing, Dong Shiliang, Zhou Yuanjun, *Stability Analysis of More Electric Aircraft Power System with 18-Pulse ATRU Feeding Constant Power Loads*, International Journal of Automation and Power Engineering (IJAPE), Vol. 2, Issue 4, May 2013.

VASYL I. HUDYM*, PIOTR DROZDOWSKI**, ANDRZEJ POSTOLIUK***,
DOMINIK MAMCARZ**

MATHEMATICAL MODEL OF THE SIX ELECTRODE PULSE CURRENT ELECTRIC ARC FURNACES

MODEL MATEMATYCZNY SZEŚCIOELEKTRODOWEGO PIECA ŁUKOWEGO PRĄDU IMPULSOWEGO

Abstract

In the article based on the fundamental laws of physics and mathematics has been formulated mathematical model to analyze the electromagnetic waveforms in electrical power systems with non-linear loads, such as arc furnaces.

Keywords: six-electrode electric arc furnace

Streszczenie

W artykule na podstawie fundamentalnych praw fizyki i matematyki został sformułowany model matematyczny do analizy przebiegów elektromagnetycznych w układach zasilania energią elektryczną odbiorów nieliniowych, np. pieców łukowych.

Słowa kluczowe: sześcieelektrodowy elektryczny piec łukowy

* Prof. D.Sc. Ph.D. Eng. Vasyl I. Hudym, Institute of Electromechanical Energy Conversion, Faculty of Electrical and Computer Engineering, Cracow University of Technology, Lviv State University of Life Safety.

** D.Sc. Ph.D. Eng. Piotr Drozdowski prof. PK, M.Sc. Eng. Dominik Mamcarz, Institute of Electromechanical Energy Conversion, Faculty of Electrical and Computer Engineering, Cracow University of Technology.

*** M.Sc. Eng. Andrzej Postoliuk, Engineer of the first category of work states calculation sector in Department of Western Electrical Power Networks, Lviv, Ukraine.

1. Introduction

Modern electrical networks containing power lines with different voltages form rigid, hierarchical structures that make experimental research on their electrical states difficult and extremely dangerous. The same is true for power supply systems for large loads that contain magnetic core machines, machines in which commutation occurs, electrical power converters, and electromagnetic state controllers for converters. The complexity of electromagnetic connections between the branches of the circuits of such systems makes it obvious that writing a system of equations of the electromagnetic state is very difficult in terms of assessing electromagnetic waveforms using mathematical modeling [2, 3]. Usually, analysis of steady states in electrical systems, in which electromagnetic relationships are not taken into account, the system of equations is written using the node-voltage method. This helps to greatly reduce the system of equations compared to the traditional methods or even, frequently, the mesh current method [1, 2]. However, analysis of transient electromagnetic processes in the power supply systems for various loads, in which the electromagnetic relationships between the separate branches or parts of the circuit are very important, requires the system of equations to be written in contour coordinates (contour currents and contour magnetic fluxes) [3, 4]. Due to the limited capability of analytical methods for solving large systems of equations and the availability of modern computers, effective software, and numerical methods, the easiest way to solve systems of differential equations is through numerical methods [4–6].

Another important property of the electromagnetic circuits in modern power supply systems is the significant non-linearity of the characteristics of their individual components. This non-linearity leads to errors and instabilities in calculations that concern systems of differential equations. In such a case, care should be taken to select an appropriate numerical method for solving a rigid system of equations [4–6].

Mathematical experiments have to be repeated multiple times during research in order to obtain the results required for a given task, which is why it is especially important to use automated software that is based on adequate mathematical models of the objects in question. If such software is unavailable, it needs to be developed and adapted to modern software and technical means.

Impact assessments of electric arc furnaces (EAFs) on power supply systems indicate that within the last few decades, DC EAFs have begun to compete with three-phase AC EAFs. Compared to three-phase EAFs, power supply systems are much more complicated due to the use of rectifiers, i.e., semiconductive parts with non-linear current–voltage characteristics that lead to current deformations in the power supply system.

Despite the prevalence of DC EAFs over AC EAFs due to the negative effect on power supply systems and the environment, the application of the former is limited by certain factors. The most significant of these are multiple overvoltages that occur as a result of the technical gap related to the high current of the arc. Short technical breaks in operation require DC EAFs to be shut down directly under load using switches, which are installed on the side of the primary coil of the furnace transformer. This leads to overvoltages between the terminals of the switches and parts of the EAF power supply system. The proposed power supply system for an impulse current EAF can terminate the current of the arc during

a technical break by raising the electrodes, after which the furnace shuts down in a no-load state. This helps to practically eliminate overvoltages occurring due to the termination of the no-load current, which in turn helps to considerably extend commutation breaks of the switches, thus improving the operation conditions for the insulation of the primary component of an EAF. However, the working conditions for a given subsystem require extensive research, primarily on quasi-steady states. For a given stage, this research can be done – as an exception – through mathematical modeling. Consequently, an important technological task arises to create an adequate mathematical model of a power supply system for a DC EAF that would enable research on the electromagnetic processes and show differences in them in quasi-steady and commutation states [8–10].

2. Mathematical model of six electrode EAF

Figure 1 shows a diagram of the proposed power supply system for a six-electrode pulse current EAF, in which the arc currents can be terminated by raising the electrodes [10]. The three-phase electric system, by means of an overhead power line, a mains transformer, and a cable line, powers the furnace transformer, in which the secondary coil is connected through a short-distance network and a power module for one-phase AC-DC rectifiers to a group of anode and cathode electrodes (cathode electrodes 1', 2', 3' and anode electrodes 1'', 2'', 3''), located over the feed surface in the furnace chamber.

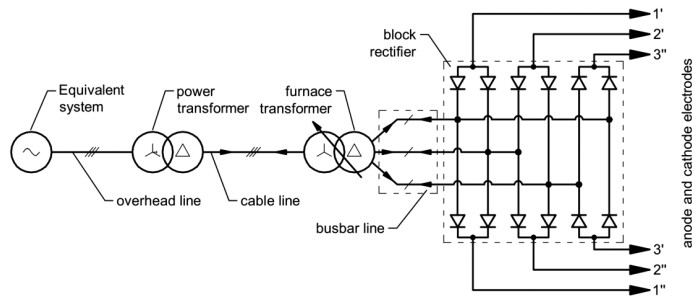


Fig. 1. Schematic of the power supply pulse current EAF

To allow the system of equations of the electromagnetic state to be written, Fig. 2 shows an equivalent circuit, in which the voltage source has a limited power, and the overhead and cable lines are substituted for quadripoles that contain components with linear characteristics. Due to the limited length of the cable lines, the partial capacity and partial conductivity between the cables and between the cables and the frame (screen) are not taken into account. The models of the mains transformer and the furnace transformer divide the magnetic fluxes into the main flux and the leakage flux. The characteristics of non-linear elements i.e., transformers, diodes and electric arc are given in [4, 6, 9, 11].

In the equivalent circuit, the branches with the non-linear components $X_{\mu 1}$ and $X_{\mu 2}$ are the branches of the main magnetic flux routes of the mains transformer and the furnace transformer, whereas the linear components X_{01} and X_{02} are the branches of the magnetic

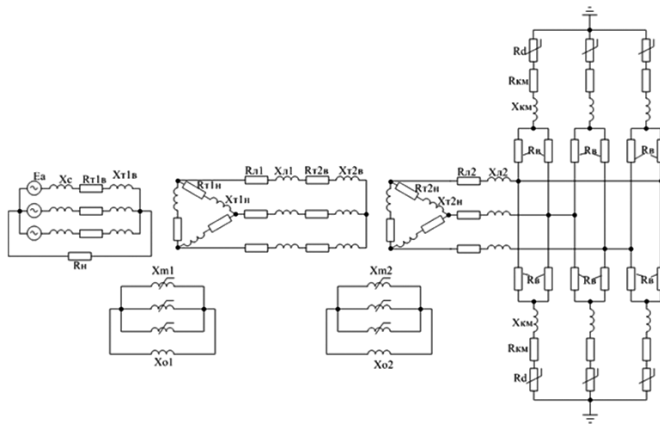


Fig. 2. Equivalent circuit of the power supply pulse current EAF

flux routes outside the magnetic circuit of the transformers. Note that the model must describe the processes in both the magnetic and the electric contours at the same time, as a single electromagnetic process in the power supply system. Due to the complexity and multidimensionality of the equivalent circuit, the system of equations of the electromagnetic state should be created automatically. This can be easily achieved based on matrix and vector mathematical operations. To this end, a graph of the electromagnetic circuit needs to be drawn. Afterwards, the previously designed algorithms should be used to draw the mesh incidence matrix, which in turn will allow for an automatic creation of the system of equations. Fig. 3 shows the graph of the electromagnetic circuit for the equivalent circuit in question (Fig. 2). The dashed lines indicate the chords of the graph (the number of chords corresponds to the number of independent contours). The solid lines indicate the branches of the graph tree.

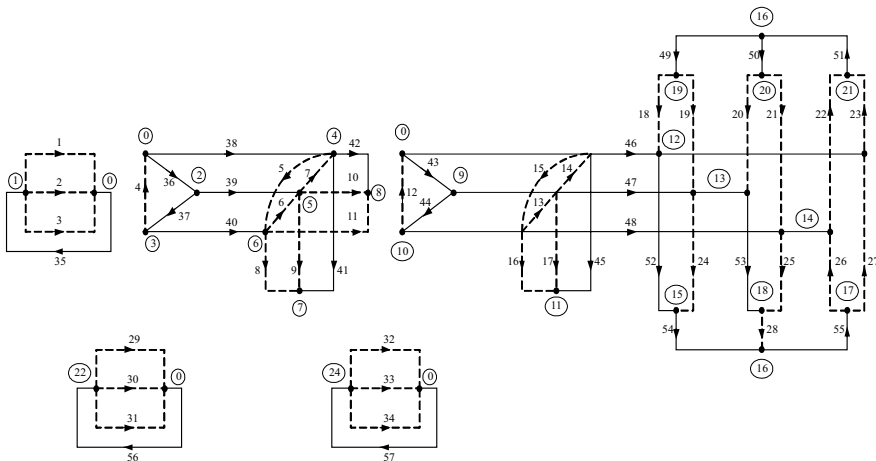


Fig. 3. Graph for electromagnetic circuit shown in Fig. 2

where:

Π, Γ	– topological matrixes electromagnetic circuit graphs of power system,
\mathbf{R}	– diagonal matrix resistance circuits,
M	– static leakage inductance matrix of transformer, inductors and the others branches of equivalent circuit,
$K_{12} = \begin{vmatrix} 0 & W_1^{-1}W_2 \\ W_1 & W_2 \end{vmatrix}$	– winding ratio matrix of delivery and furnace transformers,
W_1, W_2	– matrix of the number of turns primary and secondary windings of transformer,
R_μ	– diagonal identity matrix of the dynamic reluctance (referred to the square of the number of turns primary windings of transformers),
$\vec{i}, \vec{\psi}$	– vectors-columns of currents and mutual flux of phases primary windings of transformers,
$\frac{d\vec{i}}{dt}, \frac{d\vec{\psi}}{dt}$	– vectors derivatives by time with current of electrical circuits and mutual flux of magnetic circuits,
\vec{u}_{ne}	– vector of voltage on the nonlinear resistive elements,
\vec{u}_C	– vector of voltage on the capacitors,
\vec{e}	– vector of phase electromotive force,
\mathbf{C}	– capacity matrix of electrical circuits.

The final mathematical model of power network of pulse current EAF writing with taking into account backward differentiation formula, are given [3, 4]:

$$(\vec{d}\bar{y} / dt)_{k+1} = a_0 h^{-1} \bar{y}_{k+1} + h^{-1} \sum_{s=1}^p a_s \bar{y}_{k+1-s} \quad (3)$$

where:

\bar{y}	– integrating function of vector,
a_0, \dots, a_s	– factors of approximating series, which define a matrix given in [3–6],
p	– order of method,
h	– integration step.

Taking into account formula (3) mathematical model of the power supply (given by equations 1 and 2) will be writing in the differential form [4, 6].

$$\begin{aligned} & \Pi \cdot \begin{pmatrix} \vec{i}_{k+1} \\ \vec{\psi}_{k+1} \end{pmatrix} = 0; \\ & \Gamma \cdot \begin{vmatrix} \mathbf{R} + a_0 h^{-1} \mathbf{M}_{k+1} & a_0 h^{-1} \mathbf{K}_{12} \\ a_0 h^{-1} \mathbf{K}_{21} & -a_0 h^{-1} \mathbf{R}_{\mu 12} \end{vmatrix} \times \begin{pmatrix} \vec{i}_{k+1} \\ \vec{\psi}_{k+1} \end{pmatrix} + \\ & + \Gamma \left(h^{-1} \cdot \begin{vmatrix} \mathbf{M}_{k+1} & \mathbf{K}_{12} \\ \mathbf{K}_{21} & -\mathbf{R}_{\mu k+1} \end{vmatrix} \times \sum_{s=1}^p a_s \begin{pmatrix} \vec{i}_{k+1-s} \\ \vec{\psi}_{k+1-s} \end{pmatrix} + \begin{pmatrix} \vec{u}_{ne k+1} + \vec{u}_{C k+1} - \vec{e}_{k+1} \\ 0 \end{pmatrix} \right) = 0; \\ & a_0 h^{-1} \mathbf{C}_{k+1} \vec{u}_{C k+1} + h^{-1} \mathbf{C}_{k+1} \sum_{s=1}^p a_s \vec{u}_{C k+1-s} = \vec{i}_{k+1}. \end{aligned} \quad (4)$$

Voltage of capacitor in $(k + 1)$ step is defined as:

$$\vec{u}_{Ck+1} = a_0^{-1} h \mathbf{C}_{k+1}^{-1} \vec{i}_{k+1} - a_0^{-1} \sum_{s=1}^p a_s \vec{u}_{Ck+1-s} \quad (5)$$

which substitute to the second equations of equations (4) and get:

$$\begin{aligned} & \mathbf{\Pi} \cdot \begin{pmatrix} \vec{i}_{k+1} \\ \vec{\Psi}_{k+1} \end{pmatrix} = \mathbf{0}; \\ & \mathbf{\Gamma} \cdot \begin{pmatrix} \mathbf{R} + a_0 h^{-1} \mathbf{M}_{k+1} + a_0^{-1} h \mathbf{C}_{k+1}^{-1} & a_0 h^{-1} \mathbf{K}_{12} \\ a_0 h^{-1} \mathbf{K}_{21} & -a_0 h^{-1} \mathbf{R}_{\mu 12} \end{pmatrix} \times \begin{pmatrix} \vec{i}_{k+1} \\ \vec{\Psi}_{k+1} \end{pmatrix} + \\ & + \mathbf{\Gamma} \left(h^{-1} \cdot \begin{pmatrix} \mathbf{M}_{k+1} & \mathbf{K}_{12} \\ \mathbf{K}_{21} & -\mathbf{R}_{\mu k+1} \end{pmatrix} \cdot \sum_{s=1}^p a_s \begin{pmatrix} \vec{i}_{k+1-s} \\ \vec{\Psi}_{k+1-s} \end{pmatrix} + \begin{pmatrix} \vec{u}_{ne k+1} + a_0^{-1} \sum_{s=1}^p a_s \vec{u}_{Ck+1-s} - \vec{e}_{k+1} \\ 0 \end{pmatrix} \right) = \mathbf{0}; \end{aligned} \quad (6)$$

After spreading system of nonlinear equations (5) in a limited Taylor series [4], we get a mathematical model described by the currents and mutual magnetic fluxes of primary windings of transformers.

$$\begin{aligned} & \mathbf{\Pi} \cdot \begin{pmatrix} \Delta \vec{i}_{k+1}^{(l)} \\ \Delta \vec{\Psi}_{k+1}^{(l)} \end{pmatrix} = \mathbf{\Pi} \cdot \begin{pmatrix} \vec{i}_{k+1}^{(l)} \\ \vec{\Psi}_{k+1}^{(l)} \end{pmatrix}; \\ & \mathbf{\Gamma} \cdot \begin{pmatrix} \mathbf{R}_{k+1}^{(l)} + a_0 h^{-1} \mathbf{M}_{k+1}^{(l)} + a_0^{-1} h \mathbf{C}_{k+1}^{-1} & a_0 h^{-1} \mathbf{K}_{12} \\ a_0 h^{-1} \mathbf{K}_{21} & -a_0 h^{-1} \mathbf{R}_{\mu k+1}^{(l)} \end{pmatrix} \times \begin{pmatrix} \Delta \vec{i}_{k+1}^{(l)} \\ \Delta \vec{\Psi}_{k+1}^{(l)} \end{pmatrix} = \\ & \mathbf{\Gamma} \cdot \begin{pmatrix} \mathbf{R}_{k+1}^{(l)} + a_0 h^{-1} \mathbf{M}_{k+1}^{(l)} + a_0^{-1} h \mathbf{C}_{k+1}^{-1} & a_0 h^{-1} \mathbf{K}_{12} \\ a_0 h^{-1} \mathbf{K}_{21} & -a_0 h^{-1} \mathbf{R}_{\mu k+1}^{(l)} \end{pmatrix} \times \begin{pmatrix} \vec{i}_{k+1}^{(l)} \\ \vec{\Psi}_{k+1}^{(l)} \end{pmatrix} + \\ & + \mathbf{\Gamma} \left(h^{-1} \cdot \begin{pmatrix} \mathbf{M}_{k+1}^{(l)} & \mathbf{K}_{12} \\ \mathbf{K}_{21} & -\mathbf{R}_{\mu k+1}^{(l)} \end{pmatrix} \cdot \sum_{s=1}^p a_s \begin{pmatrix} \vec{i}_{k+1-s}^{(l)} \\ \vec{\Psi}_{k+1-s}^{(l)} \end{pmatrix} + \begin{pmatrix} \vec{u}_{ne k+1-s}^{(l)} + a_0^{-1} \sum_{s=1}^p a_s \vec{u}_{Ck+1-s}^{(l)} - \vec{e}_{k+1}^{(l)} \\ 0 \end{pmatrix} \right) = \mathbf{0}; \\ & \begin{pmatrix} \vec{i}_{k+1}^{(l+1)} \\ \vec{\Psi}_{k+1}^{(l+1)} \end{pmatrix} = \begin{pmatrix} \vec{i}_{k+1}^{(l)} \\ \vec{\Psi}_{k+1}^{(l)} \end{pmatrix} - \begin{pmatrix} \Delta \vec{i}_{k+1}^{(l)} \\ \Delta \vec{\Psi}_{k+1}^{(l)} \end{pmatrix} \end{aligned} \quad (7)$$

In order to write a mathematical model in the contour coordinates (contour currents and contour mutual flux) the second equation of the model 6 will be replaced by vector of branch currents and mutual fluxes by the contour coordinates and their vectors use relationship:

$$\begin{aligned} & \begin{pmatrix} \vec{i}_{k+1}^{(l)} \\ \vec{\Psi}_{k+1}^{(l)} \end{pmatrix} = \mathbf{\Gamma}_l \begin{pmatrix} \vec{i}_{K,k+1}^{(l)} \\ \vec{\Psi}_{K,k+1}^{(l)} \end{pmatrix}; \\ & \begin{pmatrix} \Delta \vec{i}_{k+1}^{(l)} \\ \Delta \vec{\Psi}_{k+1}^{(l)} \end{pmatrix} = \mathbf{\Gamma}_l \begin{pmatrix} \Delta \vec{i}_{K,k+1}^{(l)} \\ \Delta \vec{\Psi}_{K,k+1}^{(l)} \end{pmatrix} \end{aligned} \quad (8)$$

After substitution we get:

$$\Gamma \cdot \left\| \begin{array}{cc} \mathbf{R}_{k+1}^{(l)} + a_0 h^{-1} \mathbf{M}_{k+1}^{(l)} + a_0^{-1} h \mathbf{C}_{k+1}^{-1} & a_0 h^{-1} \mathbf{K}_{12} \\ a_0 h^{-1} \mathbf{K}_{21} & -a_0 h^{-1} \mathbf{R}_{\mu k+1}^{(l)} \end{array} \right\| \times \Gamma_t \left(\begin{array}{c} \Delta \bar{i}_{k+1}^{(l)} \\ \Delta \bar{\Psi}_{k+1}^{(l)} \end{array} \right) =$$

$$\Gamma \cdot \left\| \begin{array}{cc} \mathbf{R}_{k+1}^{(l)} + a_0 h^{-1} \mathbf{M}_{k+1}^{(l)} + a_0^{-1} h \mathbf{C}_{k+1}^{-1} & a_0 h^{-1} \mathbf{K}_{12} \\ a_0 h^{-1} \mathbf{K}_{21} & -a_0 h^{-1} \mathbf{R}_{\mu k+1}^{(l)} \end{array} \right\| \times \Gamma_t \left(\begin{array}{c} \bar{i}_{k+1}^{(l)} \\ \bar{\Psi}_{k+1}^{(l)} \end{array} \right) + \quad (9)$$

$$+ \Gamma \left(h^{-1} \cdot \left\| \begin{array}{cc} \mathbf{M}_{k+1}^{(l)} & \mathbf{K}_{12} \\ \mathbf{K}_{21} & -\mathbf{R}_{\mu k+1}^{(l)} \end{array} \right\| \Gamma_t \cdot \sum_{s=1}^p a_s \left(\begin{array}{c} \bar{i}_{k+1-s}^{(l)} \\ \bar{\Psi}_{k+1-s}^{(l)} \end{array} \right) + \left(\begin{array}{c} \bar{u}_{ne k+1-s}^{(l)} + a_0^{-1} \sum_{s=1}^p a_s \bar{u}_{C k+1-s}^{(l)} - \bar{e}_{k+1}^{(l)} \\ 0 \end{array} \right) \right) = 0;$$

$$\left(\begin{array}{c} \bar{i}_{K,k+1}^{(l+1)} \\ \bar{\Psi}_{K,k+1}^{(l+1)} \end{array} \right) = \left(\begin{array}{c} \bar{i}_{K,k+1}^{(l)} \\ \bar{\Psi}_{kK,k+1}^{(l)} \end{array} \right) - \left(\begin{array}{c} \Delta \bar{i}_{K,k+1}^{(l)} \\ \Delta \bar{\Psi}_{K,k+1}^{(l)} \end{array} \right) \quad (10)$$

where:

- $\mathbf{R}_{k+1}^{(l)} + a_0 h^{-1} \mathbf{M}_{k+1}^{(l)} + a_0^{-1} h \mathbf{C}_{k+1}^{-1}; a_0 h^{-1} \mathbf{K}_{21} - a_0 h^{-1} \mathbf{R}_{\mu k+1}^{(l)}$ – elements of Jacobian matrix for the iteration and $(k + 1)$ integration step,
- h – numeric integration step,
- $\mathbf{R}_{k+1}^{(l)}$ – resistance matrix of linear and nonlinear elements of equivalent circuit for iteration and $(k + 1)$ integration step,
- \mathbf{C}_{k+1} – capacity matrix of electrical circuits for $(k + 1)$ integration step,
- $\bar{e}_{k+1}^{(l)}$ – vector of electromotive force of schema branch for the l iteration and $(k + 1)$ integration step,
- $\bar{u}_{C k+1-s}^{(l)}$ – vectors of voltage on the capacitors and mutual flux for l iteration and $(k + 1 - s)$ integration step,
- $\bar{u}_{ne k+1-s}^{(l)}$ – vector of voltage on the nonlinear resistive elements of schema (branch of EAF arcs) for l iteration and $(k + 1 - s)$ integration step,
- $\bar{i}_{K,k+1}^{(l+1)}, \bar{\Psi}_{K,k+1}^{(l+1)}, \bar{i}_{K,k+1}^{(l)}, \bar{\Psi}_{K,k+1}^{(l)}$ – vectors of contours currents and contours mutual magnetic flux of transformers for $(l + 1)$ and l iteration and $(k + 1)$ integration step,
- $\Delta \bar{i}_{K,k+1}^{(l)}, \Delta \bar{\Psi}_{K,k+1}^{(l)}$ – vectors of increments contours currents and contours mutual magnetic flux of transformers for l iteration and $(k + 1)$ integration step,
- $\mathbf{M}_{k+1}^{(l)}$ – matrix of own and mutual inductance of electrical circuit for iteration and $(k + 1)$ integration step.

Currents, mutual magnetic flux and voltage on the capacitors after their calculating for $(l + 1)$ iteration we define by the following formula:

$$\bar{u}_{C,k+1}^{(l+1)} = a_o^{-1} \cdot \left(\mathbf{C}_{k+1}^{(l)} \right)^{-1} \cdot h \cdot \bar{u}_{C,k+1}^{(l+1)} - a_o^{-1} \sum_{s=1}^p a_s \bar{u}_{c,k+1-s}^{(l)} \quad (11)$$

where:

$\vec{i}_C^{(l+1)}$ – vectors of branch currents with capacitors for $(l + 1)$ iteration and $(k + 1)$ integration step.

The mathematical model has been implemented in the form of automated software for the analysis of electromagnetic processes in the instantaneous values of currents, voltages and magnetic fluxes in the programming environment DELPHI [7]. Developed software package based on the minimum input information (connection arrays of electromagnetic circuit graph, parameters of the branch of schema, characteristics of a voltage source and array of magnetic association between the branches of the schema) forming in an automatic cycle of the system of equations. The adequacy of the mathematical model is checked by comparing the instantaneous values of voltage and current of 35 kV power supply system of EAF with a capacity of 100 tons obtained by measurements (Fig. 5a) with simulation results (Fig. 5b).

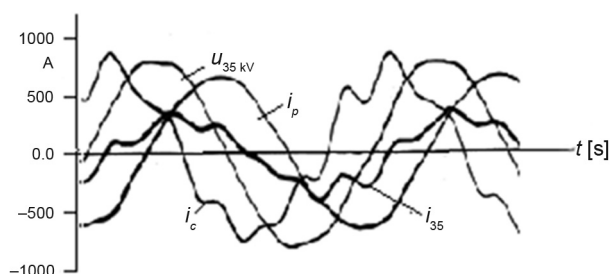


Fig. 5a. Instantaneous values of voltage and current in the power system of EAF (measurement)

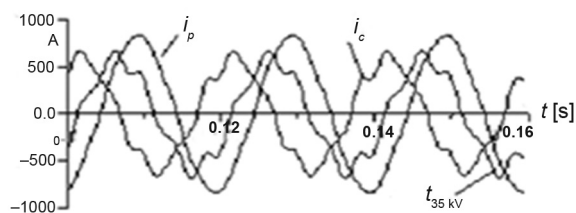


Fig. 5b. Instantaneous values of voltage and current in the power system of EAF (simulation)

From the comparison of the presented results we can see that the characteristic of these processes are very similar, which confirms the correctness of the mathematical model in the quasi steady state. Fig. 6 shows the waveforms of the instantaneous current after switching the filter (series connected capacitor banks with inductor) to the rails 35 kV received by measurement (Fig. 6a) and received in a simulation (Fig. 6b), which shape is similar, that confirms the correctness of the mathematical model in transient state.

The mathematical model was also verified by statistical comparing analysis of the second current harmonic when the EAF melting metal, which also confirms the enough adequacy at the time of melting. It should be noted that the model is useful to simulate the steady state and transient electrical power systems with a large selection of electrical devices (transformers,

inductors, capacitors, cable and overhead lines, harmonic filters, semiconductors and others) and may be used to predict and estimate the various states in the design and as well as during operation such electrical devices. The software package, created based on a mathematical model and implemented in DELPHI environment, equipped with a graphical user interface (GUI) for entering and displaying information and process control of simulation, provides comfort and easiness of use.

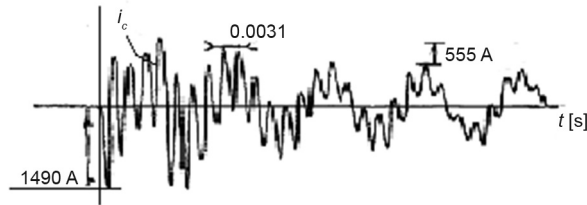


Fig. 6a. Instantaneous value of capacitor current after switching the filter (measurement)

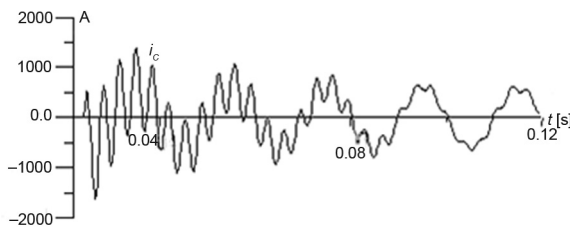


Fig. 6b. Instantaneous value of capacitor current after switching the filter (simulation)

3. Conclusions

1. Based on classical approach control vector formulation for the mathematical model of complex electromagnetic circuits is universal in the sense of creating a state space representation of electromagnetic state for any structure diagrams.
2. The correctness of the mathematical model was confirmed by comparing the results of measurements of real object and mathematical simulation in steady state and transient state for the same schemes with similar electrical parameters.
3. The mathematical model allows to model the electromagnetic processes in complex systems with electrical installations having non-linear characteristics, for the account choice of an effective method of numerical solution of non-linear stiff equation.

References

- [1] Idelčik V.I., *Rasčety i optimizaciâ pežimow električeskih setej i sistem*, M.: Energoatomizdat, 1988, 288.

- [2] Chua L.O., Pen-Min Lin, *Computer-Aided Analysis of Electronic Circuits: Algorithms and Computational Techniques*, Prentice-Hall, Inc., Englewood Cliffs, New York 1975.
- [3] Denisenko G.I., Perhač V.S., Skrypnik A.I., *Algoritm avtomatičeskogo formirovaniâ i rešeniâ uravnenij elektromagnitnogo sostoâniâ dvuhmostovogo kompensacionnogo preobrazovatelâ*, Elektriceskie seti i sistemy, vyp. II, Lvov, Vysšaâ škola 1975, 80–90.
- [4] Perhač V.S., *Matematični zadači elektroenergetiki*, 3-e vidannâ, pererob i dop., Lviv, Viša škola 1989, 464.
- [5] Hall G., Watt J.M., *Modern numerical methods for ordinary differential equations*, Oxford University Press, 1976.
- [6] Perhač V.S., Skrypnik A.I., Gudym V.I., *Cifrovaâ model sistemy elektrosnabženiâ dugovyh staleplavilnyh pečeij i ventilnymi filtrokompensatorami*, Tehn. elektrodinamika, No. 6, 1982, 84–91.
- [7] Kron G., *Tensor analysis of networks*, J. Wiley, New York 1939.
- [8] Gudim V.I., Šelepeten T.M., *Problemi elektromagnitnoj cumisnosti elektropostačalnih sistem z nelinejnim navantažennâm.*, Tehnični visti, Ukrainske inženerne tovaristvo u Lvovi, 1(8), 2(9), 1999, 17–21.
- [9] Gudim V.I., *Rečimi vmikannâ filtriv viših garmonik ctrumiv na osnovi ctatičnih kondensatoriv*, Vestnik priazovskogo gosudarstvennogo universiteta, vyp. 8, 1999, 197–203.
- [10] *Sistema elektropostačannâ dugovoj elektropeči impulsnogo strumu*, Patent No 101412. UA. MPK H02J 3/18. vid. 25.03.2013. Avtori: Gudim V.I., Postolúk A.Â., Drozdovskij P., Karbovniček M.
- [11] *Zagadnienia energetyczne wybranych urzędzeń elektrycznych systemów stalowniczych*, red. Antoni Sawicki, Wydawnictwo Politechniki Częstochowskiej, Częstochowa 2010.

PIOTR BOGUSZ, MARIUSZ KORKOSZ, JAN PROKOP*

ANALYSIS OF ENERGY-SAVING STRUCTURES OF ELECTRIC MACHINES FOR DOMESTIC DRIVE

ANALIZA ENERGOOSZCZĘDNYCH KONSTRUKCJI MASZYN ELEKTRYCZNYCH NAPĘDÓW SPRZĘTU AGD

Abstract

In the paper, alternative technologies of electric machines for domestic appliances were discussed. Nowadays, domestic appliances are used on a mass scale. In most households, there are domestic appliances where electric machines are used. Commutator motors are generally used in domestic appliances due to low costs of production. This is one of their few advantages, whereas to their disadvantages can include low energy efficiency and durability, which is limited by the sliding contact of brush-commutator. In consequence, devices equipped with these motors have low efficiency of energy conversion and are very often unreliable. In recent years, the vacuum cleaner became the receiver of relatively high power from the mains. Therefore, vacuum cleaners were covered by EU regulations. An increase of the energy efficiency of domestic appliances where electric machines are used is possible, among others, by introducing energy-saving technologies in electric machines. They are characterized not only by higher energy efficiency, but also by much longer failure-free operation of domestic appliance drive.

Keywords: domestic drive, commutator motor, brushless motor direct current motor; BLDCM; SRM; mechanical characteristics, waveforms

Streszczenie

W artykule omówiono alternatywne technologie maszyn elektrycznych możliwe do zastosowania w sprzęcie AGD. W większości gospodarstw znajduje się sprzęt AGD, w których są stosowane maszyny elektryczne. Zazwyczaj w sprzęcie AGD stosuje się silniki komutatorowe. Są one stosowane ze względu na niskie koszty produkcji. Jest to ich jedna z nielicznych zalet. Natomiast ich wadą jest niska sprawność energetyczna oraz trwałość ograniczona istnieniem zestyku ślizgowego szczotka-komutator. W konsekwencji urządzenia wyposażone w te silniki charakteryzują się niską sprawnością przetwarzania energii oraz znaczną awaryjnością. Jednym z urządzeń sprzętu AGD który w ostatnich latach stał się odbiornikiem o stosunkowo dużej mocy pobieranej z sieci zasilającej jest odkurzacz. Z tego też powodu stał się on obiektem wprowadzonych obecnie obostrzeń w Unii Europejskiej. Wzrost efektywności energetycznej sprzętu AGD, wykorzystującej maszyny elektryczne możliwy jest m.in. poprzez stosowanie energooszczędnych technologii maszyn elektrycznych. Charakteryzują się one nie tylko wyższą efektywnością energetyczną, ale również zapewniają znacznie dłuższą pracę bezawaryjną układu napędowego sprzętu AGD. W artykule porównano właściwości klasycznego silnika z komutatorem mechanicznym z właściwościami maszyn z komutacją elektroniczną typu BLDC i SRM. Zamieszczono wyniki badań laboratoryjnych autorskiego prototypu silnika reluktancyjnego przełączalnego do napędu agregatu ssącego odkurzacza.

Słowa kluczowe: napęd sprzętu AGD, silniki bezszczotkowe prądu stałego, BLDCM, SRM, charakterystyki mechaniczne, przebiegi czasowe

* Ph.D. Eng. Piotr Bogusz, D.Sc. Ph.D. Eng. Mariusz Korkosz, D.Sc. Ph.D. Eng. Jan Prokop, Department of Electrodynamics and Electrical Machine Systems, Faculty of Electrical and Computer Engineering, Rzeszów University of Technology.

1. Introduction

Domestic appliances, which are used on a mass scale in households, contribute to energy consumption on the European or the global scale. The energy efficiency improvement of electric devices used in domestic appliances has recently been a priority of the EU. An example of such domestic appliance can be a vacuum cleaner, which is used in almost all households. It is estimated that, in Poland alone, there are over 13 million of such devices. Vacuum cleaners were covered by EU regulations, which introduced limitations of input power consumed by them in order to decrease the global energy consumption [1]. Electric motors used in vacuum cleaners consume power, which has significant influence on the overall power consumption. In almost all vacuum cleaners, a classic electric motor with a mechanical commutator, which has many disadvantages like low efficiency or low durability of sliding contact of brush-commutator, is generally used. One of the directions of the development of electric drives used in vacuum cleaners, which can cause a limitation of the global energy consumption, is the application of energy-saving electric machines with electronic commutation.

The aim of the paper is to show test results of the novel drive with an electric motor with electronic commutation and to assess its energy efficiency in comparison with the classic motor with a mechanical commutator [2].

In the paper, a comparison of the properties of a classic electric motor with a mechanical commutator and a motor with an electronic commutation was presented. Results of laboratory tests of the novel switched reluctance motor prototype for a suction unit drive of a vacuum cleaner were presented. Finally, conclusions concerning the benefits of using energy-saving machines in vacuum cleaner drives were presented.

2. Energy-saving structures of electric machines

Brushless electric motors with electronic commutation belong to alternative technologies of electric machines [2–6]. The following structures can be included: brushless motors with permanent magnets (BLPM) and switched reluctance motors (SRM). Brushless machines with permanent magnets can be divided into: brushless DC machines with permanent magnets (BLDC) and synchronous machines with permanent magnets (PMSM). Brushless DC motors with permanent magnets, where the classic commutator is replaced by a dedicated power electronics system with a control system, are preferred in domestic appliances. Both structures of motors differ significantly from each other despite the common thing, which is the electronic commutator. Fig. 1 shows the structures of a classic commutator motor (Fig. 1a), a brushless DC motor with permanent magnets (Fig. 1b) and a switched reluctance motor (Fig. 1c).

The classic structure of a commutator motor has a wound rotor. The electromagnetic torque is produced by the interaction of a magnetic field between stator winding and rotor winding. The mechanical commutator allows to change the direction of current in individual coils of rotor winding. The mechanical commutator is the weakest element of this kind of motors. In a brushless DC motor, the electromagnetic torque is produced between

a magnetic field generated by stator winding and a magnetic field from permanent magnets mounted on the rotor. In a switched reluctance motor, a magnetic field is produced only by stator winding. The electromagnetic torque is produced due to the minimization of the reluctance between the stator and the magnetic field of the rotor. Therefore, the rotor tends to the position where reluctance is the smallest. In both BLDC and SRM motors, commutation of currents in stator phases must occur during the rotation. In Table 1, the most important properties of structures shown in Fig. 1 are presented.

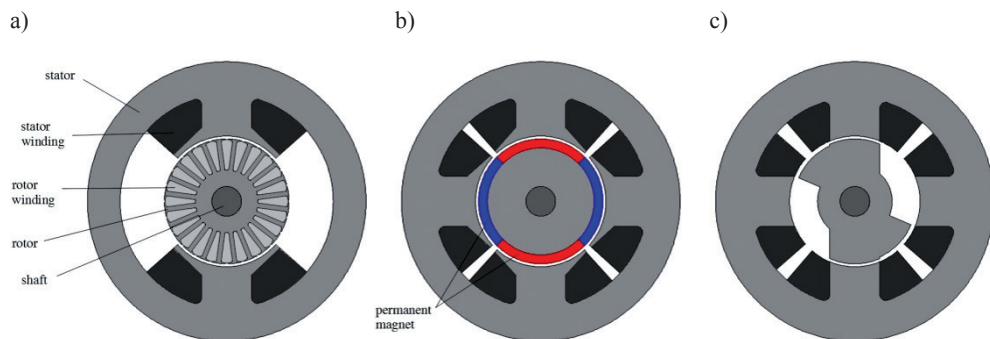


Fig. 1. Structures of: a) the classic commutator motor, b) the brushless DC motor, c) the switched reluctance motor

The authors were designing high-speed classic (commutator) motors and brushless motors with electronic commutation (both BLDC and SRM) for the suction unit drive, which should fulfil current restrictions associated with power consumption from the mains. During the design process, it was assumed that the motors should provide power on the shaft of no less than 700 W at a speed of 45000 rpm. The classic commutator motor should provide the required power at a lower speed. Such a high speed is caused by using a single-stage turbine, which produces subatmospheric pressure. Additionally, it was assumed that their structure should provide the possibility to mount standard bearing discs and a suction unit from one of domestic appliances manufacturers. In Table 2, chosen results of simulation tests of both designed structures at rated working point are presented.

Table 1

Chosen properties of structures from Fig. 1

	Commutator motor	BLDCM	SRM
Direct AC supply	yes	No	No
Number of phases	1	1	recommended 2
Start-up torque	high	medium	medium
Power electronics system	recommended	required	required

Smooth start-up	possible	yes	yes
Range of speed regulation	wide	wide	wide
Possibility of input power control	very hard	possible	possible
Efficiency	average	high or very high	high
Protection of motor for high-speed operation	required	required	not required
Necessity of using rotor position sensors	unnecessary	recommended	required
Influence of temperature on the rotor	Serious – problems with heat dissipation from rotor	Serious – change of permanent magnets parameters with temperature	No effect
Typical motor durability	Average – limited mostly by durability of sliding contact of brush-commutator	High – limited mainly by durability of bearings	High – limited mainly by durability of bearings

Table 2

Chosen tests results of designed structures of motors for suction unit

Parameter/Type of motor	commutator	BLDCM	SRM
Supply voltage U [V]	230 AC	320 DC	320 DC
Input power P_{in} [W]	1202	896	896
Output power P_{out} [W]	708	706	700
Speed at rated power n [rpm]	35000	45000	45000
Motor efficiency η_M [%]	59.5	80.4	79.8
Overall efficiency h [%]	–	78.8	78.1
Electromagnetic torque ripple e [%]	365	112	352
Length of stator stack L_{Fe} [mm]	25	15	20

Both of the designed structures do not consume more than 900 W from the mains at the required working point, but at the same time, they produce the required output power on the shaft. The overall efficiency of the BLDC motor is slightly higher (78.8%). In a switched reluctance motor, the efficiency obtained in simulation tests was slightly lower and equaled

78%. The commutator motor definitely has the lowest efficiency (59.5%). However, after using the speed control, the system efficiency will be more reduced. All motors are characterized by rather high ripples of the generated electromagnetic torque. It is caused by high maximum values of generated electromagnetic torque T_{emax} and small minimum values of electromagnetic torque T_{emin} . Electromagnetic torque ripples were calculated from equation:

$$\varepsilon = \frac{T_{emax} - T_{emin}}{T_{eav}} \quad (1)$$

where:

- T_{emax} – maximum electromagnetic torque,
- T_{emin} – minimum electromagnetic torque,
- T_{eav} – average electromagnetic torque.

The BLDC motor has the smallest torque ripple (112%). A higher number of phases can significantly decrease them, but this is associated with significantly higher costs of production of the power electronics system. The same situation is present in a switched reluctance motor. In a two-phase switched reluctance motor, it is possible to significantly limit ripples of the generated electromagnetic torque by using e.g. current regulation [6]. A power electronics system, which allows a much faster energy return, is another possibility of ripples limitation [7]. In a commutator motor supplied directly from AC network, there is no possibility to limit ripples of the electromagnetic torque. Ripples are directly connected with the shape of the motor current. However, compared to brushless motors with electronic commutation, in a commutator motor, the basic frequency of ripples of the generated electromagnetic torque equals the power frequency and it does not depend on the motor speed. The length of the commutator motor stack is definitely the longest. The BLDC motor has the shortest stack length.

3. Results of laboratory tests of the prototype SRM motor

The switched reluctance motor was made and tested in laboratory conditions. Fig. 2 shows the classic commutator motor and the prototype of switched reluctance motor, both with comparable electric parameters.



Fig. 2. An example of the commutator motor and the prototype of switched reluctance motor

Tests in laboratory conditions were conducted for the prototype of switched reluctance motor. The influence of the control parameters on features of the prototype was tested. Due to limitation of the maximum speed of the eddy-current dynamometer ($n_{\max} = 50000$ rpm), all tests corresponding with simulation conditions were not conducted. Figs. 3–4 show exemplary dependence of speed n on the function of load torque T_L for various control parameters i.e.

- variable conduction angle $\theta_c = \text{var}$ and constant turn-on angle $\theta_{on} = \text{const}$,
- variable turn-on angle $\theta_{on} = \text{var}$ and constant conduction angle $\theta_c = \text{const}$ at decreased value of supply voltage ($U_{dc} = 100$ V).

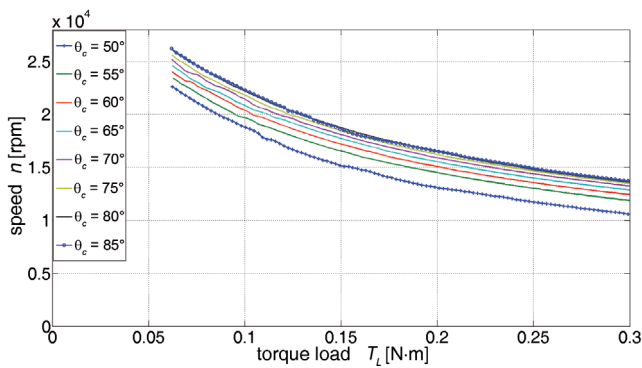


Fig. 3. Mechanical characteristics of the switched reluctance motor prototype obtained in laboratory conditions at variable conduction angle and constant turn-on angle

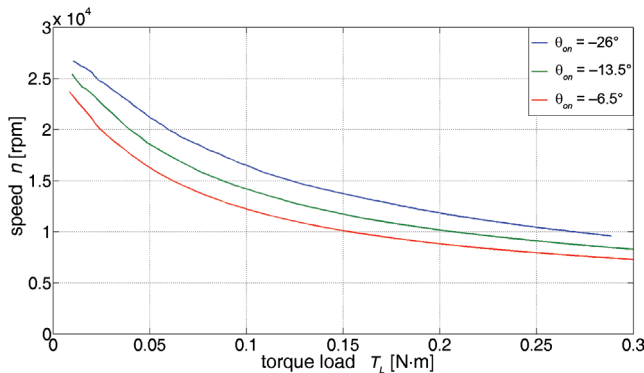


Fig. 4. Mechanical characteristics of the switched reluctance motor prototype obtained in laboratory conditions at variable turn-on angle and constant conduction angle

By changing the control parameters, it is possible to regulate speed in a very wide range. Therefore, it is possible to obtain the required working point by changing the control parameters of a motor even at decreased supply voltage ($0.9U_N$). The statement of laboratory

test results was prepared to compare the switched reluctance motor prototype with the commutator motor. Tests of the switched reluctance motor were conducted at control parameters, which do not allow reaching a speed of 50000 rpm. The commutator motor was tested at supply voltage equaling $U = 230$ V AC. Figs. 5–6 show the dependence of speed n (Fig. 5) and efficiency (Fig. 6) on the function of the load torque T_L .

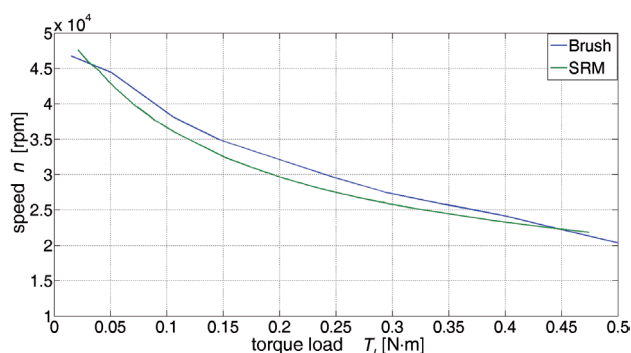


Fig. 5. Mechanical characteristics of the commutator motor and the switched reluctance motor from laboratory tests

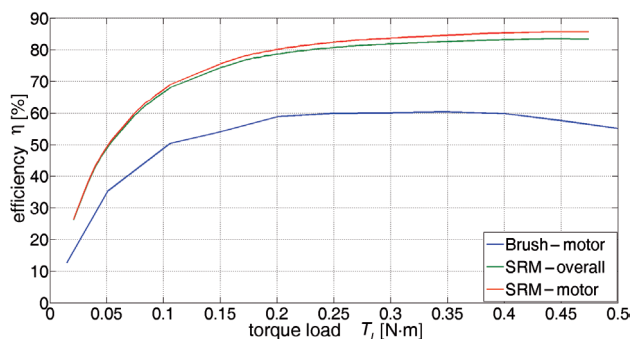


Fig. 6. Efficiency characteristics of the commutator motor and the switched reluctance motor from laboratory tests

The obtained mechanical characteristic of the switched reluctance motor prototype is below the characteristic of the commutator motor due to forced control parameters, which limit the maximum speed of the motor. Despite the limited speed, the overall efficiency of the switched reluctance motor equals 83.4%, whereas the efficiency of the alone motor equals 85.7%. In the case of the commutator motor, efficiency equals 60.4%. The commutator motor was tested without a control system of the motor speed, but even after using such a system, the efficiency of the motor will be slightly decreased. This is caused by the changing current shape (Fig. 7), which is caused by the operation of the speed control system.

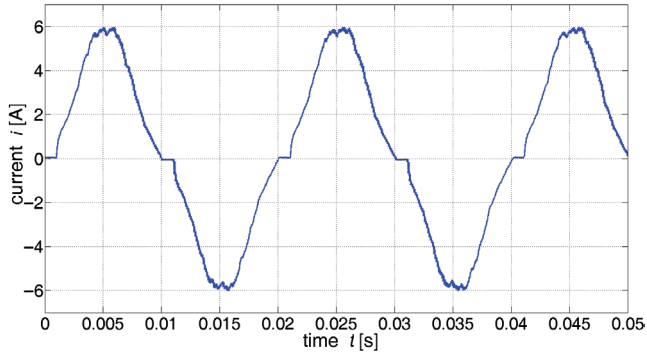


Fig. 7. Waveform of current of the commutator motor after mounting the speed control system

The tested prototype of the switched reluctance motor achieved much higher efficiency (about 23%) than the commutator motor, despite the limited output power. The efficiency of the prototype alone was higher by about 25.3%. The stator stack of the prototype switched reluctance motor was 25% shorter than the stack of the commutator motor at the same outer diameter of the rotor. Nevertheless, a 20% increase in the output power was achieved at the same value of input power. It is a very desirable with respect to current energy efficiency classes and classes, which will be applied after 01.09.2017. It should also be noted that, when the commutator motor will consume less than 900 W from the mains, the efficiency will be significantly lower. In the case of the brushless DC motor with electronic commutation, the overall efficiency will also be decreased when output power will be lower. However, the difference between the classic commutator motor and the brushless DC motor with electronic commutator will decrease, but for the benefit of the second one.

4. Conclusions

The application of energy-saving electric machines with electronic commutation in suction unit drives of vacuum cleaners on a mass-scale is one of the directions of the development of vacuum cleaners. However, on the one hand, it can cause a decrease in the global energy consumption, but on the other hand, customers will pay all of the costs, which are associated with the introduction of domestic appliances with improved energy efficiency. The purchase of a vacuum cleaner with an energy-saving motor should guarantee at least over a decade of failure-free operation. The domestic appliance with the A class or higher could be profitable only when the lifetime of this device will be significantly extended. The extension of failure-free operation of most domestic appliances with electric motors to about 10 years by using energy-saving electric machines can cause both a limitation of the global energy consumption by individual consumers, but also a limitation of e-waste production. This way, using much more expensive technologies could have a greater influence on the increase of consumers' awareness. Unfortunately, during the current tendency of domestic appliance manufactures to reduce the lifetime of their products, the purchase of an energy

efficient device is not economically justified. Therefore, this is a very serious problem, which has to be solved not only on the country scale, the European scale, but also on the global scale. One of the ways of solving this problem is to force manufacturers of domestic appliances with energy-saving technologies to extend the failure-free operation time. The paradox of history is that domestic appliances which, were produced decades ago, allowed for operation over decades, despite the lack of formal guarantees of such long failure-free operation. However, the parameters of such devices were far from desirable. The application of modern energy-saving technologies allows for the increase of operation efficiency of the domestic appliance with a significant increase of its energy class. This should be the main aim of introducing new energy efficiency norms of chosen domestic appliances.

Acknowledgements

The authors would like to thank the Zelmotor Ltd. Company for providing the test results of the suction unit and chosen devices for practical tests.

References

- [1] Official Journal of the European Union, Commission regulation (EU) No 666/2013 of 8 July 2013 implementing Directive 2009/125/EC of the European Parliament and of the Council with regard to ecodesign requirements for vacuum cleaners (2013).
- [2] Gieras J.F., Wing M., *Permanent Magnet Motor Technology – Design and Applications*, Second Edition, Revised and Expanded, Marcel Dekker Inc., New York 2002.
- [3] Krishnan R., *Permanent Magnet synchronous and Brushless DC Motor Drives*, CRC Press, New York 2009.
- [4] Chiba A., Fukao T., Rahman M.A., *Performance characteristics and parameter identification for inset type permanent magnet bearingless motor drive*, IEEE Power Engineering Society General Meeting, Vol. 2, 2004, 1272–1275.
- [5] Ziyuan Huang, Jiancheng Fang, *Multiphysics Design and Optimization of High-Speed Permanent-Magnet Electrical Machines for Air Blower Applications*, IEEE Transactions on Industrial Electronics, Vol. 63, Issue 5, 2016, 2766–2774.
- [6] Dong-Hee Lee, Huynh Khac Minh Khoi, Jin-Woo Ahn, *The performance of 2-phase high speed SRM with variable air-gap rotor poles for blower system Machines for Air Blower Applications*, International Conference on Electrical Machines and Systems (ICEMS), 2010, 1595–1598.
- [7] Ahn J.W., Liang J., Lee D.H., *Classification and Analysis of Switched Reluctance Converters*, Journal of Electrical Engineering & Technology, Vol. 5, No. 4, 2010, 571–579.

VASYL HUDYM*, ADAM JAGIEŁŁO**, JANUSZ PRUSAK**,
IRENEUSZ CHRABĄSZCZ**, PAWEŁ TRĘBACZ***

PREVENTING THE FORMATION OF ICE ON THE CATENARY LINES

ZAPOBIEGANIE POWSTAWANIU OBLODZENIA NA PRZEWODACH SIECI TRAKCYJNEJ

Abstract

Atmospheric icing on traction lines is very important problem because it causes difficulties of using electric vehicles by people and can result to breaking of traction lines. Heating the wire can preventing atmospheric icing.

Keywords: traction lines, icing, wire

Streszczenie

Powstawanie oblodzenia na przewodach sieci trakcyjnej jest bardzo ważnym problemem, ponieważ wprowadza utrudnienia w korzystaniu z pojazdów elektrycznych przez ludzi i może prowadzić do zerwania przewodów trakcyjnych. Podgrzewanie przewodu może zapobiegać powstawaniu oblodzenia.

Słowa kluczowe: linie trakcyjne, oblodzenie, przewód

* Prof. D.Sc. Ph.D. Eng. Vasyl I. Hudym, Institute of Electromechanical Energy Convers, Faculty of Electrical and computer Engineering, Cracow University of technology.

** Prof. D.Sc. Ph.D. Adam Jagiełło, Ph.D. Eng. Janusz Prusak, Ph.D. Eng. Ireneusz Chrabąszcz, Department of Traction and Traffic Control, Faculty of Electrical and Computer Engineering, Cracow University of Technology.

*** M.Sc. Eng. Paweł Trębacz, Department of Automation and Information Technologies, Faculty of Electrical and Computer Engineering, Cracow University of Technology.

1. Introduction

In most countries, combustion-powered traction vehicles have been replaced with electric vehicles. In order to deliver power to their engines, a traction line is needed. The line is located in an environment whose parameters change depending on the season. The winter is the most difficult season for traction lines, as with the environmental temperature at around -5°C and precipitation in the form of wet snow or sleet, a layer of icing forms on traction lines. Depending on the duration of the precipitation and the decrease in the temperature, the thickness of the ice changes and a situation in which the entire line will be covered with ice can occur. In such a case, the electric locomotive can not receive electricity via a pantograph which is separated from the line with a layer of ice. That is why the issue of preventing the formation of icing on traction lines is crucial [9].

The lines can be covered in grease that prevents icing from forming on the line. However, it is troublesome, expensive and requires the line to be disconnected from the source of energy. The carrying out of this idea is not economical and is technically difficult to implement.

A method that can be implemented relatively easily is to heat up the traction line to a positive temperature at which icing can not form. The best way to do it is to heat it using electrical current [1, 3, 4, 7].

The main purpose of this article is to analyze different variants and suggest a system of carry out the aforementioned concepts of heating.

2. Theoretical part of atmospheric icing on traction lines

The first task is to define the dependency of the temperature of the wire on the current density and heating time. In this case, it is possible to use rectifying units which already exist in rail applications in order to carry out this task, which will lower the cost compared to an the installation of additional sources.

It is extremely important to determine the duration of electricity transit in the wires in order to heat them. The current will be tied to active power losses in the network. The time needed to heat the wire to a given temperature and the length of the wire at a given current density are crucial factors. For that purpose, theoretical principles of heating a wire with direct current need to be taken into consideration. This case will be analyzed for a wire free of atmospheric icing.

As practice of overhead lines usage shows, three types of residues exist: wet snow, crystalline residue and atmospheric icing. Wet snow coats the lines when wind occurs with the air temperature of 0°C . Residues on lines occur together with fog or mild wind at temperature from -3°C to -10°C . Atmospheric icing occurs with the negative temperature of approximately -5°C , rain precipitation and wet snow precipitation and with the presence of wind at the speed of $12 \frac{\text{m}}{\text{s}}$, which causes rapid icing of the lines. Obviously, at the same time, car routes are covered with similar residues. That is why, most people take advantage of passenger trains and, for that reason, the role of such trains becomes very important. The

coating of the traction lines with ice significantly decreases the contact surface between the line and the pantograph of an electric locomotive. Apart from that, there exists the risk of line tearing and network damage during locomotive's movement, which is the result of mechanical influence on the line.

Experiments point that in order to melt the ice with a current in overhead lines made of steel-aluminum wires, the current density is selected within the range of $4 - 4.5 \frac{\text{A}}{\text{mm}^2}$.

The current will allow for the ice to melt within 20 min, whereas for steel wires the current density is selected between $2 \frac{\text{A}}{\text{mm}^2}$ to $3 \frac{\text{A}}{\text{mm}^2}$. If the time of melting is acceptable to be at 60 min, the current density for wires of such a construction ranges between $3.5 \frac{\text{A}}{\text{mm}^2}$ and $4 \frac{\text{A}}{\text{mm}^2}$. In such case, the mechanical characteristics of materials the overhead line is

manufactured of are taken into account. Current density in traction line wires can be higher because copper wires of the traction line will have their bay length much shorter than the bays of an overhead line of high and very high voltage [6–9].

Figure 1 presents the scheme of powering of one segment of the traction network from the rectifier of a two-rail substation of a DC voltage U_d .

In case of a traction network, catenary wire which supports the traction wires and cross-connectors all transmit electricity. The catenary wire and the connectors are made of copper and together with the traction lines make a parallel connection. A reference drawing is included below.

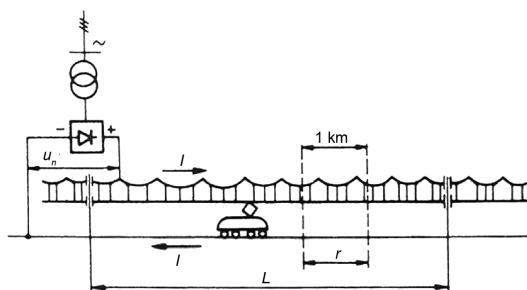


Fig. 1. A reference scheme of a segment of traction line powering

A segment l between railway substations is on average 15–25 km, and the resistance of this segment equals around 1.6Ω . In such a case from a DC voltage of a traction network in the value of 3300 V, the electrical value on that segment can reach over 2000 A. In case of insufficient power of one of the rectifiers, two rectifiers connected in parallel or a higher power rectifier should be used.

A wire of a cross-section of 100 mm^2 has the long term electrical ampacity within range of 400 A. It has to be taken into consideration that a traction line is dual (2 lines connected in parallel) and that, additionally, it – as a whole – is hanging on a copper catenary wire of a cross-section of about 95 mm^2 . That is why rope will transmit about 30% of the current and the remaining 70% will be more or less equally distributed between both lines, which

will give maxim working current within the range of 800 A. It is sufficient and the value of several additional amperes stemming from the need to heat up a traction line can be disregarded. The speed of heating up of such a wire will depend mostly on the temperature of the surroundings and the density of the current [2, 5].

It has to be specified how quickly a copper wire will heat up in various atmospheric conditions in order to prevent the formation of ice on the traction line; that is why relevant examinations or calculations need to be carried out.

An experimental examination requires a significant amount of time, equipment and the access to statistical data over the period of several years. That is why, this method is expensive. The required result can be achieved by analyzing a system model, most conveniently in the form of dependence of the temperature of the line on the time of heating and the density of the current being transmitted through this line. For this purpose, a mathematical model which takes into consideration the parameters of the material of which the line is made and the construction of such lines [1, 3, 4, 7].

A mathematical model will be created using basic equation for electrical circuits and processes of heating based on the laws of electrical engineering and thermodynamics. From the formula of energy balance in the following form:

$$RI^2 = KS(\theta - \theta_0) \quad (1)$$

we can determine the value of current depending on the temperature which is expressed by the following formula:

$$I(\theta - \theta_0) = \sqrt{\frac{KS(\theta - \theta_0)}{R}} \quad (2)$$

where:

- K – heat coefficient through convection and radiation $\left[\frac{\text{W}}{\text{m}^2 \cdot \text{C}} \right]$,
- S – the surface of the wire $[\text{m}^2]$,
- θ, θ_0 – temperature of wire and environment $[^\circ\text{C}]$,
- R – resistance of the wires segments $[\Omega]$.

It has to be noted that the resistance of wires is expressed by the following formula:

$$R = \rho \frac{4l}{\pi d^2} \quad (3)$$

where:

- ρ – proper resistance of the wire's material,
- l – the length of the wire,
- d – the diameter of the traction wires.

After taking into consideration the parameters of the wires' resistance, the value of current is expressed using following formula:

$$I(\theta - \theta_0) = \sqrt{\frac{K_0 d^2 (\theta - \theta_0)}{\rho}} \quad (4)$$

where:

K_0 – factor of proportionality.

Formula (4) allows us to determine the value of current, which raises the wires's temperature to θ . For practical applications, however, the formula (4) will not allow us to obtain the relationship between the time of heating a wire to a given temperature and the different values of heating current. In order to obtain the heating a wire with electrical current based on Newton-Richman law in the following form:

$$RI^2 dt = mCd\theta + \alpha(\theta - \theta_0)Adt \quad (5)$$

where:

A – wire's circumference,

l – the wire's length,

α – heat transfer coefficient onto the borderline between the wire and air,

m – the wire's mass,

C – heat absorption coefficient by the material the wire is made of,

θ_0 – the temperature of the surrounding air,

θ – the wire's temperature after certain heating time.

If we observe that $R = \rho \frac{l}{S}$, $m = \gamma \cdot l \cdot S$, and $A = 2\pi r l$ and insert into equation (5) we will get:

$$\rho \frac{l}{S} \cdot J^2 \cdot S^2 dt = \gamma \cdot l \cdot S \cdot Cd\theta + \alpha(\theta - \theta_0) \cdot 2\pi r l dt \quad (6)$$

where:

r – the wire's radius.

Having taken into consideration that $S = \pi r^2$ we receive:

$$\rho \cdot l \cdot J^2 \cdot \pi r^2 dt = \gamma \cdot l \cdot \pi r^2 \cdot Cd\theta + \alpha(\theta - \theta_0) \cdot 2\pi r l dt \quad (7)$$

After reducing identical values we obtain:

$$\rho \cdot J^2 \cdot r dt = \gamma \cdot r \cdot Cd\theta + 2\alpha(\theta - \theta_0) dt \quad (8)$$

After rewritings, we can write down the final differential equation:

$$\frac{d(\theta - \theta_0)}{dt} + \frac{2\alpha}{\gamma r C} (\theta - \theta_0) = \frac{\rho J^2}{\gamma C} \quad (9)$$

An equation characteristic for differential equation:

$$p + \frac{2\alpha}{\gamma r C} = 0 \quad (10)$$

from where we receive the equation's root:

$$p = -\frac{2\alpha}{\gamma r C} \quad (11)$$

The solution of the homogenous equation (9), that means with the right-hand side equal to zero, can be expressed as:

$$\theta - \theta_0 = B e^{-\frac{2\alpha}{\gamma r C} t} \quad (12)$$

where:

B – is a constant of integration, which is being determined.

The coerced component is determined by the condition which, for the time $t = \infty$ the derivative equals zero, and $\theta - \theta_0 = \frac{\rho \cdot r \cdot J^2}{2 \cdot \alpha}$.

The complete solution to the equation (5) can be written in the following form:

$$\theta - \theta_0 = \frac{\rho \cdot r \cdot J^2}{2 \cdot \alpha} + B e^{-\frac{2\alpha}{\gamma r C} t} \quad (13)$$

from where, we can finally write down the relationship between the temperature and time in the following form:

$$\theta(t) = \frac{\rho \cdot r \cdot J^2}{2 \cdot \alpha} + \theta_0 + B e^{-\frac{2\alpha}{\gamma r C} t} \quad (14)$$

To specify the constant of integration, we can apply the boundary conditions for $t = 0$:

$$\theta_{t=0} - \theta_0 = \frac{\rho \cdot r \cdot J^2}{2 \cdot \alpha} + B \quad (15)$$

from where:

$$B = \theta_{t=0} - \theta_0 - \frac{\rho \cdot r \cdot J^2}{2 \cdot \alpha} \quad (16)$$

After inserting into the formula (14) we get:

$$\theta(t) = \frac{\rho \cdot r \cdot J^2}{2 \cdot \alpha} + \theta_0 + \left(\theta_{t=0} - \theta_0 - \frac{\rho \cdot r \cdot J^2}{2 \cdot \alpha} \right) e^{-\frac{2\alpha}{\gamma r C} t} \quad (17)$$

The final equation allows us to calculate the temperature of heating of an item with the radius r and proper resistance of the wire's material ρ with the specific weight of $\gamma \left[\frac{\text{N}}{\text{m}^3} \right]$,

current density of $J \left[\frac{\text{A}}{\text{mm}^2} \right]$, in time of t in the case when the temperature of the wire, from the moment the current is switched on, until the moment of heating up is different than the temperature of the surrounding air.

3. Experimental part

The wire's temperature, when switching on the current until the heating of the wire aimed towards melting the glazed ice usually equals the temperature of the surrounding air. That is why the equation (17) will be expressed as:

$$\theta(t) = \frac{\rho \cdot r \cdot J^2}{2 \cdot \alpha} + \theta_0 - \frac{\rho \cdot r \cdot J^2}{2 \cdot \alpha} e^{-\frac{2 \cdot \alpha}{\gamma \cdot r \cdot C} \cdot t} \quad (18)$$

The diagram in Fig. 2 depicts a graphic presentation of the equation (18) for the selected values of current density.

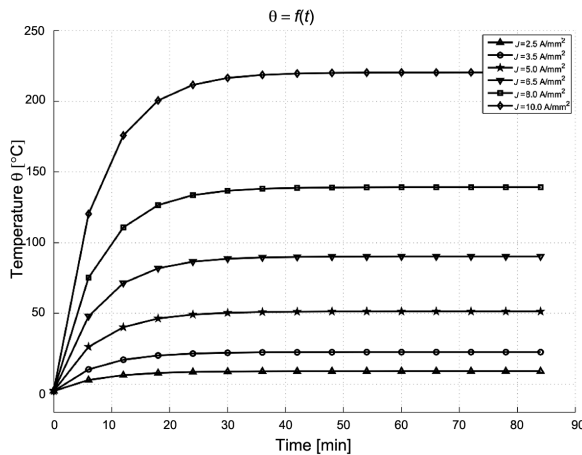


Fig. 2. The dependence of the wire's temperature on the heating time

For the above diagram, it was assumed that the initial temperature value is -5°C . The maximum temperature value, however, remains limited by current density.

For the same equation, a diagram of dependence of the wire's heating temperature on current density, while assuming different heating duration, was created. The results are presented in Fig. 3.

Analogously to the diagram from Fig. 2 – the initial value of temperature also equals -5°C , and the maximum value is limited only by the time of heating.

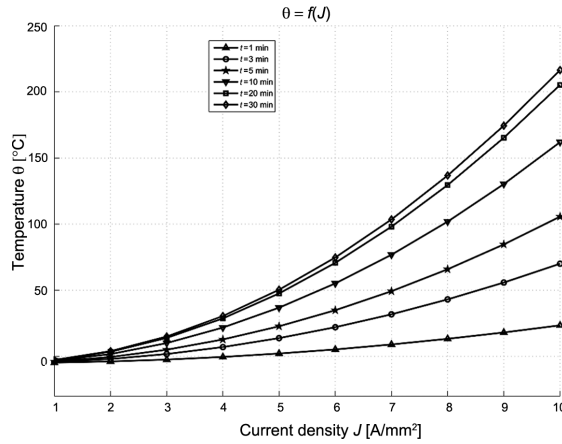


Fig. 3. The dependence of the wire's temperature on current density

From the equation (18) we can write:

$$e^{-\frac{2\alpha}{\gamma \cdot r \cdot C} \cdot t} = \frac{\frac{\rho \cdot r \cdot J^2}{2 \cdot \alpha} + \theta_0 - \theta(t)}{\frac{\rho \cdot r \cdot J^2}{2 \cdot \alpha}} \quad (19)$$

Equation (19) is re-written into the following form:

$$\frac{1}{e^{\frac{2\alpha}{\gamma \cdot r \cdot C} \cdot t}} = \frac{\frac{\rho \cdot r \cdot J^2}{2 \cdot \alpha} + \theta_0 - \theta(t)}{\frac{\rho \cdot r \cdot J^2}{2 \cdot \alpha}} \quad (20)$$

where:

$$e^{\frac{2\alpha}{\gamma \cdot r \cdot C} \cdot t} = \frac{\frac{\rho \cdot r \cdot J^2}{2 \cdot \alpha}}{\frac{\rho \cdot r \cdot J^2}{2 \cdot \alpha} + \theta_0 - \theta(t)} \quad (21)$$

After applying the logarithm to the formula (21), we get the following equation:

$$\frac{2 \cdot \alpha}{\gamma \cdot r \cdot C} \cdot t = \ln \left(\frac{\frac{\rho \cdot r \cdot J^2}{2 \cdot \alpha}}{\frac{\rho \cdot r \cdot J^2}{2 \cdot \alpha} + \theta_0 - \theta(t)} \right) = \ln \left(\frac{\rho \cdot r \cdot J^2}{2 \cdot \alpha} \right) - \ln \left(\frac{\rho \cdot r \cdot J^2}{2 \cdot \alpha} + \theta_0 - \theta(t) \right) \quad (22)$$

From this equation (22), we can obtain the formula to determine the time of transmission of a given value of DC current density, depending on the temperature of the surrounding air and the temperature necessary to melt the ice. The formula has the following form:

$$t = \frac{\gamma \cdot r \cdot C \left[\ln \left(\frac{\rho \cdot r \cdot J^2}{2 \cdot \alpha} \right) - \ln \left(\frac{\rho \cdot r \cdot J^2}{2 \cdot \alpha} + \theta_0 - \theta(t) \right) \right]}{2 \cdot \alpha} \quad (23)$$

Figure 4 presents the block diagram for the connection of a rectifier in order to melt the ice on the line of a monorail railway.

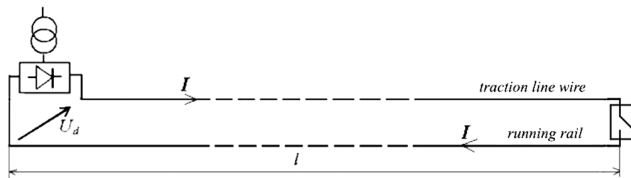


Fig. 4. Block diagram of a ice melting system

The following examination is determining the value of current needed to heat up a wire from the initial temperature -10°C to the following temperatures: 10°C , 35°C and 60°C in time 5 min, 10 min and 20 min. The diagram below presents the results obtained.

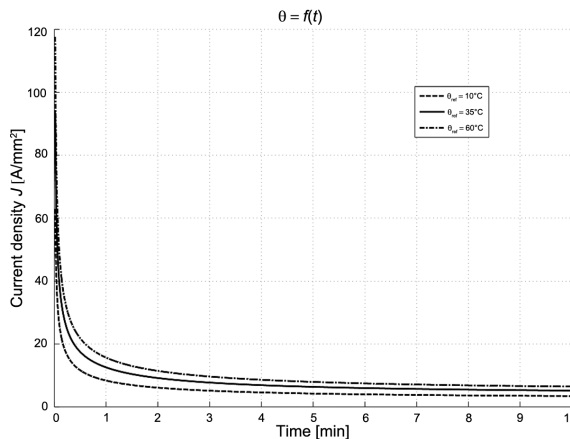


Fig. 5. The dependence of current density on the time of wire's heating

The values of current density for the necessary heating time were extracted from the Fig. 5, a marker tool, displaying the values of X and Y axes in a given point of diagram was used to that end. The results are presented in Table 1.

The current density values extracted from the diagram for the three conditions required in the task

Heating time	Target temperature		
	10°C	35°C	60°C
5 min	4.252 A/mm ²	6.378 A/mm ²	7.954 A/mm ²
10 min	3.461 A/mm ²	5.192 A/mm ²	6.475 A/mm ²
20 min	3.084 A/mm ²	4.626 A/mm ²	5.770 A/mm ²

Analyzing the courses in Fig. 5, we can see that, in the initial temperature range, the value of current decreases rapidly, whereas in the subsequent part of the diagram the changes are smaller.

4. Conclusions

The analyses of the railway situation presented in this article allow us to determine that the occurrence of atmospheric icing on traction lines is a current and important issue which needs to be resolved. The occurrence of icing impacts train schedules by causing problem with supplying electric locomotives with power.

Preventing the formation of icing on traction lines requires the increase of the wire's temperature to the value, in which ice can not deposit on wires. Heating a wire to that temperature in most easily delivered through the transit of electric current through the wire. This, however, requires specifying the dependency of temperature on current density in traction wires, which can be determined experimentally or analytically. Because the antithetical method is the cheapest and does not require interfering with the traction network, and as such does not cause obstacles in the functioning of trains during tests, this article formulates a mathematical model based on the laws of electrical engineering and thermodynamics. The obtained model allows us to adequately examine the processes of heating a wire with electricity.

The analysis that was carried out proved that the wire can be heated from temperature of -5°C to the temperature of 6°C , in time 10 min, with the electricity of current density as low as $2.5 \frac{\text{A}}{\text{mm}^2}$. Further heating of the wire in the aforementioned conditions can allow it to reach the maximum temperature of $8-9^{\circ}\text{C}$. It is obvious that the increase in current density will cause a quicker heating of the wire. If we use the electricity with the current density of $5 \frac{\text{A}}{\text{mm}^2}$, then after the time of 10 min, the wire will reach temperature of about 40°C and can reach maximum temperature of 50°C after 30 min. The simulation results presented above are obtained for the case of the wire being cooled with wind and the velocity $12.5 \frac{\text{A}}{\text{mm}^2}$ and the temperature of -5°C its surroundings.

References

- [1] Siemiński T., Jarosz T., *Current collectors and its cooperation with the overhead contact line*, Wydawnictwo Komunikacji i Łączności, Wydanie trzecie zmienione, Warszawa 1993.
- [2] Głowacki K., Onderka E., *Traction systems*. „Emtrak s.c.”, wydanie I, lipiec 2002.
- [3] Kotarski F., Solarek T., *Traction systems*, Politechnika Łódzka, Łódź 1988.
- [4] Onderka E., *Methods of eradication hoarfrost and icing on traction system*, TTS Technika Transportu Szynowego, nr 3/2010, 58 60, 72.
- [5] Chrabąszcz I., Prusak J., Drabik S., *Direct current traction system, power supply systems*, Praca zbiorowa pod redakcją Jana Strojnego, Warszawa, Bełchatów, 2009.
- [6] Nikonec L.A., Koniuhov A.I., *Powyszenie nadiożności raboty WL wyższych klassow napriażenia w gololiednyh uslowijah*, II Respublikanskaja konferencija „Sowremiennyje problemy enegietyki”, Kiew, 1976.
- [7] Genrih G.A., *Osnovy plawki gololioda na WL s ispolzowanijem preobrazowatielej (ispolzowanie shem plawki i uslowij raboty osnonogo oborudowania*, Autoreferat dys. dokt. teh. nauk., Lwow 1972.
- [8] *Obobszczenie opyta projektowania, stroitielstwa i eksploatacji UPG postojannogo toka na prowadach i trosach WL 110–500 kV*, Južnoje Odilenie WGPI i NII „Energosiecprojekt”, No. 1015TM-t. I.44, 1979.
- [9] Jagiełło A.S., Dudzik M., *Catenary – pantograph dynamic aspects of cooperation*, XV Ogólnopolska Konferencja Naukowa z zakresu Trakcji Elektrycznej SEMTRAK 2012, Zakopane 18–20 października 2012.

MARIUSZ KORKOSZ, GRZEGORZ PODSKARBI*

LABORATORY TEST OF SURFACE MOUNTED PERMANENT MAGNET BRUSHLESS MOTOR

BADANIA LABORATORYJNE BEZSZCZOTKOWEGO SILNIKA Z MAGNESAMI TRWAŁYMI MONTOWANYMI POWIERZCHNIOWO

Abstract

In the paper, the results of laboratory tests of a surface mounted permanent magnet brushless motor were presented. Two power electronics systems, which are made as inverters for PMSM and BLDC motors, were used. The PMSM inverter supplies the motor with sinusoidal currents and the BLDC inverter supplies the motor with trapezoidal voltage. The motor characteristics and its waveforms were determined when the motor was supplied from the BLDC inverter and the PMSM inverter. A comparison of the influence of the motor supply method on its features and parameters was performed.

Keywords: brushless motor with permanent magnets, BLDCM, PMSM, mechanical characteristics, waveforms

Streszczenie

W artykule zamieszczono wyniki badań laboratoryjnych bezszczotkowego silnika z magnesami trwałymi montowanymi powierzchniowo. W badaniach zastosowano dwa układy energoelektroniczne, które zostały wykonane jako falowniki do silnika PMSM oraz BLDCM. Falownik PMSM zasila silnik prądami sinusoidalnymi. Falownik BLDCM zasila silnik napięciem trapezoidalnym. Zostały wyznaczone charakterystyki silnika oraz jego przebiegi czasowe przy zasilaniu go jako PMSM oraz BLDCM. Dokonano porównania wpływu sposobu zasilania silnika na jego właściwości i parametry.

Słowa kluczowe: bezszczotkowy silnik z magnesami trwałymi, BLDCM, PMSM, charakterystyki mechaniczne, przebiegi czasowe

* D.Sc. Ph.D. Eng. Mariusz Korkosz, Eng. Grzegorz Podskarbi, Department of Electrodynamics and Electrical Machine Systems, Faculty of Electrical and Computer Engineering, Rzeszow University of Technology.

1. Introduction

Brushless motors with permanent magnets are an alternative for other types of electric machines. High-energy magnetic materials used in permanent magnets, e.g. rare-earth elements, allow obtaining very good magnetic parameters [1–7]. Magnets made from NdFeB (neodymium magnets) allow obtaining very good features of brushless machines with permanent magnets, such as high efficiency of energy conversion, very good ratio of the generated torque to the machine volume unit. One method of permanent magnets mounting is fastening them on the surface of a rotor (SPM – surface permanent magnets). The surface mounting method has both advantages and disadvantages. The advantages include: easier shaping of the induced voltage, eliminated reluctance torque, great opportunities of permanent magnet shaping. Surface-mounted magnets also have disadvantages, such as necessity of magnets protection from the centrifugal force, much greater impact of a stator flux on magnets, which leads to greater susceptibility to demagnetizing. In surface mounted magnets, losses from eddy-currents are greater and it is a serious problem. To protect magnets from the centrifugal force, a greater air-gap is required.

Two ways of supplying brushless motor with permanent magnets are possible, regardless of the magnets' mounting method. It depends on the shape of the induced voltage, so brushless DC machines with permanent magnets can be divided into three groups:

- with sinusoidal voltage or close to sinusoidal,
- with trapezoidal voltage or close to trapezoidal,
- with voltage that is not similar to sinusoidal or trapezoidal.

The shape of the induced voltage is important when a method of supplying is selected. In the case of a motor with the trapezoidal induced voltage or close to trapezoidal, the inverter with the trapezoidal voltage is preferred. Theoretically, it is the most optimal solution in the point of view of the generated electromagnetic torque and its ripple.

In the paper, laboratory tests of a brushless motor with surface-mounted permanent magnets with trapezoidal induced voltage were conducted. The motor was supplied from two different power electronics systems, which realize inverter functions for supplying the BLDC motor and the PMSM motor. Identical laboratory tests were conducted in both variants. Line currents of the motor were presented both during no-load operation and under load operation. Standard mechanical characteristics and efficiency characteristics (for various speeds), dynamic characteristics (start-up on no-load and under load, reversal), were determined. It was possible to set the working point in both stationary states and dynamic states. Based on the test results, conclusions concerning possibility of supplying BLDC motor with sinusoidal current were presented.

2. The laboratory setup for tests of brushless dc motor with surface-mounted permanent magnets

In Table 1, parameters of the tested brushless DC motor with surface-mounted permanent magnets are presented.

Table 1

Parameters of tested brushless motor with surface-mounted permanent magnets

Parameters	Value
Supply voltage U_N [V]	3×400
Rated power P_N [kW]	4
Rated stator current I_N [A]	11.5
Rated speed n_N [rev/min]	1500
Number of stator poles N_s	48
Number of rotor poles N_r	4
Winding type	Distributed
Magnets type	Neodymium

Fig. 1 shows a schematic diagram of the laboratory setup.

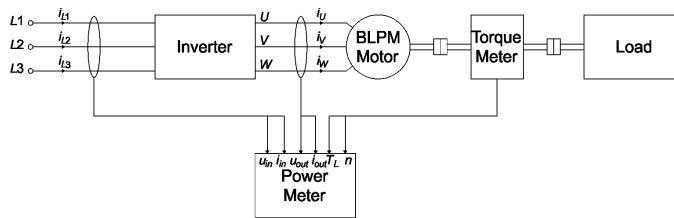


Fig. 1. A schematic diagram of the laboratory setup for tests of brushless motor

In the laboratory setup, Yokogawa WT1600 six-channel digital power meter was used to measure electric parameters (currents and voltages). The power meter was additionally equipped with a motor module, which allows measuring the load torque T_L and speed n . The tested brushless motor with permanent magnets was coupled with a DC machine. The torque meter, which was mounted between the DC machine and the tested motor, was used to measure the load torque. Selected waveforms in dynamic states were registered with a four-channel digital oscilloscope. The power meter allows registering waveforms of all parameters (currents, voltages, load torque and speed) only in steady states. Currents and voltages were measured before and after the inverter, which allows determining not only the overall efficiency of the whole drive system, but also the efficiency of the motor and the power electronics system.

Two inverters were used in the tests. Both systems were built based on the Twerd MFC710 vector inverter. One of the inverters was adapted to operation with a brushless DC motor with permanent magnets (BLDC). The second one was designed for operation with a synchronous motor with permanent magnets (PMSM). Both inverters were adapted for operation in the first regulation zone, i.e. with a constant torque. Moreover, inverters were supposed to operate in a closed loop speed control.

3. Waveforms

3.1. Induced voltage

Theoretically, the shape of the induced voltage is very important in terms of supply method selection. Fig. 2 shows the registered waveforms of line-to-line induced voltages of the tested motor at a speed of 1000 rev/min.

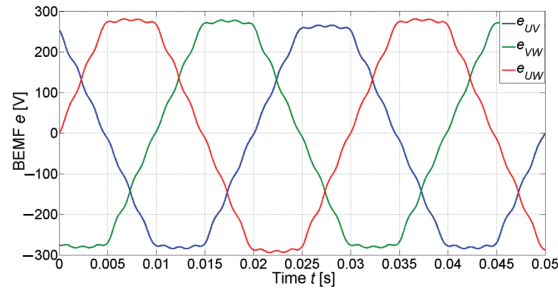


Fig. 2. Induced voltages of the tested motor

The shape of the induced voltage is trapezoidal. Therefore, the tested motor is suitable for supply with trapezoidal voltage (BLDC inverter).

3.2. Waveforms in steady states

Waveforms of currents and voltages of the brushless DC motor were registered without load and under load with $T_L = 20 \text{ N}\cdot\text{m}$ at speed $n = 1500 \text{ rev/min}$. Figs. 3–4 show line currents i of motor during no-load (Fig. 3) and under load (Fig. 4).

Currents are highly distorted, regardless of the supply method during no-load. This is typical for brushless motors with permanent magnets. During operation under load, waveforms of currents seem to be similar to a square wave during BLDC operation (Fig. 4a) and a sine wave during PMSM operation (Fig. 4b). Visible distortions of currents are mainly caused by the speed regulator. The speed regulator controls the instantaneous value of currents to maintain speed on a defined level (by current regulator).

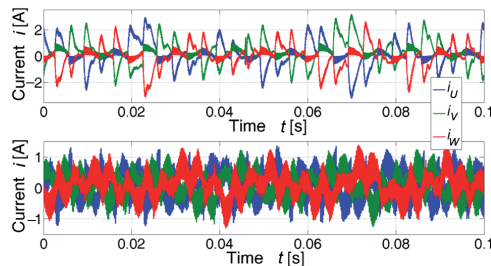


Fig. 3. Waveforms of line currents of the motor at $T_L = 0 \text{ N}\cdot\text{m}$ working as: a) BLDCM, b) PMSM

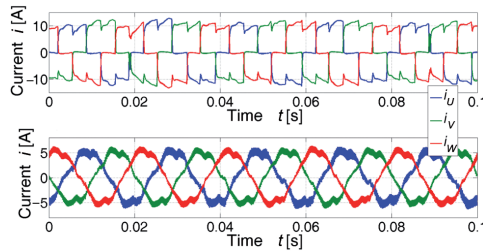


Fig. 4. Waveforms of line currents of the motor at $T_L = 20$ N-m working as: a) BLDCM, b) PMSM

3.3. Waveforms in dynamics states

Start-up and reversal of the motor was tested in laboratory conditions. Start-up time t_r , braking time t_h and stopping time t_s were possible to be changed in control units of both power electronics systems and they were set up to: $t_r = 4$ s, $t_h = 3$ s, $t_s = 3$ s. Additionally, it was assumed that, during start-up, the motor current can reach 150% of the rated value and the electromagnetic torque can reach 150% of the rated torque.

Two cases were analyzed during tests in dynamic states. In the first one, a separately excited DC generator was not loaded. In the second case, the generator was producing load of the tested motor. Figs. 5–6 show waveforms of speed during start-up without and under load, respectively. Start-up time was set to $t_r = 4$ s.

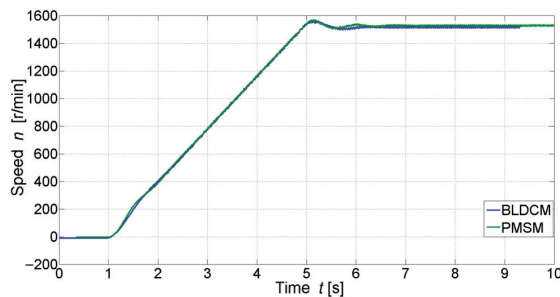


Fig. 5. Speed of the tested motor during the start-up at $T_L = 0$

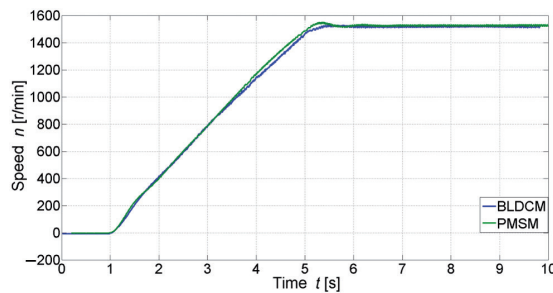


Fig. 6. Speed of the tested motor during the start-up at $T_L > 0$

Figs. 7–8 show waveforms of the line current i of the phase U during the start-up

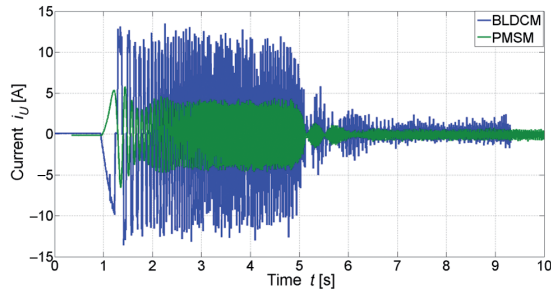


Fig. 7. Waveforms of the motor current i_U of the phase U of the tested motor during the start-up at $T_L = 0$

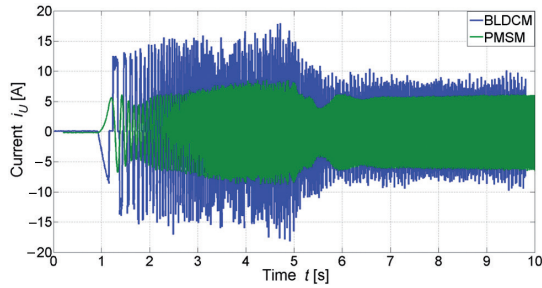


Fig. 8. Waveforms of the motor current i_U of the phase U of the tested motor during the start-up at $T_L > 0$

During the start-up under load, the motor reaches the defined speed in time exceeding 4 s. Both power electronic systems ensure comparable dynamic parameters of the motor. However, during operation as BLDC, a higher value of currents is required. Similar results were achieved during motor stoppage or during reversal. Fig. 9 shows the speed during reversal.

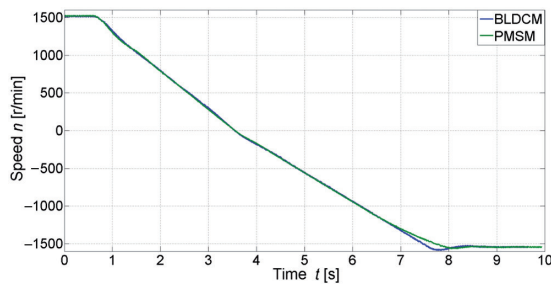


Fig. 9. Speed of the tested motor during reversing at $T_L = 0$

4. Static characteristics

4.1. Test conditions

Laboratory tests were conducted at several values of speed, which were set up in the speed regulator i.e. 250 rev/min, 750 rev/min and 1500 rev/min. The value of the load torque T_L was increased to achieve at least the rated value. Both power electronics systems were forcing operation with constant speed taking into account the limitations of control algorithms.

4.2. Supply from BLDC inverter

Fig. 10 shows speed n in the function of the load torque T_L .

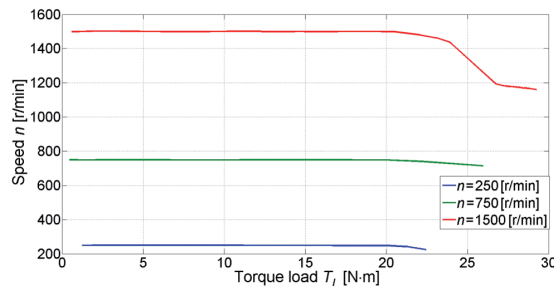


Fig. 10. A dependence of speed n in the function of the load torque T_L during BLDC operation

In the case of BLDC operation, the used power electronics system was not able to maintain a defined speed when the load torque increased over 21 N·m, which in turn caused the motor working point to change. It was noticeably visible at the rated speed (1500 r/min).

Figs. 11–13 show the overall efficiency η (Fig. 11), motor efficiency η_M (Fig. 12) and efficiency of power electronics system η_{inv} (Fig. 13) in the function of the load torque T_L .

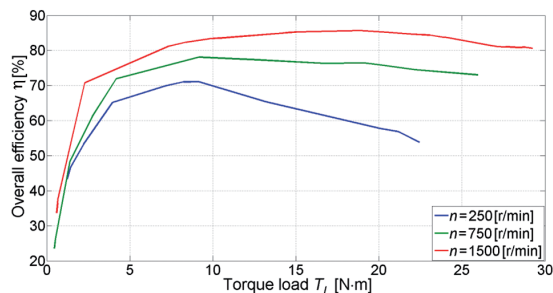


Fig. 11. A dependence of overall efficiency η in the function of the load torque T_L during BLDC operation

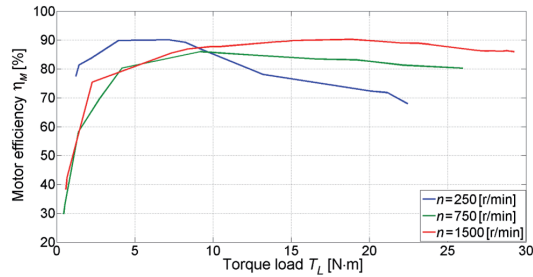


Fig. 12. A dependence of motor efficiency η_M in the function of the load torque T_L during BLDC operation

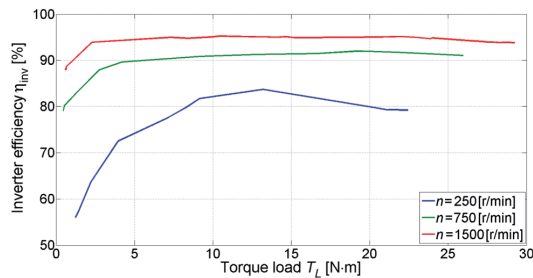


Fig. 13. A dependence of efficiency of power electronics system η_{inv} in the function of the load torque T_L during BLDC operation

The highest efficiency was achieved at rated speed. The efficiency of the power electronics system decreases significantly during decreasing motor speed. Therefore, it has significant influence on the overall efficiency. The efficiency of motor did not exceed 90%.

4.3. Supply from PMSM inverter

The characteristics of the tested motor supplied from PMSM inverter were determined for the same settings of the speed regulator. Fig. 14 shows speed n in the function of the load torque T_L .

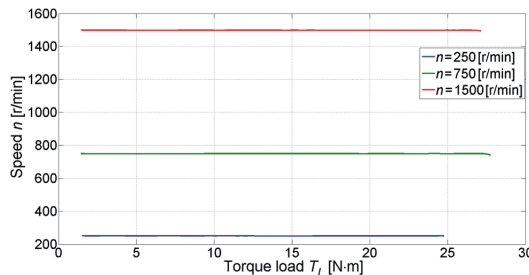


Fig. 14. A dependence of motor speed n in the function of the load torque T_L during PMSM operation

The motor supplied from the PMSM inverter allows obtaining a higher value of the load torque T_L than the rated value at adjusted speed.

Figs. 15–17 show the overall efficiency η (Fig. 15), motor efficiency η_M (Fig. 16) and efficiency of power electronics system η_{inv} (Fig. 17) in the function of the load torque T_L .

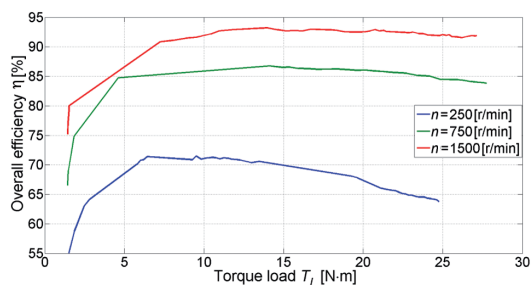


Fig. 15. A dependence of overall efficiency η in the function of the load torque T_L during PMSM operation

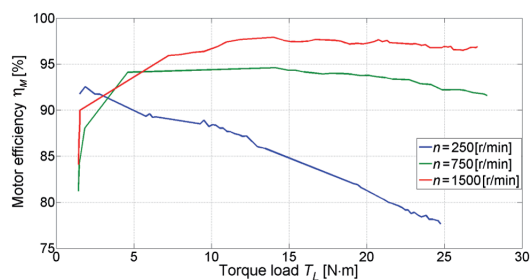


Fig. 16. A dependence of motor efficiency η_M in the function of the load torque T_L during PMSM operation

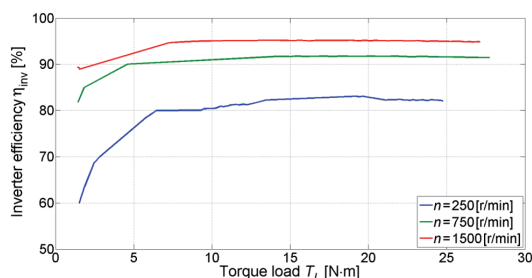


Fig. 17. A dependence of efficiency of power electronics system η_{inv} in the function of the load torque T_L during PMSM operation

The tested brushless motor with permanent magnets during operation as PMSM was reaching higher overall efficiency in the whole speed range.

5. Summary of test results

In table 2, chosen parameters of the tested motor in two variants were set up. In both cases, the load torque equaled 20 N·m.

Table 2

Chosen parameters of the drive for three values of speed during different control methods

	Parameter	250 rev/min	750 rev/min	1500 rev/min
BLDCM	Supply current I_{L1}	3	5.8	9.3
	Motor current I_U	10.7	10.8	10.9
	Overall efficiency η	58	76	86
	Motor efficiency η_M	72	83	90
	Inverter efficiency η_{inv}	80	92	95
PMSM	Supply current I_{L1}	2.7	5.2	8.6
	Motor current I_U	9	9	9
	Overall efficiency η	68	86	92
	Motor efficiency η_M	81	94	97
	Inverter efficiency η_{inv}	83	92	95

The motor supplied from the PMSM inverter ensures higher drive efficiency regardless of the working point. Higher rms phase current is required to obtain the same load torque T_L when the motor is supplied with trapezoidal voltage. It means that the torque constant of the motor, which is supplied with trapezoidal voltage, is lower than of that supplied with sinusoidal voltage (PMSM). Therefore, losses (copper losses, iron losses and also losses in magnets) are higher during supply with trapezoidal voltage. The efficiency of both BLDC and PMSM inverters was comparable. However, the presented results of laboratory tests concern the case when voltage was trapezoidal. When induced voltage will be close to sinusoidal, higher differences between BLDC and PMSM supply should be expected in favor of PMSM. It will be a subject of future research works.

5. Conclusions

In the paper, the results of laboratory tests of a brushless motor with permanent magnets were presented. The tested motor was supplied from two different power electronics systems, which realize inverter functions for supplying the BLDC motor and the PMSM motor. The

tested motor has permanent magnets mounted on the surface of the rotor. Simultaneously, the shape of the induced voltage is trapezoidal. Therefore, it prefers this motor to be supplied from the BLDC inverter. However, the conducted tests showed that instead of a trapezoidal shape of the induced voltage, higher efficiency was achieved when the motor was supplied from the PMSM inverter. When the motor was supplied from the BLDC inverter, especially at a low speed, higher ripples were visible, which in turn were not visible when the motor was supplied from the PMSM inverter.

References

- [1] Staton D.A., Deodhar R.P., Soong W.L, Miller T.J.E, *Torque Prediction Using the Flux-MMF in AC, DC, and Reluctance Motors*, IEEE Transactions on Industry Applications, Vol. 32, No. 1, 1996, 180–188.
- [2] El-Refaie A.M., *Fractional-slot concentrated windings synchronous permanent magnet machines: opportunities and challenges*, IEEE Transactions on Industrial Electronics, Vol. 43, Issue 1, 2010, 107–121.
- [3] Gieras J.F., Wing M., *Permanent Magnet Motor Technology – Design and Applications*, Second Edition, 2002.
- [4] Tae-Jong Kim, Sang-Moon Hwang, Kyung-Tae Kim, Weui-Bong Jung, Chul-U Kim, *Comparison of dynamic responses for IPM and SPM motors by considering mechanical and magnetic coupling*, IEEE Transactions on Magnetics, vol. 37, Issue 4, 2001, 2818–2820.
- [5] Dorrell D.G., Hsieh M.F., Popescu M., Evans L., Staton D.A., Grout V., *A Review of the Design Issues and Techniques for Radial-Flux Brushless Surface and Internal Rare-Earth Permanent-Magnet Motors*, IEEE Transactions on Industrial Electronics, vol. 58, Issue 9, 2011, 3741–3757.
- [6] Bianchi N., Bolognani S., Dai Pre M., *Magnetic Loading of Fractional-Slot Three-Phase PM Motors With Nonoverlapped Coils*, IEEE Transactions on Industry Applications, vol. 44, Issue: 5, 2008, 1513–1521.
- [7] Wu L., Qu R., Li D., Gao Y., *Influence of Pole Ratio and Winding Pole Numbers on Performance and Optimal Design Parameters of Surface Permanent-Magnet Vernier Machines*, IEEE Transactions on Industry Applications, vol. 51, Issue 5, 2015, 3707–3715.
- [8] Korkosz M., Podskarbi G., *Badania laboratoryjne bezszczotkowego silnika prądu stałego z magnesami trwałymi montowanymi powierzchniowo*, Proceedings of Conference on Selected Issues of Electrical Engineering and Electronics (WZEE 2016), 4–8.05.2016 Rzeszow, 2016 (in polish).

GRZEGORZ NOWAKOWSKI*

CONVERSION OF FUZZY QUERIES INTO STANDARD SQL QUERIES USING ORACLE 11G XE

TRANSFORMACJA ZAPYTAŃ NIEPRECYZYJNYCH NA ZAPYTANIA W STANDARDZIE SQL PRZY WYKORZYSTANIU ORACLE 11G XE

Abstract

This article presents various forms of fuzzy queries with a particular emphasis of two different approaches to the representation of fuzziness, a detailed analysis of these queries and their conversion into standard SQL queries using Oracle 11g XE. The actions discussed above point out to the methods of obtaining fuzzy information from the database that have been easy to implement. A qualitative and quantitative study about the use of fuzzy queries on relational databases has been included in this article, as well. This research takes into account the fact that obtaining this type of information is not supported by any commercial database management system.

Keywords: fuzzy logic, fuzzy queries, SQL, Oracle 11g XE

Streszczenie

W artykule przedstawiono różne formy zapytań nieprecyzyjnych do bazy danych ze szczególnym uwzględnieniem dwóch konkretnych podejść do reprezentacji nieprecyzyjności, dokonano szczegółowej analizy tych zapytań oraz ich transformacji na zapytania w standardzie SQL z zastosowaniem Oracle 11g XE. W artykule ujęto również jakościowe i ilościowe badanie dotyczące wykorzystania nieprecyzyjnych zapytań w relacyjnych bazach danych. Omawiane działania wskazują na łatwe w implementacji sposoby pozyskiwania nieprecyzyjnych informacji z bazy danych oraz uwzględniają fakt, że pozyskiwanie tego typu informacji nie jest wspierane przez żaden komercyjny system zarządzania bazami danych.

Słowa kluczowe: logika rozmyta, zapytania nieprecyzyjne, SQL, ORACLE 11g XE

* M.Sc. Eng. Grzegorz Nowakowski, Department of Automatic Control and Information Technology, Faculty of Electrical and Computer Engineering, Cracow University of Technology.

1. Introduction

Classic query languages (with SQL being the most widely applied) define the scope of data as well as conditions to be met by data throughout the entire process of searching for information in databases. These conditions should be precisely defined, as precision is the basic requirement when defining conditions in query languages. At the same time, these conditions impose limitations. For example, a customer of a car dealership looking for a cheap car has to precisely define the price range he is willing to pay. Regardless of how the limits of the range are defined, a car priced slightly above the set limit will not meet the conditions of the query. This shows that the limits in question result from the necessity of precisely defining the conditions, which were initially expressed in a natural language with imprecise terms.

The problem can be solved by the use of linguistic terms modelled and processed with fuzzy logic in queries addressed to a database. These are the so-called fuzzy queries. Linguistic terms are presented as fuzzy sets in an appropriate, usually numerical, space. Therefore, matching data to the query is no longer perceived as dichotomy: matched – unmatched. For this reason, the notion of a degree of matching the data to the query is introduced and one assumes that the value of this degree of matching corresponds (in a somewhat simplified view) to the degree to which the data belongs to the fuzzy set representing the condition of the query [1, 2].

This article discusses various forms of fuzzy queries with a particular emphasis of two different approaches to the representation of fuzziness; it also includes a detailed analysis of fuzzy queries as well as documents their conversion into SQL standard queries using Oracle 11g XE. Described actions point to easy to implement methods of obtaining fuzzy information from databases and take into account the fact that obtaining such information is not supported by any commercial database management system.

2. Fuzzy queries

A fuzzy query addressed to a relational database [1, 2] is a query including overtly used expressions of the natural language, referred to as linguistic terms (modelled with fuzzy logic), defining the following: imprecise values, imprecise comparisons and non-standard methods of aggregation of degrees of meeting partial conditions of the query.

Particular rows meet the conditions of such a query to a certain degree expressed with a number from $(0,1]$ range, where 1 means that the query requirement is fully met, and 0 means that the query requirement is fully unmet. Therefore, the result of the query is a set of rows arranged according to the degree of meeting the conditions of the query. This way, it is easier to reflect the attempts undertaken by a given individual to match the data to the query. In the case of complex queries, which include both fuzzy linguistic terms as well as non-standard aggregation schemes, meeting conditions of the query is gradual. In such a situation, a human being naturally evaluates the data and perceives it as data, which meets his/her requirements to a greater or a lesser degree instead of distinguishing only between the data, which meets or does not meet the set requirements. The notion of the degree of meeting

conditions of the query allows us to formally present these complex queries and by the same token naturally arrange the results in such a manner, as to make sure the data, which meets the conditions of the query to the greatest degree is at the onset of the list of results.

When analysing the problem of calculating the degree to which conditions of a fuzzy query are met, one should accept a significantly simplified view of the execution of such a query by a database system. It is assumed that when a query is executed, the whole table is examined sequentially and that the degree to which the query is met is calculated for each row. Database system carries out the steps presented in Table 1.

Table 1

Calculation of the degree to which conditions of a fuzzy query are met (prepared based on [1, 2])

Step	Database system:
1	downloads a row from the table;
2	calculates partial degrees of meeting all (or only selected, depending on the structure of the query and the applied optimization) simple conditions of the query by substituting the attributes with their values form a given row;
3	aggregates partial degrees to which conditions of the query are met as calculated in the previous step up to the total degree of meeting conditions the query;
4	if the total degree of meeting conditions of the query is sufficiently high (exceeds the user-defined or default threshold value), the row is added to the reply to the query along with the degree of meeting its conditions;
5	moves to step 1;
6	if there are no more rows, STOP.

An overview of the process of calculating the degree to which conditions of a simple, fuzzy query are met can be presented on the following example. Let us assume that I am looking for a cheap car in the offer of a car dealership. Let us assume that u denotes the numerical range specifying prices of the vehicles (in kPLN) and that the term *cheap* is modelled with the fuzzy set A characterized by the following membership function:

$$\mu_A(u) = \begin{cases} 1 & u \leq 200 \\ \frac{400-u}{200} & 200 < u \leq 400 \\ 0 & u > 400 \end{cases} \quad (1)$$

Then, for a car represented by tuple t and characterized by the price $t.price$, the degree of meeting conditions of the above query md is calculated as follows: $md = \mu_A(t.price)$. The provided example illustrates the general rule of interpretation of fuzzy queries: the degree to which conditions of the query are met is equated with the value of the membership function of the relevant fuzzy set. In the case of complex queries, partial degrees of meeting

conditions of the query calculated in the above-mentioned manner, corresponding to particular conditions contained in the query, are aggregated with selected operators.

As it was mentioned above, the possibility of non-standard aggregation of conditions contained in the query is a significant feature of fuzzy queries. This feature significantly extends the classic scheme based predominantly on the use of conjunction and alternative as well as allows expressing often complex interrelations among partial conditions of the query. Among aggregation operators, linguistic quantifiers are particularly important as they are widely applied in the natural language and well represented in fuzzy logic.

3. Conversion of fuzzy queries into SQL standard queries using Oracle 11g XE

Construction of fuzzy queries as well as their execution and the applied grammar of fuzzy queries are usually strongly connected with the query language of a given database. This item discusses the problem of conversion of fuzzy queries into SQL standard queries using Oracle 11g XE database, in the case of which, similarly to most contemporary relational databases [6], SQL query language is used.

There are numerous fuzzy elements in queries addressed to databases:

- atomic predicates based on linguistic terms: young, tall,
- atomic predicates based on similarity of linguistic terms: information technology \approx artificial intelligence,
- complex predicates: fuzzy sum and product operators,
- modified predicates: very, around, rather, antonyms,
- fuzzy operators: approximately, a little more, etc.,
- linguistic quantifiers,
- fuzzy combination of relations,
- fuzzy aggregate functions,
- grouping by fuzzy values.

In order to discuss the problem of approach towards the representation of imprecision, examples of imprecise elements in queries addressed to database contained in the first three items of the above list were taken into account.

Two approaches towards the representation of imprecision can be distinguished [11]:

- *based on distribution of possibilities*

The approach based on the distribution of possibilities changes the method of representation of values of attributes from numerical to linguistic. Linguistic variables (also referred to as *possibility* type variables) can be presumed for attributes with a continuous domain. Values of such a variable are linguistic terms with corresponding fuzzy sets represented in the form of distribution of possibilities.

Example 1: on the *prod_year* attribute, whose domain is originally numerical, one can introduce the following linguistic terms: *New*, *Average*, *Old*, which are defined by relevant distributions of possibilities.

Example 2: the condition: ‘new car’ will be formulated conventionally as: *prod_year* is *NEW*, where *NEW* is a fuzzy set corresponding to the linguistic term *NEW* for the attribute *prod_year*.

- based on similarity

Here, values of linguistic variables are also linguistic terms, yet they are interpreted as distributions of similarity (the so-called similarity matrix is defined which stores the degree of similarity for each pair of linguistic terms). Such variables can be defined exclusively for attributes with a finite domain.

From the above reasoning, it stems that the whole interpretation of fuzzy queries comes down to the following general rule: the degree of meeting conditions of the query equates with the value of the membership function of the relevant fuzzy set. Whereas in the case of complex queries, partial degrees of meeting conditions of the query calculated in the above-mentioned manner, corresponding to particular conditions contained in the query, are aggregated with selected operators discussed in item 3.3.

3.1. Exemplary data

Assuming there are already exemplary tables with data in Oracle 10g XE database. Another column, i.e. *fuzzy_degree*, with the initially set value of 1.0 for each row, which belongs to it, was added to the table labelled *tbl_cars* presented in Fig. 1. This denotes the initial state – total degree of membership of a given row to the table labelled *tbl_cars*.

```
SELECT * FROM tbl_cars;
```

ID_SAM	MODEL	TYPE	PROD_YEAR	ENGINE_CAPACITY	PRICE	FUZZY_DEGREE
1	VOLVO	SEDAN	2010	1.6	35500	1.000000000
2	ASTON MARTIN	COUPE	2015	6.0	900000	1.000000000
3	MAZDA	CABRIO	2012	2.0	43990	1.000000000
4	OPEL	COMBI	1993	1.7	1500	1.000000000
5	VOLKSWAGEN	SEDAN	2007	1.9	23900	1.000000000
6	AUDI	COUPE	2005	1.9	21000	1.000000000

Fig. 1. Exemplary data from *tbl_cars* table

Tables *tbl_possibility* and *tbl_similarity* contain data, which will be used at the stage of conversion of fuzzy queries into typical SQL queries. The *tbl_possibility* table, as presented in Fig. 2, stores linguistic variables described by the membership function.

```
SELECT * FROM tbl_possibility;
```

username	table_name	column_name	linguistic_variable	a	b	c	d	type
user	tbl_cars	prod_year	NEW	2010	2015	2050	2050	trapezoid
user	tbl_cars	prod_year	AVERAGE	1995	2000	2010	2015	trapezoid
user	tbl_cars	prod_year	OLD	0	0	1995	2000	trapezoid
user	tbl_cars	engine_capacity	SMALL	0	0	0	1	trapezoid
user	tbl_cars	engine_capacity	MIDDLE	0	1	1.6	2.5	trapezoid
user	tbl_cars	engine_capacity	HIGH	1.6	2.5	5	8	trapezoid

Fig. 2. Exemplary data from *tbl_possibility* table

The *linguistic_variable* column stores the name of the linguistic variable. The *type* column contains information on the type of the membership function describing the linguistic variable (in the table in question all variables are described by the trapezoidal membership function presented in Fig. 3). Columns *a*, *b*, *c* and *d* contain parameters of the function. Columns *table_name* and *column_name* store the following information: on which

column and from which table the linguistic variable was presumed. The column labelled *username* contains information on the name of the user to which a given definition applies; this way various users can describe linguistic variables with identical names, presumed for the same columns of the same tables, in a different way.

$$\mu_A(x; a, b, c, d) = \begin{cases} 0 & x \leq a \\ \frac{x-a}{b-a} & a < x \leq b \\ 1 & b < x \leq c \\ \frac{d-x}{d-c} & c < x \leq d \\ 0 & x > d \end{cases}$$

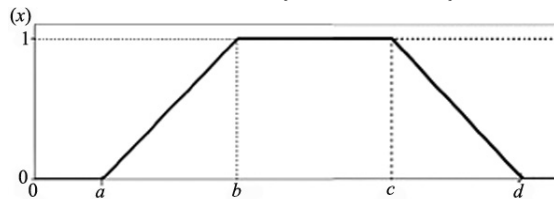


Fig. 3. Trapezoidal membership function

The table labelled *tbl_similarity* presented in Fig. 4 stores pairs of linguistic values along with the degree of their similarity. The data pertains to the column describing the type of bodywork of the car (Table 2).

```
SELECT * FROM tbl_similarity
WHERE username = 'user' AND table_name = 'tbl_cars' AND column_name = 'type'
ORDER BY value_1, value_2;
```

username	table_name	column_name	value_1	value_2	degree
user	tbl_cars	type	cabrio	cabrio	1
user	tbl_cars	type	cabrio	combi	0.2
user	tbl_cars	type	cabrio	coupe	0.2
user	tbl_cars	type	cabrio	sedan	0.2
user	tbl_cars	type	combi	cabrio	0.2
user	tbl_cars	type	combi	combi	1
user	tbl_cars	type	combi	coupe	0.6
user	tbl_cars	type	combi	sedan	0.6
user	tbl_cars	type	coupe	cabrio	0.2
user	tbl_cars	type	coupe	combi	0.6
user	tbl_cars	type	coupe	coupe	1
user	tbl_cars	type	coupe	sedan	0.8
user	tbl_cars	type	sedan	cabrio	0.2
user	tbl_cars	type	sedan	combi	0.6
user	tbl_cars	type	sedan	coupe	0.8
user	tbl_cars	type	sedan	sedan	1

Fig. 4. Exemplary data from *tbl_similarity* table

Columns *value_1*, *value_2* contain the original value and the similar value, whereas column *degree* stores the degree of similarity between the two elements. Interpretation of the remaining columns is similar as in the case of their counterparts in the table labelled *tbl_possibility*.

It needs pointing out that similarity can be presumed for columns with a discrete domain. Additionally, when defining the similarity relation one should remember that the relation must be reflexive, symmetric and transitive.

Table 2

Similarity relation for *tbl_cars* table on *type* attribute

	cabrio	combi	coupe	sedan
cabrio	1.0	0.2	0.2	0.2
combi	0.2	1.0	0.6	0.6
coupe	0.2	0.6	1.0	0.8
sedan	0.2	0.6	0.8	1.0

3.2. Fuzzy queries – fuzzy condition for possibility type variable

In a classic SQL query, the query condition can be either met or unmet. Each result row meets the conditions of the query to the same degree. In fuzzy relations, a row can appear partially, which can be interpreted as certainty or a degree of meeting conditions of the query.

A fuzzy query converted to an equivalent SQL standard query using Oracle 11g XE, as presented in Table 3, will display the offer of *new* cars. A fuzzy condition was applied in the query and a defined fuzzy set was used, which corresponds to the term *new* for the *prod_year* attribute.

Table 3

Example: display new cars for sale

Fuzzy query (conventional form)	An equivalent query in SQL-Oracle 11g XE
<pre>SELECT * FROM tbl_cars WHERE prod_year IS 'NEW';</pre>	<pre>SELECT c.*, FP_TRAPEZOID(prod_ year,a,b,c,d) FUZZY_DEGREE FROM tbl_cars c, tbl_possibility WHERE FP_TRAPEZOID(prod_ year,a,b,c,d)>0 and (linguistic_variable='NEW' and column_name='prod_year');</pre>

In the discussed example, all variables are defined by the trapezoidal membership function, the definition of which (presented in Fig. 5) was formulated in PL/SQL in Oracle 10g XE database.

In Fig. 6, the column labelled *fuzzy_degree* contains the information on the degree to which a given row meets conditions of the query. In this case, it tells us to what degree the car is *new*. It is calculated as $\mu_{\text{prod_yearNEW}}(\text{prod_year})$, and its definition is presented in Tab. 2.

```

create or replace FUNCTION
FP_TRAPEZOID(x IN NUMBER, a IN NUMBER, b IN NUMBER, c IN NUMBER, d IN NUMBER)
RETURN NUMBER IS
y number(6,5);
BEGIN
IF (x <= a) THEN y:= 0.0;
ELSIF (x > a AND x <= b) THEN y:= (x - a)/(b - a);
ELSIF (x > b AND x <= c) THEN y:= 1.0;
ELSIF (x > c AND x <= d) THEN y:= (d - x)/(d - c);
ELSE y:= 0.0;
END IF;
RETURN Y;
END FP_TRAPEZOID;

```

Fig. 5. Trapezoidal membership function defined in PL/SQL in Oracle 10g XE database

```

SELECT c.*, FP_TRAPEZOID(prod_year,a,b,c,d) FUZZY_DEGREE
FROM tbl_cars, tbl_possibility
WHERE FP_TRAPEZOID(prod_year,a,b,c,d)>0 and (linguistic_variable='NEW' and column_name='prod_year');

```

ID_SAM	MODEL	TYPE	PROD_YEAR	ENGINE_CAPACITY	PRICE	FUZZY_DEGREE
2	ASTON MARTIN	COUPE	2015	6.0	900000	1.000000000
3	MAZDA	CABRIO	2012	2.0	43990	0.400000000

Fig. 6. Result of the fuzzy query from Table 2 – fuzzy condition for possibility type variable

The parameters and the type of the membership function of the defined linguistic term can be easily read from *tbl_possibility* table presented in Fig. 2. This has been presented in Fig. 7.

```

SELECT linguistic_variable, a,b,c,d, type
FROM tbl_possibility
WHERE username='user' and table_name='tbl_cars' and column_name='prod_year'
ORDER BY a,b,c,d;

```

linguistic_variable	a	b	c	d	type
NEW	2010	2015	2050	2050	trapezoid
AVERAGE	1995	2000	2010	2015	trapezoid
OLD	0	0	1995	2000	trapezoid

Fig. 7. Result of the query – parameters and type of the membership function of the defined linguistic term

As indicated by the result of the query shown in Fig. 7, the fuzzy set $PROD_YEAR_{NEW}=(2010, 2015, 2050, 2050)$ corresponds to the term *new* for the attribute *prod_year*.

3.3. Fuzzy query – combining fuzzy conditions

Fuzzy queries, similarly to classic SQL queries, can contain complex conditions resulting from combining single conditions with logical operators. In SQL, the keyword AND corresponds to the conjunction operator, the keyword OR corresponds to the alternative operator and the keyword NOT to the negation operator.

Identical keywords are applied in the case of fuzzy queries, yet they correspond, respectively, to: fuzzy conjunction, fuzzy alternative and fuzzy negation.

Nevertheless, it needs pointing out that in the theory of fuzzy sets [7], there is a number of operators carrying out intersection operation (product operation which corresponds to the logical operation AND). These are applied interchangeably depending on the problem at hand. Most of these operators meet the criteria of the so-called triangular norm *T* (*T*-norm):

$$\mu_{A \cap B}(x) = T(\mu_A(x), \mu_B(x)) \quad (2)$$

Similarly to the execution of the intersection operation, numerous operators are used for the purpose of the operation of joining (logical sum which corresponds to the logical operation OR). The most commonly applied operators meet the criteria of the so-called triangular norm S (S -norm) also referred to as T -conorm:

$$\mu_{A \cup B}(x) = S(\mu_A(x), \mu_B(x)) \quad (3)$$

The criteria defining triangular norms consist of four fundamental conditions and due to a limited length of this article will not be presented here. These conditions were described, among others, in [1, 2, 8, 9].

The most commonly used T -norms (mapping logical operator AND) are the minimum $\text{MIN}(a, b)$ and the product (PROD) $a \cdot b$. Whereas the most commonly used S -norm operators (mapping logical operator OR) are the maximum $\text{MAX}(a, b)$ and the so-called algebraic (probabilistic) sum $a + b - a \cdot b$.

A relevant S -norm corresponds to each T -norm, provided that the following condition is met:

$$T(a, b) = 1 - S(1 - a, 1 - b) \text{ or } S(a, b) = 1 - T(1 - a, 1 - b) \quad (4)$$

Operators that meet the condition (4) form the so-called complementary (conjugate, dual) pairs. Numerous operators meeting the conditions of T -norms and S -norms have been developed and described. These operators are divided into non-adjustable, with a constant mode of operation, and adjustable (parametrized), also referred to as families of triangle norms, in the case of which the mode of operation changes depending on the accepted parameter (the degree of freedom) for the operator in question. Table 4 presents selected triangle norms forming complementary pairs.

Operators of triangle norms indicated in Table 4 execute operations only on two fuzzy (variable) sets. Operations on a greater number of sets can be executed gradually, by combining sets into pairs with the sequence of combining sets into pairs having no effect on the result (coherency quality).

From the above reasoning, it results that the degree of meeting a complex condition is calculated based on the degrees of meeting partial conditions as well as selected T -norm and its complementary S -norm.

A fuzzy query converted to an equivalent SQL standard query using Oracle 11g XE, as presented in Table 5, will display the offer of *new* cars with *high* engine cubic capacity. All variables are defined by the trapezoidal membership function, the definition of which (presented in Fig. 5) was formulated in PL/SQL in Oracle 10g XE database. In the query in question:

- a defined fuzzy set corresponding to the term *new* for the attribute *prod_year* was applied,
- a defined fuzzy set corresponding to the term *high* for the attribute *engine_capacity* was applied,
- a conjunction of both of the above-mentioned fuzzy conditions was carried out, which resulted in defining T -norm as the minimum operation.

Table 4

**Selected non-adjustable triangle norms forming complementary pairs
(prepared based on [7–10])**

No.	$T(a, b)$	$S(a, b)$
1	Minimum $\text{MIN}(a, b)$	Maximum $\text{MAX}(a, b)$
2	PROD algebraic product $a \cdot b$	Algebraic sum (probabilistic product) $a + b - a \cdot b$
3	Limited difference (Łukasiewicz's) $\text{MAX}(0, a + b - 1)$	Limited sum (Łukasiewicz's) $\text{MIN}(1, a + b)$
4	Drastic product $\begin{cases} \min(a,b), & \text{if } \max(a,b) = 1 \\ 0, & \text{otherwise} \end{cases}$	Drastic sum $\begin{cases} \max(a,b), & \text{if } \min(a,b) = 0 \\ 1, & \text{otherwise} \end{cases}$
5	Hamacher product $\frac{a \cdot b}{a + b - a \cdot b}$	Hamacher sum $\frac{a + b - 2 \cdot a \cdot b}{1 - a \cdot b}$
6	Einstein product $\frac{a \cdot b}{2 - (a + b - a \cdot b)}$	Einstein sum $\frac{a + b}{1 + a \cdot b}$

Table 5

Example: display *new* cars for sale with *high* engine capacity (first way)

Fuzzy query (conventional form)	An equivalent query in SQL – Oracle 11g XE
<p>SELECT * FROM tbl_cars WHERE prod_year IS 'NEW' AND engine_capacity IS 'HIGH'</p>	<pre> SELECT * FROM (SELECT c.model, c.type, c.prod_year, c.engine_ capacity, MIN(CASE column_name WHEN 'prod_year' THEN FP_ TRAPEZOID(prod_year,a,b,c,d) WHEN 'engine_capacity' THEN FP_ TRAPEZOID(engine_capacity,a,b,c,d) END) AS FUZZY_DEGREE FROM tbl_cars c, tbl_possibility WHERE (linguistic_variable='NEW' or linguistic_variable='HIGH') AND (column_ name='prod_year' or column_name='engine_ca- pacity') group by c.model, c.type, c.prod_year, c.engine_ capacity) WHERE FUZZY_DEGREE > 0;</pre>

Table 6

Example: display *new* cars for sale with *high* engine capacity (second way)

Fuzzy query (conventional form)	An equivalent query in SQL – Oracle 11g XE
<pre>SELECT* FROM tbl_cars WHERE prod_year IS 'NEW' AND engine_capacity IS 'HIGH'</pre>	<pre>SELECT c.model, c.type, c.prod_year, c.engine_capacity, MIN(CASE column_name WHEN 'prod_year' THEN FP_ TRAPEZOID(prod_year,a,b,c,d) WHEN 'engine_capacity' THEN FP_ TRAPEZOID(engine_capacity,a,b,c,d) END) AS FUZZY_DEGREE FROM tbl_cars c, tbl_possibility WHERE (linguistic_variable='NEW' or linguistic_variable='HIGH') AND (column_ name='prod_year' or column_name='engine_ capacity') group by c.model, c.type, c.prod_year, c.engine_ capacity having MIN(CASE column_name WHEN ,prod_year' THEN FP_ TRAPEZOID(prod_year,a,b,c,d) WHEN ,engine_capacity' THEN FP_ TRAPEZOID(engine_capacity,a,b,c,d) END) >0;</pre>

The value of the column labelled *fuzzy_degree*, the result of which was presented in Fig. 8, was set as $\min(\mu_{\text{prod_yearNEW}}(\text{prod_year}), \mu_{\text{engine_capacityHIGH}}(\text{engine_capacity}))$, the definition of which can be found in Table 5.

```
SELECT *
FROM (
  SELECT c.model, c.type, c.prod_year, c.engine_capacity,
  MIN(CASE column_name
  WHEN 'prod_year' THEN FP_TRAPEZOID(prod_year,a,b,c,d)
  WHEN 'engine_capacity' THEN FP_TRAPEZOID(engine_capacity,a,b,c,d)
  END) AS FUZZY_DEGREE
  FROM tbl_cars c, tbl_possibility
  WHERE (linguistic_variable='NEW' or linguistic_variable='HIGH') AND
  (column_name='prod_year' or column_name='engine_capacity')
  )
group by c.model, c.type, c.prod_year, c.engine_capacity
)
where FUZZY_DEGREE > 0;
```

MODEL	TYPE	PROD_YEAR	ENGINE_CAPACITY	PRICE	fuzzy_degree
ASTON MARTIN	COUPE	2015	6.0	900000	0.666666667
MAZDA	CABRIO	2012	2.0	43990	0.400000000

Fig. 8. Result of the fuzzy query from Table 5 – joining fuzzy conditions

3.4. Fuzzy queries – fuzzy condition for a similarity type variable

As it was already mentioned in item 3.1, for attributes with a discrete domain, in the case of which similarity between pairs of elements of the domain was defined, a similarity type fuzzy condition can be used. In the exemplary database, a similarity relation was defined on the *type* attribute of *tbl_cars* table (Table 2).

A fuzzy query converted into an equivalent SQL standard query using Oracle 11g XE, as presented in Table 7, will display cars with bodywork similar to coupe. Additionally, the cut-off threshold was set to 0.7.

Table 7

Example: display cars with bodywork *similar* to *coupe*. Set cut-of threshold to 0.7

Fuzzy query (conventional form)	An equivalent query in SQL-Oracle 11g XE
<pre>SELECT THRESHOLD 0.7 c.* FROM tbl_cars c WHERE type IS 'COUPE';</pre>	<pre>SELECT c.model, c.type, c.prod_year, c.engine_ capacity, c.price, s.degree FROM tbl_cars c, tbl_similarity s WHERE (c.type, s.degree) in (SELECT value_2,degree FROM tbl_similarity WHERE value_1='COUPE' and degree > 0.7) GROUP BY c.model, c.type, c.prod_year, c.engine_capacity, c.price, s.degree ORDER BY s.degree</pre>

As a result of the query, we received four offers presented in Fig. 9. The column labelled *fuzzy_degree* contains the information on the degree to which a given row meets conditions of the query. Due to the set cut-off threshold, only values greater than 0.7 have been included.

```
SELECT c.model, c.type, c.prod_year, c.engine_capacity, c.price, s.degree fuzzy_degree
FROM tbl_cars c, tbl_similarity s WHERE (c.type, s.degree) in
(
SELECT value_2,degree
FROM tbl_similarity
WHERE value_1='COUPE' and degree > 0.7
)
GROUP BY c.model, c.type, c.prod_year, c.engine_capacity, c.price, s.degree
ORDER BY s.degree
```

MODEL	TYPE	PROD_YEAR	ENGINE_CAPACITY	PRICE	fuzzy_degree
VOLKSWAGEN	SEDAN	2007	1.9	23900	0.80000000
VOLVO	SEDAN	2010	1.6	35500	0.80000000
ASTON MARTIN	COUPE	2015	6.0	900000	1.00000000
AUDI	COUPE	2005	1.9	21000	1.00000000

Fig. 9. Result of the fuzzy query from Table 7 – fuzzy condition for a similarity type variable

Needless to say, a fuzzy query can contain complex conditions resulting from joining single conditions with logical operators according to the rule presented in item 3.3.

3.5. Tests

Two different tests on the Oracle 11g XE database have been performed to analyze proposal presented in this article [19]:

- varying complexity of the query (examples of queries presented in this article),
- varying the number of tuples computed on a same query, to analyze the system scalability.

Tests have been conducted on a PC equipped with an Intel Core i5 2.80 GHz and 12 GB of memory. Queries that vary in complexity, are represented in Table 8 together with a description of them.

Table 8

Set of queries

Query ID	Fuzzy Query	Description
$Q1$	<i>new cars for sale</i>	fuzzy condition for possibility type variable
$Q2$	<i>new cars for sale with high engine capacity (first way)</i>	combining fuzzy conditions
$Q3$	<i>new cars for sale with high engine capacity (second way)</i>	combining fuzzy conditions
$Q4$	<i>cars with bodywork similar to coupe</i>	fuzzy condition for a similarity type variable

Table 9

Execution times (in milliseconds) varying number of tuples

Number of tuples	$Q1$	$Q2$	$Q3$	$Q4$
10	3	3	13	4
50	8	3	13	4
100	12	4	13	4
200	21	6	14	4
300	22	6	14	3
400	36	9	18	3
500	46	9	19	5
1000	54	13	22	8

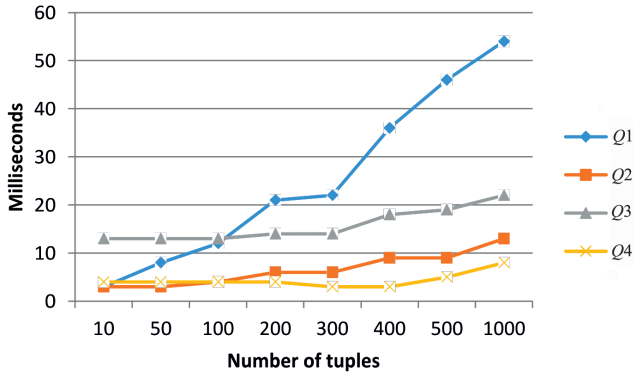


Fig. 10. Execution times in queries performed on Oracle 11g XE

Scalability was measured by varying the number of tuples in the database from 10 to 1000. To do that, examples of queries presented in this article have been executed. Execution times are shown in Table 9 and they have been illustrated in Fig. 10. In this figures, we can notice how the scalability grows accordingly with the number of computed rows in the queries. The ones that have more computational needs and/or have more complex syntax (e.g. this same example of a query (in Table 9 marked as Q2, Q3) are presented in Table 5 and Table 6 has different execution times). However, it is noticeable that varying the number of rows is not enough to distinguish the delay provoked by the changes in the number of computed rows, especially in the simplest queries [19].

4. Comparison of most relevant features in fuzzy query systems [19]

A comparison between the features of the main fuzzy relational databases in the literature [19] and proposal presented in this article is shown in Table 10. First models were mainly theoretical proposals of fuzzy relational databases. Prade H. and Testemale C. [13] have presented the original code in MACLISP on DPS8 for fuzzy query processing. Umamo [12] and Fukami have presented FOODB in SQL. The most complete implementations were provided by: Bosc P. and Pivert O. [17] called Sqlf and Kacprzyk J. and Zadrozny S. [18] called FQuery in Microsoft Access. In addition, Medina et al. [15] proposed a conceptual framework for fuzzy representation called GEFRED (Generalized Model for Fuzzy Relational Databases) and a language called FSQ (Fuzzy SQL, SQL extension) in Oracle. An implementation presented in this article is based on a Kacprzyk J. and Zadrozny S. and Medina's proposal (Table 10). It is worth noting that there are a few functionalities, that GEFRED has defined theoretically [19], that neither have been included in the implemented version, i.e. fuzzy joins and fuzzy quantifiers, nor in implementation presented in this article.

Table 10

Comparison of most relevant features in fuzzy query systems [19]

Model	Buckles B.P., Petry F.E. [12]	Prade H., Testemale C. [13]	Zemankova M., Kandel A. [14]	Medina J.M., Pons O., Vila M.A. [15]	Umamo M., Hatono I., Tamura H. [16]	Bose P., Pivert O. [17]	Kacprzyk J., Zadrozny S. [18]	Martinez-Cruz C., Noguera J.M., Vila M.A. [19]	Proposal pre- sented in this article
Manage scalar data	X	X	X	X	X	X	X	X	X
Manage non-scalar data	X	X	X	X				X	
Similarity relationship	X		X	X				X	X
Possibility distributions		X	X	X		X	X	X	X
Degree in attributes level	X	X	X	X	X	X	X	X	
Degree in tuple level		X	X	X	X	X	X	X	X
Fuzzy modifiers			X			X			
Fuzzy quantifiers				X		X	X		
Fuzzy comparison operators	X	X	X	X	X	X	X	X	X
Fuzzy group by						X	X		
Fuzzy joins		X		X	X	X			
Store fuzzy data	X	X	X	X	X				
Fuzzy queries	X	X	X	X	X	X	X	X	X
Extension SQL language				X	X	X	X	X	X

5. Conclusions

Fuzzy queries enable using a natural language. Nevertheless, in order to maintain the fuzzy nature of these expressions, they are modelled with fuzzy sets. This way, fuzzy queries enable improved representation of the requirements of the user through direct expression of the same with linguistic terms and through the use of complex methods of aggregation of partial conditions.

Fuzzy queries can be applied even if the user precisely defined his/her requirements. Yet, their application is only justified in the event there is no data, which meets these requirements. When a classic query with precisely defined conditions yields an empty data set, a fuzzy query with imprecisely defined conditions may yield a data set, which is not empty. Some of the obtained results (with the highest degree of meeting conditions of the query) may be accepted by the user. This way, the user will have a better chance of learning the content of the database and consequently will have the opportunity to modify the query. A modified query may take into account the content of the database and may better reflect the actual requirements of the user. The following conclusion can be drawn: as fuzzy queries arrange results according to the degree of meeting conditions of the query, it is easier to analyze the results and the risk of obtaining an empty reply is reduced thanks to an extended interpretation of the conditions of the query.

The provided examples of conversion of fuzzy queries into SQL standard queries using Oracle 11g XE point to easy to implement methods of obtaining fuzzy information from the database and by the same token expand its functionality. Moreover, a qualitative comparison between the most relevant fuzzy query systems in the literature and proposal presented in this article has addressed the strengths and drawbacks of this contribution [19].

Acknowledgment

Presented results of the research, which was carried out under the theme No. E-3/627/2016/DS, were funded by the subsidies on science granted by Polish Ministry of Science and Higher Education.

References

- [1] Zadrozny S., *Zapytania nieprecyzyjne i lingwistyczne podsumowania baz danych*, Akademicka Oficyna Wydawnicza, Warszawa 2006.
- [2] Myszkorowski K., Zadrozny S., Szczepaniak P.S., *Klasyczne i rozmyte bazy danych: modele, zapytania i podsumowania*, Warszawa 2008.
- [3] Zadrozny S., Kacprzyk J., *Bipolar Queries Using Various Interpretations of Logical Connectives*, Foundations of Fuzzy Logic and Soft Computing, 2007.
- [4] Mesiar R., Thiele H., *On T-Quantifiers and S-Quantifiers*, [In:] Novak V., Perfilieva I. (eds.), *Discovering the World with Fuzzy Logic*, Physica-Verlag, Heidelberg 2000, 310–326.
- [5] Novak V., Perfilieva I., *Fuzzy Logic on the Basis of Classical Logic*, Kacprzyk J., Krawczak M., Zadrozny S. (red.), *Issues in Information Technology*, EXIT, 2002.

- [6] Nowakowski G., *Open source relational databases and their capabilities in constructing a web-based system designed to support the functioning of a health clinic*, Technical Transactions, vol. 1-AC/2013, 53–65.
- [7] Baczyński D., Bielecki S., Parol M., Piotrowski P., Wasilewski J., *Sztuczna inteligencja w praktyce*, Oficyna Wydawnicza Politechniki Warszawskiej, Warszawa 2008.
- [8] Rutkowska D., Piliński M., Rutkowski L., *Sieci neuronowe, algorytmy genetyczne i systemy rozmyte*, Wydawnictwo Naukowe PWN, Warszawa 1997.
- [9] Yager R., Filev D., *Podstawy modelowania i sterowania rozmytego*, WNT, Warszawa 1995.
- [10] Czogała E., Pedrycz W., *Elementy i metody teorii zbiorów rozmytych*, Wydawnictwo Naukowe PWN, Warszawa 1985.
- [11] Rozmyte zapytania do baz danych, (online) homepage: <http://www.cs.put.poznan.pl/mhapse/LR-Rozmyte%20zapytania%20do%20baz%20danych%20II.pdf> (date of access: 2016-06-30).
- [12] Buckles B.P., Petry F.E., *A fuzzy representation of data for relational databases*, Fuzzy Sets and Systems, Vol. 7, Issue 3, May 1982, 213–226.
- [13] Prade H., Testemale C., *Generalizing database relational algebra for the treatment of incomplete or uncertain information and vague queries*, Information Sciences, Vol. 34, Issue 2, November 1984, 115–143
- [14] Zemankova M., Kandel A.: *Implementing imprecision in information systems*, Information Sciences, Volume 37, Issue 1–3, Dec. 1985, 107–141
- [15] Medina J.M., Pons O., Vila M.A., *GEFRED. A Generalized Model of Fuzzy Relational Databases*, Information Sciences, vol. 76(1–2), 1994, 87–109
- [16] Umamo M., Hatono I., Tamura H.: *Fuzzy database systems*, Proceedings of the FUZZ-IEEE/IFES'95 Workshop on Fuzzy Database Systems and Information Retrieval, Yokohama, Japan, 1995, 53–36
- [17] Bosc P., Pivert O., *SQLf: a relational database language for fuzzy querying*. IEEE transactions on Fuzzy Systems 3 (1), 1995, 1–17.
- [18] Kacprzyk J., Zadrozny S.: *SQLf and FQUERY for Access*, Proceedings of the IFSA World Congress and 20th NAFIPS International Conference, vol. 4, 2001, 2464–2469.
- [19] Martinez-Cruz C., Noguera J.M., Vila M.A., *Flexible queries on relational databases using fuzzy logic and ontologies*, Information Sciences, Vol. 366, 20 October 2016, 150–164.

VOLODYMYR SAMOTYY*

EVOLUTIONARY OPTIMIZATION OF DC MOTOR CONTROL SYSTEM

OPTYMALIZACJA EWOLUCYJNA UKŁADU STEROWANIA SILNIKIEM PRĄDU STAŁEGO

Abstract

The mathematical model of a DC motor control system's dynamic work with series impulse was designed. Control is performed by thyristor's ignition angle changing with doubling voltage. The parametric optimization was realized by genetic algorithm. The main genetic operators were crossover and mutation.

Keywords: genetic algorithm, individual, population, mutation, target function, DC motor

Streszczenie

Przedstawiono model matematyczny badania dynamiki układu sterowania silnika prądu stałego z wzbudzeniem szeregowym. Sterowanie zostało wykonane za pomocą zmiany kąta opóźnienia załączenia tyrystorów prostownika z podwajaniem napięcia. Optymalizacja parametryczna układu realizowana jest za pomocą algorytmu genetycznego. Głównymi operatorami genetycznymi wybrano krzyżowanie i mutację.

Słowa kluczowe: algorytm genetyczny, osobnik, populacja, mutacja, funkcja celu, silnik prądu stałego

* Prof. D.Sc. Ph.D. Eng. Volodymyr Samotyy, Department of Automation and Information Technologies, Faculty of Electrical and Computer Engineering, Cracow University of Technology.

1. Introduction

All electric motors are divided into DC and AC motors. AC motors are controlled by a frequency converter. These devices are controlled by voltage supplying. These devices are cumbersome and greatly complicate the regulatory process. DC motors are much more comfortable regarding these criteria. So, they are widely used in a large amount of technical systems. Sometimes, other actuators besides the motor, such as electromagnetic relays are used. However, their application is limited as they perform only a switching action.

In this work a system is considered, in which a single-phase rectifier with a doubling of voltage is used. It serves as the voltage regulator, which can control engine speed and at the same time increase its maximum amplitude. The regulation occurs by the changing of the thyristor's opening angle. It leads to the output voltage's changing that feeds the motor. The motor voltage changing directly affects the speed of its rotation. Numerical values changing the system's parameters will change the dynamics of its work. So, selecting a certain value, it is possible to optimize the transient characteristics of the motor. This problem is called a parametric optimization. It is a key element of this work.

The combination of electric motor and regulated converter of AC voltage into DC voltage is called the electric drive. The electric drive is the electromechanical system. It consists of mechanical, converting, transmitting devices and control circuit. It is possible to differ a controlled electric drive, the parameters of which can be changed and uncontrolled. The most widespread type of controlled electric drive is an electric drive of DC voltage, in which the regulation process occurs by the changing of DC motor's average meaning. The example of controlled DC voltage is thyristor's converters. Such electric drives are called thyristor drives. The main requirements to an electric drive are the support of specified rotation speed, acceleration and minimum acceleration time.

The main technical parameters of the thyristor's controlled electric drives are nominal current and voltage. The nominal current of the thyristor's controlled electric drive must be larger than the nominal current motor. The nominal voltage of the motor must be smaller than the nominal voltage of the controlled drive by 5–10%, which provides the stock for speed regulation. The choice of the thyristor's controlled electric drive is executed depending on the technical task, in which voltage, current and speed is determined. It is possible to estimate quality of the device's work according to its electromechanical characteristics. The frequency's dependence on rotating moment is called motor's mechanical characteristic. These characteristics show that frequency of motor's rotation could be regulated by supply voltage. It is achieved by changing the kindling angle of the thyristor's voltage converter. So, we select the asymmetrical straightening scheme by doubling voltage.

The DC motor's design parameters have a large impact on its characteristic. It includes an active winding bearing and its inductance. Also it includes a moment of the motor's inertia. A special interest causes the dependence of angle speed of motors' rotation on time. A transitional process in the motor's racing time must be minimized. Such work's regime can be achieved only with optimal constructive motor's parameters.

The task of parametric optimization of the motor's control system predicates the search of parameters, which provides its stable standard. To achieve this aim it is necessary

to implement its casual surplus with further estimation of motor condition. It gives an opportunity to achieve such a set of parameters, which will supply the stableness of its output characteristics. To achieve this it is necessary to use the genetic algorithm.

2. Analysis of publications

The implementation of the genetic algorithm can be found in different tasks. For example, in [1] it is proposed to use a genetic algorithm for the searching of differential equations' marginal condition. It is balanced to a two-point marginal problem's solution. The hybrid method was used, which combines two algorithms. It is a genetic and classical algorithm. In [2] the genetic algorithm was used to reduce the power consumption of mobile robots. The wheels are moved by DC motor. Power consumption's reduction was achieved during the robot's moving on uneven area. The parametric optimization of the traction drive is shown in the work [3], where parallel data processing has been used. It gives an opportunity to reduce accounting time. The genetic algorithm gives good results for nonlinear system's optimization [4]. Such an approach gives an opportunity to find a global optimum. The fields' analysis problem was explored with a genetic algorithm. The large dimension of this task, which was caused by using the method of final elements, gave an opportunity for authors to find a new decision. It is proposed to use the parametric models of lower order to account for the target function. In [6] the brushless micro motor MBDCM with structural genetic algorithm using was explored (RSGA). It combines the advantages of simple genetic algorithm and optimal structural genetic algorithm of optimal control. The calculations are confirmed by experimental results. In [7] the original idea, where a genetic algorithm was used for optimization of material's division in electric machines was suggested. The optimization of stator's jags' topology in the DC motor was executed. It reduced the pulsation of rotation moment without decrease of average rotation moment. In [8] the scheme of the motor's disturbance compensation was suggested. In conjunction with a classic feedback controller it improves the motor's reaction to micro shunting. The controller's parameters are selected by genetic algorithm. In [9] an algorithm of dynamic coding (DEAS) was shown as an alternative to the genetic algorithm. The digital modeling of an asynchronous motor's start is examined. However, this approach has the limit tasks' class. It is possible to select the parameters of the DC motor's regulation using the genetic algorithm. The microcontroller was used as a PID- regulator. The preparation of the regulator's parameters is executed by genetic algorithm. To sum up, it is possible to make the conclusion that genetic algorithms give good results during optimal parameters of control systems selecting.

3. The mathematical model of control system

The investigated system includes such two elements as an asymmetrical monophase rectifier with double voltage multiplication and DC motor with wound series. The rectifier includes two thyristors, which are controlled by the separate scheme. The dynamic equation of these elements is shown in rotation.

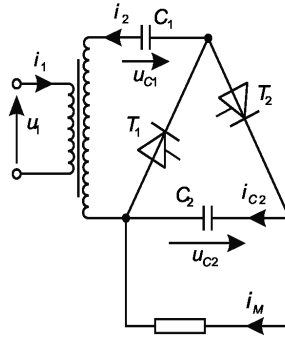


Fig. 1. The principal scheme of asymmetrical rectifier with double voltage multiplication

The asymmetrical monophaser rectifier with double voltage multiplication. In Fig. 1 the principal scheme of rectifier is shown. Voltage doubling occurs in such a way. Using doubling voltage on the transformer's exit the thyristor T_1 and capacitor C_1 are charged. The change of polarity of output voltage leads to a drop of the thyristor T_1 opening of thyristor T_2 . In this period the output transformer's and capacitor's voltage would have the same direction. Then the capacitor C_1 begins to charge. This sum would be nearly twice larger than output voltage. So, double voltage would be added to capacity. Thyristor's modeling has been executed using the scheme of ideal key. So, this scheme would have a changeable structure of electric circuit. The modeling of these schemes was executed by additional binary variables introduction in to device's dynamic equation. It assumes the values 0, 1. Zero value corresponds to closed valve's condition and the value 1 corresponds to open valve's condition. It gives the opportunity to describe all combinations of open and closed valves by single equations system. It would have three combinations.

The final equations system for monophaser rectifier with double voltage multiplication was written [12]:

$$\frac{dX_1}{dt} = BZ(t), \quad (1)$$

where:

$X_1 = [\psi, i_2, u_{C1}, u_{C2}]^T$ – the matrix of rectifier's variable condition;

$Z(t) = [u_1 - r_1 i_1, u_{C2} k_2 - u_{C1} - r_2 i_2, i_2, -k_2 i_2 - u_{C2} / R_H]^T$ – time functions' vector;

$B = \text{diag}[M, C_1^{-1}, C_2^{-1}]$ – coefficients' matrix;

$$M = \begin{bmatrix} g_1 & g_2 \\ a_{21} & a_{22} \end{bmatrix}, \quad g_1 = \frac{\alpha_1}{\alpha'' + \alpha_1 + (k_1 + k_2)\alpha_2}, \quad g_2 = \frac{(k_1 + k_2)\alpha_2}{\alpha'' + \alpha_1 + (k_1 + k_2)\alpha_2},$$

$$a_{21} = -\alpha_2 g_1, \quad a_{22} = (k_1 + k_2)\alpha_2 (1 - g_2).$$

These physical values' denominations were used here.

ψ – the transformer's flux linkage;

i_1, i_2 – the current of primary and secondary winding;

u_1 – the voltage of the transformer's power;

- u_{C1} – the capacitor's voltage C_1 ;
 u_{C2} – the capacitor's voltage C_2 ;
 r_1, r_2 – the resistance of primary and secondary transformer's windings;
 R_H – the load impedance;
 α'' – the inverse differential inductance;
 α_1, α_2 – the inverse inductance of primary and secondary windings' scattering of transformer;

The inverse differential inductance α'' is determined by magnetic curve $\varphi(\psi)$ as a derivative of:

$$\alpha'' = \partial\varphi(\psi)/\partial\psi. \quad (2)$$

It is necessary to add the dynamic equation (1) by the conditions of valves' open and close moment. These conditions determine time moments, when binominal variables k_1, k_2 change their meaning.

If two valves are closed ($k_1 = k_2 = 0$), it is necessary to control its opening conditions:

$$-d\psi / dt - u_{C1} \geq 0, \quad (3)$$

$$d\psi / dt + u_{C1} - u_{C2} \geq 0. \quad (4)$$

If the condition (3) is executed, the thyristor T_1 will be opened ($k_1 = 1$). If the condition (4) is executed, the thyristor T_2 will be opened ($k_2 = 1$).

If the thyristor T_1 is opened ($k_1 = 1$), but T_2 is closed ($k_2 = 0$) the condition of closing thyristor T_1 will be checked.

$$i_2 = 0, \quad \frac{di_2}{dt} < 0. \quad (5)$$

If the condition (5) is executed, the thyristor T_1 will be closed ($k_1 = 0$).

If the thyristor T_1 is closed ($k_2 = 0$), but T_2 is opened ($k_1 = 1$), the condition of the closing thyristor T_2 will be checked.

$$i_2 = 0, \quad \frac{di_2}{dt} > 0. \quad (6)$$

If condition (6) is executed the thyristor T_2 will be closed ($k_2 = 0$).

DC motor with series wound. It attitudes to electromechanical devices and it is described by differential equations' system of fourth order.

$$\left. \begin{aligned} \frac{di_A}{d\tau} &= S_A u_A - T_A u_F + E_A, & \frac{di_F}{d\tau} &= -T_F u_A + S_F u_F - E_F, \\ \frac{d\omega}{d\tau} &= (c\Phi i_A - M_O) / J, & \frac{d\gamma}{d\tau} &= \omega, \end{aligned} \right\} \quad (7)$$

where:

$$\begin{aligned} S_A &= 1 / (L_A + L_{AF} L_{FA} / L_F), T_A = S_A L_{AF} / L_F, E_A = S_A (L_{AF} r_F i_F / L_F - c\omega\Phi - \Delta u - r_A i_A), \\ T_F &= S_A L_{FA} / L_F, S_F = (1 - L_{FA} T_A) / L_F, E_F = (L_{FA} E_A + r_F i_F) / L_F. \\ L_A &- \text{the summary inductance of series anchor's circle;} \end{aligned}$$

- L_F – the inductance of excitation winding;
 L_{AF}, L_{FA} – the mutual inductance of an anchor's circle and an excitation's circle;
 r_A, r_F – the active supports of an anchor's circle and an excitation's circle;
 ω, γ – the angular velocity of DC motor's angle rotation;
 Φ – the magnetic flow of the motor;
 c – the constructive constant motor's anchor;
 Δu – the voltage fall in brush contact;
 J – the moment of motor's rotor inertia;
 M_O – the moment of resistance;
 u_A, u_F – the voltage of the anchor's circle and excitation's circle nourishment.

In compensated motors the consideration of a magnetic conductor's saturation could be executed approximately by magnetic curve.

In unsaturated motor it would be:

$$\Phi = L_F i_F / w_F, \quad (8)$$

To receive the DC motor's equation with series wound the equation (9) must be added by these conditions:

$$i_A = i_F = i_M, \quad u_M = u_A + u_F, \quad (9)$$

If the (7) and (9) is solved the DC motor's equation with series excitation will be received.

$$\frac{di_M}{d\tau} = C_A u_M + C_F, \quad C_A = \frac{S_A S_F - T_A T_F}{T_A + S_A + T_f + S_F}, \quad C_F = \frac{E_A (S_F + T_F) - S_A E_F - T_A T_F}{T_A + S_A + T_f + S_F}. \quad (10)$$

Now it is necessary to combine the motor's equation and the equation of asymmetric rectifier with double voltage. In equation (10) it is necessary to replace the voltage of nourishment u_M by the output rectifier's voltage u_{C2} . Then, the equation (10) will be receive the form:

$$\frac{di_M}{d\tau} = C_A u_{C2} + C_F. \quad (11)$$

In the rectifier's equation the current of capacitor C_2 is determined by this formula:

$$i_{C2} = -k_2 i_2 - u_{C2} / R_H. \quad (12)$$

In this expression the current's load is determined as a u_{C2} / R_H . Because the rectifier is loaded by the motor's windings, the current's load will be equal to motor's current i_M . It means that expression (12) will get a form of:

$$i_{C2} = -k_2 i_2 - i_M. \quad (13)$$

So, in formula (1) the vector of time functions $Z(t)$ will be:

$$Z(t) = [u_1 - r_1 i_1, \quad u_{C2} k_2 - u_{C1} - r_2 i_2, \quad i_2, \quad -k_2 i_2 - i_M]^T. \quad (14)$$

4. Optimal parameters of selection using the genetic algorithm

The GA belongs to the class of evolutionary algorithms. It can be used for solving optimization tasks and modeling, in which the method of consecutive casual selection, combination and variation of researched parameters is executed. It is reached by special mechanisms, which are similar to biological evolution. At the base of each GA the procedures of natural selection and heredity are filled. The evolutionary principle where the most adapted survive is used. It greatly differs from classic parametric optimization algorithms. For example, the task can be solved using the simple number's combination but it requires the large amount of calculations. The second classical approach is the method of gradient descent. It has a large rapid performance, but usually it attains to local solution. Instead of this, the GA always leads to global optimum and requires much lower amount of computations than the method of simple computation.

The GA's universality means that it is not connected with the nature of investigated algorithm. In the process of work it needs each chromosome's estimation, which will mean it accommodation. During selection the chromosomes with the highest estimation are chosen. So, it reproduces more often than chromosomes with lower estimation. New chromosomes' reproduction occurs using a recombination of parent's chromosomes and gene. So, the new gene's combination with its new characteristic appears. In reproduction the operations of crossover and mutation are used. Interbreeding is the creation of new chromosomes using a recombination of parent's gene. Mutation occurs only the changes in some chromosomes.

The GA's main meaning is the fitness function. Sometimes it is called the target function. In our case it is built as a difference between desirable standard output signal and real. So, the object's parameters are combined, the fitness function reaches the minimum meaning. In each generation each individual is estimated using fitness function. Then, the next generation is created, which is draws the input signal to desirable one.

If two genetic crossover operators and the mutation were compared the last one would play the secondary role. For this reason, a crossover operator can always be used, but mutation never can be used. At the first stage of crossing the couples of the chromosome are chosen from the parent's population. It is a temporary population, which consists of chromosomes, chosen by selection. It is appointed to future transformations by crossover operators and mutation. The new population is formed. At this stage the parent's population chromosomes are coupled. It is implemented by an accidental method according to the expectancy of crossover. Then, for each couple the genetic position is charged, which determines the point of the crossover. If each parent's chromosome consists of N genes, it is evidently that the point of crossing NC_C is a natural number, which is less than N . That's why the crossover point fixation becomes an accidental choice of number from interval $[1, N-1]$.

In the result of a parent's chromosome couple the pair of following descendants are formed: 1) its chromosome from 1 to N_i consists of first parent's genes but in the position from N_{i+1} to N consists of second parent's gene; 2) its chromosome from 1 to N_i consists of second parent's genes but in the position from N_{i+1} to N consists of the first parent's gene. Mutation operator with p_m probability changes the gene meaning in chromosome on reverse (from 0 to 1 and wise versa). For example if in chromosome [11101110101] the gene in the 9th position can be mutated, so its meaning, which is equal to 0, will be changed on 1. It leads to chromosome [11101111101] creation. The mutation probability is more than small.

The classic GA consists of these stages. Firstly the primary population is generated. It is a set of the task's solution. Usually it is executed by accidental way. Inside this population the reproduction must be modeled. For this task several individual's pairs are chosen accidentally, the crossover between chromosomes is executed in each couple but newly received chromosomes are placed in the new generation population. In the GA the leading principle of natural selection is saved. If the individual is more accommodated, so with the larger possibility it will take a part in crossover. Now the mutation is modeled in such accidentally chosen individuals of the new generation, which genes are changed. Then, the old population is partially or fully destroyed and we pass to the new population's examination. In mostly GA realization the next generation population includes such an amount of persons as in primary realization but taking into the results of selection generally its accommodation is larger.

The chromosomes' accommodation estimation in population is executed using a fitness function. It is accounted in each chromosome in population. If the meaning of this function is larger the quality of chromosome will be higher. Fitness function's form depends on character of solved task. It is predicated that fitness function always takes only positive meanings and, except of it for optimization tasks' solving this function must be minimized. The determination of genetic algorithm stopping condition depends on its specific using. In optimization tasks it is necessary to determine the accuracy which will be used to achieve fitness function's minimum meaning, than GA will be stopped. The algorithm stoppage can be occurred if its execution doesn't lead to an improvement of the achieved task. The algorithm can be stopped after a determined iteration amount executing. In the GA the stage of selection is extracted, where the individuals, which have been received the largest meaning of fitness function from current population, are selected from the current population and inserted to THE parents' population. The identification of stopping genetic algorithm condition depends on its specific usage. In optimization tasks it is necessary to know the accuracy, by which the minimal meaning of fitness function can be reached and the GA algorithm will be stopped. Algorithm stoppage can be occurred if its execution doesn't lead to improving achieved meaning. The algorithm can be stopped after the execution of the adjusted amount of iteration. In the GA the selection stage in which the individuals are chosen and selected from current population and included to parents' population with the largest meaning of fitness function are extracted. At the next stage, sometimes called evolution the genetic operators of crossover and mutation are used, which executes the recombination of genes in chromosomes.

5. The results of computer simulation

Based on received mathematic model of control system the program for parametric optimization of an investigated object was developed. The mathematical model is described by the system of six nonlinear differential equations. The equations' data are solved by the Runge-Kutta method of fourth stage of accuracy with constant stage of iteration. This method gives an opportunity to solve differential equation with established primary conditions. For this task the primary conditions is established as zero. It gives an opportunity to estimate the dynamic of systems work. The asymmetric rectifier with double is performed as control element. The rectifier's voltage is determined by expression $u_1 = 311 \sin(100\pi t)$ V.

The calculations were executed using such transformer's parameters: $r_1 = 2.0$ Ohm; $r_2 = 1.6$ Ohm; $\alpha_1 = \alpha_2 = 270$ H⁻¹; $C_1 = 2.0$ mF, $C_2 = 2.0$ mF. The magnetization curve is approximated by expression with accounting formula:

$$\varphi(\psi) = \begin{cases} a_1\psi, & |\psi| > \psi_1, \\ S_3(\psi), & \psi_1 \leq |\psi| \leq \psi_2, \\ a_2\psi - a_0, & |\psi| > \psi_2, \end{cases} \quad (15)$$

where:

$a_1 = 1$ H⁻¹; $a_2 = 52$ H⁻¹; $a_0 = 29.4$ A; $\psi_1 = 0.15$ W; $\psi_2 = 0.7$ Wb; $\varphi(\psi_1) = 0.15$ A; $\varphi(\psi_2) = 7.0$ A; $S_3(\psi)$ is a cubical spline. It is necessary to make a mark that $\alpha'(\psi_1) = a_1$, $\alpha''(\psi_2) = a_2$.

Motor's parameters: $L_A = 4.67$ mH; $L_{FF} = 75.8$ H; $r_A = 0.0332$ Ohm; $r_F = 45$ Ohm; $L_{AF} = L_{FA} = 0.03$ mH; $M_O = 75$ N·m; $J = 0.2$ N·m·s²/rad; $c = 70.8$ N·m/(Wb·A).

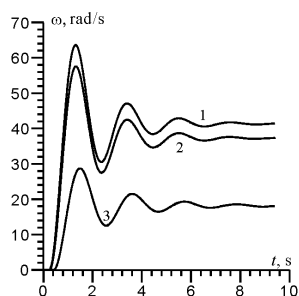


Fig. 2. The transient process' curves of motor's angular speed for ignition's angle 0° (curve 1), 30° (curve 2), 90° (curve 3) before optimization

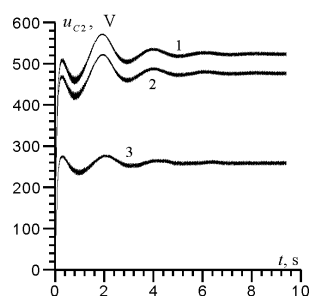


Fig. 3. The transient process' curves of output rectifier's voltage for ignition's angle 0° (curve 1), 30° (curve 2), 90° (curve 3) before optimization

Rectifier's capacitors impact on DC motor's dynamic was investigated. Firstly the accounts for appointed capacitor's capacitance were executed, it means that $C_1 = 2.0$ mF, $C_2 = 2.0$ mF. The results for a different ignition's angle 0°, 30°, 90° of thyristors were received using described data. In fig. 2 the transient process' curves of motor's angular speed for ignition's angle 0° (curve 1), 30° (curve 2), 9° (curve 3) 0° were used. To compare these results it is possible to make such conclusions. These received curves have a similar dynamic. It has a significant overshoot and quickly damped fluctuations. The difference is a constant speed meaning. For angle 0° (curve 1) the constant meaning of angle speed is equal to 41.2 rad/s, for angle 30° (curve 2) 37.2 rad/s, but for angle 90° (curve 3) 27.5 rad/s. In all cases the transient process is finished after 10 s. In all cases the overshoot is not larger than 55% from the constant meaning. In fig. 3 The transient process' curves of output rectifier's u_{c2} voltage for ignition's angle 0° (curve 1), 30° (curve 2), 90° (curve 3) are shown. These dependences include pulsations, which are connected with the process of rectification. In fig. 3 the transient process' curves of output rectifier's voltage for ignition's angle 0° (curve 1), 30° (curve 2), 90° (curve 3) are shown. In stable routine this voltage has constant and variable part. Moreover, the changeable part isn't larger than 3% of constant.

Using genetic algorithm we selected the optimal meaning of a capacitor's capacitance for different ignition's angle. In fig. 4 the the transient process' curves of motor's angular speed for ignition's angle 0° (curve 1), 30° (curve 2), 90° (curve 3) are shown. The meanings of the capacitor's capacitance $C_1 = 0.121$ mF, $C_2 = 0.61$ mF (curve 1), $C_1 = 0.104$ mF, $C_2 = 0.1422$ mF (curve 2), $C_1 = 3.88$ mF, $C_2 = 0.98$ mF (curve 3). So, it is possible to optimize the transient process only for a small ignition's angle.

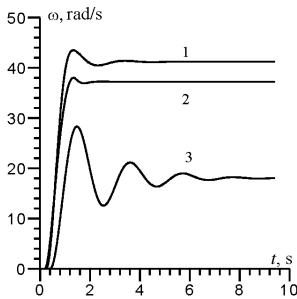


Fig. 4. The transient process' curves of motor's angular speed for ignition's angle 0° (curve 1), 30° (curve 2), 90° (curve 3) after optimization

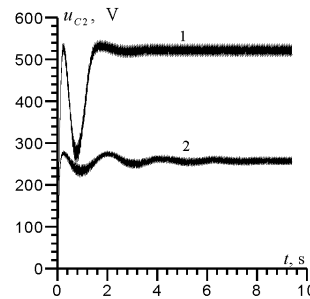


Fig. 5. The transient process' curves of output rectifier's voltage for ignition's angle 0° (curve 1), 90° (curve 2) after optimization

For ignition's angle 0° (curve 1) the transient process has a small amount of overshoots. The best result has an ignition's angle 30° (curve 2). It has the smallest overshoot and the shortest transient process (< 2.5 s). If the ignition's angle becomes larger the quality will decrease but the overshoot and transient process will increase. It is not possible to find the optimal meanings of capacitor's capacitance. In Fig. 5 the transient process' curves of output rectifier's u_{c2} voltage for ignition's angle 0° (curve 1), 90° (curve 2) The result was received by the same data exploration as in Fig. 4. In comparison with the previous example (Fig. 3) the amount of changeable parts has been increased. For curve 1 it is not larger than 7% and for curve 2 it is $< 10\%$.

This rectification scheme gives an opportunity to change a rapidity of motor's rotation using capacitor's capacitance alteration. Moreover, the ignition's angle can be equal to zero. The capacitor's capacitances were determined by genetic algorithm.

In Fig. 6 the transient process' curves of motor's rotation speed for constant meanings ω_{fixed} = 5 rad/s, $C_1 = 53.6$ mF, $C_2 = 32.14$ mF (curve 1), 2) $\omega_{\text{fixed}} = 10$ rad/s, $C_1 = 64$ mF, $C_2 = 42$ mF (curve 2), 3) $\omega_{\text{fixed}} = 20$ rad/s, $C_1 = 72$ mF, $C_2 = 100$ mF (curve 3), 4) $\omega_{\text{fixed}} = 30$ rad/s, $C_1 = 85$ mF, $C_2 = 355$ mF (curve 4), 5) $\omega_{\text{fixed}} = 40$ rad/s, $C_1 = 113$ mF, $C_2 = 495$ mF (curve 5) were shown. The appropriate curves of transient process of output rectifier's u_{c2} voltage is shown on Fig. 7.

To compare the results for the zero ignition's angle in Fig. 6 it is possible to make this conclusion. It is possible to select a capacitor's capacitance for all constant meanings of motor's speed ω_{fixed} . Furthermore, the overshoots are mostly absent and a time of transient process isn't larger than 2.5 s. The manipulation of an ignition's angle (Fig. 4) reaches the worse results and it needs the usage of appropriate regulators.

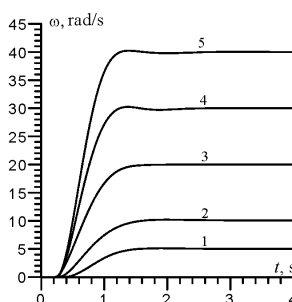


Fig. 6. The transient process' curves of motor's angular speed for constant meaning $\omega_{\text{fixed}} = 5$ rad/s, (curve 1), 10 rad/s (curve 2), 20 rad/s (curve 3), 30 rad/s, (curve 4), 40 rad/s, (curve 5)

In Fig. 7 transient process' curves of output rectifier's voltage u_{c2} for constant meaning 1) $\omega_{\text{fixed}} = 20$ rad/s (curve 1), 2) $\omega_{\text{fixed}} = 30$ rad/s (curve 2), 3) $\omega_{\text{fixed}} = 40$ rad/s (curve 3).

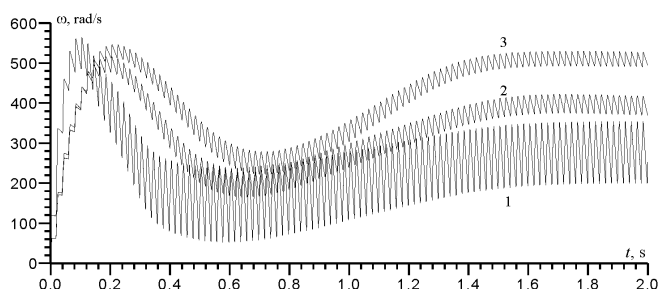


Fig. 7. The transient process' curves of output rectifier's voltage for constant meaning $\omega_{\text{fixed}} = 20$ rad/s (curve 1), 30 rad/s (curve 2), 40 rad/s (curve 3)

In comparison with the previous regime (Fig. 5) the amplitude of the changeable part is larger. For $\omega_{\text{fixed}} = 20$ rad/s (curve 1) it consists in 28% of constant part. Moreover, this system is stable enough. The change of the capacitor's capacitance and the moment's load doesn't exceed the stable limit.

It is possible to control an angular motor's speed changes to one of capacitor's capacitance. The results of analysis shows that it is more efficient to change capacitor's capacitance C_1 if the capacitor's capacitance will have a stable meaning $C_2 = 0.2$ mF. In Fig. 8 the calculated dependence of constant meanings of angle motor's speed ω_{fixed} on capacitor's capacitance C_1 is shown. It is possible to separate an area from 0.04 mF to 15 mF, where the angle motor's speed changes from 2 rad/s to 40 rad/s. The following capacitor's capacitance increase will not lead to significant increase of angle speed. In Fig. 9 the curves of transient process of motor's rotating speed for $C_1 = 0.05$ mF (curve 1), $C_1 = 0.07$ mF (curve 2),

$C_1 = 0.13$ mF (curve 3) are represented. In all cases the time of transient process isn't larger than 3.5 s. Overshooting is observed if the angle speed will have a maximum meaning. So, there curves have a very good dynamic characteristics and it is recommended to use the capacitor's overshoot for these schemes.

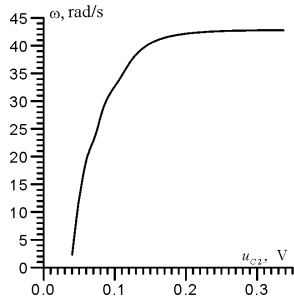


Fig. 8. The calculating steady-state values meaning's dependence of angle motor's speed ω_{fixed} on capacitor's capacitance C_1

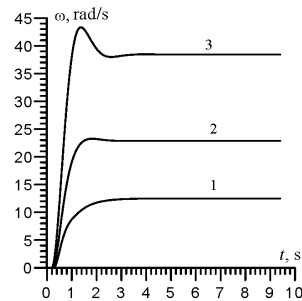


Fig. 9. The transient process' curves of motor's rotation speed $C_1 = 0.05$ mF (curve 1), $C_1 = 0.07$ mF (curve 2), $C_1 = 0.13$ mF (curve 3)

6. Conclusions

The mathematical model of control system of an angle DC motor's speed was represented. The parametric optimization of the capacitor's capacitance for different ignition's angle of thyristor's was executed. Optimization works only for small ignition angles and if it will be increased the dynamic picture of transient process becomes worse. It was proposed to select capacitor's capacitance for angle motor's speed overshooting instead of ignition's angle changing. Moreover the control's quality is provided by a wide diapason of angle speed unless 40 rad/s. In this work it is approved that it is possible to select a constant meaning of capacitance C_2 and to execute the controlling only by change the capacitance C_1 . In all concrete cases it is necessary to define what is more easy to realized, the change of ignition's angle or capacitor's capacitance. The advantages of the last approach are better for a dynamic system's characteristics.

References

- [1] Kawecki L., Niewierowicz T., *Hybrid Genetic Algorithm to Solve the Two Point Boundary Value Problem in the Optimal Control of Induction Motors*, IEEE Latin America Transactions, vol. 12, 2014, 176–181.

- [2] Yacoub M.I., Neculescu D.S., Sasiadek J.Z., *Experimental evaluation of energy optimization algorithm for mobile robots in three-dimension motion using predictive control*, 21st Mediterranean Conference on Control & Automation (MED'13), Plataniias-Chania, Crete-Greece, 2013, 437–443.
- [3] Pahner U., Hameyer K., Belmans R., *A parallel implementation of a parametric optimization environment – Numerical optimization of an inductor for traction drive systems*, IEEE Transactions on Energy Conversion, vol. 14, 1999, 1329–1334.
- [4] Gan Junying, Zhang Youwei, *Parametric optimization in nonlinear system based on genetic algorithms. 5th International Conference on Signal Processing Proceedings, WCCC-ICSP 2000*, vol. 3, Beijing, China 2000, 2037–2041.
- [5] Burgard S., Farle O., Loew P., Dyczij-Edlinger R., *Fast Shape Optimization of Microwave Devices Based on Parametric Reduced-Order Models*, IEEE Transactions on Magnetics, vol. 50, 2014, 629–632.
- [6] Chili-Wei Tsai, Chun-Liang Lin, Ching-Huei Huang, *Microbrushless DC Motor Control Design Based on Real-Coded Structural Genetic Algorithm*, IEEE/ASME Transactions on Mechatronics, vol. 16, 2011, 151–159.
- [7] Ishikawa T., Yonetake K., Kurita N., *An Optimal Material Distribution Design of Brushless DCMotor by Genetic Algorithm Considering a Cluster of Material*, IEEE Transactions on Magnetics, vol. 47, 2011, 1310–1313.
- [8] Tzes A., Pei-Yuao Peng, Guthy J., *Genetic-based fuzzy clustering for DC-motor friction identification and compensation*, IEEE Transactions on Control Systems Technology, vol. 6, 1998, 462–472.
- [9] Jong-Wook Kim, Sang Woo Kim, *Parameter identification of induction motors using dynamic encoding algorithm for searches (DEAS)*, IEEE Transactions on Energy Conversion, vol. 20, 2005, 16–24.
- [10] Neenu Thomas, Dr. P. Poongodi, *Position Control of DC Motor Using Genetic Algorithm Based PID Controller*, Proceedings of the World Congress on Engineering, WCE 2009, vol. II, 2009, 1618–1622.
- [11] Samoty V., *Optymalizacja genetyczna przetwornika liczby faz*, Technical Transactions, vol. 1-E/2012, 111–119.
- [12] Samoty V., Labiak A., *Matematyczna model nesymetrycznoji schemy wypriamlennia z podwojenniam napruhy*, Awtomatyka, wymiriuwannia ta keruwannia: Wisnyk DU “Lwiwska politechnika”, № 283, 1994, 67–69.

SERGII TELENYK*, MAKSYM BUKASOV**

DATA CENTER RESOURCE MANAGEMENT FOR SAAS

ZARZĄDZANIE ZASOBAMI CENTRUM DANYCH DLA SAAS

Abstract

The paper summarizes models and methods of data center resource management for SaaS. An approach for the allocation of computing resources for single-tenant SaaS was proposed. Different cases of this problem for excess and lack of computing resources were considered. Those problems belong to the classes of linear and nonlinear Boolean programming. In order to solve the mentioned problems, heuristic and genetic algorithms have been proposed. A comparison of their effectiveness was made.

Keywords: data center, SaaS, resource management, virtualization

Streszczenie

W artykule przedstawiono modele i metody zarządzania zasobami centrum danych dla SaaS. Zaproponowano podejście do alokacji zasobów obliczeniowych dla jednego dzierżawcy SaaS. Rozpatrzono różne przypadki tego problemu dla nadmiaru i braku zasobów obliczeniowych. Problemy te należą do klasy liniowego i nieliniowego programowania boolowskiego (logicznego). Do rozwiązania wymienionego problemu zaproponowano algorytmy heurystyczne i genetyczne. Porównano ich skuteczność.

Słowa kluczowe: centrum danych, SaaS, zarządzanie zasobami, wirtualizacja

* Prof. D.Sc. Ph.D. Sergii Telenyk, Department of Automatic Control and Information Technology, Faculty of Electrical and Computer Engineering, Cracow University of Technology.

** Ph.D. Maksym Bukasov, Department of Automation and Control in Technical Systems, National Technical University of Ukraine "Kyiv Polytechnic Institute".

Definitions

- S_i – physical server in cluster, $i = 1, \dots, n$,
- e_i – power consumption of server S_i , $i = 1, \dots, n$,
- R_k – resource of type k (e.g. CPU, memory), $k = 1, \dots, l$,
- r_{ki} – amount of resource R_k on server S_i ,
- V_j – virtual machine, $j = 1, \dots, m$,
- w_j – importance weight of applications in V_j , $j = 1, \dots, m$,
- p_{kj} – demands of V_j in resources R_k ,
- x_{ij} – Boolean variable; $x_{ij} = 1$ for V_j placed on S_i , otherwise $x_{ij} = 0$.

1. Introduction

Software as a service (SaaS) is a software licensing and delivery model in which software is licensed on a subscription basis and is centrally hosted. Multi-tenant Software as a Service is an architecture where multiple customers (tenants) share the same application instances. Those instances are typically logically divided to prevent the customers from accessing each other's data. There are considerable savings in hardware and power consumption because of the use of shared resources. Financial efficiency is a major advantage of multi-tenant SaaS [1]. Single-tenant Software as a Service is an architecture where each customer has his own application instance (i.e. a separate physical or virtual machine for each customer is needed). By having a single hosted instance, the customer can tweak and customize the software to meet their needs. With single-tenant SaaS, there is only one instance of application for a customer and it is impossible to affect another customer's tasks, so reliability and security is a major advantage of single-tenant SaaS. Single-tenant systems are generally more expensive than multi-tenant solutions because they are not the most efficient use of resources, unless fully loaded. To solve these problems, it is necessary to create flexible solutions that are built on load balancing and resource allocation [2]. This in turn requires appropriate mathematical models and methods [3–6].

2. The problem

Consumers and hosting companies agree on service level requirements, which usually include: the availability and manageability of IT infrastructure, data integrity, security, reliability, scalability. Achievement of user requirements for the lowest cost is the essence of the problem of development and functioning of the IT infrastructure.

Methods of adding more resources for a particular application fall into two broad categories: horizontal and vertical scaling [7, 8]. To scale horizontally (or scale out/in) means to add more nodes to (or remove nodes from) a system, such as adding a new computer to a distributed software application. To scale vertically (scale up/down) means to add resources to (or remove resources from) a single node in a system, typically involving the addition of CPUs or memory to a single computer or a Virtual Machine (VM).

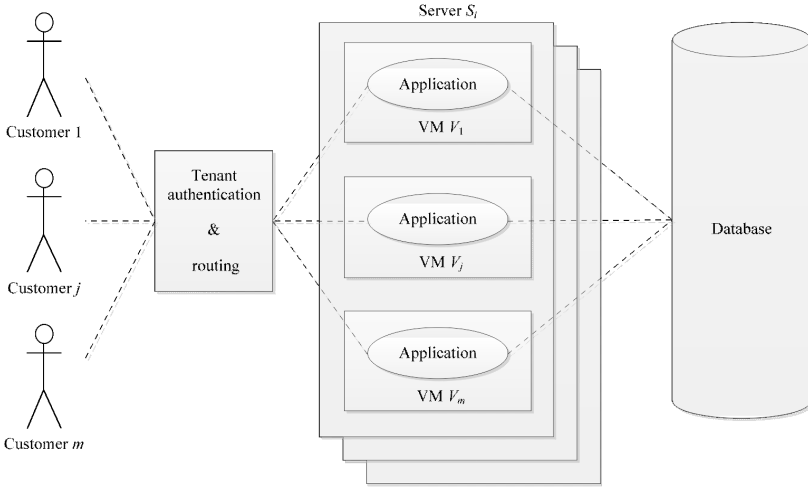


Fig. 1. Resource allocation for single-tenant SaaS

In order to meet the customer's requirements and to maximize own profit in the best way possible, the provider can solve one of the next three problems depending on resource availability.

Problem 1. If vertical scaling is not used too often, it makes sense to find a VM distribution where they will be allocated on the servers most tightly to free up most of the computing resources for other tasks or to provide a high level of energy efficiency by turning off unused servers. Also, this makes it easy to perform horizontal scaling by adding new VM with application instances to unused servers.

Firstly, demands in resources of all VMs on server S_i must not exceed the available resources of this server:

$$\sum_{j=1}^m x_{ij} p_{kj} \leq r_{ki}; k = 1, \dots, l; i = 1, \dots, n. \quad (1)$$

Secondly, all VMs should be placed on, and each of them should be placed no more than on one server:

$$\sum_{i=1}^n x_{ij} = 1; j = 1, \dots, m. \quad (2)$$

Let us define the indication of no VMs on server S_i as:

$$\prod_{j=1}^m \overline{x_{ij}} = 1, i = 1, \dots, n. \quad (3)$$

Then, in order to minimize power consumption of servers, let us use the following criteria:

$$\max \sum_{i=1}^n e_i \prod_{j=1}^m x_{ij}, \quad (4)$$

and formulate the problem as follows: satisfy (4) under constraints (1), (2).

Problem 2. If application's load can often change, it is necessary to provide the possibility of the vertical scaling i.e. adding computing resources to VMs. In order to complete this task quickly (without migration of VMs to a different physical server), we need to assure that the server will already have free (reserved) resources. To do this, instead of constraints (1), we will use:

$$\sum_{j=1}^m x_{ij} P_{kj} \leq r_{ki} - \Delta r_{ki}; k = 1, \dots, l; i = 1, \dots, n, \quad (5)$$

where:

Δr_{ki} – reserved resources of type k on server S_i .

Then, let us formulate the problem as follows: satisfy (4) under constraints (2), (5).

Problem 3. If no acceptable solution to Problem 1 was found due to a lack of resources, we have a situation in which it is not possible to place all the VMs under resource constraints (1). In this case, it would be appropriate to allocate all the needed resources among the most important VMs at the first phase, and residual resources among the rest of VMs at the second phase. So instead of constraints (2), the following should be used:

$$\sum_{i=1}^n x_{ij} \leq 1; j = 1, \dots, m, \quad (6)$$

and criteria:

$$\max \sum_{i=1}^n \sum_{j=1}^m x_{ij} w_j. \quad (7)$$

Then, let us formulate the problem as follows: satisfy (7) under constraints (1), (6).

3. Resources allocation methods

Problems described above belong to a widespread class of 0–1 programming problems. To solve these problems, we will use a heuristic greedy algorithm and guided genetic algorithm [9].

Heuristic algorithm. Since we are interested in the densest distribution of VM through the servers, let us formulate an idea of the algorithm as follows:

while (the list of unallocated VM is not empty)
 {
 try to place VM with the highest requirements to CPU;
 try to place VM with the highest requirements to RAM;
 }

Genetic algorithm GA. Since each *VM* can be placed not more than on one server, for encoding genes, let us move from $n*m$ matrix x_{ij} of Boolean variables to the length m vector y_j of discrete variables. Each element of that vector is the server's number $I = 1, \dots, n$, which contains the appropriate *VM*. For example:

$$x_{ij} = \begin{bmatrix} 0 & 0 & 0 & 0 & 1 & 0 & 1 & 1 \\ 0 & 1 & 0 & 1 & 0 & 0 & 0 & 0 \\ 1 & 0 & 0 & 0 & 0 & 1 & 0 & 0 \\ 0 & 0 & 1 & 0 & 0 & 0 & 0 & 0 \end{bmatrix}$$

$$y_j = [3 \ 2 \ 4 \ 2 \ 1 \ 3 \ 1 \ 1].$$

This method of coding genes allows, firstly, to reduce the dimension of the problem, and secondly, to provide automatic execution of constraints (3). Herewith, the mutation operation will correspond to *VM* transferring from one server to another and the crossover operation – to multiple *VM* migrating between servers [10].

To provide the possibility of turning off unused servers in problems 1 and 2, we must provide the most dense allocation of *VM* on servers under resource constraints (1). Let us define the fitness function for this task as:

$$f = \sum_{i=1}^n F_i, \quad (8)$$

$$F_i = \begin{cases} A_i^2, A_i \geq 0 \\ -B(A_i), A_i < 0 \end{cases}, \quad (9)$$

where:

- A_i – free resources on server S_i ,
- B – penalty function.

4. Experimental results

The effectiveness of the proposed algorithms was carried out as follows. Cluster of n servers ($n = 4, 8, 12, 16$) had been simulated. Each server in cluster had 8 CPU cores and 32 Gb of RAM. *VMs* with random demands to CPU and RAM had been created and placed on the first server where it can be placed according to resource constraints (3). If a new *VM* cannot be placed on either server, we had tried to optimize *VMs* allocation scheme. Two series of experiments, differed by the spread of demands to CPU and RAM, were done. For each series 100 samples were randomly generated. Each problem was solved with heuristic and genetic algorithm. Total numbers of servers that can be turned off after migration of *VMs* in all 100 experiments are shown in the Table 1 and Fig. 2.

Experimental results

<i>n</i>	Serie 1 (100 experiments, low spread) CPUmin = 3, CPUmax = 5, RAMmin = 10, RAMmax = 20		Serie 2 (100 experiments, high spread) CPUmin = 1, CPUmax = 8, RAMmin = 1, RAMmax = 32	
	Heuristic algorithm	Genetic algorithm	Heuristic algorithm	Genetic algorithm
4	14	102	3	112
8	42	212	18	239
12	72	295	38	366
16	88	379	62	487

The number of servers in cluster deferred on *x*-axis. On *y*-axis – the total number of servers in 100 experiments that can be successfully turned off. The results of heuristic algorithm are labeled as «H», genetic – as «GA», series of experiments are labeled with numbers 1 and 2.

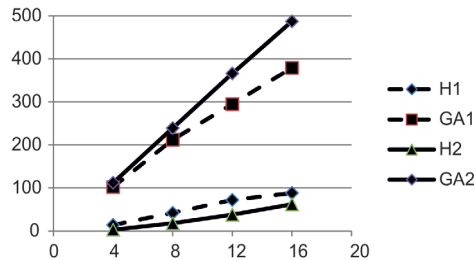


Fig. 2. Comparison of heuristic and genetic algorithms effectiveness

5. Conclusions

Models and methods for solving the resource allocation problem in data centers providing single-tenancy SaaS were proposed.

Formulated problems were reduced to problems of Boolean programming. Greedy heuristic and genetic algorithms were proposed. Genetic algorithm provides much better results for both series of experiments.

Results of the experiments confirmed the efficiency of the proposed approach for SaaS service providers.

References

- [1] Lebrun C., *The Benefits of Multi-tenancy to Manage IT & Communication Expenses*, Cimpl Blog, 2016, <http://blog.cimpl.com/the-benefits-of-multi-tenancy-to-manage-it-communication-expenses>.
- [2] Resource Management with VMware DRS, VMware Infrastructure, 2006, https://www.vmware.com/pdf/vmware_drs_wp.pdf.
- [3] Katyal M., Mishra A., *A Comparative Study of Load Balancing Algorithms in Cloud Computing Environment*, International Journal of Distributed and Cloud Computing, Vol. 1, Issue 2, 2013.
- [4] Beloglazov A., Buyya R., *Optimal online deterministic algorithms and adaptive heuristics for energy and performance efficient dynamic consolidation of virtual machines in Cloud data centers*, Concurrency and Computation: Practice and Experience, vol. 24, no. 13, 2012, 1397–1420.
- [5] Horri A., Mozafari M.S., Dastghaibiyar G., *Novel resource allocation algorithms to performance and energy efficiency in cloud computing*, The Journal of Supercomputing, vol. 69, no. 3, 2014, 1445–1461.
- [6] Xiao Z., Song W., Chen Q., *Dynamic resource allocation using virtual machines for cloud computing environment*, Parallel and Distributed Systems, IEEE Transactions on, vol. 24, no. 6, 2013, 1107–1117.
- [7] Schluting C., *Practical VM Architecture: How Do You Scale*, Enterprise networking planet, 2008, <http://www.enterprisenetworkingplanet.com/netos/article.php/3753836/Practical-VM-Architecture-How-Do-You-Scale.htm>.
- [8] Ellis J., *Thinking Differently about Scalability with Cloud Computing*, VMware Cloud Blog, 2010, <http://blogs.vmware.com/vcloud/2010/11/thinking-differently-about-scalability-with-cloud-computing.html>.
- [9] Telenyk S., Rolik O., Bukasov M., Halusko D., *Models and methods of resource management for VPS hosting*, Technical Transactions, Vol. 4-AC/2013, 41–52.
- [10] Telenyk S., *Resource Management for Server Virtualization in the Limitations of Recovery Time Objective*, S. Telenyk, M. Bukasov, M. Yasochka, Proceedings of International Congress on Information Technology, Computational and Experimental Physics (CITCEP'2015), 18–20 December, Cracow 2015, 247–250.

VOLODYMYR SAMOTYY*, ANDRII PAVELCHAK**,
ULYANA DZELENDZYAK**

THE METHOD SELECTION OF CONTROL SYSTEM'S PARAMETRIC OPTIMIZATION

WYBÓR METODY OPTYMALIZACJI PARAMETRYCZNEJ SYSTEMÓW STEROWANIA

Abstract

In this article the methods' review of a control system's parametric optimization have been performed. According to the revealed analysis, the genetic algorithms have been chosen as the most appropriate tools for these tasks. Using genetic algorithms, the global optimum could be identified. To demonstrate it the system's parametric optimization, which consists of controlled three phase half wave rectifier and DC motor with independent excitation has been executed, using a classic genetic algorithm.

Keywords: evolutionary algorithms, DC motor, controlled three-phase rectifier, PID-regulator

Streszczenie

W artykule rozpatrzono przegląd metod optymalizacji parametrycznej systemów sterowania. Analiza wykazała, że najbardziej odpowiednią dla takiego rodzaju zagadnień są algorytmy genetyczne, ponieważ umożliwiają obliczenie optimum globalnego. Dla ilustracji realizowano optymalizację parametryczną układu: sterowany trójfazowy prostownik jednopółkowy – silnik prądu stałego z niezależnym wzbudzeniem, na podstawie klasycznego algorytmu genetycznego.

Słowa kluczowe: algorytm genetyczny, silnik DC, trójfazowy prostownik sterowany, regulator PID

* Prof. D.Sc. Ph.D. Eng. Volodymyr Samotyy, Department of Automation and Information Technologies, Faculty of Electrical and Computer Engineering, Cracow University of Technology.

** Assoc. Prof. Ph.D. Eng. Andrii Pavelchak, Assoc. Prof. Ph.D. Eng. Ulyana Dzelendzyak, Department of Computerized Automatic System, Lviv Polytechnic National University, Ukraine.

1. Introduction

The problem of parametric optimization is not new. Its algorithms' realization could be used for an enterprise's costs optimization, traffic interchanges, models of people's life, animals' population in farms. Also it should be performed for mathematical models' parameters selection, control's rules, cryptography, approximation tasks and others. In fact the abilities of using optimization algorithms are limited only by scientist's imagination. The essence of the parametric optimization task is to find some parameters, using which the local and global optimum will be received for target function. For this reason, the last is the most significant result. The parametric optimization of control system gives an opportunity to design it in the best way for its responsibility to the quality criteria. The process of optimization method selection depends on the amount of information about exploration object, its mathematical model, linearity or nonlinearity and other factors. If the methods depend on exploration of an object some methods such as evolutionary methods can be used for the most widespread fields of tasks.

In our article the parametric optimization for DC motor control system has been performed by genetic algorithm. In fact this article is a continuation of a previous one [1] with contribution of controls' system modifications.

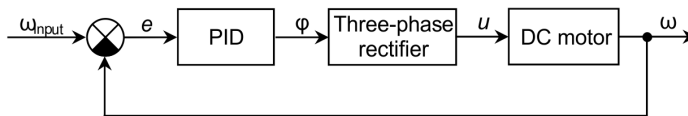


Fig. 1. Structural scheme of DC motor's control system

In system (Fig. 1) the DC motor with independent excitation in which the winding is fed on a separate source of DC voltage has been chosen as an element of control. The feed of the anchor's windings is executed by the thyristor's constant voltage rectifier to alternating voltage. The power of armature windings and motor control is executed by the thyristor's rectifier AC voltage to DC voltage. To reduce feeding voltage pulsations the three phase half wave rectifier was chosen. It gives an opportunity to improve the dynamic characteristics of control system. A DC motor has been connected to a rectifier using a capacity filter, which provides the filtration of the output voltage pulsation of the rectifier.

The regulation of DC motor's speed is executed using a PID-regulator, which is algorithmically realized in the existing microcontroller. The microcontroller receives the meaning of the anchor's speed rotation ω using an incremental encoder, which is connected to the motor's billow and it is compared with set value ω_{input} . Accuracy regulation e , as a difference between this meaning is transmitted on a PID-regulator. Rework set regulation e , the regulator forms the angels of late opening thyristor's valves ϕ . Thus, we change the voltage meaning in the output rectifier and accordingly the angle of the DC motor's valve rotation is also changed. The developed mathematical model of this system gives an opportunity to explore the parameter's impact on the system's work and the parametric optimization of the output system's mechanic characteristics can be executed using genetic algorithms.

2. Analysis of publications

In automatic control's general theory the regulator type is chosen depending on the model of a control object. In our case, the PID regulator has been selected. The most complicated part in PID regulator realization is the process of the coefficient K_p, T_i, T_d selection.

The methodology of PID regulator parameters was proposed by Ziegler and Nichols for the first time in 1942. Two methods of PID regulator were suggested [11]. The first method was based on the parameters of a control's object output signal during the single signal input. The second method based on object's frequency characteristics. The different approach has been proposed in a CHR method [12]. The maximum speed increase criteria could be used if the overshoot does not exist or the overshoot takes no more than 20 percent. In comparison with the Ziegler-Nichols method it has larger reserve of resistance. The methods are easy but it does not provide the sufficient accuracy of regulator's settings.

To increase the precision the regulator's synthesis has been occurred. The regulator parameters are calculated based on the system's model. The approximation of object dynamic by the model of the first and second order occurs with delay. It does not give an opportunity to provide an analytical solution of the equation's system and consider the nonlinear characteristics of control object, which is important during the higher stage model's solution.

The manual selection of PID regulator parameters is frequently used. It is the method of mistakes and attempts. To improve the process of parameters research rules based on experience the theoretical analysis and numerous experiments are used.

To take into account all specifics, especially the nonlinearity of control's object, the numeric methods of optimization should be used. It gives an opportunity to customize the regulator's parameters optimally for the different complexity models. During the process of establishing PID regulator parameters the optimization methods execute the minimization for the quality criteria or even complex criteria consisting of several criteria with different weight coefficient. To receive the necessary form of output characteristic some limits ought to be imposed. The optimization methods give an opportunity to receive an accurate meaning of PID regulator and it does not need the control system simplification. Despite this, these methods could have the continued process of minimum research.

The optimization algorithms used for optimal control system determination have been divided into two classes: deterministic and probabilistic [2]. In each step of deterministic algorithm execution the single variant for its work duration could be used. If it is absent the algorithm will finish its work. Usually for the same input data the deterministic algorithm proposes the same results. But, sometimes, the situation could occur where deterministic algorithms find only a local optimum. If the feedback between the received result and its suitability is not obvious, it changes dynamically, or becomes too complicated, so the usage of the most deterministic approach is not effective. In such situations the probability algorithms could be performed. Usually, the accurate algorithms could be much more effective than probability algorithms in large amount of areas. Moreover, the probability algorithms have an additional disadvantage, it could cause different results when launching the same data.

Between deterministic algorithms [3, 4] the following method's group could be chosen: State space search, the method of Branch and bound, Cutting-plane method and others.

Between probability algorithms the following methods could be chosen [5]: Hill climbing algorithm, Cutting-plane method, Tabu Search, method of extremal optimization, Downhill simplex method. The probability algorithms should be marked as a separate group [5–8]: genetic algorithms, evolutionary strategies, genetic programming, evolutionary programming, differential evolution, the algorithm of division estimation.

During PID parameters optimization the local optimums ought to be exist, so the usage of deterministic methods have not been appropriated. For example, the method of gradient descent gives an opportunity to find the global optimum for convex function. The existing probability optimization methods have been analyzed and genetic algorithms have been chosen as the most optimal solution for our task.

3. The mathematical model of control system

The model of a DC motor's control system with independent excitation, which was explored in the previous article [1], was insignificantly changed. Instead the tachogenerator incremental encoder had been used (Fig. 2). Also additional resistance to the anchors windings and the motor's stator was connected. This resistance is appropriated to quality improvement of motor's dynamic characteristics.

Because the full derivation of dynamic equation for three phase half wave rectifier and DC motor with independent excitation was shown in [1], the final equations would be performed in this article. The parameters of secondary windings have been led to the primary parameters by the amount of wind.

In normal Cauchy form the equation's condition of three phase half wave rectifier has the following performance:

$$\frac{dX}{dt} = BZ(t), \quad (1)$$

where:

$$X = (\psi_A, \psi_B, \psi_C, i_{2A}, i_{2B}, i_{2C}, u_C)^T, \quad B = \text{diag}(M, 1/C), \quad M = (D^{-1}\Lambda, A)^T,$$

$$D = P + \alpha_0 \cdot E_{33} + \alpha_1 + \alpha_2, \quad P = \text{diag}(\alpha''_A, \alpha''_B, \alpha''_C), \quad \Lambda = (\alpha_1, \alpha_2),$$

$$\alpha_1 = \text{diag}(\alpha_{1A}, \alpha_{1B}, \alpha_{1C}), \quad \alpha_2 = \text{diag}(k_A \alpha_{2A}, k_B \alpha_{2B}, k_C \alpha_{2C}),$$

$$A = (-\alpha_2 D^{-1} \alpha_1, \alpha_2 (E - D^{-1} \alpha_2)), \quad E_{33} = (E_3, E_3, E_3), \quad E_3 = (1, 1, 1)^T,$$

$$Z(t) = (U - RI, i_{2A} + i_{2B} + i_{2C} - i_a)^T, \quad U = (u_{1A}, u_{1B}, u_{1C}, -u_C, -u_C, -u_C)^T,$$

$$R = \text{diag}(r_{1A}, r_{1B}, r_{1C}, r_{2A}, r_{2B}, r_{2C}), \quad i = (i_{1A}, i_{1B}, i_{1C}, i_{2A}, i_{2B}, i_{2C})^T,$$

$$i_{1j} (j = A, B, C) = \varphi(\psi_j) + \alpha_0 \cdot (\psi_A + \psi_B + \psi_C) - i_{2j}.$$

Values determination: u_{1A}, u_{1B}, u_{1C} is the input three phase voltage; Ψ_A, Ψ_B, Ψ_C is the working linkage phase; $i_{1A}, i_{1B}, i_{1C}, i_{2A}, i_{2B}, i_{2C}$ is the working winding's current of primary

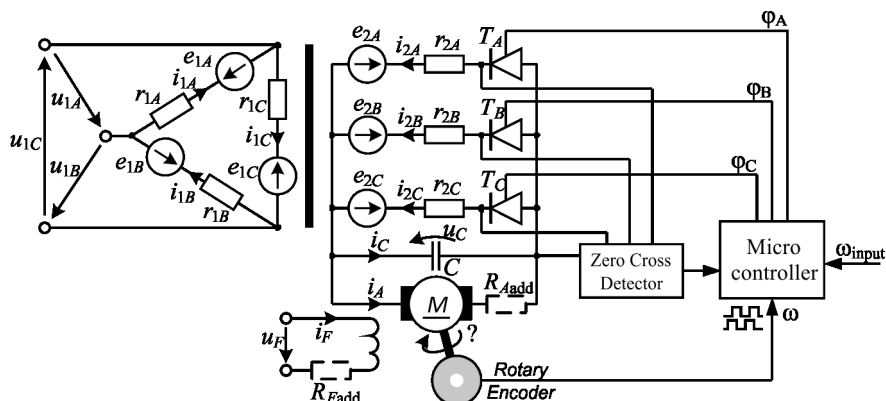


Fig. 2. Control system of DC motor with independent excitation

and secondary transformer's; $r_{1A}, r_{1B}, r_{1C}, r_{2A}, r_{2B}, r_{2C}$ is the transformer windings' resistance; $\alpha_{1A}, \alpha_{1B}, \alpha_{1C}, \alpha_{2A}, \alpha_{2B}, \alpha_{2C}$ is the inverse scattering windings' inductance; $\varphi(\Psi_A), \varphi(\Psi_B), \varphi(\Psi_C)$ is the magnetic voltage in the transformer's core, determined by its magnetization curves; α_0 is the inverse inductance of zero sequence scattering; C is the filter capacitor; k_A, k_B, k_C is the additional logical changes, which could receive the meaning 0 or 1.

The thyristors would be opened if the additional voltage was higher than the voltage of the thyristor's inclusion and administer microcontroller's permission signal:

$$-\frac{d\Psi_i}{dt} - u_C > U_{ON}; \quad i = A, B, C. \quad (2)$$

In our model the simplifications were introduced and charged with the minimal anode voltage. Using it the thyristor will switch on and it will be equal to zero $U_{ON} = 0$.

If the microcontroller does not manage the input voltage of thyristor's rectifier it usually ought to pass the permission signal on thyristors' work will be determined only by the condition (2). In our mathematical model the permission signal of thyristors' open are modeled by logical variables. k_A, k_B, k_C . If it is necessary to model output voltage of the thyristor's rectifier for microcontroller in determined time moments it should pass the control signals on thyristors. The additional detection modulus of zero intersection determines the points of intersection (from negative to positive area) for all thyristors.

Then, the administer microcontroller using peripheral timers account for the necessary holdbacks for the thyristor's opening. For example if a frequency of input voltage 50 Hertz and the angle of the holdback thyristor's opening is 30° the time of holdback is $\Delta\tau = 30^\circ / (50 \cdot 360^\circ) \approx 1.67$ msec. So, the microcontroller individually for each phase pass the administer signal for this thyristor's opening after its zero intersection. The administer

signal is decontaminated during the part of time equal to period's half of input signal minus $\Delta\tau$. Also this interval of time is accounted by peripheral timers of administer microcontroller.

Thyristors are closed if the administer signal is absent and if the current is less than current of thyristor's hold.

$$i_{2i} = 0, \quad \frac{di_{2i}}{dt} < 0; \quad i = A, B, C. \quad (3)$$

In mathematical model the thyristors' are closed if condition (3) is performed, the additional variables get the meaning $k_i = 0$. During modeling when the current is $i_{2i} \leq 0$, then the additional logical variables assigned $k_i = 0$ and the current is established in zero.

The mathematical model of control system, apart from the seven condition equations of three phase half wave rectifier, includes two differential equations for DC motor and one equation of movement.

The differential current's equations of DC motor winding with independent excitation are shown as:

$$\frac{di_A}{dt} = S_A \cdot u_C + T_A \cdot u_F + E_A, \quad \frac{di_F}{dt} = T_F \cdot u_C + S_F \cdot u_F + E_F, \quad (4)$$

where:

$$S_A = 1 / (L_A + L_{AF}L_{FA} / L_{FF}), \quad T_A = -S_A L_{AF} / L_{FF}, \quad T_F = -S_A L_{FA} / L_{FF},$$

$$E_F = -(L_{FA} \cdot E_A + (r_F + R_{Fadd}) \cdot i_F) / L_{FF}, \quad S_F = (1 - L_{FA} \cdot T_A) / L_{FF},$$

$$E_A = S_A (L_{AF} \cdot (r_F + R_{Fadd}) \cdot i_F / L_{FF} - c \cdot \omega \cdot \Phi - \Delta u - (r_A + R_{Aadd}) \cdot i_A).$$

The description of values: L_A – is the summary inductance of series anchor's circle; L_{FF} is the inductance of excitation winding; L_{AF} , L_{FA} are the mutual inductances of the anchor's circle and excitation circle; ω is the angle speed of anchors rotation; Φ is the magnetized motor's flow; c is the constructive anchor's stable MPC; Δu is voltage reduction in brush contact.

In compensated motors the consideration of a magnetic conductor's saturation could be executed approximately by the magnetized curve $\Phi = \Phi(i_F)$, $L_{FF} = L_{FF}(i_F)$. In an unsaturated motor $\Phi = ki_F$, $L_{FF} = \text{const}$.

The dynamic equation is written according to Dalamber's equation:

$$\frac{d\omega}{dt} = (c\Phi i_A - \text{sign}(\omega) \cdot M_O) / J, \quad (5)$$

where:

J – a moment of a motor's rotor inertia,

M_O – a moment of resistance.

During D motor's work modeling the condition of the motor's rotation start is important

$$|c \cdot \Phi i_A| > M_O, \quad (6)$$

If condition (6) is not executed, the meaning $\omega = 0$ is charged.

4. Implementation of PID-controller

For this system of DC motor control it is necessary to keep some speed of motor's shaft according to charged meaning ω_{input} . The charged meaning could rapidly change in time. The PID-regulator is involved in the system. It is realized in administering the microcontroller. For algorithm implementation of PID-regulator its discrete form, in which continual integration is performed using the method of rectangles.

$$u(n) = K_p \cdot \left(e(n) + \frac{\Delta t}{T_i} \cdot \sum_{k=0}^n e(k) + \frac{T_d}{\Delta t} \cdot (e(n) - e(n-1)) \right), \quad (7)$$

where:

- Δt – a time of discretization,
- K_p – a proportional coefficient,
- T_i, T_d – constants of time integration and differentiation.

For control system the implementation of discrete PID-regulator has a range of specifics: it is necessary to limit the meaning of integrator's sum accumulation, to choose the form administer signal's presentation; to establish the additional limits on the range of control signal meanings. In this system the administer signal from entrance of PID-regulator is performed by the angle of holdback of thyristor's open. The particularity of DC motor control's system means that the DC motor's shaft will be rotated if the holdback's angle of thyristor's opening gets the meaning from 0 до 150°. This fact was fixed during of thyristor rectifier modeling. Taking in to account these comments the algorithmic implementation of discrete PID-regulator could be performed by this pseudocode:

```

error = inputOmega - currentOmega
integral = integral + error
if(integral > Imax) than integral = Imax
if(integral < Imin) than integral = Imin
derivative = (error - previous_error)
output = Kp * (error + dt / Ti * integral + Td / dt * derivative)
if(output >= 150) than angleThyristor = 0
else if(output <= 0) than angleThyristor = 150
else angleThyristor = 150 - output
previous_error = error

```

Before the first usage of PID-algorithm the variables *previous_error* and *integral* are performed by zero. The meaning of current mistake for each time is saved for repeated usage in following iterations of PID-algorithm. The meaning of time discreet *dt* is selected. It should have meaning less than 1/10 of constant meaning of transient objet characteristics. In this case for transient objet characteristic of rotation motor's spindle. In our case transitional characteristic is performed as a speed of motor's rotation. The meaning *dt* determines the periodicity of PID-algorithm download.

5. Implementation of genetic algorithm

The parametric optimization of this task is executed by classic binary genetic algorithm. [6, 7]. For optimization in binary genes the coding of chosen parameters are executed by quantization of possible parameters' meaning.

$$step_i = \frac{valueMax_i - valueMin_i}{2^n - 1}, \quad gene_i = \frac{param_i - valueMin_i}{step_i} \quad (8)$$

The inverse decode is executed by formula (9).

$$param_i = valueMin_i + gene_i \cdot step_i \quad (9)$$

In this algorithmic implementation the chromosome is performed by genes structures of unsigned whole data type. For parameters codation an arbitrary number of bits could be chosen. In this case it could be from 8 to 32 bits. The lower amount of bits gives an opportunity to cover the field of investigation more quickly. The larger amount provides better accuracy of investigation. For a genetic algorithm operator the developed algorithms could work only in chosen bits. The remaining bits in the gene structure have been established in zero and could be ignored:

The developed realization of binary genetic algorithm has the following sequence of actions:

1. *The creation of primary population with chromosomes initialization and fitness meaning calculations.* The engeneration of the binary strip is executed bit by bit using a randomizer. The primary amount of population depends on task type, which should be optimized. Theoretically, the larger amount of population will be occurred, the better result is received. But in practice the execution requires a significant time expenses. Then, in the process of genetic algorithm execution the amount of population could be reduced or increased. For our task the amount of population are 30–40 chromosomes, because the calculation of mathematical model's transcendent process is protracted operation. The calculation of fitness meaning is parallelized depending on the amount of physical and logical nucleus of PC's processor.
2. *Population's sorting by fitness meaning.* It is executed by the best fitness meanings (minimal or maximal). The best fitness meaning locates at the bottom of population. The worst fitness meaning locates in the beginning of population.
3. *Selection.* The chromosomes selection for population is executed by linear ranking:

$$Fitne\beta(Pos) = 2 - SP + 2 \cdot (SP - 1) \cdot \frac{Pos - 1}{Nind - 1} \quad (10)$$

where:

- $Nind$ – chromosomes' amount in population,
- Pos – chromosomes' position in population (the worst accommodated chromosomes have $Pos = 1$, the best accommodated chromosomes have $Pos = Nind$),
- SP – a pressure selection's coefficient, which reaches the meaning in limits [1; 2].

According to received meaning Fitness the amount of chromosome's inputs is determined. The additional best chromosomes' copies are compared with the worse replacement in the beginning of the population. During genetic algorithm's testing the coefficient *SPhave been shown as optimal* with the meaning 1.6–1.8.

1. *The elite chromosomes' selection.* The preset amount of the best chromosomes should be copied into intermediate buffer.
2. *Crossing.* The binary operator of crossing (crossover) is used. Mating is executed according to ranking. At the first time the best would be ranked then the worst would be ranked. In general the option when the best chromosomes are ranked with the worst chromosomes has given the worst result as the option of accidental chromosomes' selection for crossing.
3. *The fitness meaning calculation for received population after crossing.* The calculation of fitness meaning is parallelized and depends on amount of physical and logical nucleus of PC's processor.
4. *The sorting of population according to fitness meaning.* At this stage sorting is necessary for the most accommodated chromosome determination, which would not be mutated.
5. *Mutation.* For this procedure the percent of expectation in the whole population is defined. Based on this meaning the amount of bits, which should be mutated (inverted its meanings from 0 into 1 or vice versa) had been calculated. The structure of masks, where the positions of these bits have been determined casually, should be created. Firstly in population the chromosome's number is determined casually, than the number of bits will be determined. The masks' structure is added to the chromosomes' structure by labeled XOR operation. Thus, the inversion operation is executed. The most accommodated chromosome is excluded from the mutation procedure. During genetic algorithm testing the meaning of mutation percentage has been optimal in 1–5% limits.
6. *The fitness meaning calculation for mutated succession.* The calculation of fitness meaning is parallelized depending on the amount of physical and logical nucleus of PC's processor.
7. *Population's sorting by fitness meaning.* This step could be excluded if the elitism's meaning would be equal to 0.
8. *Elitism.* This procedure pastes selected chromosomes in 4 with worse chromosomes' changes in the beginning of population.
9. *Population's sorting by fitness meaning.*
10. *Population's copies creation.* These copies would be necessary if the optimum research continued using genetic algorithm. It is possible that during genetic algorithm some parameters could be changed as an optimization's object or as an algorithm. For example, some research limits ought to be replaced for investigated parameters. For this it is necessary to stop genetic algorithm's work, choose new parameters and continue optimization.
11. If the adjusted amount of the population was reworked the genetic algorithm's performance would be finished. If the genetic algorithm's performance wouldn't be finished step 3 has been executed. The genetic algorithm implementation was executed in C# language. Appropriately, the built-in integrator of pseudorandom numbers with equable divisions' law was used. NET Framework, based on subtractive algorithm of D. Knuta has been created. To fitness meaning parallelization the meaning's class Task

has been used. The genetic algorithm implementation was approved on the tests' task for optimization [10]: De Jong's function 1, Axis parallel hyper-ellipsoid function, Rotated hyper-ellipsoid function, Rastrigin's function 6, Schwefel's function 7. For all testes' tasks the realized algorithm has found determined function's minimum and maximum.

6. Results of control system optimization

For development of our system's mathematical model the program was written in C# and its dynamical process' simulation was executed.

The feeding voltage of three phase half wave rectifier was preset by expressions:

$$u_{1A} = U_m \sin(2\pi ft), u_{1B} = U_m \sin(2\pi ft - 2\pi / 3), u_{1C} = U_m \sin(2\pi ft + 2\pi / 3), \quad (11)$$

where:

$$U_m = 311 \text{ V}, f = 50 \text{ Hz}.$$

The calculations of the system's dynamic process have been executed by these meanings. Transformator's parameters:

$$r_{1A} = r_{1B} = r_{1C} = 2 \Omega; r_{2A} = r_{2B} = r_{2C} = 1 \Omega; \alpha_{1B} = \alpha_{1C} = 172 \text{ H}^{-1}; \alpha_{1C} = 172 \text{ H}^{-1};$$

$$\alpha_{2A} = \alpha_{2B} = \alpha_{2C} = 200 \text{ H}^{-1}; \alpha_{2B} = \alpha_{2C} = 200 \text{ H}^{-1}; \alpha_0 = 1.2 \text{ H}^{-1}; C = 9 \text{ mF}.$$

The magnetized curve was approximated by expression:

$$\varphi(\psi) = \begin{cases} m_1 \psi & \text{if } |\psi| > \psi_1 \\ S_3(\psi) & \text{if } \psi_1 \leq |\psi| \leq \psi_2; \\ m_2 \psi - m_0 & \text{if } |\psi| > \psi_2 \end{cases} \quad (12)$$

where:

$$m_1 = 0.25 \text{ H}^{-1}, m_2 = 3 \text{ H}^{-1}, \alpha_0 = 1.8 \text{ A}, \psi_1 = 0.2 \text{ Wb}, \psi_2 = 0.9 \text{ Wb},$$

$$\varphi(\psi_1) = 0.05 \text{ A}, \varphi(\psi_2) = 0.9 \text{ A}, S_3(\psi) \text{ is a cubic spline.}$$

DC motor's parameters:

$$L_A = 9.67 \text{ H}, L_{FF} = 110.8 \text{ H}, L_{AF} = L_{FA} = 0 \text{ H}, r_A = 33.2 \Omega, r_F = 173 \Omega,$$

$$J = 0.09 \text{ Nms}^2/\text{rad}, M_O = 4 \text{ Nm}, c = 70.8 \text{ Nm}/(\text{WbA}), u_f = 300 \text{ V}, k = 0.04.$$

On Fig. 3a the results of our system work simulation by DC motor without PID-regulator have been shown. The transient motor's characteristic has the overshoot before system's entrance into steady-state regime. On Fig. 3b condenser's voltage fluctuation has been shown in increase measure. These fluctuations consist $< 0.5 \text{ V}$ that's why it could be not taken into account.

On Fig. 4 the main dependences of control system without PID-regulator taken in steady-state regime were shown. The input voltage dependence u_C of filter's capacity rectifier on feeding voltage of three phase half wave rectifier has linear character. The dependence of DC motor's shaft speed rotation on input voltage also has a linear dependence (Fig. 4a). It is important to mark that voltage u_C for DC motor's start with independent excitation and established parameters ought to have the meaning no less than 28 V. These values' dependences on angle of delays have a nonlinear character (Fig. 4b).

Fig. 3. Transient response of control system of DC motor without PID-controller

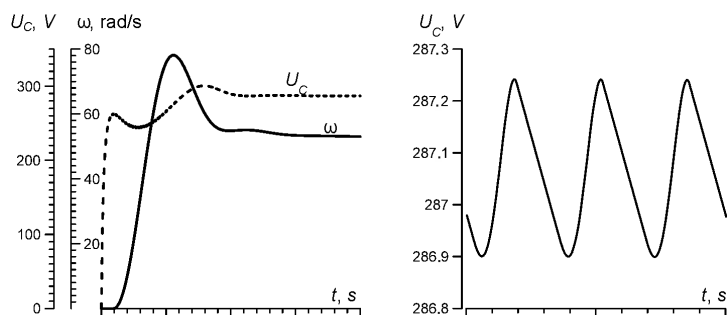
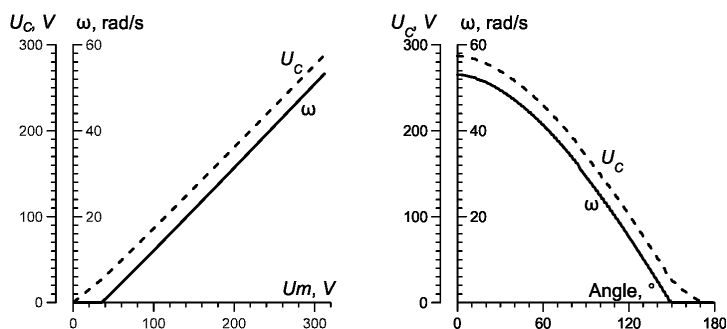


Fig. 4. Main dependences of control system without PID-controller



The parametric optimization of our control system has two components. The first

predicates the improvements of dynamic characteristics using additional resistances R_{Add} , R_{Add} , and the second predicates the selection of PID-regulator coefficients.

Using control system modeling it is established, that resistance R_{Add} reduces reregulation and the speed of DC motor's shaft will be also reduced. The resistance R_{Add} gives an opportunity to increase the speed.

For dynamic characteristic optimization of control system the described in chapter 5 genetic algorithms has been used. As the criteria for fitness function meaning the deviation of discrete instantaneous points on set meaning has been used. So, fitness-meaning is calculated by such a formula:

$$Fitness = \sum_i |\omega_{input} - \omega(t_i)|. \quad (13)$$

The control system modeling is executed by the Runge-Kutta method of fourth order. At the first investigation stage system's optimization is executed only for PID regulator parameters: K_p , T_i , T_d and the meaning of the integrator's commutation sum. Optimization

was executed for $\omega_{input} = 40 \text{ rad/s}$. At this stage it was charged that the optimal meaning for integrator's limit is ± 62 .

At the second investigation stage the system's optimization was executed by 5 parameters for which those limits was determined: $K_p = [0; 30]$, $T_i = [0; 1]$, $T_d = [0; 1]$, $R_{Add} = [0; 30] \Omega$, $R_{Fadd} = [0; 100] \Omega$. System's integration was executed during 4 seconds.

For genetic algorithm such settings have been chosen: 16 or 32 bites for gene's meaning quantization, the amount of population differs between 30–50 chromosomes, the probability of mutation differs in limits of 1–5%, pressure coefficient of selection was chosen as 1.7 or 1.8, for elitism 1 chromosome was chosen.

For optimized parameters $\omega_{input} = 40 \text{ rad/s}$ the dynamic characteristic of control system has a quality performance but for another determined meanings the dynamic characteristic becomes worse. So, it was decided to sum the fitness meaning for several ω_{input} (10 and 40 rad/s).

On Fig. 5 the transient processes were received and shown by genetic algorithm parameters meaning using: $K_p = 19.86$, $T_i = 0.172$, $T_d = 0.282$, $R_{Add} = 21,49 \Omega$, $R_{Fadd} = 66,63 \Omega$, $R_{Fadd} = 66,63 \Omega$.

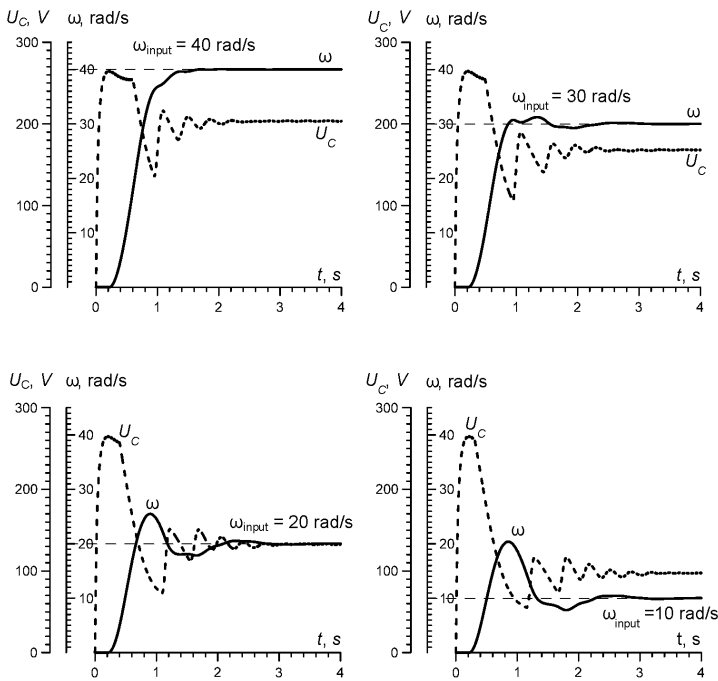


Fig. 5. Dynamic characteristics of the control system for different ω_{input}

On Fig. 6 the dynamic characteristics for optimized PID-regulator's coefficients and additional resistance have been shown. Determined meanings ω_{input} changed every 3 second (40, 10 and 30 rad/s). During this control system has been shown quality dynamic characteristic and stable character.

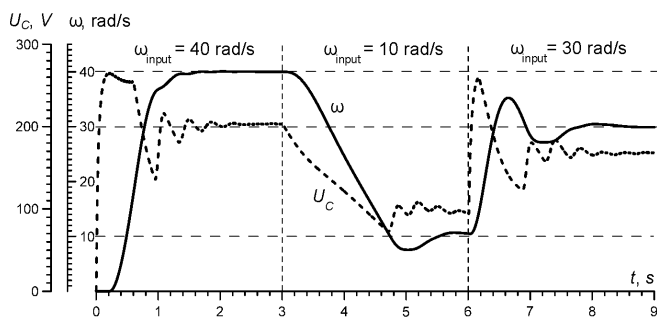


Fig. 6. Dynamic characteristic of the control system with change ω_{input}

7. Conclusions

Using the proposed mathematical model of thyristor control system of a DC motor's speed rotation with independent excitation the parametric optimization of control system has been executed. Using binary genetic algorithm the coefficients of PID-regulator and additional resistances for DC motor have been selected. The executed optimization gives an opportunity to receive the quality dynamic characteristics of DC motor's control system with independent excitation. The developed mathematical model of control system is universal and simple for algorithmization.

References

- [1] Samoty V., Dzelendzyak U., *Mathematical model of thyristor's system control of DC motor with independent excitation*, Technical Transactions, vol. 1-AC/2013, Cracow University of Technology Press, 2013, 79-91.
- [2] Chong E.K.P., Zak S.H., *An Introduction to Optimization*, 4th Edition, John Wiley & Sons, 2013.
- [3] Reiner Horst, Tuy Hoang, *Global Optimization: Deterministic Approaches*, 3rd edition, Springer-Verlag GmbH: Berlin, Germany, 1996.
- [4] Mordecai Avriel, *Nonlinear Programming: Analysis and Methods*, Dover Publications: Mineola, NY, USA, 2003.
- [5] Weise T., *Global optimization algorithms: theory and application*, 3rd Edition, Thomas Weise, 2011.
- [6] Sivanandam S.N., Deepa S.N., *Introduction to Genetic Algorithms*, Springer-Verlag Berlin Heidelberg, 2008.
- [7] Randy L. Haupt, Sue Ellen Haupt, *Practical genetic algorithms*, 2nd ed., John Wiley & Sons, Inc., Hoboken, New Jersey 2004.
- [8] Mitchell M., *An Introduction to Genetic Algorithms*, A Bradford Book The MIT Press, 1999.
- [9] Astrom K.J., Hagglund T., *Advanced PID control*, ISA - The Instrumentation, Systems, and Automation Society; Research Triangle Park, NC, 2006.
- [10] Hartmut Pohlheim, *Examples of Objective Functions*, 2006, www.geatbx.com.

CONTENTS

Czuchra W.: The influence of converter cables screening attenuation on radiated electromagnetic disturbances from converter drive	3
Lerch T., Rad M.: Influence of higher harmonics on losses in induction machines.....	13
Boguslawsky I., Kruchinina I., Liubimtcev A., Shtainle L.: Method of EMF total harmonic distortion calculation of the salient pole synchronous generator (using 2D simulation package).....	25
Dudzik M., Drapik S., Prusak J.: Approximation of overloads for a selected tram traction substation using artificial neural networks.....	39
Borkowski D.: Voltage and frequency control of A stand-alone induction generator using sVPWM converter in a small reservoir hydropower plant	51
Hudym V.I., Drozdowski P., Mamcarz D.: Influence of a passive controlled L-C filter on higher voltage and current harmonics in the power supply network for electric arc devices.....	65
Mysiński W., Pragłowska-Ryłko N.: Use of middlebrook's method in frequency analysis of power electronic circuits	75
Czuchra W., Mysiński W., Woszczyzna B.: Electromagnetic compatibility of SiC technology power converter	87
Tulicki J., Petryna J., Sułowicz M.: Fault diagnosis of induction motors in selected working conditions based on axial flux signals	99
Mazgaj W., Warzecha A.: Anisotropic Properties of dynamo Steel Sheets	115
Szczurek P., Mazgaj W., Banach A.: Influence of the magnetization direction ON power losses in transformer steel sheets.....	127
Setlak L., Ruda E.: Analysis and simulation of advanced technological solutions in the field of power high-voltage direct current (HVDC) of modern aircraft in line with the trend of more electric aircraft (MEA)	139
Hudym V.I., Drozdowski P., Postoliuk A., Mamcarz D.: Mathematical model of the six electrode pulse current electric arc furnaces	151
Bogusz P., Korkosz M., Prokop J.: Analysis of energy-saving structures of electric machines for domestic drive.....	163
Hudym V., Jagiełło A., Prusak J., Chrabaszcz I., Trębacz P.: Preventing the formation of ice on the catenary lines	173
Korkosz M., Podskarbi G.: Laboratory test of surface mounted permanent magnet brushless motor	185
Nowakowski G.: Conversion of fuzzy queries into standard SQL queries using oracle 11G XE.....	197
Samoty V.: Evolutionary optimization of dc motor control system.....	215
Telenyk S., Bukasov M.: Data center resource management for SAAS	229
Samoty V., Pavelchak A., Dzelendzyak U.: The method selection of control system's parametric optimization	237

TREŚĆ

Czuchra W.: Wpływ tłumienności ekranowania kabli przekształtnikowych na emisję zaburzeń elektromagnetycznych promieniowanych napędu przekształtnikowego.....	3
Lerch T., Rad M.: Wpływ wyższych harmonicznych na straty w maszynie indukcyjnej	13
Boguslawsky I., Kruchinina I., Liubimcev A., Shtainle L.: Metoda obliczenia współczynnika zawartości harmonicznych w sile elektromotorycznej dla wydawnobiegunowego generatora synchronicznego (z użyciem pakietu symulacyjnego 2D).....	25
Dudzik M., Drapik S., Prusak J.: Aproksymacja przeciążeń wybranej tramwajowej podstacji trakcyjnej z wykorzystaniem sztucznych sieci neuronowych	39
Borkowski D.: Sterowanie częstotliwości i napięcia autonomicznego generatora indukcyjnego przez przekształtnik SVPWM w zbiornikowej elektrowni wodnej.....	51
Hudym V.I., Drozdowski P., Mamcarz D.: Wpływ sterowanego filtra pasywnego na wyższe harmoniczne napięcia i prądu w sieciach zasilających urządzenia łukowe	65
Mysiński W., Pragłowska-Ryłko N.: Wykorzystanie metody middlebrook'a do analizy częstotliwościowej układów energoelektronicznych.....	75
Czuchra W., Mysiński W., Woszczyzna B.: Kompatybilność elektromagnetyczna przekształtnika energoelektronicznego wykonanego w technologii SiC	87
Tulicki J., Petryna J., Sułowicz M.: Diagnostyka silnika indukcyjnego w wybranych stanach pracy na podstawie sygnału strumienia poosiowego.....	99
Mazgaj W., Warzecha A.: Anizotropowe właściwości blach prądnicowych.....	115
Szczurek P., Mazgaj W., Banach A.: Wpływ kierunku magnesowania na straty mocy w blachach transformatorowych.....	127
Setlak L., Ruda E.: Analiza i symulacja zaawansowanych rozwiązań technologicznych w zakresie zasilania wysokiego napięcia prądu stałego (HVDC) współczesnych samolotów zgodnych z trendem samolotu bardziej elektrycznego (MEA)	139
Hudym V.I., Drozdowski P., Postoliuk A., Mamcarz D.: Model matematyczny sześcieelektrodowego pieca łukowego prądu impulsowego	151
Bogusz P., Korkosz M., Prokop J.: Analiza energooszczędnych konstrukcji maszyn elektrycznych napędów sprzętu AGD	163
Hudym V., Jagiełło A., Prusak J., Chrabąszcz I., Trębacz P.: Zapobieganie powstawaniu oblodzenia na przewodach sieci trakcyjnej	173
Korkosz M., Podskarbi G.: Badania laboratoryjne bezszczotkowego silnika z magnesami trwałymi montowanymi powierzchniowo	185
Nowakowski G.: Transformacja zapytań nieprecyzyjnych na zapytania w standardzie SQL przy wykorzystaniu Oracle 11G XE	197
Samoty V.: Optymalizacja ewolucyjna układu sterowania silnikiem prądu stałego.....	215
Telenyk S., Bukasov M.: Zarządzanie zasobami centrum danych dla SAAS	229
Samoty V., Pavelchak A., Dzelendzyak U.: Wybór metody optymalizacji parametrycznej systemów sterowania	237